Max-Planck-Institut für Physik
(Werner-Heisenberg-Institut)

The MAGIC Telescope: development of new technologies and first observations

Dissertation an der Fakultät für Physik
der Technischen Universität München

vorgelegt von

David Paneque

August 2004

The real voyage, is not to travel to new landscapes,
but to see with new eyes...

Marcel Proust

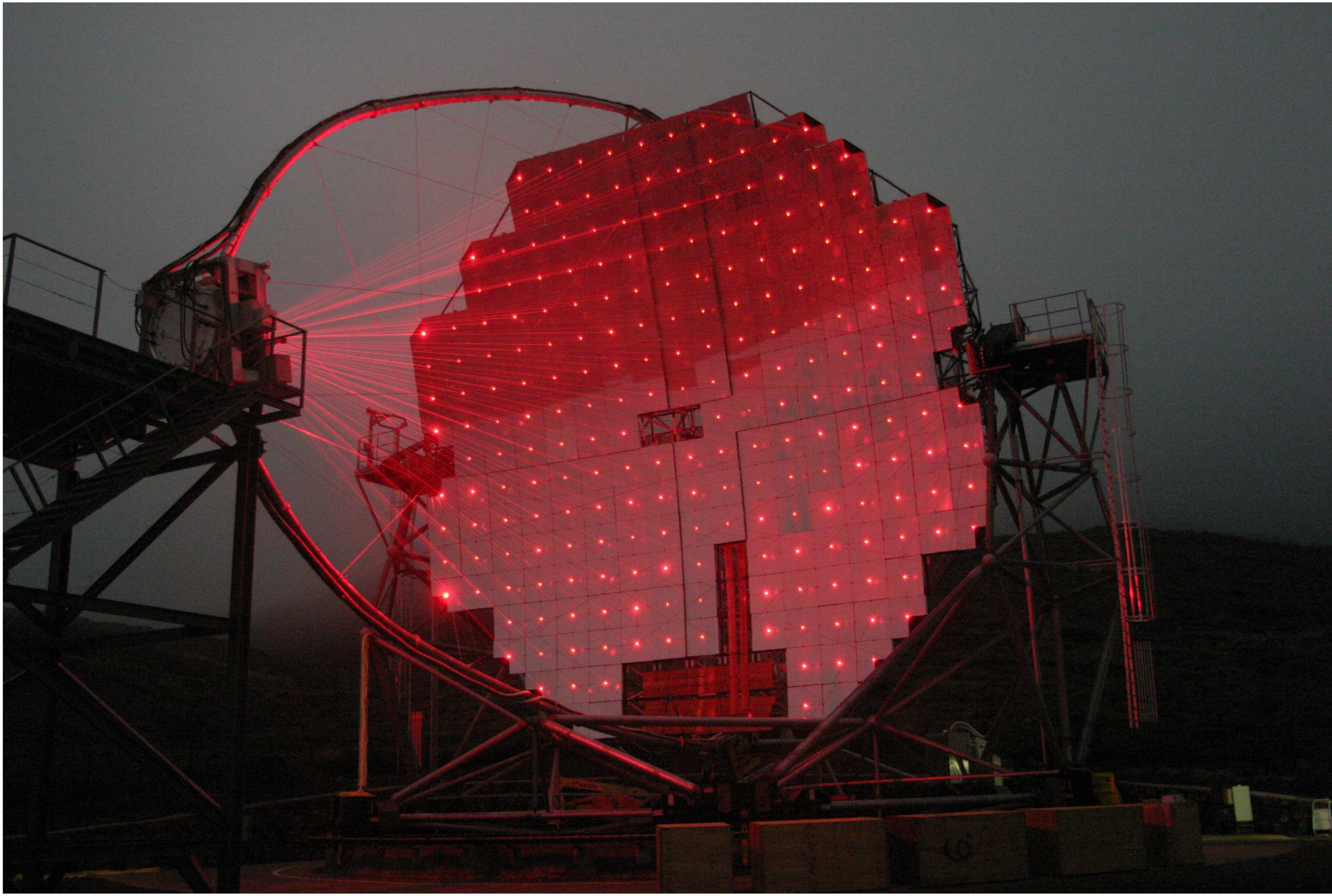

The MAGIC Telescope during the mirror alignment in a foggy night (winter 2003). The fog scatters the reference laser beams of the active mirror control system. Courtesy of R. Wagner.

Summary

The MAGIC Telescope is an *Imaging Air Cherenkov Telescope* (*IACT*) located on the Canary island of La Palma (28.8°N, 17.9°W), at the *Roque de los Muchachos Observatory* (2200 m above see level). The main goal of the experiment is to cover with high sensitivity the energy region between 10 GeV and 300 GeV in $\gamma - ray$ astronomy, which is inaccessible up to now, by lowering the *threshold energy* E_{th} as compared to the previous generation of *IACTs*. Observations in this new window of the electromagnetic spectrum are expected to provide key data for the understanding of a wide variety of astrophysical phenomena belonging to the so-called "non-thermal Universe", like the acceleration processes in *Active Galactic Nuclei* (*AGN*), the radiation mechanisms of *pulsars* and *Supernova Remnants* (*SNR*s), and the enigmatic *Gamma Ray Bursts* (*GRB*s). In addition, MAGIC may also contribute to the understanding of some open questions in fundamental physics, like the *Lorentz Invariance*, or the *Dark Matter* in the Universe.

The E_{th} of an *IACT* is primarily determined by its Cherenkov light collection and detection efficiency, which depends mainly on the mirror size and the photon detection efficiency of the camera. In order to achieve the lowest possible E_{th}, many new technologies had to be developed, thus entering also into a "new domain" from the technological point of view. The "key" elements of the MAGIC Telescope are the *large reflector* dish (17 m ϕ), the largest world-wide, and the *fine pixelized camera* with a *high photon detection efficiency.*

This thesis contains detailed studies about the development of new technologies which improved the sensitivity and the performance of the telescope camera. The thesis also reports about the extraction of the first significant γ signals from the first observations performed with the MAGIC Telescope.

As I mentioned above, a high photon-to-photoelectron conversion efficiency is very important to decrease the E_{th} of an *IACT*. I studied the possibility to increase the sensitivity of the MAGIC camera by enhancing the *quantum efficiency* (*QE*) of the photomultipliers (PMTs). The PMTs used in MAGIC are the 9116A and 9117A type from *Electron Tubes*. Both have a bialkali photocathode (*PhC*) with a hemispherical borosilicate window of 25 mm ϕ and

38 *mm* ϕ respectively. I found that a lacquer consisting of a *Wavelength Shifter* (*WLS*), a plastic binder and a rapidly evaporating solvent results (after application onto the hemispherical window of the PMT) in a milky layer that scatters the photons before they reach the *PhC*. This effect increases the path length of the photons inside the *PhC*, which enhances their probability to produce photoelectrons (*phe*). The net effect of the milky layer is a substantial increase in the PMT *QE* over the entire wavelength (λ) range where the PMT is sensitive. At the *QE* peak ($\lambda \sim$ 370-410 *nm*), the *QE* increases from 25% to about 30% when the PMT is coated with this lacquer; and the *QE* enhancement is even larger at longer wavelengths. Because of the use of the *WLS*, the PMT becomes substantially more sensitive also to light below 310 *nm* (which is the spectral cut-off mid point of the borosilicate window); at $\lambda \sim$280 *nm*, the *QE* of the coated PMT is still about 20%. In addition, due to the scattering of the photons in the milky layer, this special coating improves the spatial uniformity in the response of the PMTs.

The impact of this technique on the detection efficiency of MAGIC was estimated by folding the enhanced *QE* with the Cherenkov light spectrum (at 2200 *m* above see level) expected from the air showers. The result of this calculation was that the coating of the PMTs increases the photon conversion efficiency of MAGIC by 19 ± 2 %. This implies a reduction of the telescope E_{th} by a factor 1.19 (*i.e,* 16%). Due to the simplicity, low cost and effectiveness of this technique, the MAGIC collaboration decided to coat all the PMTs with this special lacquer.

I want to point out that the reduction of 16% in the telescope E_{th} achieved by coating the PMTs can also be obtained by increasing the area of the reflector by 19% (*i.e,* from 239 m^2 to 284 m^2); yet this modification would introduce additional problems related to the increase in the weight and the inertia of the telescope. In addition, it is worth mentioning that this increase in the reflector surface would cost about 200.000 Euros, whereas the price for coating all the PMTs of the telescope camera was less than 100 Euros. The salary of the PhD student is obviously not included in the 100 Euros.

The short (2-3 *ns* FWHM) analogue PMT signals from the telescope camera are transferred to the data acquisition building by a system based on optical fibers and Vertical Cavity

Surface Emitting Laser (VCSEL) drivers. The advantages of using optical links instead of coaxial cables are lower signal attenuation, basically no pulse dispersion, less weight and bulkiness, no crosstalk between channels, no electromagnetic pickup, no grounding problems and immunity against lightning strikes. The optical link system was built at the Max-Planck-Institut für Physik, and I was one of the responsible persons for its realization. This system was found capable of transmitting very short ($\lesssim 3ns$) pulses with almost no degradation. However, a study of the stability showed that the transmitted signal and noise performance of some channels could change significantly on time scales of several minutes. These performance problems were attributed to the activation/deactivation of transverse modes in the VCSELs (mode "hopping"), affecting the beam divergence angle and the polarization of the emitted light. The former affects the amount of light focussed into the fiber, and the latter the transmission of the light inside the optical fiber.

It was found that the dominant noise contribution came from the fluctuations in the baseline of the transmitted signal. These fluctuations were strongly correlated with the constant (forward) bias current of the VCSEL. We reduced significantly the effect of these instabilities by using a low bias current ($6\ mA$) and by increasing the amplification of the signal before it reaches the VCSELs. In addition, detailed quality checks were carried out for each single VCSEL, and all those lasers not fulfilling the strict requirements to be used in MAGIC were rejected. About 1000 VCSELs were measured, out of which 30% were rejected.

After the above mentioned VCSEL selection and modifications in the optical link system, the noise due to the mode "hopping" in the VCSELs was reduced to well below the level of the statistical photoelectron fluctuation in the PMT signal; and hence the optical system fulfilled the requirements to be used in the MAGIC Telescope.

In the last part of this thesis I present the first analysis of data taken with the MAGIC Telescope, which were recorded during the night of 14th-15th February 2004. The sources observed were the Crab Nebula and Markarian 421 (Mkn 421). The telescope was still in the commissioning phase, and these observations were made in between technical runs. The Crab Nebula was observed during 85 minutes, and Mkn 421 during 105 minutes. The purpose of the analysis was to evaluate the initial performance status of the telescope, as well as to demonstrate that significant γ signals could be extracted. In addition, these observations allowed us to test the analysis software with real data for the first time.

The analysis was carried out using the *supercuts method* to perform a *signal/background* separation based on (optimal) *cuts* in the *Hillas* image parameters [1]. The *cuts* on the image parameters were assumed to depend on the SIZE and the DIST parameters (*dynamical cuts*), which are related to the energy and the impact parameter of the showers, respectively. The *optimization of the cuts* was carried out by means of a set of classes and C++ routines that I developed.

Because of various performance problems of the telescope during these first observations, a special *preprocessing* of the shower images was necessary. This data preprocessing removed the small shower images, which are predominantly produced by low energy events. However, this special treatment of the data allowed us to detect γ signals from the Crab Nebula and Mkn 421 at significance levels of 13 and 30 sigmas. The detected rates were 6.4 ± 0.5 γ/min and 12.8 ± 0.4 γ/min for the Crab and Mkn 421 respectively. The error in the rates includes only statistical fluctuations. The computation of systematic errors would require a deeper study of the performance of the telescope, which we consider to be of minor value and interest for a detector which is still in commissioning phase.

The $\gamma - ray$ flux from Mkn 421 is usually an order of magnitude lower than that from the Crab Nebula. The two times higher detected γ rate from Mkn 421 (compared to that from the Crab Nebula) confirms the flaring state of this AGN during February 2004, which had been already detected by the the Rossi X-ray Timing Explorer satellite (RXTE) and the WHIPPLE telescope.

Using the known $\gamma - ray$ flux from the Crab Nebula (measured above 300 GeV by the WHIPPLE collaboration, and extrapolated to lower energies) and the efficiency of the MAGIC Telescope predicted by our Monte Carlo simulations, we estimated that the used analysis (data preprocessing and application of the optimized cuts) should produce a rate of detected γs of 10.4 γ/min, with a (physical) E_{th} of $\sim$150 GeV. In the real data we found a very preliminary detection γ rate from the Crab Nebula of 6.4 γ/min; which, at this stage of the experiment, can be regarded as a very satisfactory result.

Contents

Technical remark about the the references of this thesis

The thesis contains 112 references, out of which 16 are MAGIC internal notes. Many of these internal notes could eventually be published in the future; but currently they can only be accessed by the members of the MAGIC collaboration. I included them to provide those readers who work for MAGIC with additional information about some of the topics I briefly discuss along this thesis.

Chapter 1

Introduction

There is a close connection between the very small and the very large. In attempts to realize a unified field theory of the forces of nature, microphysics has been explored in Earth-based laboratories. Using our most powerful particle accelerators, we have attained knowledge about processes at a very small scale (*i.e,* at very high energies), where gluons hold together the quarks which make up the protons and neutrons of the ordinary matter. Three of the four known forces in nature (the electromagnetic force, the weak force, and the strong force) are quite well described by renormalizable quantum field theories in the context of the *Standard Model.* The signatures of unification between these forces and the fourth, gravity, might manifest themselves at extreme energies. One approach to explore this frontier of physics is to utilize the Universe as our high-energy laboratory.

It is worth recalling that the astronomical observations led in the past (directly or indirectly) to advances in fundamental and applied physics. For example, Kepler's discovery of the laws of planetary motion resulted from Tycho Brahe's magnificent set of astronomical observations. And Kepler's laws led directly to Newton's law of gravity and his laws of motion. Balmer's discovery of the formula for the wavelengths of the spectral lines of what we now call the *Balmer series of hydrogen* involved spectroscopic observations of the violet and ultraviolet lines of hydrogen in white dwarf stars. I want to point out that these lines could not be produced in the laboratory at that time. The Balmer formula was the key to Bohr's theory of the atom and consequently to the unravelling of atomic structure. Niels Bohr was awarded with a *Nobel Prize* in 1922 for this work. On the other hand, some of the best tests of the *General Theory of Relativity* were also provided by astronomical observations. One of the most spectacular of these tests has been the demonstration of gravitational radiation loss in the case of a binary pulsar system; work for which Russell A. Hulse and Joseph H. Taylor got a *Nobel Prize* in 1993. So the history has shown that important achievements in the knowledge of physics can be obtained by observing the Universe; and specially by studying those processes that take place in physical conditions which cannot be reproduced in Earth-based laboratories.

The *Cosmic Rays* (*CR*s) reaching the Earth give us information about the physical processes occurring in the most extreme cosmic environments of our Universe. The measured spectrum of *CR*s extends up to $3 \cdot 10^{20}\ eV$ [2], far above the energy scales accessible with the current terrestrial accelerators. The *CR*s consist mainly of high energy nuclear particles (predominantly protons, but also nuclei of helium and of higher elements), a small admixture of electrons (about 1% above $10^{10}\ eV$) and a still smaller fraction of $\gamma - rays$ ($< 10^{-4}$)[1]. The coarse knowledge of the *CR*s composition extends only up to energies of $\sim 10^{16}\ eV$. The differential flux spectrum of the *CR*s follows a broken power law according to $d\mathcal{F}/dE \propto E^{-a}$. The differential spectral index a has values between 2.6 and 3.1 depending on the energy region, as shown in figure 1.1. At present, we still do not know precisely neither the shape of the energy spectrum, nor the composition of the *CR*s at very high energies. And the main questions about the *CR*s still remain unresolved almost a century after their discovery in 1912 by Viktor Hess:

- Which are the sources they come from ?
- Which are the mechanisms accelerating particles to these high energies ?

The charged *CR*s are deflected in the weak galactic and intergalactic magnetic fields and thus they cannot be used to trace the particles back to their sources. Only extremely energetic ($E \gtrsim\ 10^{19} eV$) charged cosmic rays could point to their sources. However, due to the very low fluxes at these high energies, huge collection areas are needed in order to

---

[1] $\gamma - rays$ are usually defined as photons whose energy is larger than 1-10 MeV.

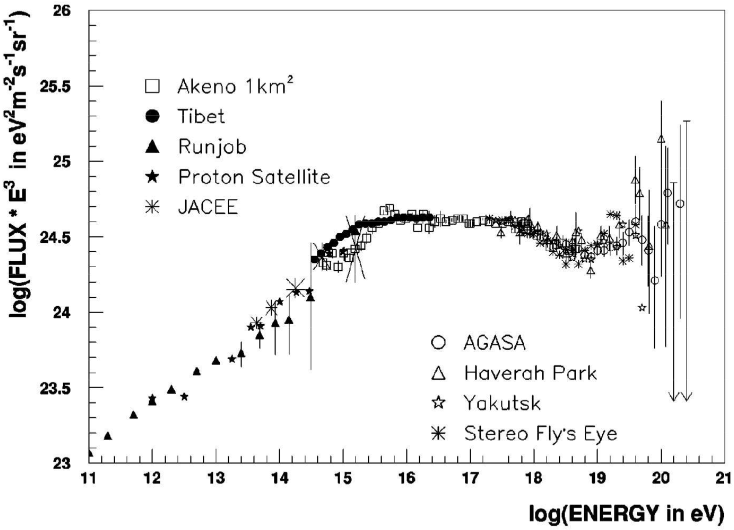

Figure 1.1: *Differential energy spectrum of primary Cosmic Rays over a broad energy range. The spectrum is multiplied by a factor* $(E/[eV])^{3.0}$ *for visual purposes. Adopted from [3].*

collect enough statistic for a reasonable study. Besides, the mechanisms accelerating these extremely high energy *CR*s might be different from the ones that produce *CR*s with energies below $10^{18} eV$. Therefore, the suitable particles for the search and investigation of the *CR*s sources are the neutral particles, namely photons, neutrons and neutrinos. Among them, free neutrons are unstable with a decay time of 886 s, and hence only the highest energy neutrons can be detected over large distances (comparable to the extension of our galaxy). As far as neutrinos are concerned, because of their small interaction cross sections, very large detectors are required, and their sensitivity is rather limited at present. Therefore, $\gamma - rays$ are the preferred messengers to investigate the processes that generate and accelerate particles up to high energies. The detected $\gamma - rays$ not only point back to their origin, but also set a lower energy limit to the initial physic processes from which they were generated. In addition, due to the fact that gamma quanta are massless, $\gamma - rays$ also allow us to study the time evolution of the acceleration mechanisms in the astrophysical sources.

The most important processes for the production of high energy electromagnetic radiation are:

- *1) Production and decay of* π^0. Neutral pions are produced in the interaction of high energy hadronic particles (mainly protons) with the ambient matter or γ-radiation. The π^0 mesons have a very short mean lifetime, 8.4 $\times 10^{-17} s$, and decay almost exclusively into 2 $\gamma - rays$ (with 99% *branching ratio*).

- *2) Inverse Compton scattering.* In this process, the high energy γ radiation is produced by the interaction of high energy electrons with low energy photons. The relativistic electrons *up-scatter* the low energy photons to higher energies, and hence the name *inverse Compton.*

- *3) Bremsstrahlung.* This radiation is emitted by charged particles when they are deflected by the Coulomb field of a nucleus or ion.

- *4) Synchrotron emission.* This radiation is emitted by charged particles when they are deflected by magnetic fields.

The mechanism *1)* requires *hadronic acceleration*, whereas the mechanisms *2)*, *3)* and *4)* occur when *acceleration of electrons* takes place in the cosmic sources. The preferred mechanisms for the production of $\gamma - rays$ of energy $\gtrsim$1 GeV are the *inverse Compton scattering* processes and the *production and decay of* π^0*s.* The $\gamma - ray$ emission above 1 GeV due to *bremsstrahlung* has typically a lower intensity than the one due to *inverse Compton scattering.* And very large magnetic fields and/or high energy electrons are needed to produce $\gamma - rays$ by *synchrotron* emission. The Crab Nebula is one of the known places where both high magnetic fields and very high energetic electrons exist. Despite these favorable conditions, the highest $\gamma - ray$ energies achieved in the Crab Nebula by the *synchrotron* mechanism are only of about 0.1 GeV [4].

The sources of *CR*s will definitely produce $\gamma - rays$ through π^0 decays; yet $\gamma - rays$ can also be produced in "non-*CR*s sources" by means of *inverse Compton scattering.* Nowadays, the determination of the physic processes (*hadronic* or *leptonic* acceleration) taking place in the detected $\gamma - ray$ sources is one of the major tasks of the high energy $\gamma - ray$ astronomy.

There are several astrophysical objects which emit high energy $\gamma - rays$ and which could be also the sources of *CR*s, namely *Supernova Remnants* (*SNR*s), *pulsars*, *Active Galactic*

Nuclei (*AGN*), *Gamma-Ray Bursts* (*GRB*s) and *binary systems* like *Cataclysmic variables*, *X-Ray binaries* and *microquasars*. The derived energy spectra of these sources, as well as the temporal variations of the photon emission observed at different wavelengths could be used to set constraints on the involved acceleration processes. Therefore, by means of detailed observations of these $\gamma - ray$ sources one might eventually understand the different production mechanisms.

The main experimental problem of $\gamma - ray$ astronomy is the very small fraction of $\gamma - rays$ within the *CR*s. As mentioned above, the γ radiation accounts for less than 0.01% of the *CR*s. In satellite-borne detectors it is possible to separate efficiently γs from charged *CR*s by means of anti-coincidence counters. However, these detectors have at most 0.1 m^2 of detection area, and since the photon flux decreases exponentially with the energy, their sensitivity for energies $\gtrsim 10\ GeV$ is limited by very low statistics. On the other hand, ground-based detectors can be used to observe indirectly $\gamma - rays$ of energies $\gtrsim 10\ GeV$ through the detection of the *Extended Air Showers* (*EAS*s) induced by the $\gamma - rays$ in the Earth atmosphere. In this case, the atmosphere serves as a calorimeter, and effective collection areas of $\sim 10^5\ m^2$ can be achieved. The main drawback of this method is that the distinction between the γ-induced showers (signal) and the much more abundant *hadron*-induced showers (background) is not an easy task.

There are three methods to observe *EAS*s, namely:

- *1)* Detection of the fluorescence light emitted by the nitrogen molecules after being excited by the (secondary) charged particles of the *EAS*s.
- *2)* Direct detection of the (secondary) charged particles of the *EAS*s at ground.
- *3)* Detection of the Cherenkov light emitted by the charged particles (mainly from $e^{\pm}$) of the *EAS*s.

The third method allows one to detect *EAS*s with the lowest energies (*i.e,* lowest *threshold energy*) compared to the other two methods. From the total energy of the primary particle, the fraction going into Cherenkov radiation is about 10^{-4} whereas the fraction converted into fluorescence light is only about 10^{-5}. Besides, the Cherenkov radiation is strongly

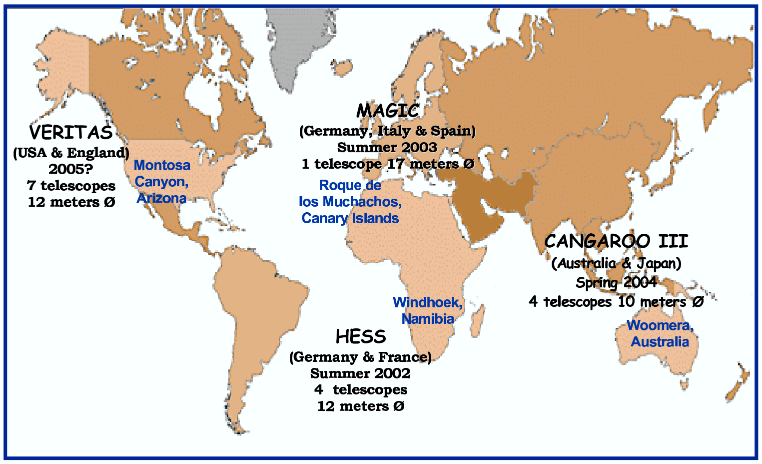

Figure 1.2: *World map with the location of the largest Imaging Cherenkov Telescope Observatories. The countries from the main groups supporting these observatories, the date at which they started (or are planned) to function, and the dimensions of the main reflector are also specified.*

collimated, while the fluorescence light is isotropically emitted, thus one typically collects a smaller amount of the radiated energy in the latter case. As compared to the method *2)*, the Cherenkov radiation can be detected even for showers whose charged secondaries do not reach the ground; and hence the lower threshold energy is obvious.

Nowadays, the most successful devices for $\gamma - ray$ astronomy based on the detection of Cherenkov light from *EAS*s are the so-called *Imaging Air Cherenkov Telescopes* (*IACTs*). Figure 1.2 shows a map with the location of the most sensitive *IACT* observatories worldwide. Because of their significant improvement in performance with respect to previous *IACTs*, they are usually called *new generation IACTs*. The general working principle and the basic characteristics of *IACTs* are explained in section 2.3. Here, I only want to point out that the minimum $\gamma - ray$ energy which can be detected depends essentially on the dimensions of the reflector and on the sensitivity of the light detectors in the camera. Before the year 2004, there was an observational gap between the highest $\gamma - ray$ energies detected by satellite-borne detectors ($\lesssim 10\ GeV$), and the lowest $\gamma - ray$ energies detected by *IACTs* ($\gtrsim 300\ GeV$).

The main goal of the MAGIC Telescope is to cover with high sensitivity the energy range between 10 GeV and 300 GeV in $\gamma - ray$ astronomy, which is inaccessible up to now, by lowering the *threshold energy* (E_{th}) with respect to previous and contemporary ground-based instruments. While the other new generation *IACTs* aim to improve the sensitivity and the energy resolution above 100 GeV by using stereoscopic systems of telescopes with medium-size (10-12m ϕ) reflectors, MAGIC aims to achieve the lowest E_{th} by using new technologies which increase the sensitivity and the performance of the telescope camera, and by having the largest reflector among the existing (and under construction) Cherenkov telescopes. In the first phase of MAGIC, in which the camera is equipped with PMTs as photodetectors, the estimated E_{th} is about 25 GeV.

The possibility to perform $\gamma - ray$ astronomy in the still unexplored energy range from about 25 GeV to 300 GeV provides MAGIC with a huge potential to observe a large variety of cosmic sources, like AGNs, *pulsars*, regions populated with *dark matter*, *SNR*s, and *GRB*s[2]. It is worth to point out that due to the absorption of the $\gamma - rays$ through interaction with the Extragalactic Background Light (*EBL*), only a few AGNs have been observed up to now by ground-based $\gamma - ray$ telescopes. The low E_{th} of MAGIC will extend the observable Universe in $\gamma - rays$ well beyond the limits of the present ground-based instruments. Furthermore, if a large sample of AGNs at different redshifts is detected by MAGIC, an indirect measurement of the infrared background light density might also be feasible.

I have devoted my thesis work to the following key tasks of the design, construction and commissioning of the MAGIC Telescope:

- The enhancement of the sensitivity of the PMT camera.
- The improvement in the quality of the optical transmission of the analogue PMT signals from the telescope camera to the data acquisition center.
- The extraction of γ signals from the first observations performed with MAGIC.

Each of these points will be described in detail in the chapters 4, 5 and 6 respectively.

---

[2] In addition to the low E_{th}, another "key" element for the observation of *GRB*s is the low inertia of the telescope; which allows MAGIC to access any position of the sky within 20s.

Chapter 2

Detection of high energy $\gamma - rays$ with *Imaging Air Cherenkov Telescopes*

In this chapter I will describe how an *Imaging Air Cherenkov Telescope* (*IACT*) can indirectly detect $\gamma - rays$ entering the Earth atmosphere. First of all, I will briefly report about the features of *Extended Air Showers* (*EAS*s) produced in the Earth atmosphere by high energy ($> 1\ GeV$) $\gamma - rays$. Afterwards I will briefly describe *EAS*s induced by charged Cosmic Rays (which are $\approx 10^4$ times more numerous in the energy range 10 GeV-10 TeV compared to $\gamma - rays$), stressing the differences with respect to γ-induced *EAS*s. Then I will report about the production of Cherenkov light in an *EAS*. Finally, I will describe how it is possible to observe *EAS*s and to distinguish between γ- and *hadron*-induced *EAS*s by using the images produced in the pixelized camera of an *IACT* by the short Cherenkov light flashes.

2.1 Development of extended air showers in the atmosphere

An *EAS* is a cascade of particles triggered by the interaction of a single high energy primary cosmic ray nucleus or photon near the top of the atmosphere (~25 km). Consequently,

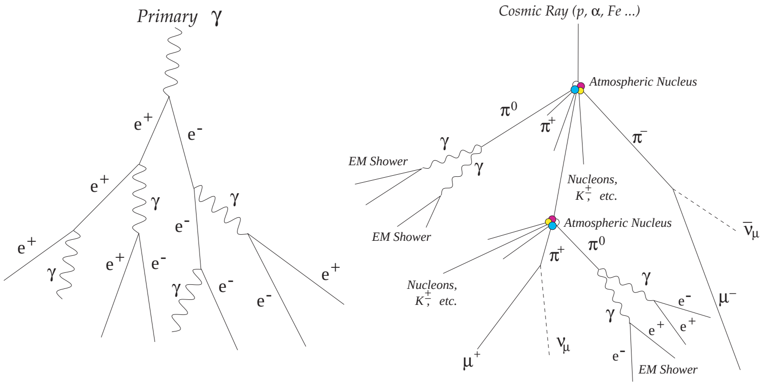

Figure 2.1: *Principal development of an EAS; a) induced by a $\gamma - ray$ and b) induced by a charged cosmic ray.*

several secondary particles are generated, which again interact with the atmosphere. At first, the number of secondary particles grows rapidly, and the *EAS* evolves. Since the energy of the primary particle is distributed over all secondary particles, at some point the energy of the particles falls below the threshold for further particle production. Then, energy losses due to ionization processes become dominant, and the shower dies out.

In the following sections I will briefly report about the development of $\gamma-$ and hadron-induced showers[1], stressing the differences between them.

2.1.1 $\gamma-$induced ***EAS*s**

The development of an *EAS* induced by a $\gamma - ray$ entering the atmosphere starts with the production of an electron-positron pair within the Coulomb field of an atmospheric nucleus. Due to the high mass of the muons, the cross section for muon-antimuon production is negligible (12 μb in air) in comparison to the cross section for electron-positron production (520 mb in air). The electrons and positrons radiate new $\gamma - rays$ in the presence of the Coulomb field of the atmospheric nuclei (*bremsstrahlung*), and then the process repeats; hence increasing the number of $e^{\pm}$ and γs (with lower energy) in the *EAS* (see figure 2.1a).

---

[1] Hadron-induced showers are the major background in the detection of γ-induced showers by *IACTs* (see section 2.3.3).

Due to the fact that nearly only electromagnetic interactions take part in this development[2], γ-induced EAS are often called *electromagnetic showers*.

The multiple scattering of the $e^{\pm}$, deflects the secondary particles away from the primary $\gamma - ray$ direction, the so-called *shower axis*, and the particles form a kind of disc of few meters thickness that moves downwards with a speed close to c. The energy of the secondary particles decrease as the shower development proceeds (and the number of particles increases). When the mean energy of $e^{\pm}$ is below a critical energy E_c ($E_c \approx 83\ MeV$ in air), the dominant energy loss process becomes ionization, rather than bremsstrahlung. In addition, when the mean photon energy decreases, the production cross section for $e^{\pm}$ pairs decreases until it becomes (at energies below few MeV) of the same order as that for Compton scattering and photoelectric absorption. Thus, the shower reaches its maximum development when the average energy of the cascade particles is about E_c. At larger depths the number of particles falls off because of ionization losses, which increase rapidly once the electrons become non-relativistic.

A very simple model, due to Heitler (1944), illustrates some general features of electromagnetic showers [6]. In the ultrarrelativistic limit, the $e^{\pm}$ radiation length for bremsstrahlung (ξ_{brems}) is approximately equal to the interaction length for pair production of photons of similar energy (ξ_{pair}) [7]. ξ_{brems} is defined as the mean distance traveled by the $e^{\pm}$ when their energy is reduced by a factor e; and ξ_{pair} is defined as the mean distance at which the initial number of $\gamma - rays$ is reduced by a factor e. In the case of air, $\xi_{brems} \sim 37\ g/cm^2$ and $\xi_{pair} \sim 47\ g/cm^2$; *i.e,* $\xi_{pair} \approx 9/7 \cdot \xi_{brems}$. Making the approximation $\xi_{pair} \approx \xi_{brems} = \xi_0$, and defining $R = \xi_0 ln2$, the energy per particle decreases by a factor $exp(-R/\xi_0) = 1/2$ after traveling through an atmospheric thickness R. Assuming that in each interaction the energy is equally distributed between the resulting electrons and photons, after traveling through a thickness nR, the number of secondary electrons and photons will be 2^n, and their mean energy $E_0/2^n$, where E_0 is the energy of the primary $\gamma - ray$. At the shower maximum, the number of $e^{\pm}$ and γs is approximately E_0/E_c. The position of the maximum (X_{max}) can be

---

[2] The cross section for *photoproduction* increases with the energy of the $\gamma - rays$, yet it is only 1-2 mb in the energy range $100 GeV$-$20 TeV$ [5].

computed as

$$X_{max} \;=\; R \cdot ln(E_0/E_c)/ln2 \;=\; ln(E_0/E_c) \cdot \xi_0 \tag{2.1}$$

The development of an electromagnetic shower was computed analytically by Rossi and Greisen in the 40s [8]. It is possible to achieve an analytical solution of the "shower equations" if some approximations are made. In the so-called "B approximation", one neglects photo-production mechanisms, the Compton effect and the production of electrons in *knock-on* interactions; and it is assumed that the electron ionization energy loss is continuous and fixed to a constant quantity in each radiation length. Defining N_e as the total number of electrons and positrons above the critical energy E_c, the "B approximation" leads to the so-called Greisen equation [9]

$$N_e(t, E_0) \;=\; \frac{0.31}{\sqrt{ln(E_0/E_c)}} \cdot exp[t \cdot (1 - 1.5lns)] \tag{2.2}$$

where t is the atmospheric depth[3] (χ) expressed in radiation lengths, and s is the *shower age*, which is a dimensionless quantity defined as $s(t, E_0) \;=\; 3t/(t + 2ln(E_0/E_c))$. The meaning of the shower age s is given by the derivative $dN_e(t, E_0)/ds$. At $0 < s < 1$, $dN_e(t, E_0)/ds > 0$, and N_e increases; at $s = 1$, $dN_e(t, E_0)/ds = 0$ and N_e is maximum and finally, when $s > 1$, $dN_e(t, E_0)/ds < 0$ and the shower starts dying out. The variation of the number of N_e with t is often called *longitudinal development* of the shower. The longitudinal developments for several values of E_0/E_c are shown in figure 2.2.

The lateral distribution of electrons can be modeled by the NKG-formula, which was derived by Nishimura and Kamata [10] and modified by Greisen [11]. The NKG-formula describes the $e^{\pm}$ density as a function of the distance r from the shower axis.

$$\rho_e(r, t, E_0) \;=\; \frac{N_e(t, E_0)}{r_M^2} \cdot \left(\frac{r}{r_M}\right)^{s-2} \cdot \left(1 + \frac{r}{r_M}\right)^{s-4.5} \frac{\Gamma(4.5 - s)}{2\pi\Gamma(s)\Gamma(4.5 - 2s)} \tag{2.3}$$

where Γ is the Gamma function and r_M is the multiple scattering Molière radius (79 m at see level).

---

[3] The atmospheric depth χ determines the thickness of the atmosphere along the shower axis $\chi \;=\; \int_h^{\infty} \rho_{air}(h)dh$, $[g/cm^2]$.

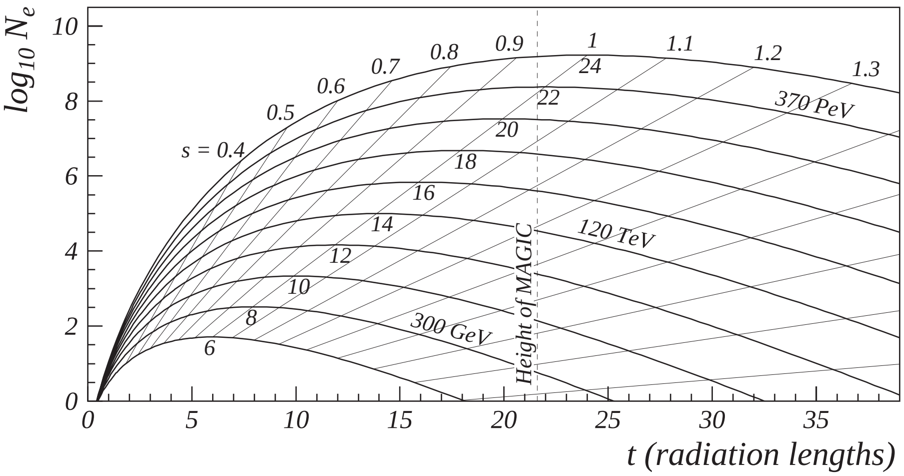

Figure 2.2: *Longitudinal development of electromagnetic showers (Greisen approximation). Several lines are used for different primary energies* E_0*. The values* $ln(E_0/E_c)$ *are shown right under the corresponding line. The atmospheric depth at see level is about 28 radiation lengths.*

2.1.2 Hadron-induced *EAS*s

An *EAS* induced by a charged cosmic ray (often called *hadronic or nucleonic shower*) starts with the collision of the incident cosmic ray with an atmospheric nucleus (see figure 2.1b), producing pions, kaons and nucleons. The secondary nucleons, charged pions and kaons which have sufficient energy continue to multiply in successive generations of nuclear collisions until the mean energy per particle drops below that required for multiple pion production (about 1 GeV). At that moment, ionization processes become dominant and the hadronic particles are brought eventually to rest.

About 90% of all secondary particles produced in a hadronic shower are pions; out of which 1/3 of are neutral pions. The π^0 mesons have a very short lifetime, 0.84 $\times 10^{-16}$ s, and decay almost exclusively into 2 $\gamma - rays$ (with 99% *branching ratio*). Each of these $\gamma - rays$ initiates an electromagnetic shower (see section 2.1.1). Since π^0 mesons carry, in average, about 30% of the energy from each hadronic interaction, this process transfers steadily energy from the hadronic to the electromagnetic part of the shower. Therefore, even hadronic showers are dominated at their tail by photons and electrons.

On the other hand, the secondary charged pions and kaons decay sometimes into muons and neutrinos through the channels $\pi^{\pm} \rightarrow \mu^{\pm} + \nu_{\mu}(\bar{\nu}_{\mu})$ (mean lifetime $\tau = 2.6 \times 10^{-8}\ s$); $K^{\pm} \rightarrow \mu^{\pm} + \nu_{\mu}(\bar{\nu}_{\mu})$ and $K^{\pm} \rightarrow \pi^{\pm} + \pi^{0}$ (mean lifetime $\tau = 1.2 \times 10^{-8}\ s$) with a branching ratio of 63.4% and 21.1% respectively. The decay channels $\pi^{\pm} \rightarrow e^{\pm} + \nu_{e}(\bar{\nu}_{e})$ and $K^{\pm} \rightarrow e^{\pm} + \nu_{e}(\bar{\nu}_{e})$ are strongly suppressed due to helicity conservation. The rate of meson decay over interaction rate is given by the ratio of the decay lengths $(\gamma \cdot c \cdot \tau)$ over the hadronic interaction lengths. At low shower ages, the Lorentz factor of these particles might be high enough so that hadronic interactions are more probable than decays. Besides pions and kaons, also some secondary baryons and charmed mesons are produced. However, they represent a minuscule fraction of the secondaries and hence they can be neglected in the general discussion.

It is worth noticing that the elastic scattering does not "bleed off" energy, and that, at high energies, the related scattering angle is substantially smaller than the transverse kick of the hadronic interactions. Therefore, the effect of the elastic scattering on hadronic showers can be ignored.

The muons have very small nuclear cross sections, and basically they only lose energy *via* ionization processes. The muons decay through the channel $\mu^{\pm} \rightarrow e^{\pm} + \nu_{e}(\bar{\nu}_{e}) + \bar{\nu}_{\mu}(\nu_{\mu})$ (mean lifetime $\tau = 2.2 \times 10^{-6}\ s$) releasing a fraction of their energy into the electromagnetic component. Many of the muons are produced with very high energy in the uppermost layers of the atmosphere, and due to their high Lorentz factors ($> 20 - 30$) they can reach the surface of the Earth intact[4]. These muons, together with the neutrinos, remove part of the shower energy from the atmosphere.

Hadron-induced EASs have three components: a hadronic core built up from high energy nucleons and mesons, a set of electromagnetic sub-showers originated mainly from π^{0} decays and a fraction of nearly non-interacting muons and neutrinos.

The most simple model of a hadronic shower is the superposition model [9], in which it is assumed that a nucleus of atomic mass A and energy E_0 is equivalent to A independent

---

[4] The presence of high energy muons at the Earth surface is one of the classical proofs of relativistic time dilation and length contraction.

protons of energy E_0/A. Being ξ_N the length of nuclear interaction of a hadronic particle in air, one can get an expression similar to equation 2.1

$$X_{max} \propto ln[E_0/(AE_c)] \cdot \xi_N \tag{2.4}$$

Therefore, for primary cosmic rays of a given energy, the showers produced by those cosmic rays of higher mass do develop at smaller atmospheric depths (*i.e,* at larger heights). On the other hand, the fluctuations of the position of X_{max} will be smaller for heavy nuclei, simply because each of them is equivalent to a beam of many (lighter) nuclei.

The nuclear interaction length in air ξ_N for protons is 83 g/cm^2, and for pions is 107 g/cm^2. Note that the nuclear interaction lengths of hadrons in air are substantially larger than the radiation length for bremsstrahlung ξ_{brems} (37 g/cm^2) and the interaction length for pair production ξ_{pair} (47 g/cm^2); which implies that the X_{max} of proton-induced showers is (in average) larger than that of gamma-induced showers of the same energy.

A much more detailed study of atmospheric hadronic showers can be achieved by means of Monte Carlo simulations. The larger uncertainties in the results obtained with these methods arise from the currently unknown details of the hadronic interactions at very high energies. It must be stressed that some of the energies ($\gtrsim$ 500 GeV) involved in the atmospheric processes described above exceed those ones explored in particle accelerators, and thus certain extrapolations must be utilized. Besides, in current storage ring experiments one mainly studies processes leading to high P_T secondaries, while in the development of an *EAS* the dominating processes are in the very forward direction.

In this work, the version *6.019* of the program *CORSIKA* (which was developed by the KASKADE collaboration [12]) was used to simulate the development of the atmospheric showers.

2.2 Cherenkov light in an *EAS*

2.2.1 Nature of the Cherenkov radiation

When a charged particle moves inside a transparent dielectric medium at a speed $v = \beta \cdot c$ larger than the light speed in this medium (*i.e,* $\beta > 1/n$, being n the refractive index of the medium), it emits light. The light emission results from the re-orientation of the instantaneous electric dipoles induced by the particle in the medium. This radiation was discovered by P.A. Cherenkov in 1934 (though the theoretical explanation was given by Frank and Tamm in 1937) and is called Cherenkov radiation.

At low speeds, the symmetry in the orientation of the charges around the position of the charged particle is such that there is no net effect at large distances, *i.e,* there is no radiation (figure 2.3a). Yet, when β is comparable to $1/n$, a net polarization of the medium occurs along the trajectory of the particle, and consequently, short electromagnetic impulses are emitted (figure 2.3b). Provided $\beta > 1/n$, the electromagnetic impulses originated in the different trajectory elements are in phase, and a net field can be produced at distant locations. The simple geometric picture for this process is that, because the particle moves "superluminally" through the medium, a shock-wave is created behind the particle, and this results in a loss of energy by the particle. The wavefront of the radiation propagates at a fixed angle θ ($cos\theta = 1/(\beta n)$) with respect to the velocity vector of the particle because only in this direction the wavefronts add up coherently according to Huygen's construction, as shown in figure 2.3c. Note that the maximum emission angle occurs when the particles are ultrarrelativistic ($\beta = 1$) and it is

$$\theta_{max} = cos^{-1}(1/n) \tag{2.5}$$

On the other hand, the minimum speed for Cherenkov light emission is $\beta_{min} = 1/n$; which sets a threshold energy (E_{th}^{Che}) for charged particles to emit Cherenkov light:

$$E_{th}^{Che} = \frac{m_0 c^2}{\sqrt{1-\beta_{min}^2}} = \frac{m_0 c^2}{\sqrt{1-n^{-2}}} \tag{2.6}$$

where m_0 is the rest mass of the charged particle. At see level, the refractive index is $n \simeq 1.00029$, which means that the E_{th}^{Che} for electrons, muons and protons is 21.3 MeV, 4.4 GeV and 39.1 GeV respectively.

2.2.2 Production of Cherenkov radiation in an *EAS*

In order to compute the threshold energy for Cherenkov emission and the maximum Cherenkov angle at different atmospheric depths, one needs to use a simplified model of the

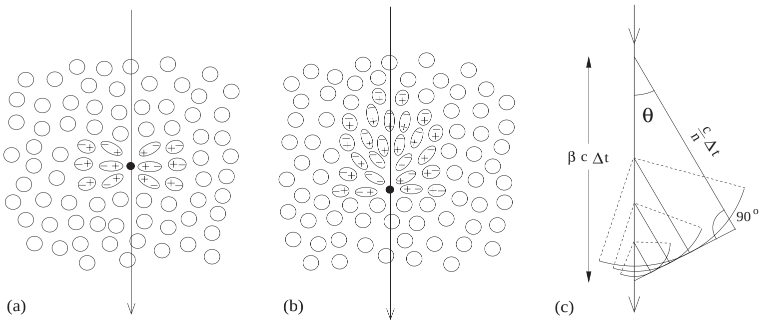

Figure 2.3: *Polarization produced in a dielectric medium by a charged particle: a) low speed; b) high speed; c) propagation of Cherenkov light derived from Huygen's principle.*

atmosphere. Most models for the atmospheric density distribution as function of altitude assume that the density ρ varies exponentially with the height h

$$\rho(h) \;=\; \rho_0 \cdot exp(-\frac{h}{h_0}) \tag{2.7}$$

where $h_0 = 7.1\ km$ and ρ_0 is the air density at see level, which is $0.0013\ g/cm^3$. Then, one can compute the refractive index n at the height h as [13]

$$n = 1 + \eta_h = 1 + \eta_0 \cdot exp(-\frac{h}{h_0}) \tag{2.8}$$

where $\eta_0 = 2.9 \cdot 10^{-4}$. The frequency dependence of the refraction index in air is very small (few % in $1-n$) and is neglected in this discussion[5]. The refractive index also depends slightly on the air temperature, which decreases with the height. The effect is small (at 15 km the difference in $1-n$ when including the temperature dependence is about 15%), and has been also neglected for simplicity. Finally, I also want to point out that this approximation is only valid at low zenith angles. At large zenith angles the curved atmosphere has to be taken into account. For simplicity, I will also neglect this effect in the general discussion.

Using the equations 2.5, 2.6, 2.8 and the fact that $\eta_h << 1$, one finds the following expressions for the height dependent threshold energy and maximum Cherenkov angle

$$E_{th}^{Che} \simeq \frac{m_0 c^2}{\sqrt{2\eta_h}} \qquad\qquad \theta_{max}(rad) \simeq \sqrt{2\eta_h} \tag{2.9}$$

---

[5] The variations of $1-n$ are about 5% for wavelengths in the range 300-600 nm (U.S. standard atmosphere at 1013.25 hPa, 15°C, [14]).

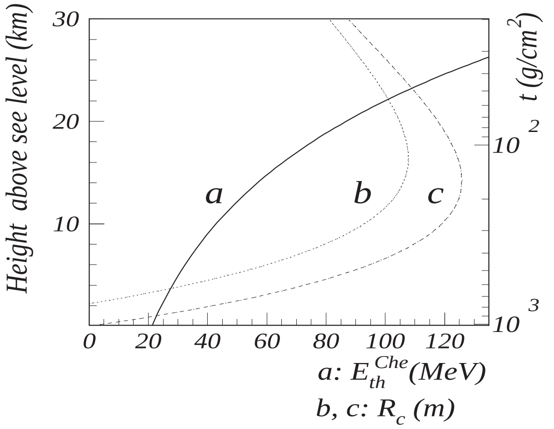

Figure 2.4: *a) Relation between* E_{th}^{Che} *and the height* h*; b) Relation between* R_c *at* $h_{obs} = 2200$ m *and the height* h *of emission; c) Relation between* R_c *at* $h_{obs} = 0$ m *and the height* h *of emission.*

It is worth noticing that, when the height h increases, η_h decreases; and hence the threshold energy to emit Cherenkov light E_{th}^{Che} increases. As an example, at 10 km above see level, $\eta_h = 7.1 \cdot 10^{-5}$, and the E_{th}^{Che} for electrons, muons and protons is 42.9 MeV, 8.9 GeV and 78.8 GeV respectively. These values are about two times larger than the ones computed for $h = 0$ km (see section 2.2.1); *i.e,* $E_{th}^{Che}(h = 10\ km) \simeq 2 \cdot E_{th}^{Che}(h = 0\ km)$.

Nearly all the Cherenkov light produced in an EAS originates from electrons. Note also that, at 10 km height, E_{th}^{Che} is smaller than the critical energy E_c ($\sim$83 MeV); and therefore most of the $e^{\pm}$ are still emitting Cherenkov light when the electromagnetic shower starts dying out (see section 2.1.1).

Knowing θ_{max}, one can compute the distance R_c from the emitted Cherenkov photons to the trajectory of the emitting charged particle at a given height h_{obs}

$$R_c \;=\; (h - h_{obs}) \cdot tan\theta_{max} \qquad (2.10)$$

Figure 2.4 shows the quantities $E_{th}^{Che}(h)$ and $R_c(h)$ for ultrarrelativistic electrons entering vertically into the atmosphere. For this calculation, the energy losses due to bremsstrahlung radiation have been neglected; and hence the electrons are ultrarrelativistic along the entire path. Two observation heights have been used; the see level ($h_{obs} = 0$ m) and the height at which the MAGIC Telescope is located ($h_{obs} = 2200$ m). Note that $R_c(h)$ has a maximum

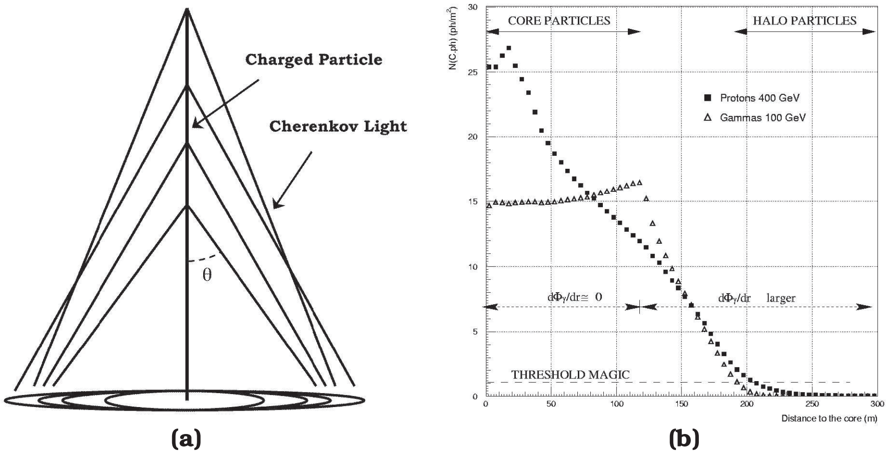

Figure 2.5: *a) Schematics of the Cherenkov light "ring" produced by an ultra-rrelativistic charged particle at the observation level; b) Lateral distributions of Cherenkov photon density for vertically incident 100 GeV gamma and 400 GeV proton showers at an altitude of 2200 m above see level.*

when the emitting particle is between 10 and 20 *km* above see level. That is the reason for the formation of a narrow circular enhancement of light density at $\sim$ 100 *m* ($\sim$ 120 *m* at see level), resulting from a large fraction of all the Cherenkov light being emitted between these two heights.

Figure 2.5a shows a schematic of how the light emitted at different heights reaches the ground at approximately the same distance from the trajectory of the emitting charged particle; thus producing a characteristic Cherenkov light density enhancement ("ring") around the impact point of the particle.

In an electromagnetic shower the directions of the emitting electrons (positrons) diverge from that of the incoming primary $\gamma - ray$ due to the multiple Coulomb scattering [15], and also due to the Earth magnetic field [16, 17]. Consequently, the above mentioned light pattern is somewhat spread out; yet it does not disappear completely for those showers developing high enough in the atmosphere. The lower the energy of the primary $\gamma - ray$ the more visible the ring structure will be.

Figure 2.5b shows a Monte Carlo simulation of the Cherenkov light density distribution at the observation level for showers induced by 100 *GeV* $\gamma - rays$ and 400 *GeV* protons.

Note the structure at $R_c \simeq 100 - 130\ m$ in the light distribution of the γ-induced showers. This is the so-called *hump*, and it is the result of the effect described previously. In the hadron-induced showers this effect is less visible due to the high transverse momentum kick of the products of the nuclear interactions which increases the dispersion of the $e^{\pm}$ directions. Besides, the mean interaction lengths for hadrons in air (83 g/cm^2 for protons and 107 g/cm^2 for pions) are longer than the radiation length for bremsstrahlung and the interaction length for pair production (37 and 47 g/cm^2 respectively), and thus hadron showers can produce locally much higher Cherenkov photon densities due to the deeply penetrating hadrons (and muons from π and K decays). This effect is well visible in figure 2.5b.

An important parameter to describe *EAS*s is the *impact parameter*; which is defined as the distance from the telescope location to the to point where the shower axis intersects the plane perpendicular to the telescope axis. The spread of the Cherenkov light over large areas at ground (the so-called *cherenkov light pool*) allows one to detect *EAS*s over a large range of impact parameters, which increases the sensitivity of the detector. Yet on the other hand, it dilutes the light flux to such an extent that very large collecting mirrors are needed to detect *EAS*s induced by low energy $\gamma - rays$ (see section 2.3).

2.2.3 Intensity and spectrum of the Cherenkov radiation in the atmosphere

Assuming $n = 1 + \eta_h$ with $\eta_h << 1$ and frequency independent, the energy radiated per atmospheric depth χ ($\equiv \int_{h_1}^{h_2} \rho_{air}(h)dh$) through Cherenkov light in the wavelength band $\lambda_1 - \lambda_2$ ($\lambda_1 < \lambda_2$) by an ultrarrelativistic electron ($\beta = 1$) can be described by the following equation (see [18]):

$$\frac{dE}{d\chi} = 4\pi^2 e^2 \cdot \frac{\eta_h}{\rho} \cdot \Big(\frac{1}{\lambda_1^2} - \frac{1}{\lambda_2^2}\Big) \tag{2.11}$$

From equations 2.7 and 2.8 one gets that $\eta_h/\rho = \eta_0/\rho_0 = 0.22\ cm^3/g$, (*i.e,* independent of the height h); which means that the amount of Cherenkov light emitted per radiation length is constant. In the wavelength band defined by $\lambda_1 = 290$ *nm* (Ozone cutoff in the atmosphere, see below) and $\lambda_2 = 600$ *nm* (PMT *QE* typically lower than 5%, see chapter 4) the energy radiated per atmospheric depth is $dE/d\chi \ = \ 1.1\ keV \cdot (g/cm^2)^{-1}$. The energy loss rate due to ionization losses in air for ultrarrelativistic electrons is $dE_{ion}/d\chi \sim 2.0\ MeV \cdot (g/cm^2)^{-1}$ [6]. Therefore the energy losses due to Cherenkov radiation in air are about $5 \cdot 10^{-4}$ of the energy losses due to ionization. It is important to note that the ratio between the *Cherenkov radiation* and the *ionization loss* is in first order constant. So the measurement of the Cherenkov light is a good measurement of the energy absorbed in the "atmospheric calorimeter"; and hence, a good estimation of the energy of the primary particle.

The number of Cherenkov photons produced per atmospheric depth $d\chi$ can be estimated from equation 2.11:

$$\frac{dN_{ph}}{d\chi} \ = \ \int_{\lambda_1}^{\lambda_2} \frac{1}{\hbar\omega} \cdot \frac{d^2E}{d\chi d\lambda} \ = \ 4\pi\alpha \cdot \frac{\eta_h}{\rho} \cdot \Big(\frac{1}{\lambda_1} - \frac{1}{\lambda_2}\Big) \tag{2.12}$$

where $\alpha = 1/137$ is the fine structure constant. In the wavelength range 290-600 *nm*, the number of photons radiated is $dN_{ph}/d\chi \ = \ 360 \cdot (g/cm^2)^{-1}$; which means that an ultrarrelativistic electron emits $1.3 \cdot 10^4$ Cherenkov photons per radiation length ξ_{brems}.

It is important to note, from equation 2.12, that most of the Cherenkov photons are emitted at short wavelengths ($d^2N_{ph}/d\chi d\lambda \propto 1/\lambda^2$). However, due to the interactions of the Cherenkov radiation with the air molecules, which have wavelength dependent cross sections, the light spectrum at the observation level is quite different from the emitted one (see figure 4.15). The processes by which the Cherenkov light interacts with the atmosphere are the following ones:

- *a)* Absorption in the Ozone layer (mainly) in the upper part ($\gtrsim 10$ *km*) of the atmosphere. Basically all photons with a wavelength below 290 *nm* are absorbed through the process $O_3 + \gamma \rightarrow O_2 + O$.

- *b)* Rayleigh scattering on the air molecules. Rayleigh scattering takes place on polarizable molecules with sizes smaller than the photon wavelength. In the range 2-15 *km* above see level, this is the process responsible for most of the Cherenkov light attenuation (when the atmospheric conditions are good). The spectral dependence of the cross section is proportional to λ^{-4}

- *c)* Mie scattering on aerosol particles. Mie scattering occurs on polarizable molecules with sizes comparable or larger to the photon wavelength. The spectral dependence of the cross section is proportional to λ^{-a} with $1 \gtrsim a \gtrsim 1.5$. Above 2 km, the light attenuation produced by this process is only important when the atmospheric conditions are bad, *i.e,* presence of dust, pollution, clouds, high humidity...

- *d)* Absorption by the molecules H_2O and CO_2. This process is important only for photon wavelengths above 800 nm, and thus it does not play an important role for Cherenkov telescopes.

The light losses due to *a)* and *b)* are well predictable and are actually included in the Monte Carlo simulation of the light propagation from the EAS to the location of the telescope. On the other hand, the light attenuation produced by *c)* depends on the weather conditions and it is highly variable; which is obviously a big problem for observations with Cherenkov telescopes. So far, $IACT$ observations have been performed only during nights of extremely good atmospheric conditions[6]. In the near future, instruments capable of quantifying the atmospheric differential extinction coefficient along the line of sight (LIDAR) will be used to correct the data when the weather conditions are not optimal [19].

2.3 Detection of γ-induced air showers with an *Imaging Air Cherenkov Telescope*

2.3.1 Basic Principle

Cherenkov telescopes, like common optical or radio telescopes, comprise three basic elements: *1)* a "tracking" mechanics to counteract the Earth movement; *2)* an element that

---

[6] The goodness of the atmospheric conditions is estimated by the naked eye of the person on shift, and by the value of the trigger rate produced by the cosmic rays in the telescope.

collects and focusses the signal (electromagnetic radiation) onto a “receiver”; and *3)* a “receiver” (camera) that converts the electromagnetic radiation into electric signals. The main difference with respect to optical or radio telescopes is that an $IACT$ does not detect directly the radiation emitted by the astrophysical objects under study, but the Cherenkov light emitted by the $e^{\pm}$ generated in the EAS that is produced when such radiation ($\gamma - rays$ with energies $\gtrsim 10\ GeV$ coming from these astrophysical sources) interacts with the Earth atmosphere. These $e^{\pm}$ produce a light pool of about 150 m radius (depending on the energy of the primary $\gamma - ray$ and zenith angle of observation) at an observation site located at 2 km above see level (see section 2.2.2). As shown in figure 2.6, the collecting mirror of an $IACT$ located within this Cherenkov light pool, can collect a fraction of the light and reflect it onto the pixelized camera situated in the focal plane of the mirror, thus forming a highly encrypted “image” of the EAS.

Another important difference of Cherenkov telescopes with respect to radio and optical telescopes is that the light sensitive elements placed in the camera of an $IACT$ do have a very short ($\sim ns$) time response. This is needed to increase the signal-to-noise ratio by exploiting the fact that the Cherenkov photons emitted in an EAS arrive to the telescope within a few ns time[7]. The light detectors used in the camera of current Cherenkov telescopes are Photomultiplier Tubes (PMT). It is worth mentioning that the construction of cameras equipped with higher sensitivity light detectors like Hybrid Photomultipliers (HPD), Avalanche Photo-Diodes (APD) and the novel Silicon Photomultipliers (SiPM) is under study [20].

A more detailed description of a Cherenkov telescope, and MAGIC in particular, is given in chapter 3.

Because of the multiple Coulomb scattering, which causes a deflection of the $e^{\pm}$ moving directions from the shower axis (see section 2.1.1), and the dependence of the Cherenkov angle emission with the height above see level (see section 2.2.2), the Cherenkov light reaches the telescope with an angle that depends in first order on the height of the emitting region. Consequently, there is a rough correspondence between the (relative) position of the detected

---

[7] The spread in the Cherenkov photon arrival times depends on the impact parameter and zenith angle of the EAS, as well as the nature of the initial particle.

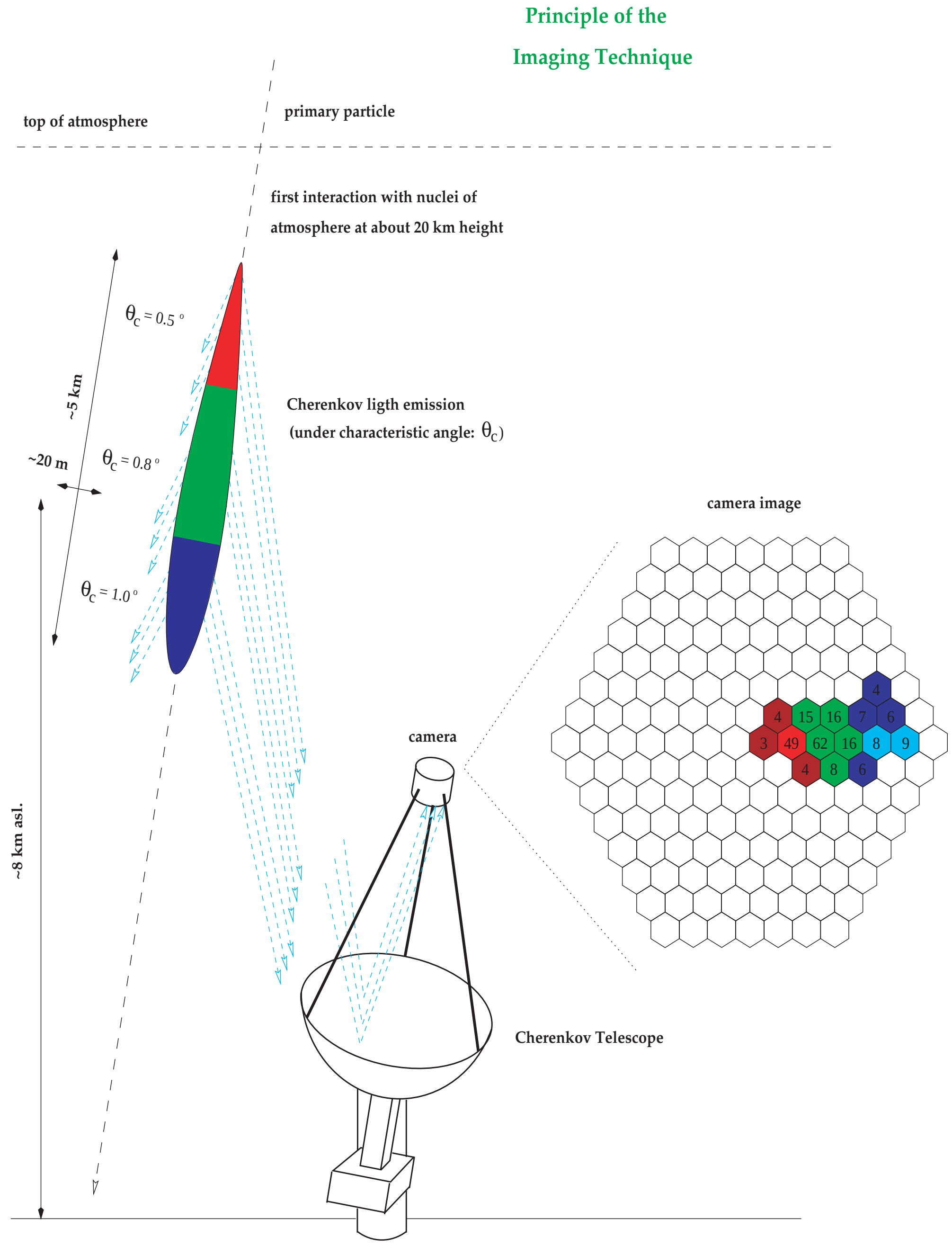

Figure 2.6: *Sketch of the detection of an EAS with an IACT. The stated dimensions are typical for 1 TeV $\gamma-ray$-induced showers. The numbers written in the pixels of the pixelised camera denote the amount of detected Cherenkov photons. Picture taken from [21].*

light in the pixelized camera of the telescope and the region the Cherenkov light comes from. For an *EAS* whose shower axis is parallel to the telescope axis, light from the upper part of the shower is mapped onto a region close to the camera center, whereas light from the lower part of the shower is mapped further away from the camera center (see figure 2.6). In this way, it is possible to take a space and time resolved "picture" of the *EAS*. However, it must be pointed out that some regions of the shower might not be contained in the image recorded in the telescope camera. This is due to the directionality of the Cherenkov radiation, which prevents some of the Cherenkov photons to reach the mirror of the telescope.

The pictures formed in the telescope camera contain information about the shower development, and thus can be used to infer information about the particle that produced the *EAS*, like the energy, incident direction and particle type (γ or hadron). The light content of the image is the main estimator of the energy of the primary particle, and the orientation and shape are used to determine the direction and the nature of the incoming particle. This method is often called *Imaging Technique*.

The *Imaging Technique* started by using the so-called *Hillas* parameters to depict the shower image produced in the pixelized camera of the telescope. The image parameters were introduced for the first time by A.M. Hillas in 1985 [1], and describe the shape, orientation and light content of the shower images. These image parameters provided Cherenkov telescopes with a very efficient tool to reconstruct *EAS*s, and specially, they improved radically the capabilities to distinguish between γ-induced showers and hadron-induced showers, which are much more numerous (see section 2.3.3). The usage of these parameters to describe the images produced in a pixelized camera allowed a Cherenkov telescope, the WHIPPLE telescope, to achieve, for first time in history, a clear detection (9 sigmas) of a source. That happened in 1989, and the source observed was the Crab Nebula [22].

Nowadays, the Hillas parameters are still the ones that parametrize most efficiently the shower images; and thus are the parameters most commonly used in ground based $\gamma - ray$ astronomy with *IACTs*. They will be also used in the analysis of the first signals observed with the MAGIC Telescope (see chapter 6).

However, I want to mention also the existence of image analyses based on semi-analytical models [23, 24, 25]. These models describe analytically the light distribution expected in the camera of a Cherenkov telescope (Monte Carlo simulations are used to describe the detector). By using the result of the fit of the shower images with the 2-D functions from the models, one performs a γ-hadron separation and reconstructs the energy and direction of the incoming $\gamma - ray$. These new *imaging techniques* are now starting to give good results. The main problem so far is that they require computing times exceeding those ones for the "classical Hillas analysis" by at least a factor 20.

2.3.2 Collection area and threshold energy of an *IACT*

As stated in section 2.2.2, the Cherenkov light is spread over a large region at the observation level. This has two consequences:

- An *IACT* is able to detect an *EAS* over a large range of impact parameters (50-200 m)[8], providing a Cherenkov telescope with a collection area of $\sim 10^5\ m^2$. This leads to a very high sensitivity in comparison with detectors mounted in satellites, which have collection areas of $\sim 0.01 - 1\ m^2$. It is worth pointing out that the collection area varies with the energy of the primary γ and with the zenith angle of observation. At zenith angles $\gtrsim\ 70^\circ$, the collection area increases by one order of magnitude.

- The Cherenkov light density is diluted, and thus large collecting mirrors and high sensitivity photon detectors are needed to observe *EAS*s induced by low energy primaries. The basic correlation between the Cherenkov light density at 2 *km* above see level, incident energy and the type of the incident particle is shown in figure 2.7. In order to perform an efficient image analysis, a minimum number of detected photons (photoelectrons in the PMTs of the telescope camera) is needed[9]. That means that an

---

[8] The efficiency in the detection of showers with impact parameters larger than 150 m (*i.e,* well outside the brightest region of the Cherenkov light pool) is quite low. However, due to the larger amount of showers at large impact distances, they are still a significant fraction of the total amount of detected gamma showers.

[9] The minimum amount of detected *phe* needed (per image) to carry out a useful analysis depends on the weather conditions, noise performance of the telescope, and also on the type of analysis used. Typically $\gtrsim 60$ *phe* are required.

$IACT$ is able to detect $\gamma - rays$ efficiently only above a given threshold energy (E_{th}), which is basically determined by the size of the collecting mirror and the efficiency in the conversion of Cherenkov photons to photoelectrons.

At energies $\gtrsim 20\ GeV$ the amount of Cherenkov photons arriving to the telescope is (in average) proportional to the number of $e^{\pm}$, which in turn is proportional to the energy of the primary $\gamma - ray$ (see section 2.1.1). Therefore, the threshold energy is inversely proportional to the collected number of Cherenkov photons and the light detection efficiency [26]:

$$E_{th} \propto \frac{1}{A_{mirror} \cdot LDE} \tag{2.13}$$

A_{mirror} is the area of the collecting mirror and LDE denotes the light detection efficiency, which is given by the product of several terms

$$LDE \ = \ R \times LG_{eff} \times QE \times CE \tag{2.14}$$

where R is the reflectivity of the mirrors, LG_{eff} denotes the light collection efficiency of the light guides[10], and QE and CE are respectively the quantum efficiency (of the photocathode) and the photoelectron collection efficiency (onto the first dynode) of the used PMTs. All these quantities are wavelength dependent.

The threshold energy is not sharp because of the shower fluctuations. The convention adopted by the community is to define the threshold energy as the peak in the differential trigger rate

$$\frac{d\mathcal{R}(E)}{dE}\Big|_{E=E_{th}} \ = \ 0 \tag{2.15}$$

I want to point out that with this definition, the telescope would have two different E_{th} when observing two $\gamma - ray$ sources that had very different spectra. The reference used to compare Cherenkov telescopes located in the northern hemisphere is the spectrum

---

[10] Nowadays, all Cherenkov telescopes use light guides coupled to the window of the PMTs in order to minimize the dead space in the camera (see section 3.3)

of the Crab Nebula. At energies larger than 300 GeV, this spectrum can be fitted by a power law with an index of about -2.6 [4, 27, 28].

It is worth noticing that at large zenith angles the Cherenkov light flux is further diluted (which increases the collection area), and hence the telescope E_{th} increases.

Before the year 2004, the lowest E_{th} among the Cherenkov telescopes was the one of the WHIPPLE telescope, which was about 300 GeV. Note that this threshold energy is substantially larger than the higher energies reachable by $EGRET$, which are about 10 GeV.

Therefore, on the one hand, Cherenkov telescopes do have collection areas ~5 orders of magnitude higher than that of satellite-borne detectors; and on the other hand, they are only able to detect radiation of energy ~2 orders of magnitude larger than that of satellite-borne detectors. This situation is indeed changing with the new generation of Cherenkov telescopes (CANGAROO III, HESS, MAGIC and VERITAS), which push for larger mirrors and higher photon conversion efficiencies to bring the E_{th} of the detector below the upper energies that will be measurable by GLAST (the next generation of satellite-borne detector for very high energy $\gamma - ray$ astronomy), which are expected to be about 300 GeV.

2.3.3 Background and background rejection

One of the major tasks in the analysis of the shower images is to distinguish between γ-induced showers (signal) and air showers induced by other particles (*background*). Figure 2.8 shows the fluxes of the most abundant cosmic rays in the energy range from 100 MeV to 10 TeV and the diffuse γs in the energy range from 100 MeV to 100 GeV. The particles that can mimic γ-induced showers are cosmic hadrons (basically protons and helium nuclei)[11], cosmic electrons and muons. As shown in figure 2.8, the diffuse γ flux (from galactic and extragalactic origin) above 30 GeV is about 5 orders of magnitude below that of cosmic

---

[11] Heavier nuclei are much less abundant (see [30]), and besides, the amount of Cherenkov light they produce is substantially lower than that of showers induced by protons and alpha particles (see figure 2.7).

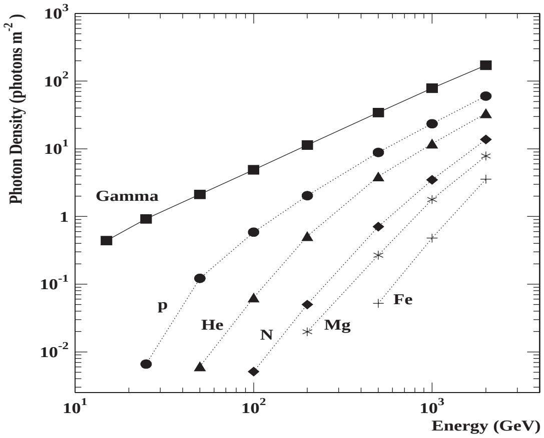

Figure 2.7: *Cherenkov photon density at 2 km above see level as a function of the energy and type of the incident particle. The photon wavelength range considered is 300-600 nm, and the photon density is averaged over an area of* 50000 m^2. *Figure taken from [29].*

hadrons (see also [31, 32]), and therefore I will neglect them in the following discussions[12]. In the next sections I will describe briefly the principles of signal-to-background separation.

Hadrons

As stated in section 2.1.2, hadron-induced showers have a longer longitudinal and wider lateral particle distribution. Besides this, most of the Cherenkov light is generated in secondary electromagnetic showers induced by gammas from π^0 decays. Because of these 2 features, hadron-induced shower images recorded in the telescope camera are in general longer and wider than the images produced by γ-induced showers, and do have many more irregularities in their structure. An example is shown in figure 2.9.

However, due to the statistical fluctuations in the air shower development, and the fact that hadron-induced showers are $\sim 10^4$ more numerous than γ-induced showers; there is always a fraction of the hadron showers that resemble γ showers, and therefore it is not possible to perform a perfect γ-hadron separation. Hadrons are, by far, the most important

---

[12] Diffuse γs may become an important background when performing observations of extended sources.

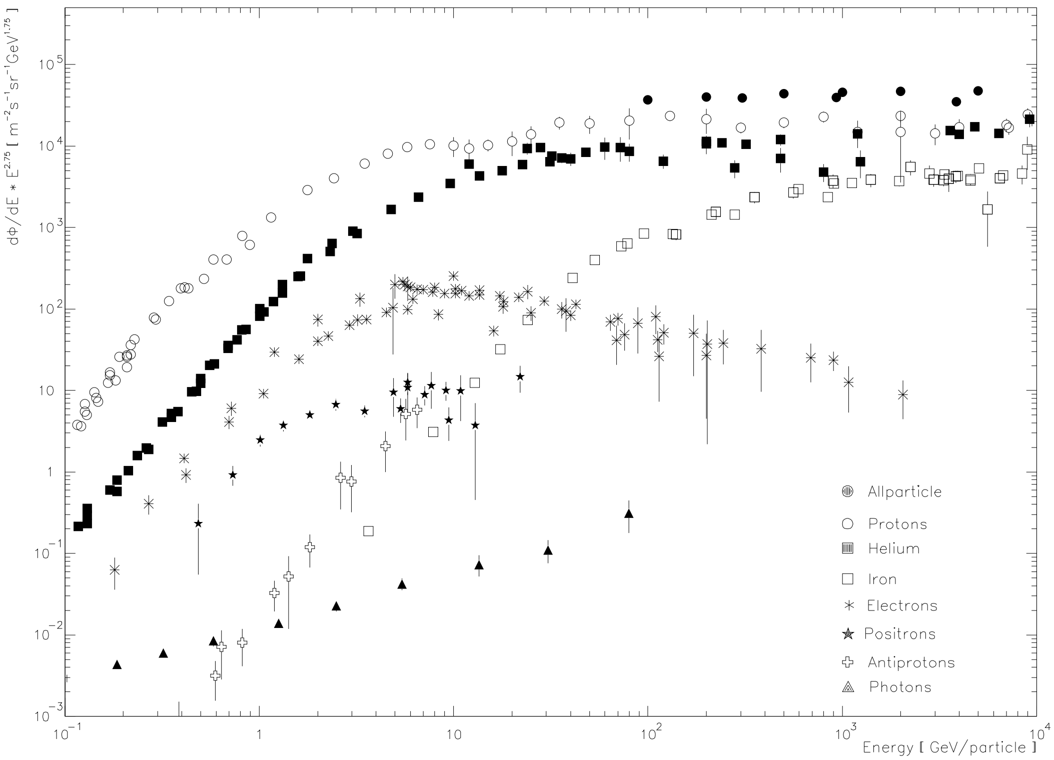

Figure 2.8: *Cosmic-ray fluxes of selected individual elements, electrons, positrons and diffuse* γ*s in the energy range from 100 MeV to 10 TeV. This energy range constitutes a small band out of a compilation by B. Wiebel-Sooth [30] encompassing a much wider energy spread. The all-particle spectrum is not given in the selected energy band.*

background for Cherenkov telescopes.

An important feature that has to be considered is that the amount of Cherenkov photons generated in a hadron shower is smaller than the one produced in an air shower induced by a $\gamma - ray$ of the same energy. This is due to the fact that in hadron showers the Cherenkov light is mostly produced in the electromagnetic component, which carries only a fraction of the total energy of the primary particle. This effect is well visible in figure 2.7. This means that γ-induced showers compete with showers produced by hadrons that have larger energies. For example, the protons that compete (in average) with 100 GeV gammas have an energy of about 300 GeV; *i.e,* 3 times larger. Since the differential spectrum of galactic hadrons follows a power law with a negative index (-2.7 for protons, -2.6 for alpha particles), this effect reduces by a big factor ($[1/3]^{-1.7} \approx 6.5$ for protons that compete with 100 GeV gammas) the total amount of hadrons contributing significantly to the background. Note from figure 2.7 that this effect is enhanced at the lowest energies; at 20 GeV, only protons of $\gtrsim$ 100 GeV are able to mimic γ showers, and the contribution of heavier elements to the background is almost negligible. On the other hand, when reducing the energy of the primaries, the statistical fluctuations in the air shower development affect much more the images in the telescope camera, and hence the γ-hadron separation capabilities based on the shape of the images are also reduced.

An additional rejection factor is achieved by exploiting the fact that the showers induced by the $\gamma - rays$ (from the observed point source) do have always the same incident angle, whereas hadron showers are isotropycally distributed (because the cosmic hadrons are randomly deflected by the magnetic fields of the galaxy). Consequently, images produced by hadron-induced showers are randomly oriented in the telescope camera, whereas images produced by γ-induced showers have always the same orientation, *i.e,* the elongated images point to the region of the camera where the source is located.

Further details about some of the methods used to distinguish between $\gamma-$ and hadron-induced showers will be given in chapter 6.

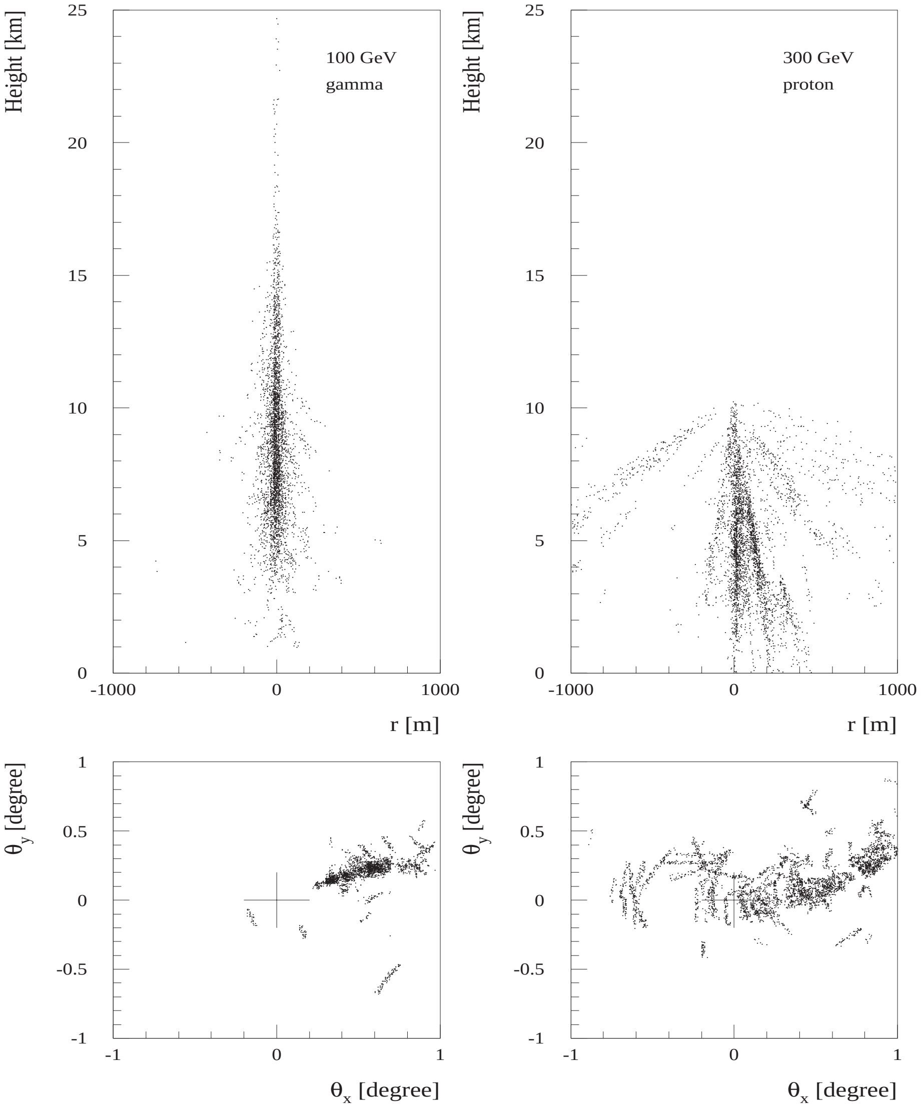

Figure 2.9: *Air shower induced by a 100 GeV γ (left) and by a 300 GeV proton (right). The upper part of the picture shows the shower development in the atmosphere, and the lower part shows the corresponding light distribution at the focal plane of the collecting mirror of an IACT. The energies are chosen such that the amount of Cherenkov photons produced in both cases is comparable. Note that the nearly straight sections are partial Cherenkov rings from high altitude tracks. Figure adopted from [33].*

Electrons

A high energy ($\gtrsim 5$ GeV) electron entering the atmosphere generates an electromagnetic shower which is completely indistinguishable from a shower induced by a primary $\gamma - ray$ of the same energy. The only possibility to reject showers induced by electrons is to use the direction of the shower (*i.e,* the orientation of the image in the telescope camera); cosmic electrons are isotropycally distributed[13] whereas $\gamma - rays$ from point sources are not. This feature allows one to decrease the electron background by a factor of ~ 10 (depending on the energy) for point-like source observations.

The differential flux of cosmic electrons above 10 GeV follows a power law with an index of -3.2 [30, 35]. However, despite of the steep power law spectrum, even at the lowest energies reachable by MAGIC ($\sim$ 20-30 GeV) the amount of cosmic electrons is about 2 orders of magnitude lower than that of hadrons (see figure 2.8). Because of that, the electron rejection based on the shower orientation is already good enough to handle this background. Our simulations show that, after the image analysis, the rate of cosmic electrons is about a factor 5 lower than that of cosmic hadrons.

Muons

The Cherenkov light generated by a muon with a large impact parameter ($\gtrsim$ 60-80 m) produces in the telescope camera an arc like image that can resemble the image produced by a γ-induced shower. Therefore, muons represent another background for $IACTs$.

There are no cosmic muons due to their short decay time ($2.2 \cdot 10^{-6}$ s); and basically all observed muons are secondary particles from air showers induced by hadrons. From all these secondary muons, only those ones with large Lorentz factors ($\gtrsim 50$) survive long enough and have enough energy to produce Cherenkov light. These muons are mostly produced at the beginning of the shower development (where the secondary particles have still a very high energy), and thus, high up in the atmosphere. Because of the directionality of the Cherenkov

---

[13] The Earth geomagnetic field disturbs the isotropy in the arrival direction of the cosmic electrons. This effect is particularly important at low energies, close to the rigidity cutoff, which is about 10-20 GeV (depending on the magnetic latitude) [34].

light, not all muons producing Cherenkov light illuminate the mirror of a Cherenkov telescope. From the large amount of secondary muons produced in the hadron showers, only a small fraction produces Cherenkov light that reaches the telescope and mimics γ showers.

Energetic charged pions and kaons also produce Cherenkov light that can sometimes reach the mirror of the telescope. For example, at 10 *km* height, the threshold energy to emit Cherenkov light E_{th}^{Che} is 12 GeV and 42 GeV for pions and and kaons respectively. However, due the fact that they interact hadronically with the atmosphere nuclei and that their decay times are very short ($\sim 10^{-8}\ s$), their contribution to the Cherenkov light recorded by an $IACT$ is about 20 times lower than that of the muons.

In [36] it is shown that only in $\lesssim 20\%$ of the hadron showers detected with the MAGIC Telescope, more than 90% of the light content is generated by a muon. These are the so-called "isolated muons", and they represent the muon background for a Cherenkov telescope. Therefore, the rate of background muon events is $\lesssim 20\%$ of the total hadron event rate. In addition, some other studies [37, 38], show that a muon rejection based on the width, the length and light content of the images (WIDTH, LENGTH and SIZE Hillas parameters) can reduce the muon background by about 2 orders of magnitude.

2.3.4 Background from the light of the night sky

The Light Of the Night Sky ($LONS$) adds to the Cherenkov light from the air showers. This can distort the images recorded in the telescope camera [39] and can produce artificial triggers (see section 4.6).

The $LONS$ has two components:

- *Diffuse component*; it comes mainly from the zodiacal light (which is the sunlight scattered by interplanetary dust), and the airglow emitted by atoms and molecules in the upper atmosphere, which are excited by the solar UV radiation during day time. In addition, the scattered light from the moon (specially important when full or almost full moon) can also contribute significantly. Small corrections to this diffuse component come from starlight scattered by interplanetary dust, faint stars (from our galaxy) and faint galaxies.

Using the diffuse *LONS* spectrum measured in [40], one finds that it produces (in average) about 0.15 (0.60) *phe/ns* in the PMTs installed in the inner (outer) part of the camera of the MAGIC Telescope (see section 4.6). The pixels that can trigger the telescope are located in the inner part of the camera (see section 3.3). It must be pointed out that the used *LONS* flux was measured at high galactic latitudes and moonless nights; therefore this background can increase significantly when observing at lower latitudes and/or specially in the presence of moon light.

- *Non-diffuse component*; it comes from "bright stars" in the field of view of the telescope camera. The definition of a "bright star" is somewhat arbitrary. In the particular case of the MAGIC Telescope, the convention is to consider a star as a "bright star" if its apparent magnitude is smaller than 7.5 [41]. On average, there are ~ 2 (4) "bright stars" in the inner (outer) region of the camera of the MAGIC Telescope. Unfortunately, the position of these stars in the camera of MAGIC is not fixed; due to the ALT-AZ mount, the stars rotate around the center of the camera when a source is tracked by the telescope [42]. That means that the pixels can not be simply disconnected, as could be done in telescopes with equatorial mount. Thus a special data treatment is needed to correct the effect produced by the "bright stars".

The distortion in the shape and light content of the images produced by the *LONS* affects the event reconstruction and the γ-*background* separation capabilities of an *IACT*. This effect is particularly sizeable close to the E_{th} because of the tiny images; the *LONS* increases the trigger rate by allowing some (very) low energy showers (that would not be able to trigger) to trigger the detector.

The effect produced by the diffuse *LONS* can be partially corrected by the application of the so-called *image cleaning* procedures (see section 6.3.2 for details). As to "bright stars", the approach chosen for the standard analysis in MAGIC is to identify the pixels illuminated by these stars (by means of their DC currents and fluctuations in their pedestals) and to replace their signal by the average signal of their neighboring pixels. Further details about the treatment of the pixels affected by "bright stars" can be found in [41].

The artificial triggers produced by the *LONS* can be easily recognized and distinguished from real *EAS*s offline; so they are not a big problem. However, if the rate of artificial events is very high, the data acquisition is overloaded and considerable dead times are produced. These rates depend strongly on the trigger requirements [43]. For the "standard trigger conditions" of MAGIC (see section 3.4), the artificial trigger rate produced by the diffuse *LONS* is about few *Hz* (see section 4.6.2), which is negligible in comparison with the trigger rate produced by hadrons, that is about 460 *Hz*. I want to stress that the above mentioned *LONS* artificial rate might increase considerably in the presence of the moon and/or the presence of bright stars in the field of view.

2.3.5 Necessity of Monte Carlo simulations to characterize the performance of an *IACT*

In high energy physics it is quite common to investigate the performance of a detector by studying its response to known fluxes of particles at known energies (the so-called "test beams"). The performance of a detector does not only depend on the hardware, but also on the way the signals are reconstructed and analyzed. By means of the "test beams" both the detector and the analysis methods are characterized. In this way one can compute the detection efficiency for both signal and background, as well as some other important quantities like the threshold energy, and the energy and position resolution.

In the case of an *IACT* it is (so far) not possible to characterize the detector performance by sending (from the space) a beam of $\gamma - rays$ of known energy; there are no cosmic "test beams" available. Therefore, the only way of estimating the performance of the detector is by means of Monte Carlo simulations[14].

The Monte Carlo simulations consist typically in two different sets of programs; *a)* the programs that simulate the atmospheric shower development and *b)* the programs that simulate the detection of these showers by the telescope. In order to simulate the development of the shower it is quite common to use a program called CORSIKA, which was developed

---

[14] A common procedure to evaluate the quality of the Monte Carlo simulations is to carry out extensive crosschecks with data from observations of known steady sources, like the Crab Nebula in the northern hemisphere.

by the Forschungszentrum Karlsruhe (Germany). CORSIKA uses experimentally measured cross sections and complex atmospheric models to simulate the EAS by tracking each particle in the shower individually [12]. As to the telescope simulation, the programs are usually developed by the local institutes, since it is required a detailed knowledge of all parts of the detector. A ray-tracing program simulates the trajectories of the Cherenkov photons to the camera of the telescope, and the simulation of the detection of the individual photons is usually performed by a separate program.

The use of the CORSIKA program in the MAGIC simulation chain is explained in [44], and a detailed description of the programs which simulate the MAGIC Telescope is given in [45, 46, 47].

A task for which simulations are indispensable is the calculation of the absolute flux of $\gamma - rays$ from a source. As I will show in section 6.3, Monte Carlo simulations are not necessarily needed to extract a convincing γ-signal from the experimental data. However, in order to compute the $\gamma - ray$ fluxes it is mandatory to know the effective collection area (A_{eff}) of the telescope, which is related to the probability ($\mathcal{P}_\gamma$) to detect and reconstruct $\gamma - rays$. This probability depends on the characteristics of the EAS (basically the energy E, the zenith angle ZA and the impact parameter r) and also on the γ-selection cuts applied in the image analysis. The probability $\mathcal{P}_\gamma(E, ZA, r)$ is determined by

$$\mathcal{P}_\gamma(E, ZA, r) \;=\; \frac{N_\gamma^{AfterCuts}(E, ZA, r)}{N_\gamma^{Simulated}(E, ZA, r)} \tag{2.16}$$

where $N_\gamma^{Simulated}$ is the number of simulated gammas and $N_\gamma^{AfterCuts}$ is the remaining number of gammas after the image analysis. Obviously, $\mathcal{P}_\gamma$ can only be computed by means of Monte Carlo simulations. Once $\mathcal{P}_\gamma$ is known, the effective collection area is calculated as

$$A_{eff}(E, ZA) \;=\; \int_0^{2\pi}\int_0^{\infty} \mathcal{P}_\gamma(E, ZA, r) \cdot r dr \cdot d\varphi \tag{2.17}$$

The differential $\gamma - ray$ flux is obtained from the distribution of detected signal events by

$$\frac{d\mathcal{F}_{\gamma}(E, ZA)}{dE} = \frac{\frac{dN_{\gamma}^{AfterCuts}(E,ZA)}{dE}}{T^{obs}(ZA) \cdot A_{eff}(E, ZA)} \tag{2.18}$$

where $T^{obs}(ZA)$ is the effective observation time at the zenith angle ZA. In reality, the calculus of $\mathcal{P}_{\gamma}(E, ZA, r)$, $A_{eff}(E, ZA)$ and $d\mathcal{F}_{\gamma}(E)/dE$ is not an integral but a discrete calculation; and it is performed by dividing the data into bins of E, ZA and r. The details of this calculation can be found elsewhere [48].

The Monte Carlo simulations are also essential for estimating the shower energy from the image parameters, as well as in the calculation of the energy and angular resolution of the telescope.

Chapter 3

The MAGIC Telescope

The name MAGIC Telescope stands for Major Atmospheric Gamma Imaging Cherenkov Telescope. MAGIC is located in the Canary island of La Palma ($28.8°N$, 17.9°W), at the *Roque de los Muchachos Observatory* ($2200\ m$ above see level); and it is currently the largest Cherenkov telescope world-wide. The first ideas and the initial concept were developed in 1995 [49], and the Technical Design Report (*TDR*) was completed in 1998 [50]. The large amount of the funds were granted at the end of the year 2000, and the construction of the telescope started in September 2001. Finally the telescope was completed and inaugurated in October 2003. The commissioning of the telescope started right after the inauguration, and it is still on going (summer 2004).

The main goal of the experiment is to cover with high sensitivity the energy gap between $10\ GeV$ and $300\ GeV$ in $\gamma - ray$ astronomy, up to now inaccessible, by lowering the *threshold energy* E_{th} with respect to contemporary instruments. The "key" elements in the MAGIC Telescope are a high *Cherenkov photon-to-photoelectron* conversion efficiency and, specially, the *largest collecting mirror* ($17\ m\ \phi$) world-wide. These 2 features reduce the E_{th} of the telescope (see equation 2.13) down to $\sim 25\ GeV$.

In the following sections I will point out the basic physic motivation to build MAGIC for performing $\gamma - ray$ observations in the above mentioned energy range; and then I will briefly describe the most relevant elements of the MAGIC Telescope, stressing the technical innovations with respect to contemporary *IACTs*, and paying special attention in the description

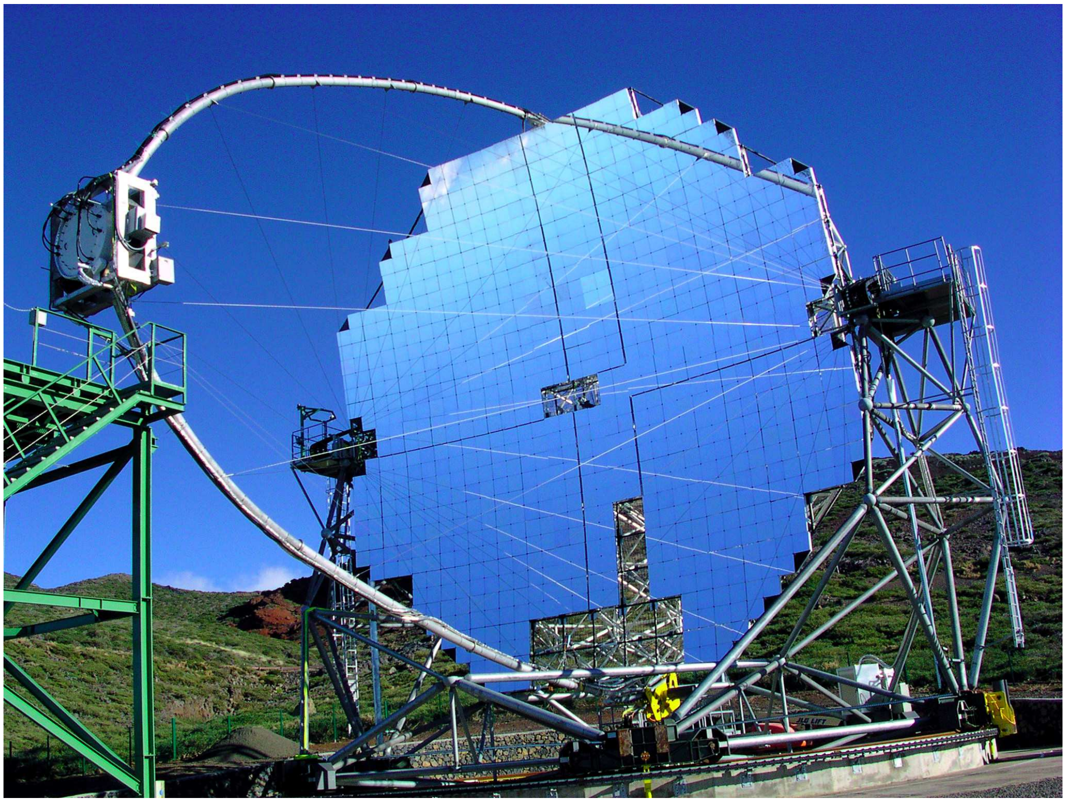

Figure 3.1: *Photograph of the MAGIC Telescope by the time of its inauguration (October 2003).*

of the telescope camera, since it is the part of the detector where I made major contributions leading to important performance improvements.

3.1 The main MAGIC physics goals

The cosmic-ray (CR) spectrum extends up to $3 \cdot 10^{20}\ eV$ in energy. For our understanding of the universe we need to investigate not only the so-called thermal universe, but also the processes that generate and accelerate energetic particles. Gamma-rays bring information of such processes and they are currently the best tool for understanding them. The many orders of magnitude more abundant charged cosmic rays are deflected by the weak galactic fields and cannot be traced back to their sources. Only extremely energetic ($E \gtrsim\ 10^{19} eV$) charged cosmic rays could point to their sources. However, due to the very low fluxes at these high energies, huge collection areas are needed in order to collect enough statistic for a reasonable study. On the contrary, $\gamma - rays$ can be back extrapolated to the place where they were produced[1]. The energy of the detected $\gamma - rays$ sets a lower energy limit to the initial physic processes from which they were generated. And in addition, due to the fact that gamma quanta are massless, $\gamma - rays$ also allow us to study the time evolution of the acceleration mechanisms in the astrophysical sources.

Below 10 GeV, $\gamma - ray$ observations are carried out by satellite-borne detectors which have at most 0.1 m^2 of detection area. Due to the exponential decrease of the $\gamma - ray$ flux with the increasing energy and the above mentioned small surface area of these detectors, their sensitivity for energies $\gtrsim$ 10 GeV is limited by very low statistics. Conversely, as stated in 2.3.2, Cherenkov telescopes do have effective collection areas of about 10^5 m^2, which provide them with huge sensitivities. However, *IACTs* are not able to measure below a given threshold energy (see section 2.3.2), which in the past was about 300 GeV. The situation is right now changing, since HESS and specially MAGIC are already starting to operate.

The Energetic Gamma Ray Experiment Telescope (*EGRET*) instrument on board of the Compton Gamma Ray Observatory (launched in 1991) made the first complete survey of the sky above 100 MeV. *EGRET*, with a sensitive area of twice this page, showed the high-energy $\gamma - ray$ sky to be surprisingly dynamic and diverse. It uncovered the tip of the iceberg, raising very many questions; and it is in the light of *EGRET*'s results that the great potential of the next generation of $\gamma - ray$ telescopes can be appreciated.

Figure 3.2 shows the point sources of γ-radiation of energy 100 $MeV <$ E $<$ 10 GeV as observed by *EGRET*. It must be stressed that many of these $\gamma - ray$ sources remain so far unidentified. Besides, the distribution of the luminosities of the *EGRET* sources is strongly peaked at the lower end, near the sensitivity limit. This suggests that in case the sensitivity of the detector could be improved, the number of detected sources would strongly increase; and in case of better angular resolution the nature of the unidentified sources might be revealed.

---

[1] Neutrinos point also to their sources and bring a very valuable information; yet due to their small cross sections to interact, gigantic detectors are needed, and so far, the sensitivity of neutrino detectors is rather limited.

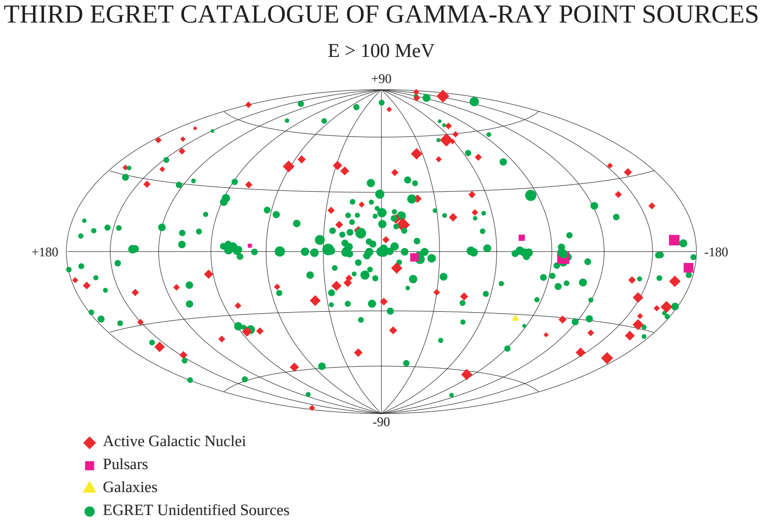

Figure 3.2: *Galactic coordinates of point sources of* γ*-radiation of energy 100* $MeV < E < 10$ GeV *as observed by EGRET. Taken from [51].*

In fact, a more sensitive successor to $EGRET$, named $GLAST$, is presently being planned at NASA. $GLAST$ will have a detection area of about 1 m^2 (*i.e,* an order of magnitude larger than $EGRET$), and it is expected to be launched in 2007.

On the other hand, figure 3.3 shows the point sources of γ-radiation of energy $E \gtrsim 300$ GeV, as observed by the various Cherenkov telescope observatories around the world. Despite having a sensitivity many orders of magnitude better than $EGRET$ (for energy spectra extrapolated to higher energies), the number of detected sources is dramatically lower. This can only mean that there are strong cut-offs in the γ-spectra of such sources somewhere in the energy range between 10 GeV and 300 GeV.

Therefore, covering the above mentioned energy gap with an $IACT$ (that has a larger sensitivity and better angular resolution than $EGRET$) would allow one to:

- Identify the unidentified $EGRET$ sources. Many of these sources are located in the galactic plane and are expected to be isolated pulsars that emit $\gamma - rays$.

- Study the mechanisms which produce the cut-offs in the spectrums of many of the unidentified and identified $EGRET$ sources.

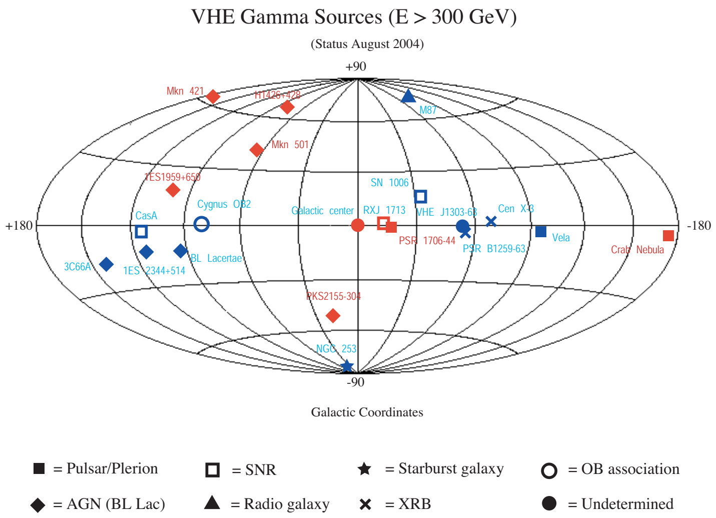

Figure 3.3: *Galactic coordinates of point sources of* γ*-radiation of energy* $\gtrsim 300\ GeV$ *as observed by the various Cherenkov telescopes around the world. Red symbols indicate sources detected with certainty, and blue symbols those which need further confirmation.*

- Discover new sources, which may show up due to the fact that their fluxes at low energies (not achievable by the 1st generation $IACTs$) should be higher than those ones at high energies.

The above mentioned arguments are the main astronomical merits for covering the unexplored energy range 10-300 GeV in $\gamma - ray$ astronomy. However, I want to stress that there are many more targets for the MAGIC Telescope, which could provide very valuable data to understand a wide variety of astrophysical phenomena belonging to the so-called “non-thermal universe”, as well as fundamental physics questions. In the following I list the most relevant ones:

- Observation of Supernova Remnants (SNR), which are currently considered to be the main objects where cosmic rays are accelerated.

- Study of $\gamma - ray$ pulsars. There are currently two models for the $\gamma - ray$ emission mechanism from the six galactic pulsars observed by $EGRET$. The models differ on the location of the emission region: near the magnetic poles (*polar cap*) or in the outer part of the pulsar magnetosphere (*outer gap*). The two theories predict slightly different cut-off energies around few tens of GeV, where observations have not been possible so far. The detection (or no detection) of a pulsed signal from these known pulsars with MAGIC will bring some light to this problem.

- Observation of many Active Galactic Nuclei (AGN) located at redshifts up to $\lesssim 2$. These observations will lead to *a)* a better understanding of the emission mechanisms that take place in these objects; *b)* the determination of the $\gamma - ray$ horizon, which could be used to make an indirect measurement of the extragalactic background light density (EBL), to set upper limits on the early star formation, and eventually, to extract cosmological parameters like the Hubble constant H_0 and the cosmological densities Ω_M and Ω_Λ. In addition, *c)* the fast flares from AGNs could be used to set constraints to quantum gravity models, like the predicted Lorentz invariance deformation that would imply a small time delay in the arrival time of high energy photons compared to that of low energy photons emitted originally at the same time.

- Search for high energy counterparts of Gamma Ray Bursts (GRBs), that surely will contribute significantly to the understanding of this enigmatic phenomenon. Once the production mechanisms of GRBs are understood, one could eventually test the Lorentz invariance on the high energetic radiation coming from the GRBs.

- Search for the signal of Dark Matter annihilation into $\gamma - rays$ (line and continuum), which could be probably detectable only at energies below 100 GeV.

Much more detailed discussions about all these topics can be found elsewhere [50, 52, 53, 54, 55]. I want to point out that many of these targets are reachable only because of the extremely low E_{th} and the very short repositioning time of the telescope (see section 3.2); which are unique features of MAGIC among the current Cherenkov telescopes.

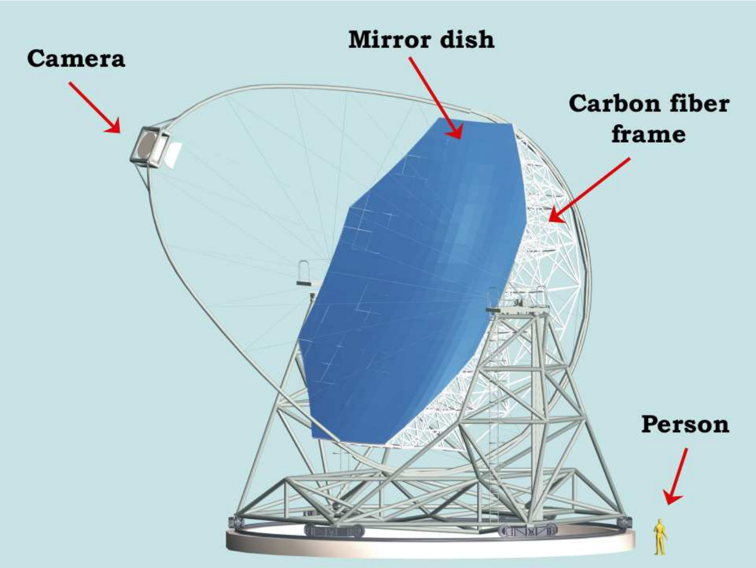

Figure 3.4: *A model of the 17 m ϕ MAGIC Telescope.*

Main Parts of the MAGIC Telescope

3.2 The frame and the mirror dish

The frame of the telescope follows roughly the concept of a large (17 m ϕ) solar concentrator, which was already built and tested a few years ago as part of the German solar power research program [50]. Figure 3.4 shows a computer generated image of the telescope. The main mirror support dish consists of a three layer space frame made from carbon fiber-epoxy tubes, which are both lightweight and rigid. This structure keeps the inertia of the telescope low enough so that it can be repositioned within 20 s at any position in the sky; which is a extremely valuable feature (and unique feature among current *IACTs*) to search for *GRB*s. A finite element analysis of the frame has shown that deformations can be held below 3.5 mm with respect to the nominal curvature at any position for a combined frame and mirror weight of less than 20 tons. It also guarantees wind resistance up to $\lesssim 170\ Km/h$ and stability for complete ice coverage up to 3 cm thickness.

MAGIC has a octagonal shape tessellated reflector of a 239 m^2 area. The overall curvature of the reflector is parabolic to minimize the spread in the arrival time of the Cherenkov

Figure 3.5: *Photograph of one of the 964 mirror elements of the mirror dish of MAGIC.*

photons at the camera plane. The focal length to diameter ratio (f/D) is about 1, which produces high optical quality images at the camera [50]. The reflector consists of 964 mirror elements of an area of $49.5 \times 49.5\ cm^2$ each, 892 of which are placed in panels of 4 mirrors, and the rest in panels of 3 mirrors that are located at the rim of the main reflector. The curvature of the individual mirror tiles is spherical, and, because of the parabolic shape of the main reflector, their focal lengths are increased following their radial position on the dish; from 17 m at the center, to 18 m at the rim[2].

The construction of the single mirror elements of the main reflector is another of the innovations of the MAGIC Telescope. The technology (adopted from the airplane industry) consists in using an aluminum honeycomb core to confer the panel lightness and stiffness [56, 57]. The front mirror plate is made of a AlMgSi1.0 alloy of 5 mm thick, machined to spherical shape and polished by diamond milling to achieve the most adequate curvature radius for its position on the parabolic reflector. After the diamond milling, the mirror is

---

[2] The reflector is divided into 8 concentric zones with different curvatures (ranging from 34 to 36 m) depending on its distance from the reflector's optical axis. The mirrors are selected for their best position to the dish [56].

coated with quartz to protect it against aging and scratches. The aluminum plate is glued together with an aluminum honeycomb inside a thin aluminum box; and the final assembly (the so-called *raw blank*) weights only $\sim 4\ kg$. A photograph of one of these mirrors is shown in figure 3.5. The reflecting surface achieved has a mean reflectivity of $\sim 85\%$ in the wavelength range 300-650 nm[3] and a roughness below 10 nm, which produces an excellent image quality: 90% of the light from a parallel beam is focused within a circle of $1.0 \pm 0.2\ cm$ diameter (less than half of the MAGIC pixel size) [57]. It is also worth to mention that each mirror panel is equipped with a heating system to prevent ice and dew formation.

Let me summarize the advantages of this structure with respect to the conventional glass mirrors: *a)* less weight, which is fundamental for fast repositioning of the telescope; *b)* the possibility to heat the mirrors to prevent the formation of dew and ice during operation; *c)* a fast production technique, as the diamond milling of the reflective surface takes only about 2 hours per mirror; *d)* a cost effective production technique, specially when a variety of slightly different curvatures are needed; and *e)* longer life; the dilatations and shrinks produced by temperature changes scratched several glass mirrors per year in the HEGRA telescopes.

Although the mount is very rigid, a system of Active Mirror Control (AMC) for making mirror adjustments and small corrections during telescope turning is used in order to counteract the small residual deformations of the frame. It works on lightweight panels of four preadjusted mirror elements together with a switchable laser pointer. The panel is tilted by two stepping motors while being monitored by a CCD videocamera that compares on demand the actual laser spot position on the casing of the camera with the nominal one. Further details about the AMC can be found elsewhere [50, 58]. I want to point out that this is the first time that such technique is proposed and used in $IACTs$.

---

[3] The reflectivity depends slightly on the photon wavelength, being the maximum 90% at $\lambda \sim 450-550\ nm$ and the minimum 80% at $\lambda \sim 340-360\ nm$.

3.3 The camera of the MAGIC Telescope

The camera is a very important element in the performance of a Cherenkov telescope. To start with, it is the place where the conversion of Cherenkov photons to photoelectrons takes place, so it is directly related to the E_{th} of the detector (see section 2.3.2). Secondly, the quality of the shower images recorded in the camera is a key factor in the γ/h separation, and also in the γ/μ and γ/e separation (see section 2.3.3), and therefore it is directly related to the $\gamma - ray$ sensitivity of the telescope.

Historically, $IACT$ cameras underwent a development from a single PMT version to cameras with a few hundred pixels. The progress of the last years can mainly be attributed to finer pixelized cameras, allowing the subtle differences between hadron and γ showers to be revealed. Hand in hand with finer pixels there has been an improvement in the trigger efficiencies for γs, the angular resolution, the γ/h separation and some modest noise reduction by limiting the image to its minimal necessary size, as well as by decreasing the acquisition time to the short durations of the Cherenkov flashes. In turn, also the energy resolution is slightly improved due to the better determination of the shower maximum location in the images, particularly for low energy events.

It is worth to point out that, on the one hand, images from low energy showers ($< 100\ GeV$) are rather compressed and rather close to the camera center, demanding fine pixelization of the camera in the central region. However, on the other hand, images from high energy showers are more extended (up to $\sim$1.5°) because they reach further down in the atmosphere, hence requiring the camera to be large enough to contain the whole picture of the gamma shower. Therefore, the diameter of the camera is, in addition to the pixel size, a critical issue, since the information about the shower tail is very useful in the energy resolution and the $\gamma/background$ ($background =$ hadrons, electrons and muons) separation.

The sensitivity of the camera has a decisive role (together with the mirrors) in lowering the threshold energy E_{th} of the telescope. As mentioned in section 2.3.2, E_{th} is inversely proportional to the the detection efficiency of the Cherenkov photons; and hence the higher the camera sensitivity, the lower the E_{th} of the telescope. The low E_{th} of the new generation of $IACTs$ is mainly attributed to the large mirror areas, but also to the use of PMTs with higher quantum efficiencies, as well as to the reduction of the non-sensitive areas (dead areas) in the camera by using light concentrators.

In order to minimize the weight, size and heat dissipation of the camera of the MAGIC telescope, most of the trigger and readout electronics is not included in the camera housing, but in the central data acquisition building, which is located 100 m away from the telescope (see figure 3.9). The very short (2-3 ns FWHM) PMT signals are transferred to the acquisition building by a system based on VCSEL drivers and optical fibers. The concept and the technical details of this system are described in section 3.3.3.

3.3.1 The layout of the camera

A schematic of the layout of the MAGIC camera is shown in figure 3.6. The inner part of the camera is equipped with 397 hexagonal pixels with an angular diameter of $0.1^\circ\ \phi$ ($30\ mm\ \phi$ at the camera plane), whereas the outer part is composed of 180 hexagonal pixels of $0.2^\circ\ \phi$ ($60\ mm\ \phi$ at the camera plane). The trigger region is formed by the central 325 pixels from the inner zone (see section 3.4). The use of two different PMT sizes is mainly due to a compromise between telescope performance and cost.

As I mentioned before, the small pixel dimensions in the center of the camera are vital to analyze low energy showers, which is the main goal of the MAGIC telescope. And the usage of only small PMTs in the whole camera would imply (for a fixed camera angular size) an increase in the camera weight and (specially) cost[4]. On the other hand, the outer ring records mostly the Cherenkov photons from the shower tails, where the effect of the statistical fluctuations in the shower development is larger (*i.e,* more diffuse images in the camera); and besides the optical quality of the image in this region of the camera is already degraded by the coma aberration. Therefore, a coarse pixel size of $0.2^\circ\ \phi$ does not deteriorate very

---

[4] The usage of 0.1° pixels in the whole 3.8° field of view camera would imply the following modifications: *a)* an increase in the number of PMTs, *b)* an increase in the amount of power lines and electronics used to handle the PMT signals in the camera (it includes optical links), *c)* the necessity to dissipate a larger amount of heat in the camera, and *d)* the increase in the amount of trigger and Flash-ADC (*FADC*) channels. All these modifications would increase significantly the complexity, weight and cost of the camera.

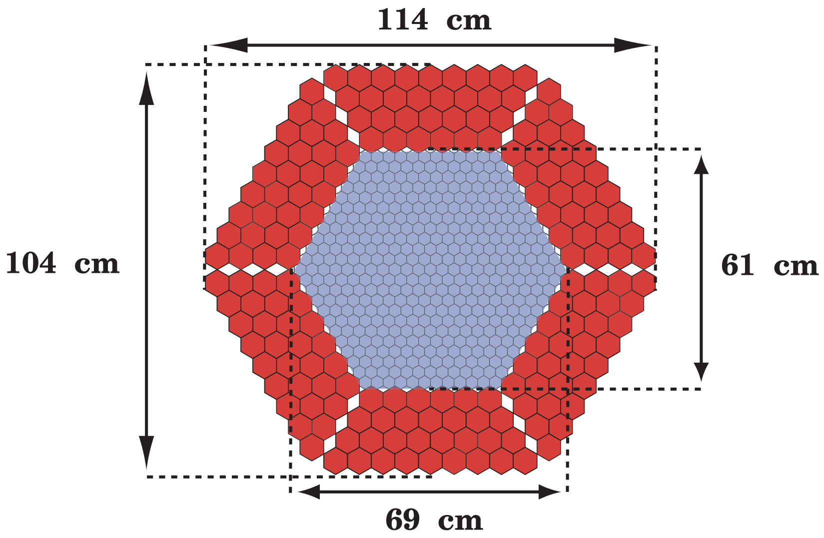

Figure 3.6: *A schematic of the camera installed in the MAGIC Telescope. The inner region (blue colored) is equipped with 397 0.1°ϕ pixels (up to 2.1°-2.3° ϕ); and the outer region (red colored) with 180 0.2°ϕ pixels (up to 3.5°-3.8° ϕ).*

much the image quality with respect to 0.1° pixels, and one saves 540 PMTs with respect to a uniform arrangement of 0.1° pixels [50].

The MAGIC camera has the following features:

- *Large field of view*: the 3.5-3.8° ϕ (for the small and the large axis respectively) camera field of view (FOV) ensures a full containment of most of the shower images ($E \lesssim 10\ TeV$), and hence a good energy resolution and $\gamma/background$ separation; specially for the very high energy ($E \gtrsim\ 1\ TeV$) showers.

- *Fine granularity*: the 0.1° ϕ pixels in the central region provide a better reconstruction of the shower images, and thus an enhancement in the $\gamma/background$ separation capabilities of the telescope; specially at low energies ($E \lesssim\ 200\ GeV$). Besides, the small pixel size also helps in the reduction of the $LONS$ in individual images. This improves the reconstruction of the shower images (*i.e,* it improves the sensitivity of the telescope) and allows one to reduce the trigger threshold preset on the discriminator level, which implies a reduction in the E_{th}.

In addition, the camera layout of the MAGIC Telescope has another important element; a plate of light concentrator cones in front of the photodetector matrix. These light concentrators achieve two goals:

- Firstly (and most important), they provide a nearly 100% active area by minimizing the dead space between pixels. The entrance window of these light concentrators has a hexagonal shape (as shown in figure 3.6), which allows for a perfect compactness of the camera pixels. The output window of these concentrators has a circular shape that couples to the round active area of the PMTs. This plate increases the photon detection efficiency of the PMT camera by about 50%. Due to the low cost of these light concentrators, they are by far the most cost efficient element in the camera of the MAGIC Telescope.

- Secondly, they reject a big fraction of the light coming with an incident angle larger than the one defined by the last ring of mirrors of the main reflector; which reduces the level of background light in the camera.

The light concentrators were designed by Daniel Ferenc [59], and constructed in the Max-Planck-Institut für Physik (München) in 2002. They are made from a plastic material covered with aluminized Mylar foil of ~85% reflectivity[5].

I want to point out that some studies that I performed on the PMTs of MAGIC had a very important impact on the design of the previously mentioned light concentrators [60, 61]. I will come back to these studies in section 3.3.2, where I will report about some relevant performance data of the PMTs used in the MAGIC camera.

Finally, the light guides and the *PhC* of the PMTs are protected from the environmental conditions by a window of 2 *mm UV* transmitting plexiglas. Due to the reflectivity of the plexiglas (n = 1.5), which is R = 4% in each of its sides, the amount of light reaching the light guides is about 92% of the light focused by the parabolic mirror onto the camera plane.

---

[5] A 3*M* foil with 99% reflectivity is being considered for a second upgraded version of MAGIC.

3.3.2 The photosensors in the camera

In the *TDR* of MAGIC, which was published in 1998 [50], several photosensors were considered for being installed in the telescope camera; namely photomultiplier tubes (PMTs), hybrid photomultiplier tubes (HPDs) and avalanche photodiodes (APDs). Since then, quite some R&D was performed on the three options, and finally, we decided to use PMTs. Despite of the higher quantum efficiency (*QE*) of HPDs and APDs, the restricted size of the active area and the high price of these two types of devices would have complicated the design of the camera and would have increased substantially the total cost of the telescope[6]. However, due to the significantly higher *QE* of these devices (which implies a reduction in the telescope E_{th}), quite some R&D is still going on in order to decrease the production cost and implement them in the camera of a second upgraded MAGIC Telescope [62, 20]. Besides, the novel silicon photomultiplier devices (SiPMT) are also a competitive option to detect low photon signals [63, 64], and thus will be likely considered for future (2-3 years) $IACT$ cameras.

The PMTs to be used in MAGIC had to fulfil the following requirements:

- Less than 30 *mm* ϕ (0.1°) and 60 *mm* ϕ (0.2°) for the inner pixel and the outer pixel respectively.
- Good photon collection inside the light cones.
- Low PMT gain ($\lesssim 2 \cdot 10^4$) because of the high $LONS$, that can induce photoelectron (*phe*) rates in excess of a few hundred *MHz* (see sections 2.3.4 and 4.6)[7].
- Fast pulse detection with a signal FWHM close to 1 ns, which improves the γ/h separation and reduce the noise generated by the $LONS$.

---

[6] In the case of the APDs, the low amplification of the signal (about 3000) is an additional problem when detecting short signals of a few photons. The required increase in the gain of the shaping amplifier introduces extra noise in the signal, and thus, reduces the signal to noise ratio.

[7] The maximum allowed gain for the PMTs is determined by a DC anode current not exceeding a few μA. Assuming a $LONS$ rate of ~0.15 *phe/ns* per pixel, the maximum allowed PMT gain is $\lesssim 3 \cdot 10^4$.

- Single photoelectron response. This feature is not strictly necessary, but it makes the calibration of the camera more simple.

- Low afterpulse rate. In *IACT* cameras, the PMT system works in a self-trigger mode; and the lowering of the trigger threshold setting is partly limited by the afterpulse rate caused by single *phe* pulses produced by the *LONS* [65].

- Dynamic range up to $5 \cdot 10^3$. This wide dynamic range is a requirement to detect the largest expected signals (which are produced by ~ 10 *TeV* gamma showers at low zenith angles), which are about $5 \cdot 10^3$ *phe*s per camera pixel, and still be able to resolve signals of few ($\gtrsim$1) *phe*s.

- High *Quantum Efficiency* (*QE*) between 300 and 600 *nm*, which is the wavelength region from where most light is expected at low zenith angles (see figure 4.15).

Because of all these particular requirements, the MAGIC collaboration started a R&D program together with the english company *Electron Tubes* (*ET*). The outcome of this collaboration was the design and construction of the new 9116A and 9117A type PMTs from *ET*. These PMTs have two features that distinguish them from conventional PMTs and make them suitable for the MAGIC Telescope: a hemispherical photocathode (*PhC*), and a dynode system with (only) 6 stages in circular-focused configuration.

The hemispherical entrance windows of these PMTs are made from borosilicate glass, and have diameters of 25 *mm* (ET9116A) and 38 *mm* (ET9117A), which match very well with the dimensions of the designed layout of the inner and outer sections of the camera of MAGIC (see section 3.3.1). I want to stress that the high aperture solid angle of the hemispherical-shaped windows provides a better light collection (than conventional flat entrance window PMTs) inside the light concentrators, and thus, minimize the losses in this light concentration process. Besides, in a hemispherical window PMT all photoelectrons have (roughly) the same path length between photocathode and first dynode; and hence the time jitter is minimized.

The 6-stage dynode system allows for a low gain ($\lesssim\ 2 \cdot 10^4$) with good interdynode electron collection efficiency and a low interdynode time spread compared to conventional PMTs

Figure 3.7: *Photograph of the PMTs 9116A and 9117A from Electron Tubes*

with 10-12 dynode stages. The 6-stages dynode system together with the hemispherical-shaped *PhC* allow these PMTs to produce signals with rise times as short as ~ 700 *ps* and $FWHM < 1 - 1.2$ *ns* [66][8]; thereby allowing for an efficient coincidence trigger design in the detection of the Cherenkov flashes from the γ-showers, as well as an efficient suppression of *LONS* induced triggers.

A good single *phe* response and low afterpulsing probability are opposite characteristics in these types of PMT. Many of the PMTs are able to work with a high enough gain in the first dynode ($\delta_1 \sim 8 - 10$) to provide a good single *phe* response. However, we observed that a high amplification in the first dynode contradicts the requirement of having a low afterpulse rate; *i.e,* by increasing the *PhC*-D1 voltage, one can promote single photoelectron response over a low afterpulsing and viceversa. We performed an extensive study of all these issues [66], and the conclusion was that by using a 3R-R-R-R-R-R-R base with an overall $HV \sim 1.1$ *kV* (hence providing an interdynode voltage of ~ 120 *V* and a photocathode-to-first dynode voltage of ~ 360 *V*), the gain was around $2 \cdot 10^4$, the afterpulsing probability was well below an

---

[8] Actually, these properties were measured only for the ET9116A type PMT. However, since the dynode system of the ET9117A type is identical, one expects a similar behavior in the ET9117A type PMT.

acceptable level[9], and still quite some PMTs were able to resolve single *phe* signals.

We also observed that a linear behavior can be achieved over the previously mentioned dynamic range of $5 \cdot 10^3$ *phe*s (*i.e,* up to 16 pC when the PMT gain is $2 \cdot 10^4$) if the inter-dynode voltages applied to the 5^{th} and 6^{th} dynodes are increased by 50 V with respect to the nominal ~ 120 V [66][10]. In the camera of the MAGIC Telescope, the voltage of the 5^{th} and 6^{th} dynodes is set to -350 V and -175 V (with respect to the anode, which is at 0 V) by an *active voltage network*, and the *PhC*-*D*1 voltage is fixed to 350 V by means of a zener diode.

In order to compensate the relatively low PMT gain, a 1 *GHz* bandwidth transimpedance amplifier has been developed. The amplifier output noise is $\sigma_{noise} \lesssim$ 0.2 mV for a gain of ~ 8, which corresponds to a total Equivalent Noise Charge (*ENC*) of $\lesssim$ 0.2 electrons at a PMT gain of $2 \cdot 10^4$; *i.e,* the amplifier noise is low enough to still resolve single *phe* signals. Further details about this transimpedance amplifier can be found in [67].

The *PhC* of the ET9116A and ET9117A type PMTs is bialkali with enhanced green sensitivity. The spectral sensitivity is slightly superior than that of the classical bialkali *PhC*, as it is shown in [60, 61] and in section 4.1 of this Thesis. The PMT *QE* exceeds 20% (25% in the peak), in the wavelength range between 330 *nm* and 470 *nm*; which matches quite well the peak in the Cherenkov photon spectrum expected at the MAGIC site (see figure 4.15). It is worth mentioning that, due to the fact that the PMT manufacture is still manual, there is always a non-negligible spread in the spectral sensitivity of all types of PMT. The *RMS* of the distribution of the *Corning Blue*[11] values for the ET9116A PMTs used in MAGIC (which were provided by *Electron Tubes*) is $\lesssim$10%.

During the studies that I performed in the years 2000-2001 on these new PMTs from *Electron Tubes*, I noticed the existence of $\lesssim 1$ *mm* grains inside some of the PMTs. These

---

[9] Fractions of percent per incoming *phe* at a detection threshold of ~ 5 *phe*s.

[10] Again, this study was carried out only for the ET9116A type. Nevertheless, since the dynamic range depends only on the dynode system, and both PMTs have the same electron multiplier, these results should be also valid for the ET9117A type.

[11] The *Corning Blue* characterizes the photon sensitivity of the PMT at $\lambda \sim 400$ *nm* (*i.e,* blue region).

grains were identified as the remnants of the Antimony (*Sb*) pill[12], which is used to activate the *PhC* in the last stages of the PMT manufacture. The *Sb*, despite being a semiconductor, is quite conductive; it has a resistivity of 390 $n\Omega/m$. For comparison purposes, note that the Rubidium (*Rb*) and the Cesium (Cs), which are the two alkali metals of the ET9116A *PhC*, have resistivities of 115 $n\Omega/m$ and 187 $n\Omega/m$ respectively. I found that, occasionally, these grains could slip between the *PhC* and the metal plate located at the entrance of the dynode system, which is connected to the first dynode. In these cases, the grains produced a short circuit between the *PhC* and first dynode, and thus prevented the PMTs to work. Note that this effect is specially important when the PMTs are used in the camera of an $IACT$. Due to the telescope movements, the orientation of the PMTs is not fixed. When the night starts they are moved from the horizontal position to the vertical one, and then back. Therefore the shortening could happen with an unpredictable rate.

This finding initiated an intensive inspection and selection of all the ET9116A and ET9117A PMTs. This task was carried out at *Max-Planck-Institut* in spring 2001. The *Sb* grains were found in 30% of the ET9116A type PMTs, but in none of the ET9117A type PMTs. All the affected PMTs were replaced by *Electron Tubes*.

I also measured that the hemispherical shape of the entrance window provides an enhancement in the detection sensitivity for those photons whose trajectories cross the *PhC* twice [60, 61]. In this case, if the photon is not absorbed in the first "hit", it still has a second chance of being absorbed at the other side of the hemispherical *PhC*, and therefore, the PMT *QE* for these *double crossing photons* is higher. The spectral enhancement in the PMT *QE* for these photons is quite sizeable, as it is illustrated in figure 4.14; at 400 *nm*, the increase is about 20%. Figure 3.8 shows that when a PMT with hemispherical entrance window is coupled to a light collector, some of the photon trajectories do cross the *PhC* twice, and therefore, the effective *QE* of the PMT is enhanced. This effect was one of the considerations taken into account when designing the light collectors for the camera of MAGIC. The shape of the light cones is such that maximizes the amount of photon trajectories crossing the *PhC* twice [59]. The number of *double crossing photons* increases when increasing the

---

[12] Private communication from *Electron Tubes* engineers.

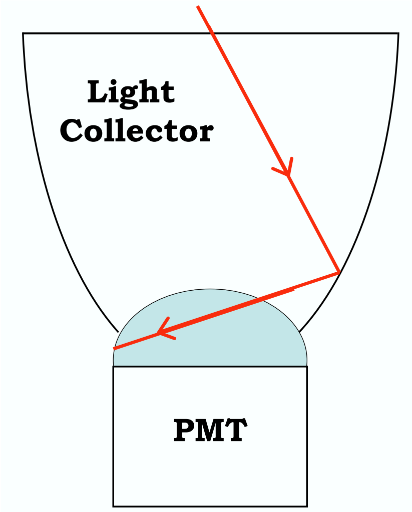

Figure 3.8: *Sketch of a hemispherical window PMT coupled to a light collector.*

photon incident angle ($\mathcal{I}$); at $\mathcal{I}\sim 27^{\circ}$ (the edge of the main reflector) the fraction of *double crossing photons* is about 60%[13].

The uniformity in the response of these two types of PMTs was also studied in detail [60, 61]. The outcome of this work was that both PMTs are quite uniform (at the level of 30%) when the central part of the *PhC* is illuminated. Yet, when the periphery of the *PhC* is illuminated (2-3 *mm* above the edge of the active area of the *PhC*) the released *phe*s are not well collected onto the dynode system, and hence the PMT response drops. I also found a clear correlation between the distance *entrance window-dynode system* and the *phe* collection efficiency at the *PhC* periphery; the larger this distance, the better the collection efficiency in this area and hence, the better the PMT sensitivity there. This distance is specially small in the ET9116A type PMT, and thus the sensitivity of this PMT type close to the edge of the *PhC* is poor, as it is illustrated in figure 4.12*a*. The sensitivity in the ET9117A type PMT is also reduced in the periphery of the *PhC*, but not that much as in the ET9116A type PMT [60].

These studies had an important impact on the design of the light collectors for the inner

---

[13] Private communication from Daniel Ferenc.

part of the camera. In order to maximize the sensitivity of the pixel, the light collectors were designed such that the output aperture has a diameter of 21 *mm* (instead of 25 *mm*, which is the diameter of the ET9116A *PhC*); and therefore only the central region of the ET9116A PMT is used.

It must be pointed out that the low sensitivity in the periphery of the *PhC* of the ET9116A type PMT reduces the enhancement in the effective *QE* produced by *double crossing photons*. This is because some of the *double crossing photons* (not converted at the first hit) are expected to be converted in those regions where the *phe* collection efficiency is quite low. We noted that the overall sensitivity of a ET9116A PMT coupled to one of the light collectors used in MAGIC varies roughly proportionally to the cosinus of the incident angle ($\mathcal{I}$); *i.e,* proportionally to the variation of the cross section of the pixel's entrance window. Therefore, as $\mathcal{I}$ increases, the enhancement in the sensitivity produced by the increase in the number of *double crossing photons* is such that compensates the sensitivity loss due to the larger amount of photons hitting the aluminized Mylar foil (85% reflectivity) of the light cone.

As stated in section 2.3.2, one of the most important challenges in Cherenkov telescopes is to maximize the conversion of photons to photoelectrons in order to reduce the threshold energy. In this context, I discovered a simple method to enhance substantially the *QE* of the used PMTs. The technique consists in the application of a light scattering lacquer doped with a wavelength shifter (*WLS*). After coating the PMTs with this lacquer, the peak *QE* increases from the above mentioned 25% to up to 30%. This technique has a significant impact in the reduction of the telescope E_{th}, and it is another of the technical innovations of the MAGIC Telescope. The details of this new technique, as well as the improvement achieved in the performance of the telescope are reported in chapter 4.

3.3.3 The optical link system to transmit the PMT analogue signals

The trigger and the readout electronics is not located in the camera, but in the central data acquisition building, which is located 100 *m* away from the telescope frame. This has several advantages with respect to cameras that contain the trigger and the signal digitization:

- The camera contains no signal processing electronics, which simplifies maintenance and repairs; particularly during night time.

- All PMT analogue signals are available in the data acquisition building; which allows one to easily inspect them for debugging purposes.

- The camera is lighter, since it contains less electronics and power supplies. This helps in controlling the camera oscillations and reduces the counterweight that has to be used. Consequently, the telescope inertia is lower, which allows a fast telescope repositioning.

- The camera has a smaller size, and hence a smaller resistance to the wind.

- In a camera with neither trigger nor $FADC$ system, the pickup noise affecting the PMT signals is significantly reduced. The trigger and, specially, the $FADC$s are known to be noisy systems. If a large amount of trigger and $FADC$ channels are packed in a place of reduced dimensions, the electromagnetic noise originated can be quite sizeable.

- The trigger and the $FADC$ system do not have constraints of weight, size and heat dissipation, which allows one to use standard methods and equipment for the data acquisition system.

- The required heat dissipation in the camera is significantly lower; thus cheaper and more simple cooling systems can be used. It is worth noticing that the power consumption of the currently used $FADC$ system is about 20 kW, while the electronics for the PMTs and the VCSEL drivers consume only 800 W. The reduction in the requirements for the cooling system has also an impact on the weight of the camera.

- The electronic pixel chain is more modular, allowing for later upgrades of the trigger and $FADC$ system without having to modify the telescope camera, which is typically a much more complex operation.

Conversely, this camera design has one disadvantage; the attenuation and distortion of the PMT signals during their transmission to the data acquisition building. Such building can be located several tens of meters away from the telescope, and on the other hand, the

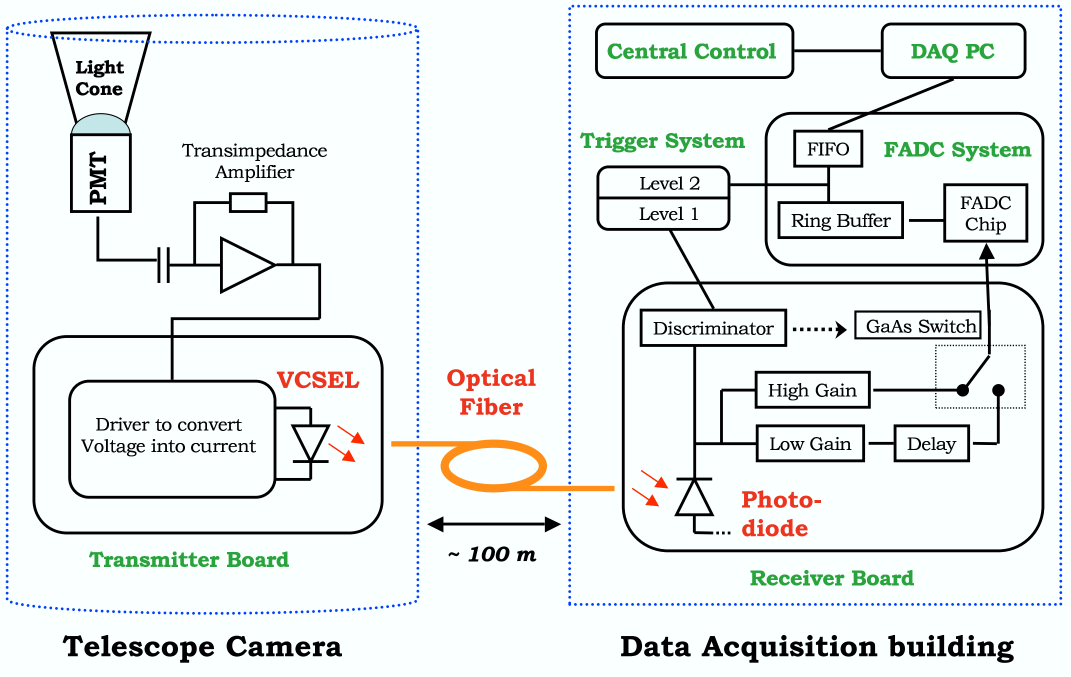

Figure 3.9: *Schematic overview of the data stream in the MAGIC Telescope.*

PMT pulses produced by the Cherenkov light flashes are very short (typically about 2-3 *ns* FWHM). Consequently the degradation of the pulses can be quite significant (see figure 5.7).

In the particular case of MAGIC, the telescope has very large dimensions, and the data acquisition building is located at about 100 *m* from the telescope frame. The real distance that the PMT signals have to travel is about 150 *m*, and thus, the distortion and attenuation of the PMT pulses is a major issue.

In order to minimize the pulse degradation, the MAGIC collaboration developed a system based on optical fibers to transfer the PMT signals from the camera to the data acquisition building. Figure 3.9 shows a sketch of the complete pixel electronic chain in MAGIC. The PMT pulses are amplified by the fast transimpedance amplifier (see section 3.3.2), and then are fed to the so-called *transmitter board*. There, the electrical pulses are transformed into light pulses by means of Vertical Cavity Surface Emitting Lasers (VCSELs) and coupled to multimode graded index fibers (50 μm ϕ core, 125 μm ϕ cladding). The details about the optical coupling between VCSELs and fibers are explained in section 5.2. The optical signals travel through the 162 *m* long fibers with minimal degradation, and arrive to the so-called *receiver board*, located in the data acquisition building. There, the optical pulses are transformed back into electrical pulses by PIN-diodes, and then are further processed by the trigger and *FADC* system as I will discuss in sections 3.4 and 3.5.

Such an optical system for transferring the PMT signals has some advantages with respect to a conventional system based on coaxial cables:

- The dispersion and attenuation of pulses of few *ns* FWHM is significantly lower. Note that the attenuation in a good quality coaxial cable (RG 58 C/U) is about 24 $dB/100\ m$ at 200 *MHz*, whereas in a multimode graded index fiber it is only about 0.3 $dB/100\ m$ at 500 *MHz*.

- The optical link system is much less bulky than a system based on coaxial cables. In the MAGIC Telescope, 72 fibers are packed in a single cable of 16 $mm\ \phi$. It is worth to note that a single RG 58 C/U coaxial cable has already a diameter of 5 *mm*.

- Optical fibers are about an order of magnitude lighter than coaxial cables, which is important to keep the load (and consequently the inertia) of the telescope low.

- There is no possible *crosstalk* between channels.

- Signals traveling through optical fibers are immune to electromagnetic interference.

- The optical fibers are made of glass (not conductive material), and therefore are immune to lightening strikes.

I would like to point out that the technique to transmit PMT pulses with optical fibers was first developed by the AMANDA collaboration [68]. The main technical innovation in the system used in MAGIC is the use of VCSELs instead of Light Emitting Diodes (LEDs), which provide a wider dynamic range at high bandwidth. As I will report in section 5.1, VCSELs have several performance advantages with respect to LEDs and conventional Edge Emitting Lasers (EELs), thus making VCSELs more suitable for being used to transmit the analogue PMT signals in Cherenkov telescopes.

Members of the MAGIC and VERITAS[14] collaboration joined efforts in 2000 to built successfully an optical link system with VCSEL drivers to transmit PMT pulses [70]. This system was then used to transmit (through 50 m long optical fibers) the signals of the 111 PMTs located in the outer ring of the camera of the WHIPPLE telescope down to the main station where the signals are digitized. The signals coming from the 379 PMTs located in the inner part of the camera were transmitted using 50 m long *RG58* coaxial cables. A study of the shape of the analogue PMT signals in the data acquisition building showed that the pulse degradation was significantly lower in those channels transmitted by optical fibers; the FWHM of the fiber channels was 8 ns, whereas that of the coaxial cable channels was 12 ns [71]. It is worth mentioning that the typical FWHM of the pulses produced by the PMT camera of the WHIPPLE telescope was already about $7ns$; therefore, the distortion of the pulse shape produced by the optical link system was hardly visible.

Unfortunately, unexpected instabilities in gain and noise performance (which were attributed to the mode "hopping" in the VCSELs) appeared in many of the channels of the optical link system. On the one hand, these instabilities made the fiber channels to be more noisy than the coaxial cable channels, and on the other hand, the fact that the measured noise and internal gain could change with time (see [71] for details) made the optical link system less reliable than the coaxial cables. Therefore, the WHIPPLE collaboration decided not to include the signals of the channels transmitted by optical fibers (outer region of the camera) into their data analyses.

It must be pointed out that VCSELs are quite novel devices. They started to be commercialized in 1996, and so far, they have been used only in digital communication applications; where relatively small instabilities in the pulse amplitude do not have any negative consequence in the performance of the system.

In order to reduce the effect of these performance problems, we carried out an extensive study on the VCSEL type *HFE4080-321* from Honeywell, which was intended to be used

---

[14] VERITAS is the name of an array of 7 Cherenkov telescopes of 12 m ϕ that will be built in Arizona in 2006 [69]. However, a large fraction of the people working in this project are part of the WHIPPLE collaboration, which operates since many years a 10 m ϕ telescope located in Arizona too.

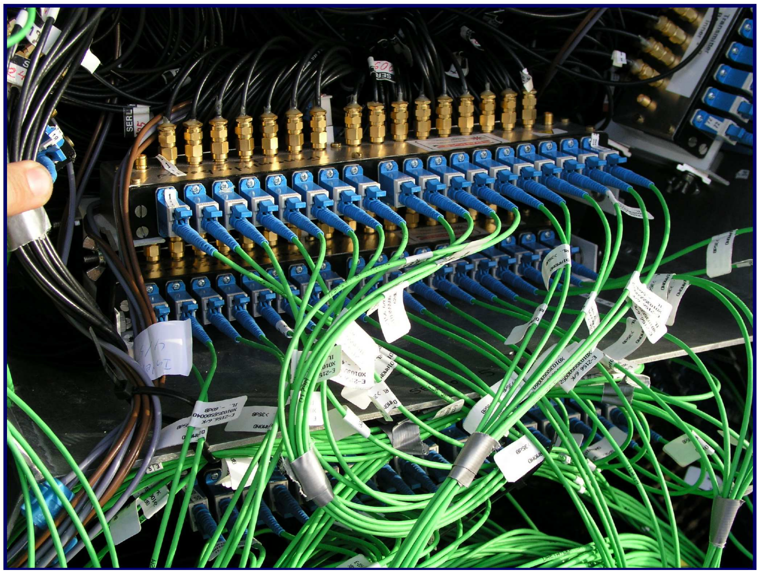

Figure 3.10: *Photograph of two transmitter boards installed in the camera of the MAGIC Telescope.*

in the MAGIC Telescope. We characterized the above mentioned instabilities and modified slightly the design of the system in order to bring these instabilities far below the statistical fluctuations of the PMT signals. In addition, detailed quality checks were carried out for each single VCSEL, and all those lasers not fulfilling the strict requirements to be used in MAGIC were rejected. The details of these studies, as well as the final performance of the optical link system used in MAGIC is reported in chapter 5.

In the following lines, I will briefly describe the transmitter and the receiver boards used in the optical link system.

Figure 3.10 shows a photograph of two transmitter boards used in the MAGIC Telescope; and figure 3.11 shows the back side of the MAGIC camera during the transmitter board installation. In the camera there are 36 transmitter boards that contain 18 VCSELs each. We use 25 transmitter boards to transfer the signals from the pixels located in the inner section of the camera, and the remaining 11 transmitter boards to transfer the signals from the outer section of the camera. Out of the 648 VCSELs installed, only 576[15] are used during

---

[15] As I mention in section 3.3.1, the MAGIC camera has 577 pixels. However, the pixel located in the center

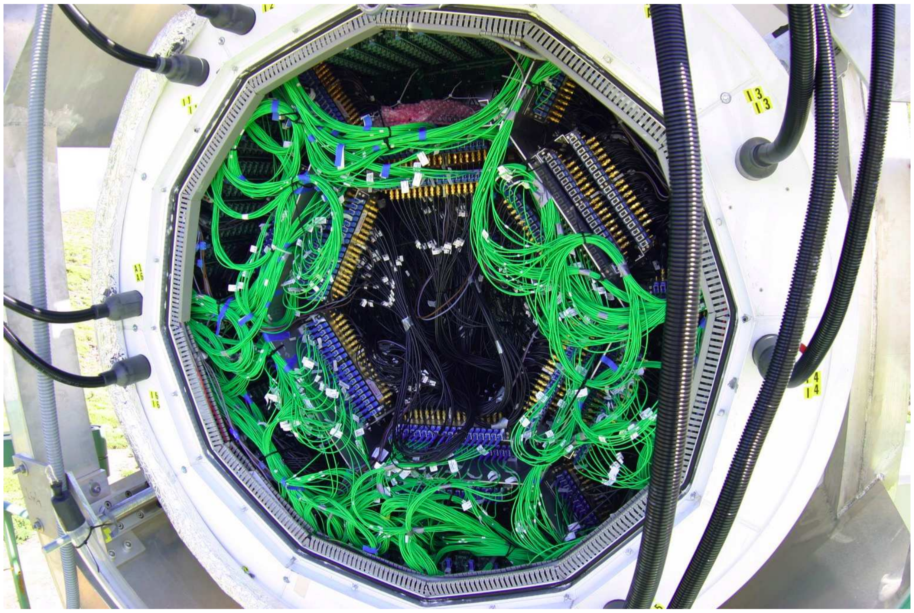

Figure 3.11: *Photograph of the back side of the camera during the transmitter board installation (May 2003).*

normal operation (16 VCSELs out of the 18 VCSELs installed in each transmitter board); the other 72 are spare lasers that allow one to replace easily a VCSEL in case of failure. The black coaxial cables (RG 174) with gold-plated SMA connectors transport the signals from the PMT bases to the transmitter boards. In the transmitter boards, the voltage signals from the PMT bases are converted into current signals that modulate the current flowing through the VCSELs, hence modulating their light output. The schematic of the circuit of the transmitter board is depicted in figure 3.12. Finally, the optical fibers, which are the green color cables (in pictures 3.10 and 3.11) connected to the VCSELs, bring the light signals down to the counting house, where the receiver boards are located.

Figure 3.13 shows a photograph of one of the receiver boards used in the data acquisition building. Each receiver board contains 8 channels that perform the light-to-electric signal conversion. In total, there are 72 boards that handle the signals from the 576 PMTs of the MAGIC camera. The schematic of the circuit of the part of the receiver board that converts

---

of the camera is treated separately, and currently that location of the camera is empty. It is planned to install a high QE photosensor for pulsars studies.

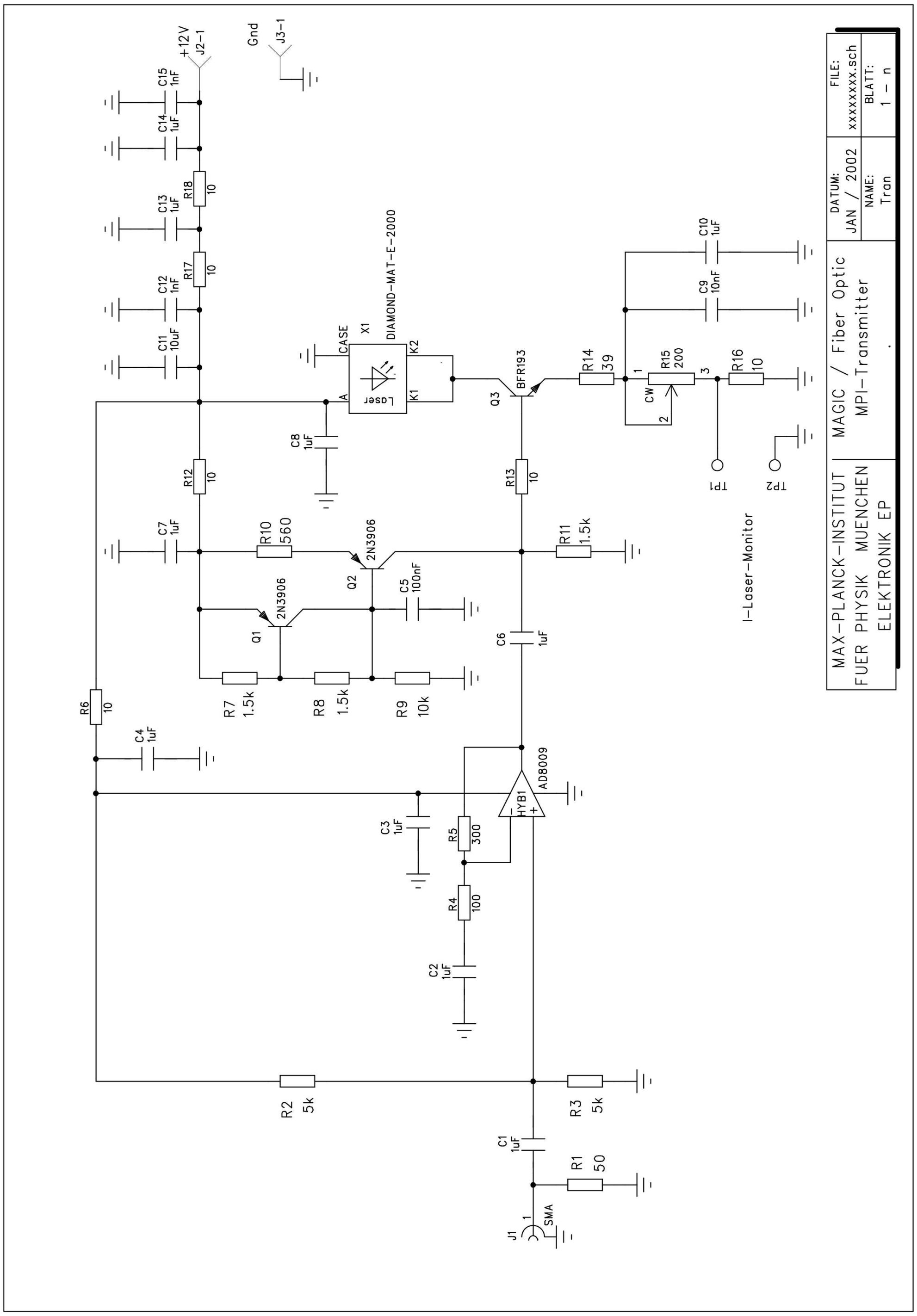

Figure 3.12: *Schematic of the circuit of the transmitter board.*

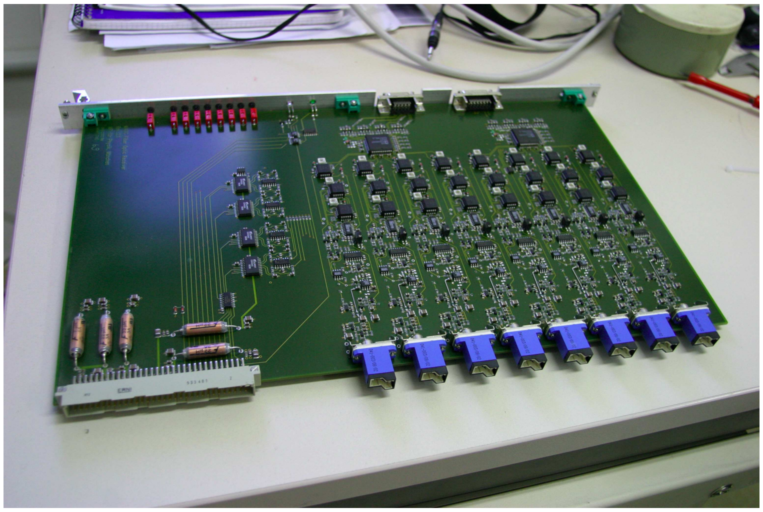

Figure 3.13: *Photograph of one of the receiver boards used in the data acquisition building of the MAGIC Telescope.*

the light signal into the electric signal is shown in figure 3.14. Note that due to the AC coupling at the input of the board, the light (in principle constant) produced by the constant forward current (bias current) flowing through the VCSELs is not amplified; only the short PMT signals are amplified.

As shown in figure 3.9, once the optical pulses are converted back into electrical pulses, they are split into 2 branches; one (the so-called *trigger signal*) going to a discriminator (located in the same receiver board) which is part of the trigger system, and the other one (the so-called *FADC signal*) going to the *FADC* system, where the electric pulses are digitized. Due to the digitization speed of 300 MSample/s of the current *FADC* units (see section 3.5), the signal is stretched (in the receiver board) to ~ 6 ns FWHM so that at least 4 points can be measured for each pulse. The *FADC signal* is split (also in the receiver board) into the so-called *high* and *low* gain channels. The high gain signal is further amplified by a factor 10, whereas the low gain signal is delayed by 50 ns. If the signal exceeds a preset threshold, the delayed low gain signal is combined with the high gain signal using a fast *GaAs* switch, and then digitized consecutively after the high gain signal by the same *FADC* channel. This procedure of splitting the signal into *high* and *low* gain signals increases the dynamic range of the 8 bit *FADC*s by at least 2 bits.

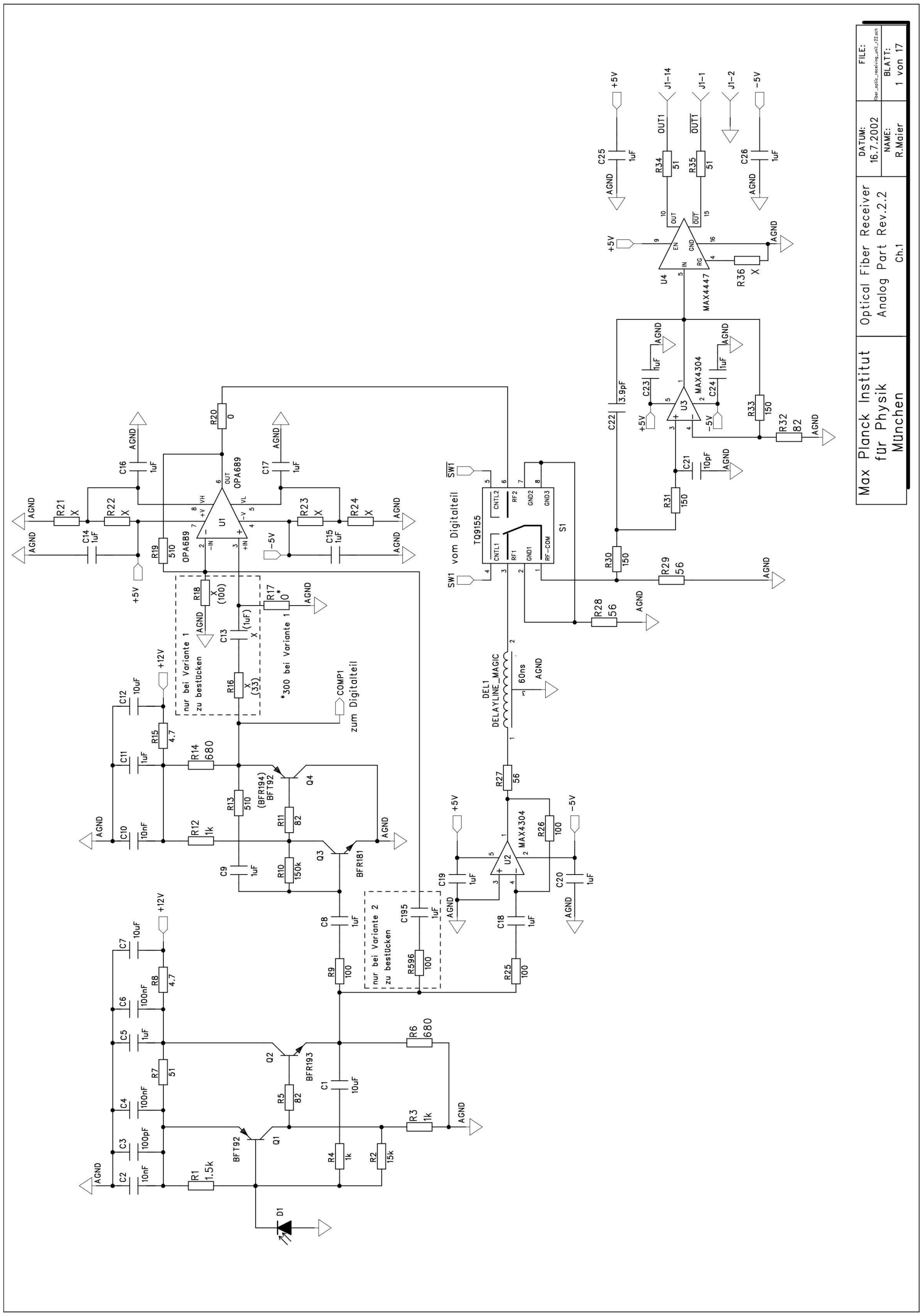

Figure 3.14: *Schematic of the circuit of the analogue part of the receiver board.*

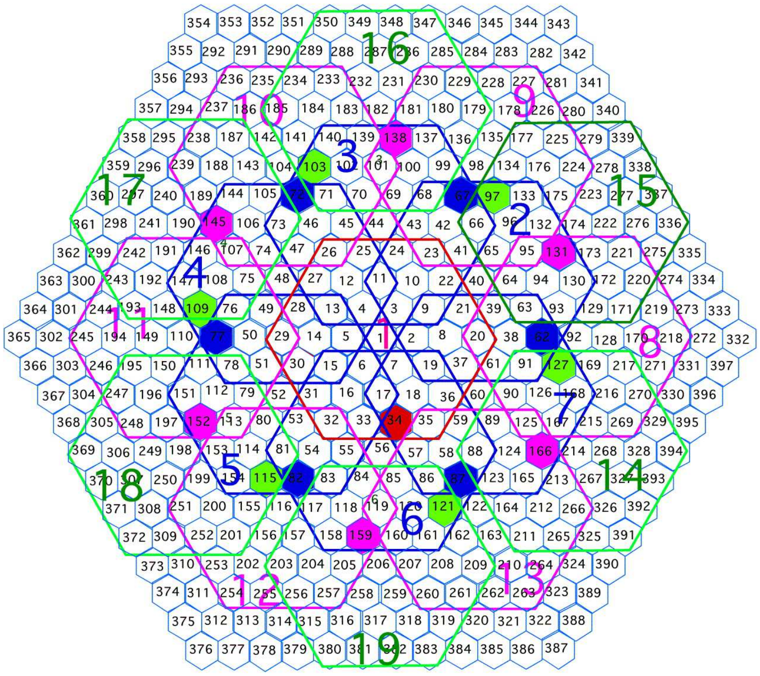

Figure 3.15: *The trigger region in the MAGIC camera.*

3.4 The trigger system

The trigger region in the camera of the MAGIC Telescope is restricted to the innermost 325 (out of 397) pixels of the camera. As shown in figure 3.15, this region is covered by 19 overlapping cells (called *macrocells*) of 36 pixels[16].

The trigger system is segmented into three stages or levels; the so-called *level 0*, *level 1*, and *level 2* trigger:

- The *level 0* trigger is located in the receiver board, and acts on individual PMT signals. As I mentioned in section 3.3.3, the pulses coming from the telescope camera arrive to the receiver board and are split into two branches; the *trigger signal* and the *FADC signal* (see figure 3.9). Whenever the amplitude of the PMT pulses is above a certain predefined value (*threshold*), the discriminator produces a square pulse of

---

[16] Topologically, each *macrocell* is formed by 37 pixels; yet there is actually one pixel (out of the 37 pixels) which is not wired to the trigger logic.

adjustable width. The width is set to 6.0 ns[17].

The discriminator threshold is set by an 8 bit DAC that is controlled by the PC in which the *Central Control* program runs. This allows one to change the discriminator thresholds remotely during telescope operation. The conversion between amplitude of the pulse after the transimpedance amplifier attached to the PMT (*i.e,* at the input of the transmitter board) and trigger DAC counts is: $1mV = 9\ DAC\ counts$. The typical discriminator threshold used in the telescope is about 36 DAC counts, which corresponds to a pulse amplitude of 4 mV at the input of the transmitter boards.

- The *level 1* trigger looks for fast coincidences of next-neighbor pixels. The signals coming from the discriminators of the receiver boards are fed into the 19 *level 1* boards (one for each of the 19 overlapping trigger cells shown in figure 3.15), and then, the boards perform a logic combination of the input signals to look for clusters of 2, 3, 4 and 5 neighbor pixels in a short (few ns) time interval. The multiplicity of the cluster of neighbor pixels can be set by the PC running the *Central Control* program, and hence, this multiplicity can be modified remotely during telescope operation. If the multiplicity is larger than 2, an additional condition is required; each pixel contributing to the trigger must have at least two fired next-neighbors. This is the so-called "closed-packed" configuration. This trigger condition reduces triggers caused by muons, yet it also might select small images which are basically round, and for which the orientation parameter ALPHA (see section 6.1.1) is not well defined. The effect of the several possible trigger configurations on the very low energy showers is still under investigation. The *level 1* trigger in the he MAGIC Telescope is typically set to coincidences of four "closed-packed" pixels.

- The *level 2* trigger performs a "digital analysis" of the shower image, and reduces the trigger rate to a value that can be processed by the Data Acquisition system (DAQ). It consists in a first stage of 19 programmable modules (the so-called *SMART*

---

[17] Actually, due to the time reaction of the electronics, the shape of these pulses is distorted and it is not really square. The FWHM of these pulses was measured to be about 5.5 ns.

modules) where the *level 1* information from each *macrocell* is divided into three 12-pixels regions, called LUT (Look-Up-Table). The outputs from the 19 modules of the first stage are fed into a second and a third stage in a tree-like structure, in order to apply cuts on the event topology (number of pixels, shape and orientation). The *level 2* allows MAGIC to perform a true online pattern recognition of the images; which increases the background rejection at the trigger level. Currently (summer 2004), the *level 2* trigger is not performing any "digital analysis" of the shower images. There are ongoing studies to find out the optimal way of using this feature [43, 72].

The *level 2* trigger communicates directly with the digital boards of the $FADC$ system (see figure 3.9) enabling the acquisition of the data whenever an event "triggers" in the above mentioned 3 trigger levels.

It must be pointed out that the *level 2* trigger contains also a *prescaler* board that can prescale the triggers (0-65535) in order not to overcome the maximum (continuous) acquisition rate allowed by the DAQ, which is 1 *kHz*. However, the *level 2* trigger can handle trigger rates up to $\sim$ 1 *MHz*. This might be a very valuable feature when performing observations at very low E_{th} ($\lesssim 20\ GeV$), as it is planned for some $\gamma - ray$ emitting pulsars, and specially, in case of observation of AGNs in flare state and GRBs, where the trigger rate might go up to several tens of *kHz*. In order to keep as much of this additional information as possible, the *level 2* trigger is able to send a *high frequency* trigger (which also can be prescaled) through a second independent line to the digital modules of the $FADC$ system.

More information about the trigger system of the MAGIC Telescope can be found elsewhere [73, 43, 74, 72].

3.5 The data acquisition system

The DAQ of MAGIC consists on 18 crates of 4 *FADC boards*, and a dual processor PC (the so-called $DAQ\ PC$) running a multithreaded C++ readout program in a Linux operative system. Each *FADC board* is prepared to digitize the signals coming from 8 channels. The components of the *DAQ* for one of the channels are shown in figure 3.9. There is a 8 bit 500 *MHz* bandwidth *FADC* chip which digitizes at a speed of 300 MSamples/*s*, a 32 *KByte* ringbuffer, and a 512 *KBytes* First Input First Output (*FiFo*) module.

The *FADC* chips continuously digitize the analogue PMT signals that come from the receiver boards and store them in the ringbuffers. As pointed out in section 3.3.3, in the receiver board the PMT signals are stretched to $\gtrsim 6$ *ns* FWHM (so that the *FADC* chips can measure the pulse amplitude at $\gtrsim 4$ points), and then the signals are divided into two branches (*high gain* and *low gain*) in order to increase the dynamic range to $\gtrsim 60$ *dB* [75]. When a *level 2* trigger arrives to the *FADC* modules, the *FADC* chip stops digitizing, the position of the signal in the ringbuffer is determined and 30 time slices of 1-*Byte* (15 for *high gain* and 15 for *low gain*) are written into the *FiFo* buffer for each pixel. This operation is performed at a maximum rate of 80 *MBytes/s*; which results in a dead time of less than 1 μs. This corresponds to less than 0.1% dead time at the design trigger rate of 1 *kHz*. The time and trigger information for each event is recorded by dedicated digital modules which are read out together with the *FADC boards*.

As mentioned in section 3.4, during observations of *AGN*s in active state, low energy signals from strong pulsars and *GRB*s, the trigger rate could exceed the ∼1 *kHz* data taking capability of the *DAQ*. Because of that, the *DAQ* is provided with a separated high frequency data stream which records only the time and trigger information of the events sent by the dedicated *high frequency 2 level* trigger, that can reach rates of up to ∼1 *MHz*.

The *FADC* data is reorganized and merged into a raw event data format. The data is saved into a RAID0 disk system at a rate of up to 20 *MBytes/s*, which can amount to up to 800 *GBytes* per night. During daytime the data is transformed into ROOT format and written to tape. During normal telescope operation, the complete readout program running in the *DAQ PC* is controlled remotely via TCP/IP by the *Central Control*.

Further information about the *DAQ* of the MAGIC Telescope can be found elsewhere [50, 76, 77, 78, 79, 75].

3.6 The calibration system

The analysis of the shower images produced in the camera of an *IACT* is based on the comparison of the measured image shape and light content with the Monte Carlo predictions. In order to perform this comparison, the conversion factors between the recorded amount of *FADC* counts and the amount of photons impinging on the camera must be known for the individual pixels[18]. It is therefore mandatory to calibrate the telescope camera with respect to the light flux.

We developed a novel system which allows one to perform the optical calibration over a large dynamic range and in an absolute manner; *i.e,* correcting also for the individual PMT sensitivity (quantum efficiency and *phe* collection efficiency) and light concentrators efficiency. The design of this calibration system is another of the technical innovations of the MAGIC Telescope (with respect to the calibration systems of contemporary *IACTs*) in which I also had the pleasure of being involved [80].

The schematic of the calibration system is shown in figure 3.16. The system is based on a box (*pulser box*) located at the center of the main reflector, which contains 16 light pulsers with LEDs emitting at three different wavelengths: 370 *nm*, 460 *nm* and 520 *nm*. There are 13 boards equipped with 5 LEDs, 1 board with 3 LEDs, and 2 boards with one single LED. In each of the 16 pulser boards, the LEDs installed are of the same type, and thus emit light at the same wavelengths. The light pulses have 3-4 *ns* FWHM duration, which is nearly as short as the Cherenkov light flashes produced by the air showers in the individual pixels. The total amount of light produced, as well as the color of the light, is selected externally by switching on and off the individual boards by a 500 *MHz* bandwidth *GaAs* analogue switch controlled through CAN bus. The pulser boards fire synchronously (with a remotely adjustable pulse rate of up to 1 *kHz*), producing a maximum of 2000-3000 *phe*s in an inner pixel when all boards are active. The light output of the LEDs is diffused by a

---

[18] Actually, it is possible to perform a γ-hadron separation and a γ-signal extraction provided all pixels have an equal response; *i.e,* without the knowledge of the *FADC* counts-to-photon conversion factors. However, in such case, one would not be able to estimate properly the energy of the primary $\gamma - ray$, which is related to the amount Cherenkov light detected by the telescope.

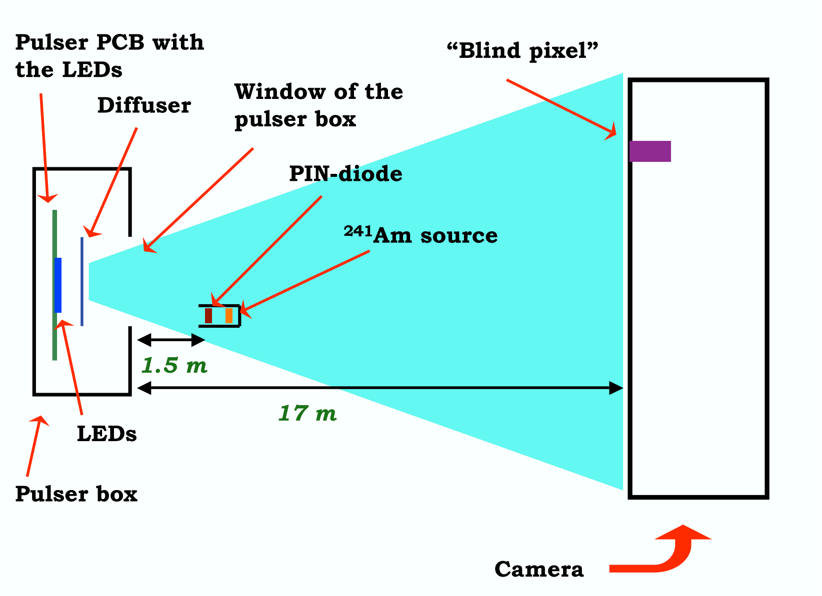

Figure 3.16: *Schematic of the calibration system used in the MAGIC Telescope.*

frosted glass plate; which allows for a homogeneous light illumination of the camera (located at 17 m distance) with an uniformity of $\lesssim 3\%$.

Finally, the calibration system is equipped with a PIN-diode located at 1.5 m away from the pulser box; and a special pixel, the so-called "blind pixel", located in the camera and operated in single photon counting mode. As I will show in the next paragraphs, these devices are used to measure the absolute quantity of photons contained in the individual calibration pulses, and thus, allow for an absolute light calibration at the above mentioned three LED emitting wavelengths. By producing known light pulses of selected intensity, the complete electronic chain (from the PMTs attached to the light concentrators to the DAQ) can be calibrated with respect to linearity.

The two methods used to calibrate the individual camera pixels with respect to the amount of photons produced in each calibration light pulse are the so-called *"blind pixel" method* and the *PIN-diode method*:

- *The "blind pixel" method* compares the signal in the camera pixels with the response of a special pixel ("blind pixel"), which is illuminated through a diaphragm of exactly 1 cm^2, and a filter that attenuates the signal by a factor 100. The "normal" pixels see strong signals while the "blind pixel" resolves single photoelectrons. The single *phe* spectrum of this pixel can be fitted by a sum of Gaussian distributions whose amplitudes are Poisson distributed

$$f(x) = \sum_{k=0}^{N} \frac{e^{-\lambda} \cdot \lambda^k}{k!} \cdot \frac{e^{-\frac{(x-\mu_k)^2}{2\sigma_k^2}}}{\sigma_k \cdot \sqrt{2\pi}} \tag{3.1}$$

The fit provides (in addition to the values of σ_k), the mean number of photoelectrons λ, which is used, together with the QE of the PMT used as "blind pixel", the emitted light spectrum of the used LED type, and the geometry of the "blind pixel" to calculate the mean number of incident photons per pulse and area at the camera plane.

- *The PIN-diode method* compares the signal in the camera pixels with the one measured by a PIN-diode located at 150 cm distance from the pulser box, and read out with a charge sensitive preamplifier (of 25 ns shaping time). The PIN-diode is calibrated with an ^{241}Am source emitting 59.95 keV gammas, which generate a charge distribution in the depletion region of the silicon diode peaking at 16570 ± 50 photoelectrons [81]. The mean number of photons per pulse and area at the camera plane is calculated from the measured number of *phe*s in the diode, the QE of the diode, the emitted light spectrum of the used LED type and the geometry of the system.

It is foreseen to use also the so-called *excess noise factor method* [82], which is a more conventional method (used already in past Cherenkov telescopes like HEGRA and WHIPPLE), to crosscheck the results obtained with the previous two methods. The *excess noise factor method* provides, for each individual PMT in the camera, the mean number of *phe*s ($\overline{m_{phe}}$) reaching the first dynode and being amplified. Such number is given by

$$\overline{m_{phe}} = F^2 \cdot \frac{(\overline{Q} - \overline{P})^2}{\sigma_Q^2 - \sigma_P^2} \tag{3.2}$$

where $\overline{Q}$ is the mean charge of the distribution, σ_Q the standard deviation of this distribution, $\overline{P}$ is the pedestal and σ_P the electronic noise. F is the so-called excess noise factor, and comes from the statistical fluctuations in the amplification of the electrons in the PMT dynode system. The quantity F is defined as

$$F \equiv \sqrt{1 + \left(\frac{\sigma_G}{\overline{G}}\right)^2} \tag{3.3}$$

where $\overline{G}$ is the gain of the PMT and σ_G its standard deviation. A typical way of measuring $\overline{G}$ and σ_G in a PMT is by studying the response of the PMT to single *phe*s. Obviously, these quantities depend on the PMT type and the high voltage settings used to drive the PMT [66]. For the PMTs and the high voltage settings used in the camera of MAGIC, the quantity F is about 1.15.

The advantage of the *excess noise factor method* with respect to the two previously mentioned methods is its simplicity and robustness. However, the big disadvantage is that the *excess noise factor method* does not take into account neither the *QE* and *phe* collection efficiency of the PMTs (which can vary from PMT to PMT) nor the transmission efficiency of the light guides, whereas the *"blind pixel"* and the *PIN-diode* methods do.

Note that such a calibration system provides three independent methods (containing different systematic errors) for the calibration of the camera; two methods measure the photon flux and a third one measures the number of *phe*s arriving to the first dynode of the PMTs. This design increases the reliability in the calibration procedure, and allows one to monitor possible variations in the performance of pixel chain, as well as in the different light measuring devices of the calibration system.

Besides, the calibration box has a continuous light source whose intensity can be remotely adjusted. The purpose is to simulate and calibrate the response of the PMTs to different conditions of background light[19]; which could be produced by the *LONS* and the presence of the moon and/or stars in the camera *FOV*.

The calibration system is connected to the trigger system of the telescope, which allows one to perform calibrations even during normal data taking. We are planning to perform an accurate calibration of the camera once or twice per night. This calibration would be performed using the three wavelengths, and several light intensities to calibrate the camera

---

[19] The background light increases the DC anode current of the PMTs, and thus, increases the noise in the PMT signal.

over the whole dynamic range. In addition, it is foreseen to perform many short (1-2 s) calibrations during normal telescope operation in order to crosscheck the stability of the calibration constants. These short calibration runs would consist of about 1000 light pulses of only one wavelength and at only one intensity.

Additional information about the calibration system of the MAGIC Telescope can be found elsewhere [80, 83, 84, 85].

Chapter 4

Enhancement in the PMT sensitivity by a special coating

The photomultipliers (PMTs) are currently the most sensitive devices for fast photon detection with large area sensors, allowing for single photon counting with good time resolution. The typical PMT peak QE values are close to 25% in the spectral range between 350 nm and 450 nm. In many applications an increase in the PMT QE is very desirable. Such a case is the use of PMTs in $IACTs$ for ground-based $\gamma - ray$ astronomy. In these detectors, an enhancement of the PMT sensitivity can be translated directly into a decrease in the minimum detectable $\gamma - ray$ energy, *i.e,* into a decrease in the telescope's threshold energy (see section 2.3.2)

$$E_{th} \propto \frac{1}{A_{mirror} \times LDE} \tag{4.1}$$

where A_{mirror} is the mirror area and LDE the photon-to-photoelectron conversion efficiency of the entire system. LDE is the product of the reflectivity of the mirror, the efficiency of the light guides and the effective QE[1] of the PMTs.

The motivation for this study was the intention to lower the E_{th} of the MAGIC Telescope by increasing the sensitivity of the PMT camera. As I will report in the next sections, this

---

[1] The effective QE is the cathode QE times the collection efficiency CE of the photoelectrons onto the first dynode of the PMT.

research was very successful; a way to increase substantially the sensitivity of our PMTs was discovered. The enhancement in the QE is achieved by applying a layer of structured lacquer acting as a photon scatterer. In addition, this lacquer contains a Wavelength Shifter (WLS), which extends the spectral sensitivity in the short wave UV range. In the following I will describe the method and I will evaluate the improvement in the performance of the MAGIC Telescope achieved by this technique.

4.1 Increase in the PMT *UV* sensitivity by a *WLS*

At ground level, the observed Cherenkov photon spectrum from Cosmic Ray induced air showers extends down to $\lambda \sim 290$ nm. On the other hand, the borosilicate window of the PMTs starts to absorb light below 350 nm, and has a spectral cut-off mid point around $\lambda \sim 310$ nm. We tried to enhance the UV sensitivity of the PMTs by coating them with a WLS that shifts the short wavelength light to a longer wavelength where the photons can pass the window. A common procedure consists of depositing some fluorescent organic compound onto the glass window by evaporation. The drawback of this technique is that the coating has a very weak mechanical resistance, thus not being suitable for PMTs for an $IACT$. In addition the method requires a vacuum-coating unit.

Another simple procedure consists of dissolving the WLS and some transparent plastic binder in an organic solvent. The window of the PMT is briefly dipped into this solution, and, after evaporation of the organic solvent, a layer of plastic binder and WLS is formed. The plastic binder has a good optical contact and a smooth surface with high internal light trapping. It was also found that the WLS to binder ratio and the thickness of the layer were not critical for $\lambda \gtrsim 220$ nm [86].

Because of the spectral characteristics of the used PMTs and the Cherenkov photon spectrum from air showers, the WLS needs to absorb below $\sim$320 nm and to re-emit at the spectral range of maximum QE. An additional requirement is that the decay time of the WLS should be of the order of 1 ns to match the time profile of typical Cherenkov light flashes from γ-induced showers. The fast response is mandatory for reducing the accidental

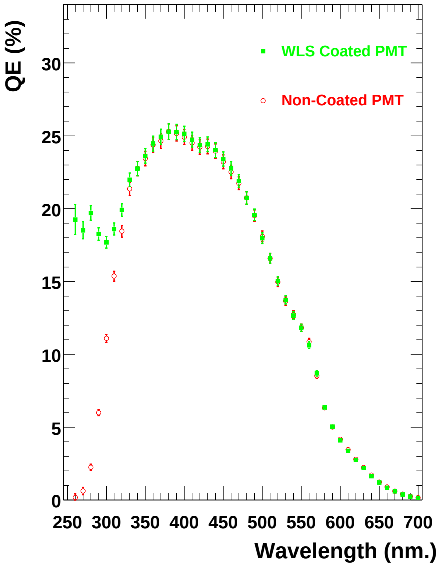

Figure 4.1: *Spectral sensitivity of a ET9116A PMT before and after being coated with a fully transparent lacquer doped with PTP.*

trigger rates caused by the *LONS* (see section 2.3.4), and for performing a good $\gamma/hadron$ separation (see section 2.3.3).

We chose 1.4 p-Terphenyl (*PTP*) as *WLS* and Paraloid B72 as binder. Paraloid B72 is an acrylic base material for lacquers which is transparent down to 220 *nm*; and *PTP* is a *WLS* that absorbs light below 320 *nm* and re-emits it around 340 *nm*, where the *QE* of the used PMTs is about 90% of the peak value. The combination *PTP*+Paraloid-B72 was measured to have a fluorescent light decay time of 0.9 *ns* (see [86] for details), thus matching our requirements.

Satisfactory results were obtained with a mixture of 0.3 *g* *PTP* and 2.0 *g* Paraloid B-72 dissolved in 50 *ml* Dichloromethane (CH_2Cl_2). The PMT (ET9116A type) was dipped into this solution and, after the evaporation of the solvent, a very thin transparent layer of *WLS* and Paraloid was formed.

The *QE* of the PMT was measured as a function of wavelength by operating the PMT as a photocell and comparing the photocathode currents with the ones obtained from a calibrated PIN-diode. The details of this measurement can be found in appendix A.

The spectral *QE* for a ET9116A PMT before and after applying the above mentioned solution is shown in figure 4.1. Note that there is a significant enhancement in the *QE* at $\lambda \lesssim 320$ *nm* and no decrease in the sensitivity at longer wavelengths. At $\lambda \lesssim 300$ *nm*, the increase in the *QE* up to $\sim 18\%$ instead of up to $\sim 25\%$ (the peak *QE* of the PMT) can be explained by *a)* the light losses due to the isotropic emission of the *PTP* (for $n = 1.5$, 13% of the light escapes into the air), *b)* a *PTP QE* somewhat below 100%, and *c)* a *PTP* peak emission around 340 *nm*, where the intrinsic *QE* of the PMT cathode is $\lesssim 23\%$.

4.2 Enhancement in the PMT sensitivity by applying a lacquer that scatters the light

In the process of liberating electrons from the photocathode (*PhC*) of a PMT, the photons have to be absorbed in the cathode layer, and then, the excited electrons must reach the vacuum interface with an energy exceeding the work function (W_{th}) of the cathode material (close to 2 eV for the Cs activation layer) in order to be able to escape the *PhC* (see figure 4.2). In this simplified model,

$$QE \ \propto \ P^{ph.}_{abs} \times P^{e-}_{esc} \tag{4.2}$$

where P^{ph}_{abs} is the probability for a photon to be absorbed in the *PhC*, and P^{e-}_{esc} is the probability for the *phe* to escape the *PhC*. P^{ph}_{abs} depends on the wavelength and path length inside the cathode, while P^{e-}_{esc} depends on the *phe*'s initial energy and its distance from the vacuum interface. In reality, the details of this process are quite complex and I refer the interested reader to the relevant literature [87].

The longer the trajectory of the photon inside the *PhC*, the higher is the probability to excite an electron. On the other hand, the longer the distance the *phe* has to travel through the cathode material, the higher is the probability to loose its energy and get recombined; *i.e,* the smaller the chances to reach the *PhC* surface and escape into the vacuum. Because of these two counteracting effects, there exists an optimum cathode thickness that maximizes the *QE* for a given wavelength range. Current bialkali cathodes have a thickness of typically few tens of *nm*; and hence they are semitransparent.

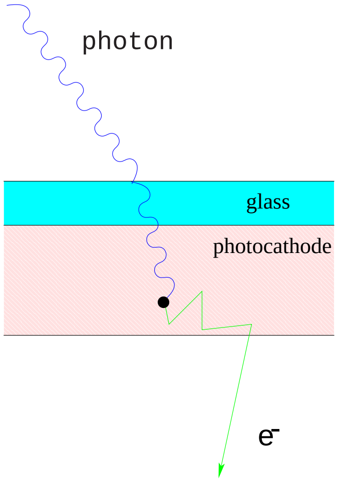

Figure 4.2: *Photon conversion process in a PMT. Note that in reality the PhC is only a few tens of nm thick, whereas the glass window is of about 1 mm thick.*

The sensitivity of a PMT should increase by increasing the path length of the photons inside the PMT cathode if one manages not to increase the path length for the excited electrons. This is the reason for the enhancement in the QE of a PMT when the light enters the photocathode with a large angle [88].

There are companies that (on special order only) treat the window of some of their PMTs (by either etching them with some aggressive chemicals or sand blasting) to scatter the incoming photons; thus increasing the photon incident angles in the PhC, like in the 9829 type PMT from *Electron Tubes*. The improvement achieved in the QE of this PMT is ~7% at 400 nm and ~16% at 600 nm[2]. The larger enhancement for long wavelengths is expected due to the fact that the absorption coefficient of the photons inside the PMT cathode decreases for longer wavelengths. A small drawback of this technique is that it is difficult to keep the window of these photomultipliers clean. Traces of dirt or grease deposited on the glass are difficult to be removed.

A layer that scatters photons before they get into the PhC can generate some other effects which can also influence the sensitivity of the PMT. Figure 4.3 sketches the photon

---

[2] Private communication: R M McAlpine from *Electron Tubes Inc.*

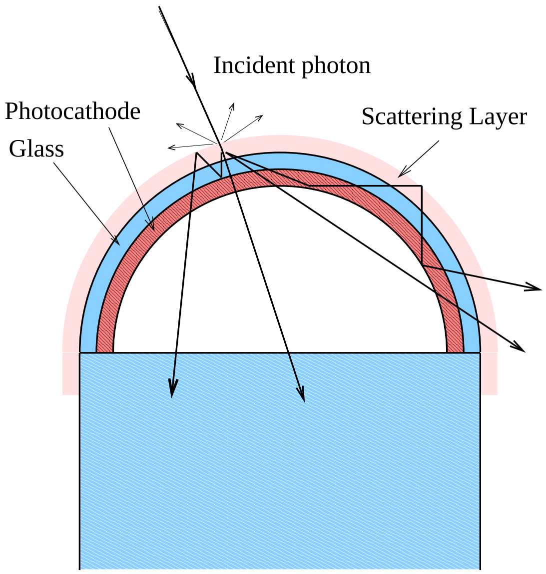

Figure 4.3: *Scattered photon trajectories in a hemispherical window PMT.*

trajectories scattered in a PMT with hemispherical entrance window (like the ET9116A). The scattering layer will cause the following effects: *a)* some photons will be scattered such that their path inside the *PhC* is elongated, and therefore the PMT *QE* is increased; *b)* for sufficiently large scattering angles, some photons will be trapped between the coating (refractive index = 1.5) and the *PhC* (refractive index ~2.5), thus having many chances of being converted into *phes*; *c)* increase in the number of backscattered photons due to the larger reflectivity of the coating with respect to that of the glass[3]; *d)* the higher reflectivity of the coating (with respect to that of the glass), will allow to re-reflect a larger fraction of the non-converted light (previously) reflected by the *PhC* (30% at 600 *nm* in a bialkali *PhC* [89]) hence increasing the production of *phes*; *e)* some photons will be deflected such that, due to the hemispherical shape of the PMT's entrance window, their trajectories will cross the *PhC* twice, thus having a second chance of being converted in case they did not

---

[3] The larger reflectivity of the scattering layer (with respect to that of the glass) is expected due to the roughness of the scattering layer. The refractive index is the same (~1.5) for both the glass and the lacquer.

Figure 4.4: *Photograph of a plain ET9116A PMT (left) and a specially coated ET9116A PMT (right). See text for further details.*

interact at the first instance.

During our studies, we found that by using high concentrations of Paraloid B72 and *PTP* the formation of the plastic and the *WLS* develops in a way that the remaining layer is not smooth, but frosty. Dipping the PMT several times with interruptions of a few minutes results in a coating layer which is no more transparent, but milky, as it is shown in figure 4.4. So the coating layer acts as an efficient light diffuser. By coating the PMT in this peculiar way, we managed to get the sizeable increase in the spectral sensitivity shown in figure 4.5. Therefore, the processes *a), b), d)* and *e)* overcompensate the loss due to *c)*, and a net increase in the *QE* occurs. The larger enhancement in the *QE* at longer wavelengths is consistent with the lower absorption coefficient in the *PhC* material for red photons, compared to that for blue photons. Besides, the reflectivity of a bialkali *PhC* also increases with the wavelength of the photon, and hence the effect *d)* will also produce a higher *QE* increase for red photons. The gain at $\lambda \lesssim 320\ nm$ is mainly due to the *WLS*.

We conducted a series of tests to find the composition of *PTP*, Paraloid B72 and Dichloromethane that optimizes this scattering effect. We varied the concentration of Paraloid from

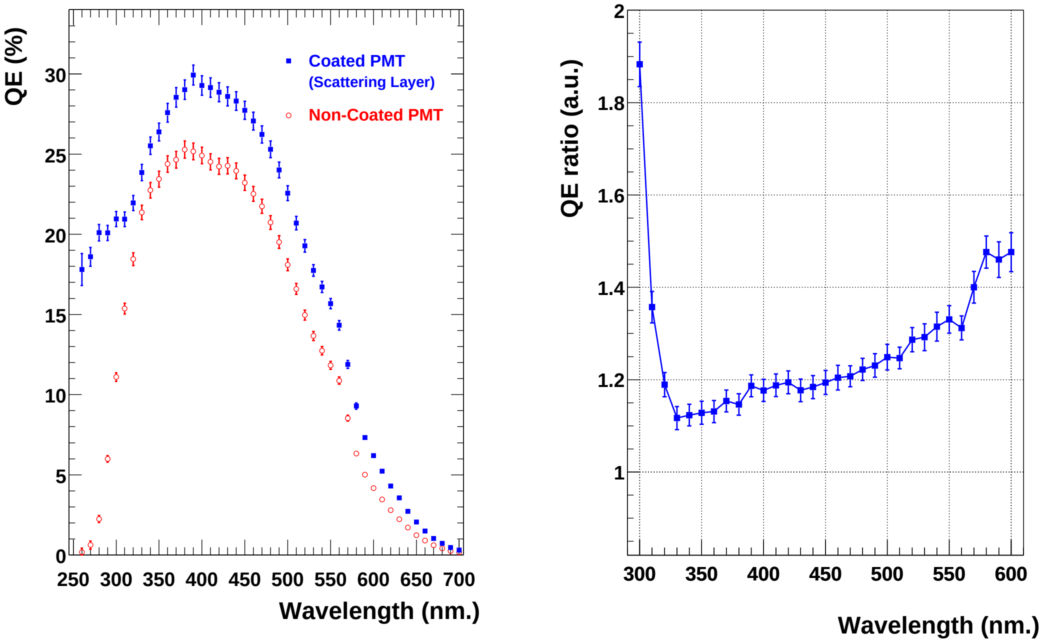

(a) (b)

Figure 4.5: *a) Spectral QE of a ET9116A PMT before and after being coated with a lacquer that scatters light and contains a WLS; b) ratio between the two QE curves shown in a). The wavelengths below 300 nm have been omitted for clarity.*

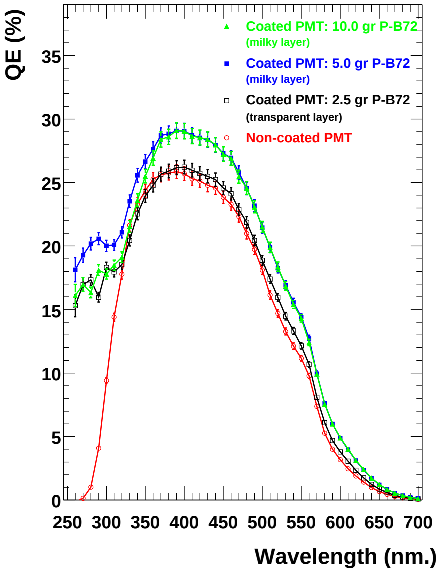

Figure 4.6: *Spectral sensitivity of a ET9116A PMT coated using different concentrations of Paraloid B72.*

1 g to 10 g for a fixed quantity of 0,5 g PTP in 50 ml Dichloromethane[4]. The spectral QE curves obtained using three different concentrations of Paraloid are shown in figure 4.6. The concentration of Paraloid is not critical provided it is above 3 $g/50$ ml solvent, which is the minimum required quantity to produce the milky layer. Once the frosted layer is formed, no significant difference in sensitivity (within the errors of our measurements) was found for the different Paraloid concentrations that were used. Only when ≥ 10 g of Paraloid was used, a slight reduction in the short wave UV sensitivity was observed. We attributed this reduction to the UV absorption of the binder.

I also changed the concentration of PTP from 0.0 g to 0.5 g (in steps of 0.1 g) dissolved in 50 ml Dichloromethane and 5 g Paraloid. The spectral PMT sensitivities obtained using three different concentrations of PTP are shown in figure 4.7. There is no significant improvement for wavelengths above 330 nm by adding the WLS. However, it was found that a higher admixture of PTP results in a faster and easier formation of the milky layer; the PTP acts

---

[4] The coating can be removed easily by wiping the PMT window with a tissue soaked in alcohol or acetone.

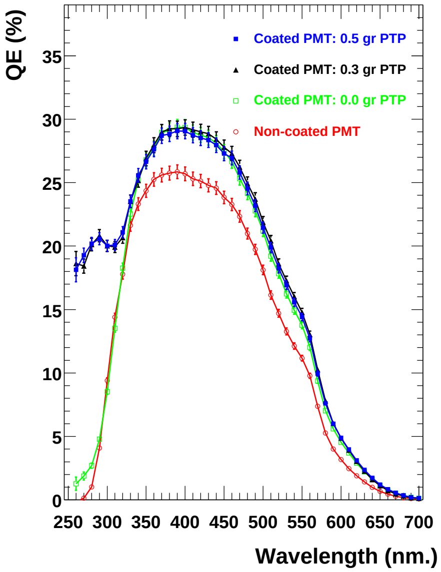

Figure 4.7: *Spectral sensitivity of a ET9116A PMT coated using different concentrations of PTP.*

apparently as a "seed". Using only Paraloid, it is necessary to speed up the evaporation rate of the solvent to form an efficient light scattering layer. This could be achieved by shaking the PMT very fast right after taking it out from the solution. It is worth to point out that if the evaporation of the solvent is slow, the deposited layer on the glass becomes rather transparent. Actually, if Toluene (instead of Dichloromethane) is used as a solvent, it is not possible to obtain a milky surface, regardless of the used quantity of *PTP* and Paraloid, and the number of times the PMT is dipped into the solution. This can be explained by the difference in the solvent's vapor pressure at room temperature. The boiling point of Toluene is 111^0C whereas that of Dichloromethane is 40^0C. Hence, a fast evaporation of the solvent is mandatory to produce the milky layer.

As I discussed before, slight variations in the concentration of the binder and the *WLS* do not produce substantial effects in the PMT *QE* enhancement. The best results were obtained with a mixture of 0,5 *g PTP* and 5 *g* Paraloid-B72 dissolved in 50 *ml* Dichloromethane. This mixture yields the highest increase in the PMT *QE*, and also allows one to produce the frosted layer in a fast and easy way. The PMTs need to be dipped only 2 or 3 times in the

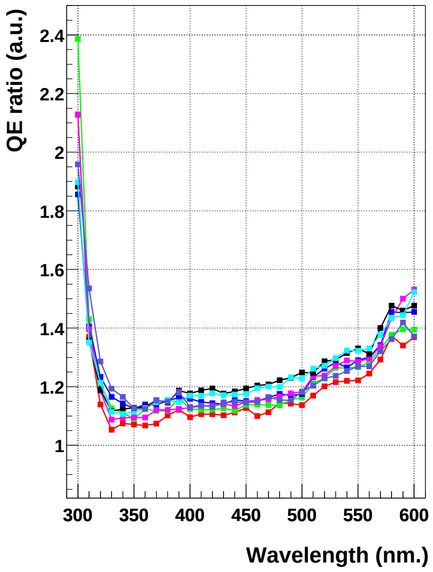

Figure 4.8: *Spectral QE enhancement observed in seven ET9116A PMTs after being coated with the standard mixture. The wavelengths below 300 nm have been omitted for clarity.*

solution, and no much shaking is needed to accelerate the evaporation of the solvent. The spectral *QE* shown in figure 4.5 was obtained by coating the PMT with this mixture. From now on, this mixture will be called *standard mixture*.

Seven PMTs were coated with the *standard mixture* in order to evaluate better the *QE* enhancement achieved by this coating procedure. Figure 4.8 shows the increase in the *QE* as a function of wavelength for the seven PMTs. Note that a significant increase in the spectral sensitivity is found for all them. The lowest spectral *QE* enhancement was obtained for the PMT with serial number *1525* (red curve in figure 4.8). I repeated the coating procedure for this PMT and I found roughly the same "reduced" sensitivity improvement. Hence the relatively low increase in the *QE* achieved for this particular PMT was not due to a defective coating. The two *QE* enhancements obtained are shown in figure 4.9. I concluded there are intrinsic features to specific PMT samples which limit the sensitivity enhancement achievable by this technique. No additional studies have been conducted to clarify this variation in the sensitivity gain. However, I would like to point out that a thicker *PhC* (with respect to the

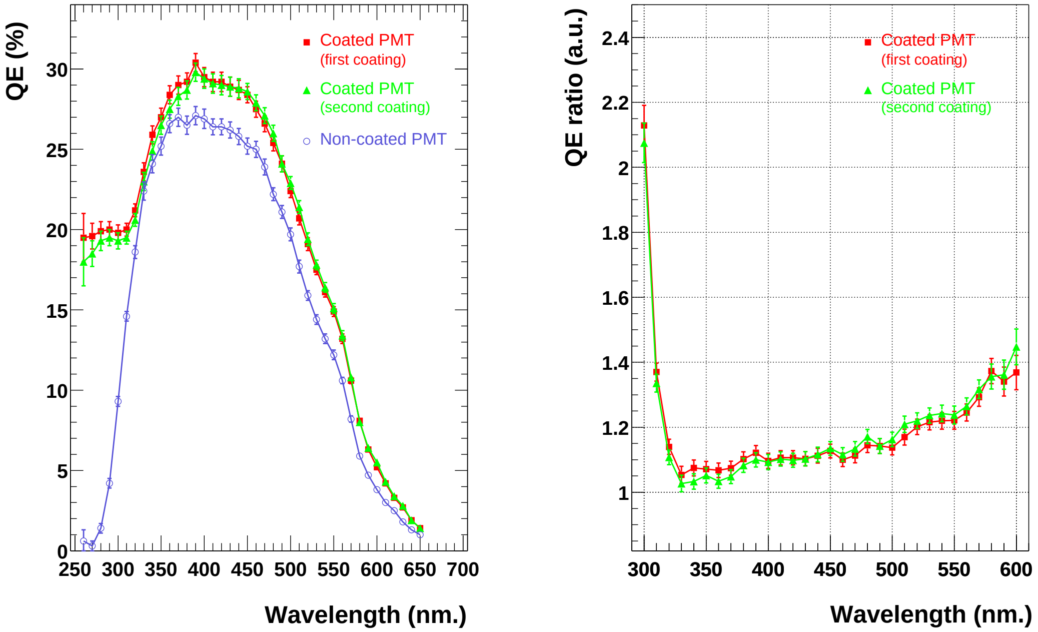

(a) (b)

Figure 4.9: *Spectral QE enhancement observed in the ET9116A PMT with serial number 1525 after being coated with the standard mixture. a) Spectral QE before being coated and after two independent coatings; b) QE enhancement achieved in the two coating trials. The wavelengths below 300 nm have been omitted for clarity.*

one of the other PMTs) would produce this effect; since the amount of non-absorbed photons in the *PhC* would be smaller, and consequently the amount of additional *phe*s produced by elongating the photon path inside the *PhC* would be also smaller.

We also tested the *standard mixture* on a PMT with a flat entrance window; the 19 *mm ø* R750 type PMT from HAMAMATSU, which has also a bialkali *PhC*. We observed also an increase in the *QE*, but not as high as for our hemispherical PMTs. At 400 *nm* the increase was $\sim$ 8%, and at 600 *nm* it was $\sim$ 19%. This reduced enhancement could be partly explained by the absence of photon trajectories crossing the *PhC* twice.

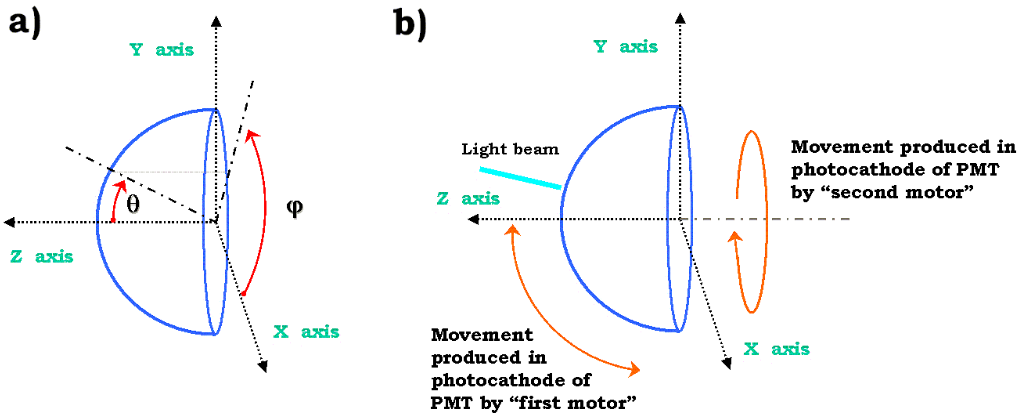

Figure 4.10: *a) Definition of the reference system; b) description of how the scan machine moves the PMT in θ and ϕ by the motion of the two stepper motors.*

4.3 The spatial response uniformity of the coated PMTs

The *spatial response uniformity* of a PMT is customarily defined as the uniformity of the output sensitivity with respect to the point of illumination on the photocathode [88]. The *spatial response uniformity* is never perfect in PMTs; differences in the PMT response arise from spatial variations in the sensitivity of the photocathode (*photocathode uniformity*) and deviations from the desired electron trajectories in the focusing and multiplication processes (*dynode section uniformity*). The *photocathode uniformity* depends mainly on the uniformity achieved in the process used to deposit the photocathode material on the inner surface of the entrance window, and the *dynode section uniformity* depends mainly on the design of the focusing electrodes and the voltage applied between the *PhC* and first dynode.

The motivation of this study was to evaluate if the coating procedure affects the *spatial response uniformity* of the used PMTs. In this section I will compare the *spatial response uniformity* of the ET9116A PMT before and after being coated.

The *spatial response uniformity* was measured by scanning, in steps of $\lesssim 1$ *mm*, the hemispherical *PhC* surface with a 1.5 *mm* diameter light spot, and then comparing the anode currents with the one obtained at the pole point of the *PhC* (reference point). This scanning

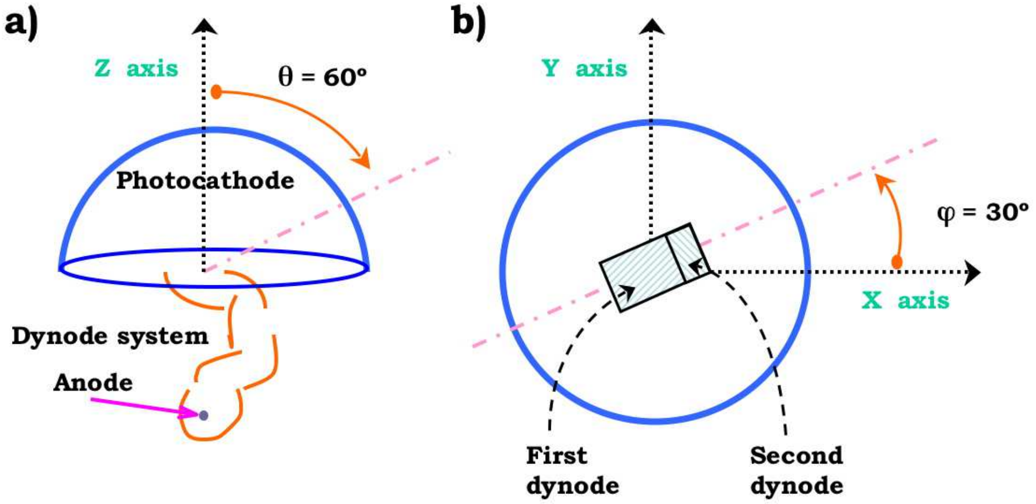

Figure 4.11: *Coordinates θ and ϕ with respect to the dynode system of the ET 9116A PMT. a) shape and location of the dynode system with respect to the PhC; b) orientation of the dynode system with respect to ϕ angle.*

procedure was performed by rotating the PMT *PhC* while keeping fixed the direction of the light beam, as shown in figure 4.10. As light beam, I used the collimated light of a blue LED from NICHIA (peak emission at 470 *nm*). And the rotation of the PMT was performed by using a home-made machine; the so-called *scan machine*. The PMT is plugged into the *scan machine* and then turned in θ and ϕ direction by means of two stepper motors, as shown in figure 4.10. In this way, the position of the light spot is shifted over the cathode, keeping always the perpendicularity between the incident light beam and the surface of the *PhC*. Further details about the *scan machine* can be found in appendix C.

The step size in θ direction for the scan was set to 4.7°, which implies a distance of 1.0 *mm* between two consecutive points. The step size in ϕ was fixed to 6.0°, which means that the distance between two consecutive points is given by $1.31 \cdot sin(\theta)\ mm$. The angle θ is 0° at the pole of the *PhC*, and the angle ϕ is 30°at the opposite side to the 1st dynode, as shown in figure 4.11.

The PMT was powered by 1100 *V* through a *3R-R-R-R-R-R-R* voltage divider, and the current was read out by a Keithley 6517A electrometer controlled by a PC.

The measured *spatial response uniformity* for an ET9116A PMT before and after being coated with the *standard mixture* is shown in figure 4.12. The lower response in some regions is basically due to a non-uniform amplification in the first dynode and, specially at large θ angles, to a poor collection efficiency of the *phe* onto the first dynode. See [60, 61] for further details. Note that the *spatial response uniformity* of the coated PMT is quite similar to that of the uncoated PMT. Similar results were obtained for other coated PMTs.

The increase in the detection efficiency (when coating the PMT) *vs.* the illuminated position in the *PhC* can be obtained by dividing the anode currents measured in the above mentioned spatial scans. The results are shown in figure 4.13. Note that the overall increase in the detection efficiency is about 20%, which is consistent with the enhancement in the *QE* observed at 470 *nm* that I reported in the previous sections. However, the increase is not uniform; it is relatively larger in those regions with low response, and relatively lower in those regions with good response. The reason for that is the scattering of the light in the lacquer, which allows photons to be converted somewhat away from their point of incidence. Therefore, the non-uniformities in the amplification and collection efficiency of the *phe*s are reduced; and hence the signal response in a coated PMT is somewhat more uniform than that in a non-coated PMT.

4.4 Spectral sensitivity increase in the coated PMT coupled to the light collector

Light collectors are needed in front of the camera PMTs to minimize the light losses due to dead areas between pixels, as well as to reject the background light outside the aperture defined by the reflector of the telescope. I already reported in section 3.3.2 that the design of light collectors used in MAGIC is such that they also enhance the chances that the photon trajectories cross the *PhC* twice, hence increasing the effective *QE* of the PMT. Note that this effect is stronger at large photon incident angles.

I found that the increase in the effective *QE* by photon trajectories crossing the *PhC* twice (*double crossing photons*) is lower (by about 50%) in coated PMTs than in the uncoated

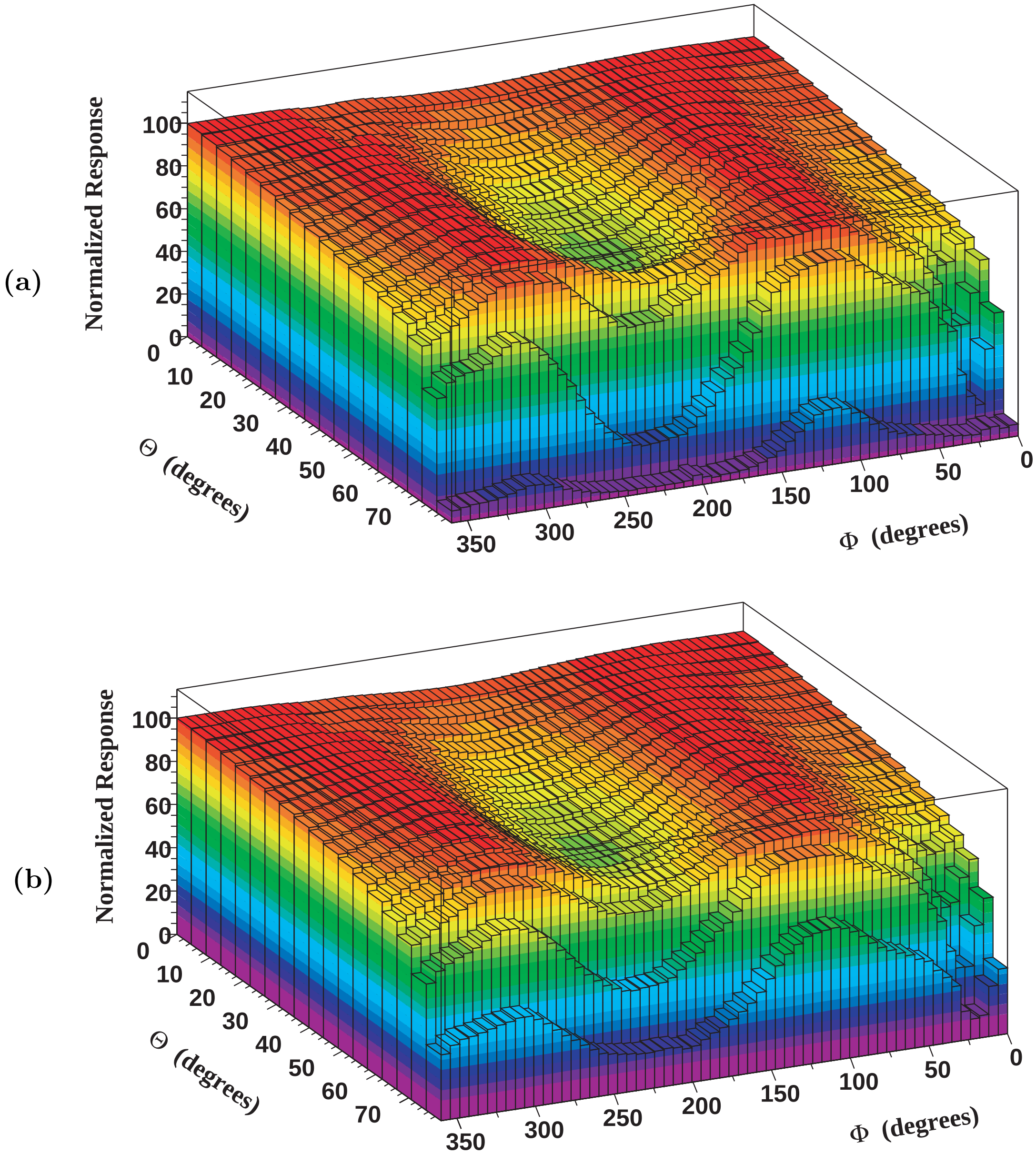

Figure 4.12: *Spatial response uniformity of a ET9116A PMT. All responses are normalized to the response at the pole of the PhC. a) before coating the PMT; b) after coating the PMT with the standard mixture. Note that the first histogram bin in the* θ *axis* ($\theta = 0°$) *corresponds to just one single illumination point regardless of the different positions in* ϕ.

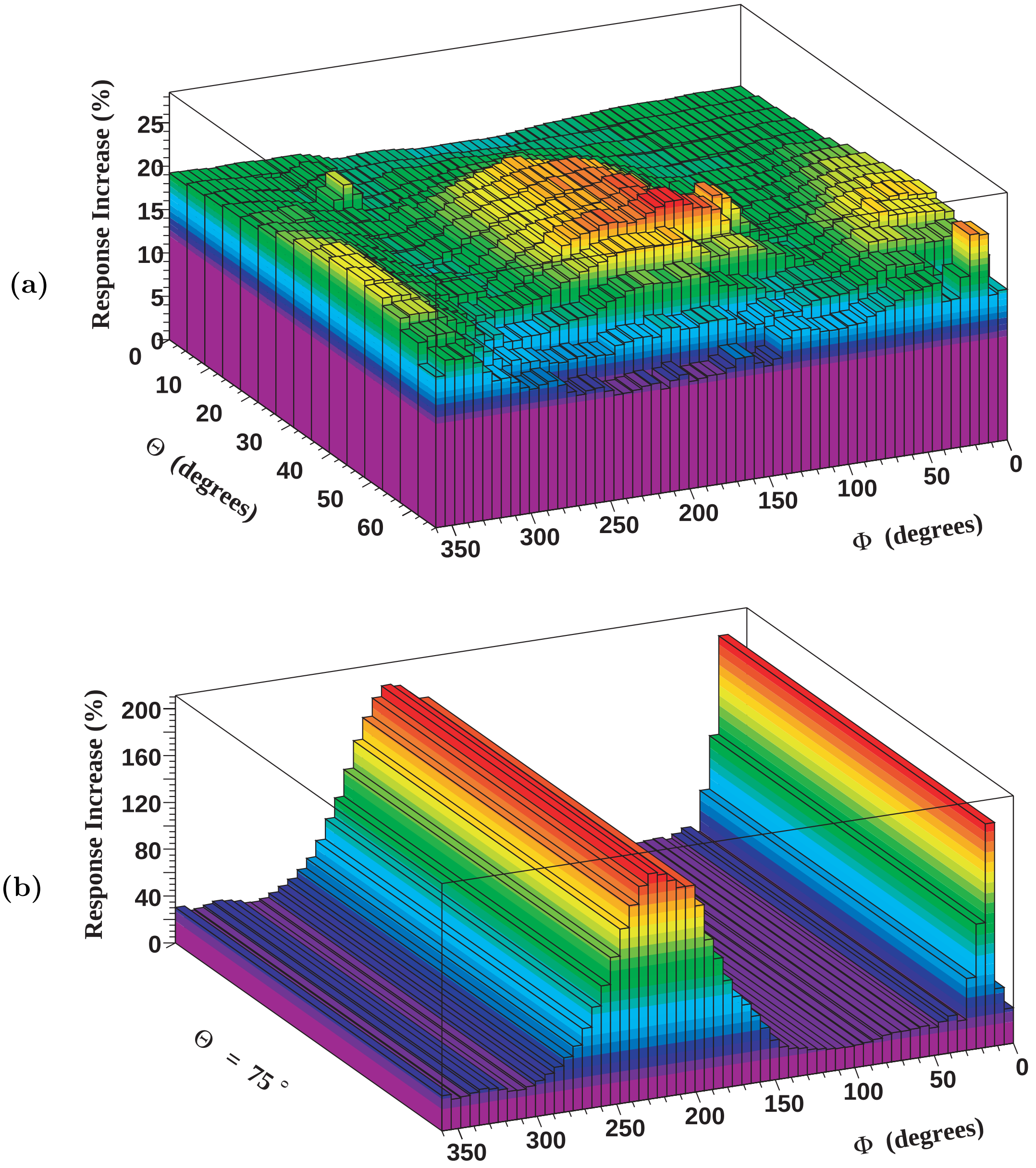

Figure 4.13: *Spatial increase in the detection efficiency of a ET9116A PMT after being coated with the standard mixture: a) up to $\theta = 66\,^{\circ}$ in bins of $4.7\,^{\circ}$; b) A single bin that corresponds to $\theta = 75\,^{\circ}$.*

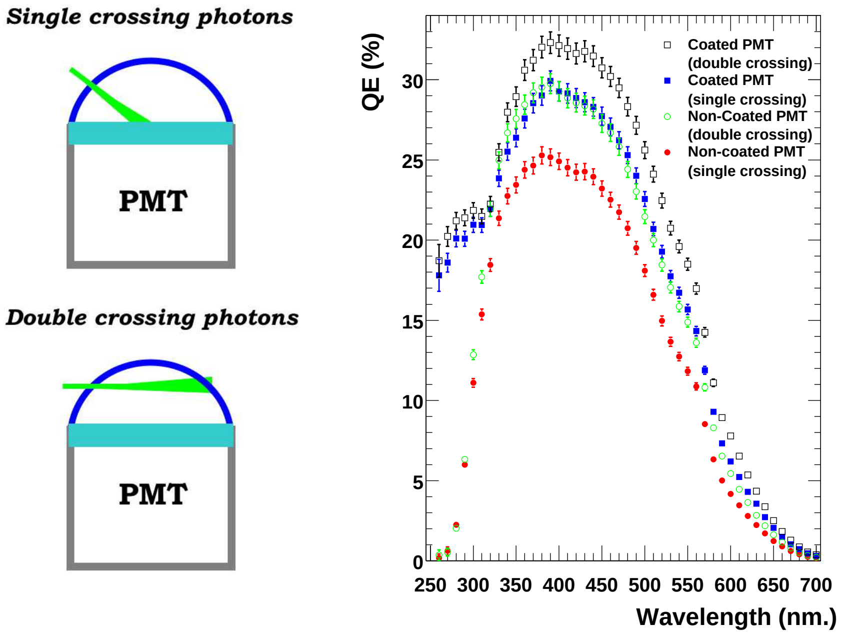

(a) (b)

Figure 4.14: *a) Sketch of a hemispherical PMT with incident light crossing the PhC once (single crossing photons) and twice (double crossing photons); b) spectral QE for different configurations of surface treatment and incident photon trajectories crossing the PhC once or twice.*

ones. This is shown in figure 4.14. The reason is that the trajectories of the (initially) *double crossing photons* are modified in the scattering layer of the coated PMTs, and the additional increase in the *QE* comes only from those photons which are not strongly scattered. It should be stressed that part of the *QE* enhancement achieved by the scattering layer is produced by *single crossing photons* that are dispersed in the frosted layer in such a way that their trajectories cross the *PhC* twice. That means that part of the increase in the *QE* of a coated PMT when being illuminated by *single crossing photons* is indeed due to "*double crossing photons*". Therefore, the relative enhancement achieved in a coated PMT when we artificially make the light beam to cross the *PhC* twice is lower than that achieved in a non-coated PMT.

It is worth noticing that when a non coated ET9116A PMT is coupled to a light collector and operated normally (high voltage applied), the effective detection efficiency is lower than the observed QE for *double crossing photons*. This is basically due to the fact that not all photon trajectories cross the PhC twice (60% at 27°, which is the largest photon incident angle), and also due to the collection efficiency of the *phe*s onto the first dynode, which is never 100%. Besides, the collection efficiency of the ET9116A PMTs is quite low close to the edge of the PhC, where some of the *double crossing photons* (not converted at the first hit) could be converted. As was mentioned in section 3.3.2, the actual detection efficiency enhancement (due to *double crossing photons*) at the largest photon incident angles ($\mathcal{I} \lesssim 27$) is such that it compensates the light losses due to the larger amount of photons hitting the aluminized Mylar foil (85% reflectivity) of the light cone.

We evaluated the detection efficiency enhancement achieved in several coated PMTs coupled to light collectors. We measured the increase in the DC anode currents produced in the PMTs under constant illumination from 3 different color LEDs; 370, 420 and 530 *nm*. The outcome of these studies was that the increase in the DC anode currents achieved by coating the PMTs is in quite good agreement (within 5% relative to the increase) with the measured spectral QE enhancement. Therefore, the increase in the spectral detection efficiency of a PMT coupled to a light collector is in first order equal to the enhancement observed in the pure spectral QE of the PMT. These studies are still not conclusive, and further and more accurate measurements are being planned.

4.5 Estimation of the increase in the MAGIC detection efficiency provided by this technique

The detection efficiency of an $IACT$ increases in first order proportionally to the increase in the number of detected *phe*s. In order to quantify the enhancement in the detection efficiency of the telescope provided by this special coating, one needs to fold the QE of a coated PMT with the Cherenkov photon spectrum that has to be measured, and then, compare this number to the one obtained using the QE of the untreated PMT.

We defined the *mean QE* for detecting Cherenkov photons ($< QE >_{Che}$) as:

$$< QE_{Che} > = \frac{N_{phe}}{N_{ph}} = \frac{\int QE(\lambda)\ N_{ph}(\lambda)\ d\lambda}{\int N_{ph}(\lambda)\ d\lambda} \tag{4.3}$$

where N_{ph} is the total number of Cherenkov photons impinging on the PMTs, N_{phe} is the total number of phes produced and λ is the wavelength of the photons[5]. The ratio between the $< QE >_{Che}$ of the PMT before and after the application of the lacquer quantifies the increase in the detection efficiency of the telescope.

For this estimate we simulated $\gamma - ray$ showers in the energy range $10GeV$-$30TeV$ (with a spectral index of -2,6) at 0°, 20°, 40° and 60° Zenith Angle (ZA) using the program CORSIKA 6.019 [12]. For each ZA, 10^6 Cherenkov photons reaching the telescope site (located at 2200 $m\ a.s.l.$) were stored in a histogram spanning 290 nm to 600 nm in 5 nm bins. The absorption in the atmosphere was taken into account; yet the spectral reflectivity of the mirrors and light collectors was neglected, since aluminum has a rather flat reflectivity between 290 nm and 700 nm.

The normalized spectral Cherenkov photon intensity reaching the PMTs of the MAGIC camera is shown in figure 4.15. The UV cut-off around 290 nm is caused by Ozone absorption. The spectrum is also strongly affected by Rayleigh and Mie scattering. Note that at 0° ZA the maximum in the relative amount of Cherenkov photons occurs at $\lambda \sim 335$ nm, whereas at 60° ZA, due to the longer path of the photons in the atmosphere, the maximum is shifted to $\lambda \sim 400$ nm.

Table 4.1 reports the relative increase in $< QE >_{Che}$ for the seven ET9116A PMTs whose spectral QE enhancements (after being coated) were shown in figure 4.8. The relative $< QE >_{Che}$ enhancements were calculated for four ZA using the four Cherenkov photon spectra displayed in figure 4.15. The average increase in $< QE >_{Che}$ (among the seven PMTs) with its related standard deviation is also shown for each ZA.

The sample of only seven PMTs is not sufficient to make a strong statement about the

---

[5] In formula 4.3, I did not consider the possible dependence on the light incident angle $\mathcal{I}$ with respect to the entrance window of the pixel. As I discussed in sections 3.3.2 and 4.4, we did not find significant variations in the pixel response (normalized to $cos\mathcal{I}$) when varying $\mathcal{I}$.

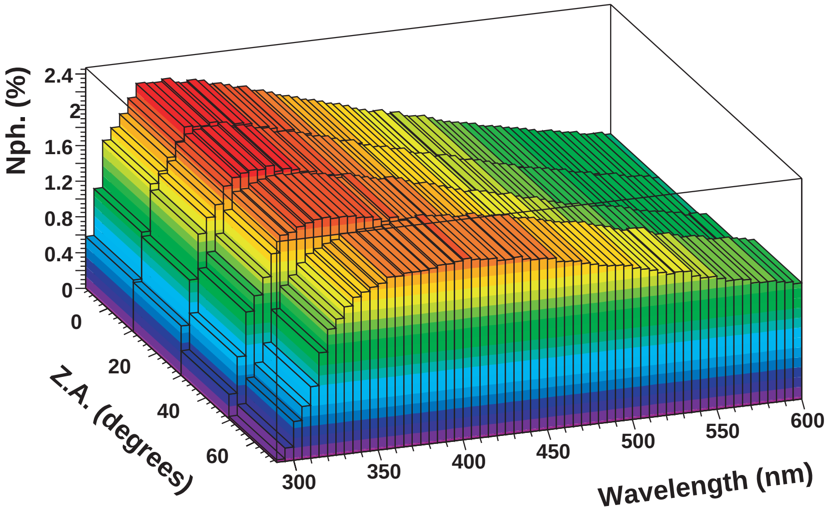

Figure 4.15: *Expected cherenkov photon spectrum reaching the MAGIC Telescope during observations at 0°, 20°, 40° and 60° ZA.*

dispersion in the measured $< QE >_{Che}$ enhancement. Yet it is clear that the spread in the $< QE >_{Che}$ enhancement (*i.e,* 2%) is substantially smaller than the mean increase in $< QE >_{Che}$, which is 19% for low ZA ($\lesssim 40°$).

The slightly smaller $< QE >_{Che}$ enhancement at large ZA is due to the lower fraction of UV light reaching the telescope (mainly due to Rayleigh scattering in the atmosphere), for which the PMT QE enhancement is largest.

Taking into account that most observations are performed at low ZA ($\lesssim 40°$), we can conclude that the use of this technique to enhance the PMT QE reduces the MAGIC E_{th} by a factor 1.19 (see equation 4.1). In principle, this reduction in the E_{th} could also be achieved by increasing the area of the reflector of MAGIC by a factor 1.19 (*i.e,* from 239 m^2 to 284 m^2); yet this would be substantially more expensive and would introduce additional problems related to the increase in the weight and the inertia of the telescope.

	PMT serial number							
	1525	*1611*	*1920*	*1929*	*1930*	*1934*	*1973*	
ZA	Relative $< QE >_{Che}$ enhancement (%)							**Average enhancement (%)**
0°	14.1	17.6	19.5	17.6	21.3	20.5	19.9	**19 ± 2**
20°	14.0	17.5	19.4	17.5	21.2	20.4	19.8	**19 ± 2**
40°	13.5	16.8	18.8	16.9	20.8	20.0	19.0	**18 ± 2**
60°	12.8	15.9	18.0	16.3	20.5	19.6	17.8	**17 ± 3**

Table 4.1: *Predicted relative* $< QE >_{Che}$ *enhancement for seven ET9116A PMTs coated with the standard mixture.*

4.6 Increase in the detection efficiency of the *LONS* in coated PMTs

In this section I will estimate the increase in the detected *LONS* photons when the PMTs are coated with the *standard mixture*. Then, I will evaluate the consequences of this effect on the signal to noise ratio and on the accidental trigger rate produced by the *LONS*.

The brightness of the night sky (at low *ZA*) above La Palma was measured on 427 CCD images taken with the Isaac Newton and Jacobus Kapteyn Telescopes on 63 nights during 1987-1996 [40]. All these measurements were performed at high ecliptic and galactic latitudes, regions free of stars, and during clear moonless nights. Using the mean brightness spectrum of all these observations (obtained from [40]), I computed the mean spectrum of *LONS* photons per second arriving to an inner pixel of the camera of the MAGIC Telescope. In this simple calculus I used an effective mirror area of 239 m^2 with 80% reflectivity and a pixel angular diameter of 0.1°. The results are shown in figure 4.16. The *LONS* photon flux for outer pixels (0.2° ϕ) is simply 4 times larger. Most of the distinctive features of this night sky spectrum are due to airglow. The NaD emission at 589 *nm* (mainly from streetlightning) is well visible, and the "spikes" above 650 *nm* are the Meinel rotation-vibration bands of OH.

As stated in section 4.2, the enhancement in the PMT *QE* produced by the scattering

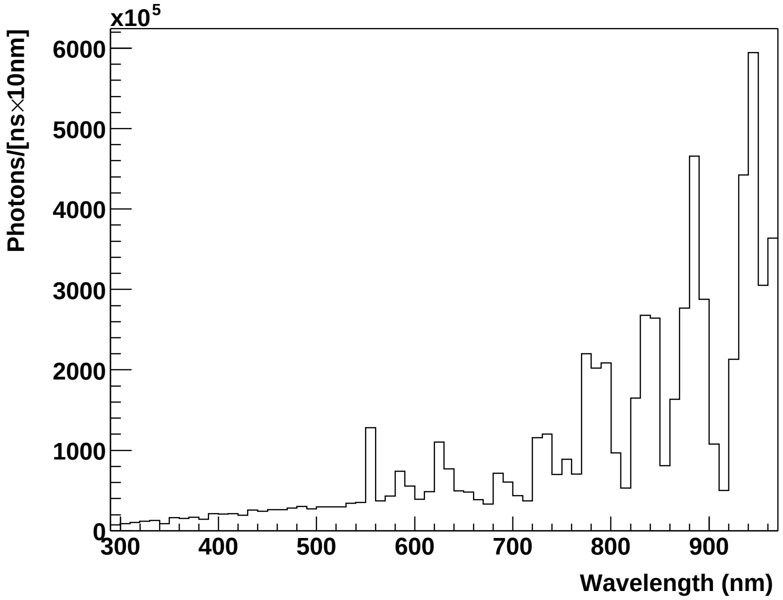

Figure 4.16: *LONS photon flux vs. wavelength at a pixel in the inner section of the camera of the MAGIC Telescope.*

layer is larger for long wavelength photons than for short wavelength photons[6]. The reason for this effect is *a)* the lower absorption coefficient in the *PhC* material for red photons, compared to that for blue photons; and *b)* the larger reflectivity for long wavelength photons in a bialkali *PhC*.

Due to the fact that the amount of *LONS* increases with the wavelength of the photons, the increase in the *mean QE* for detecting *LONS* $< QE >_{LONS}$ (*i.e,* the PMT *QE* folded with the *LONS* photon spectrum), is larger than the increase in the *mean QE* for detecting Cherenkov photons $< QE >_{Che}$ that was computed in section 4.5.

By folding the photon flux shown in figure 4.16 with the *QE* of a PMT before and after being coated, one can compute the *phe* rate produced by the *LONS*, in a non-coated and a coated PMT. I performed this calculation for the same seven PMTs used in sections 4.2 and 4.5. The results are presented in table 4.2.

---

[6] The *QE* enhancement at $\lambda \lesssim 320\ nm$ is indeed produced by the *WLS*, and not by the scattering of the photons in the frosted layer.

PMT serial number	*LONS phe* rate (*phe/ns*)		Enhancement in $< QE >_{LONS}$ (%)
	before coating	after coating	
1525	0.127	0.149	17.6
1611	0.126	0.152	20.8
1920	0.124	0.152	22.8
1929	0.119	0.145	22.7
1930	0.123	0.156	27.0
1934	0.131	0.165	26.0
1973	0.123	0.149	21.7
Average	0.125 ± 0.004	0.153 ± 0.006	**23 ± 3**

Table 4.2: *Predicted LONS phe rate and enhancement in* $< QE >_{LONS}$ *for seven ET9116A PMT coated with the standard mixture.*

In this calculation, I included the 8% light losses in the plexiglas window of the camera (see section 3.3.1) and used a value of 90% for the collection efficiency (*CE*) of the photoelectrons onto the first dynode of the PMTs. Actually, there isn't any precise measurement of the *CE* of the ET9116 PMTs. Yet engineers from the PMT company *Electron Tubes* confirmed that the used value of 90% (for all wavelengths) is reasonable for this type of PMT. I did not include the losses due to the reflectivity of the light guides, and hence the numbers are somewhat overestimated. The effect of the light guides is small, but not negligible. In the case of uniformly distributed light impinging perpendicularly on the pixel, 37% of the photons would hit the walls of the light guides; and hence, about 15% of these photons would be lost. That means that 5.5% of the incoming photons would be lost (in average). This number would increase for larger light incident angles with respect to the surface of the light guides, which complicates the estimation of this effect. However, this effect can not produce big variations in the numbers presented in table 4.2; in the extreme case in which all photons hit the wall of the light guides, the fraction of lost photons would be about 15%. Besides, as I mentioned in sections 3.3.2 and 4.4, the additional enhancement in the *QE* produced by photons whose trajectories cross the *PhC* twice compensate the increasing light losses in the wall of the light guides when the light incident angle increases.

Note from table 4.2 that, when coating our PMTs with the *standard mixture*, the *effective* or *mean QE* for *LONS* photons increases by about 23%, whereas the one for Cherenkov photons increases by 19%. In the following subsections I will analyze the consequences of this effect on the signal to noise ratio and the accidental trigger rate in the camera of the telescope.

4.6.1 *LONS* effect on the signal to noise ratio

The noise in the pixel chain of the camera of the telescope is proportional to the fluctuations in the number of *phe* produced in the cathode of the PMT. Neglecting the dark current and the afterpulse effect in the PMT, those fluctuations will be given by the statistical fluctuations in the number of *phe* produced by the Cherenkov photons (N_{Che}^{phe}), and the number of *phe* produced by the $LONS(N_{LONS}^{phe})$. Assuming that the amount of *phe* produced in the *PhC* follows a Poisson distribution:

$$\frac{Signal}{Noise} \propto \frac{N_{Che}^{phe}}{\sqrt{N_{Che}^{phe} + N_{LONS}^{phe}}} \tag{4.4}$$

where $N_{Che}^{phe} = N_{Che}^{photon} \times < QE >_{Che}$ and $N_{LONS}^{phe} = N_{LONS}^{photon} \times < QE >_{LONS}$.

Most of the Cherenkov photons from an atmospheric shower do arrive to the individual camera PMTs within 2-3 *ns*. However, due to the limited sampling rate of the current *FADC* units (300 MSample/s), the signal is stretched, and has a total duration of about 15 *ns*; *i.e,* 4-5 *FADC* slices (see section 3.3.3). Therefore, photons from the night sky and/or stars arriving within this time gate will get into the signal we are interested.

Using the average *LONS phe* rate from table 4.2 and the previously mentioned 15 *ns* as the time window in which the signal is acquired, one finds that $< N_{LONS}^{phe} >$ is 1.9 and 2.3 for the uncoated and the coated PMT respectively. On the other hand, N_{Che}^{phe} is usually larger than 5 *phe*, which is roughly the discriminator threshold for triggering single pixels. Therefore, the increase of 0.4 *LONS phe* is quite small when being compared with the increase in the number of detected Cherenkov *phe* (usually $\gtrsim 1$ *phe*), that will be the leading term in the signal noise. Consequently, the signal to noise ratio of the PMT signals improves when coating the PMTs with the *standard mixture*.

4.6.2 *LONS* effect on the accidental trigger rate

The increase in $< QE >_{LONS}$ will rise the accidental trigger rate produced by pure *LONS*. In this section I will estimate the increase in the *LONS* rate produced when coating the PMTs with the *standard mixture*, and I will show that the increment in the *LONS* accidental trigger rate does not have negative consequences for the performance of the MAGIC Telescope.

The trigger in MAGIC requires a coincidence of N "closed-packed"[7] pixels (in a given time gate W) whose signals' amplitude are above a given preset threshold. In order to simplify the calculus I will approximate the threshold in the pulse amplitude of the signals by a minimum number of *phe*s N_{th}^{phe} contained in the signals. Note that these two "thresholds" are not strictly equivalent since, in general, the *phe*s do arrive to the first dynode of the PMT at slightly different times ($\sim ns$); and thus the (mean) pulse amplitude of the signal is not simply the sum of the (mean) pulse amplitude of the PMT signals produced by the individual *phe*s. As stated in 3.4, the *standard trigger settings* in MAGIC are a multiplicity of 4 pixels and a discriminator threshold of 4 mV. In this section I will use a discriminator threshold N_{th}^{phe} of 5 *phe*s.

The accidental trigger rate produced in the telescope by the *LONS* photons ($\mathcal{R}_T$) can be estimated using the following expression:

$$\mathcal{R}_T \approx C_N \times P_1^N \times (W)^{-1} \tag{4.5}$$

where P_1 is the probability that a single PMT has a *LONS* signal above the threshold (N_{th}^{phe}) during a given time gate W, N is the multiplicity of the trigger, and C_N is a combinatorial factor that accounts for all the possible combinations of N "closed-packed" PMTs among the 325 PMTs located in the trigger region of the camera (see figure 4.17).

---

[7] The trigger configuration "closed-packed" is defined in section 3.4.

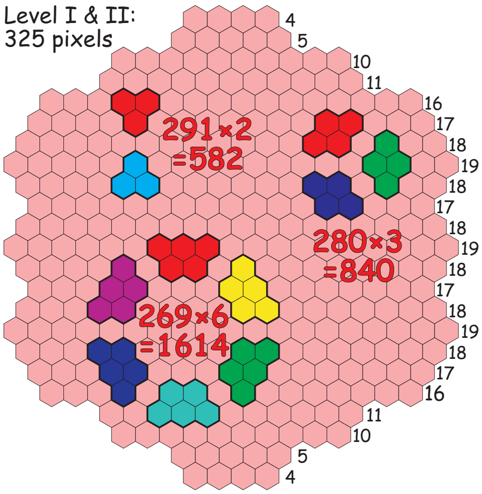

Figure 4.17: *Possible combinations of 3, 4 and 5 "closed-packed" pixels in the trigger region of the camera of the MAGIC Telescope.*

P_1 is just the Poisson cumulative probability of a *phe* signal equal or above N_{th}^{phe}, given a mean number of *phe*s due to the *LONS* $< N_{LONS}^{phe} >$ in a given time gate W,

$$P_1 \;=\; 1 - \sum_{i=0}^{i<N_{th}^{phe}} \frac{< N_{LONS}^{phe} >^i}{i!} \times e^{-<N_{LONS}^{phe}>} \tag{4.6}$$

$< N_{LONS}^{phe} >$ can be computed, since the *LONS phe* rate and the effective time gate W are known quantities. The time gate W is given basically by the electronics, and it was adjusted to be about 5-6 *ns* (see [90] for details).

Using $N_{th}^{phe} = 5$ *phes*, $N = 4$, $W = 6$ *ns* and the the average *LONS phe* rates previously computed (*i.e,* 0.125 *phe*/ns and 0.153 *phe*/ns for non-coated and coated PMTs), one finds that $P_1^{NON-Coated} = 0.11\%$, and $P_1^{Coated} = 0.26\%$ in these 6 *ns* time duration. This means an individual trigger rate of 177 kHz and 425 kHz for non-coated and coated PMTs respectively. Finally, the total accidental trigger rate $\mathcal{R}_T$ can be computed using the expression 4.5, and $C_4 = 840$. We obtained that $\mathcal{R}_T^{NON-Coated} = 0.18$ *Hz* and $\mathcal{R}_T^{Coated} = 5.9$ *Hz*.

Therefore, we can conclude that the accidental trigger rate produced purely by *LONS* photons increases significantly, by a factor 33, when coating the PMTs with the *standard mixture*. However, the estimated *LONS* rate is still well below the expected cosmic ray rate in MAGIC, which is about 460 *Hz* when using the *standard trigger conditions* [36]. Hence the increase in the *LONS* accidental trigger rate produced when coating the PMTs with the *standard mixture* does not have negative consequences for the performance of the MAGIC Telescope.

4.7 Coating of all the PMTs of the MAGIC Telescope

As I mentioned in chapters 1 and 3, the main goal of the MAGIC experiment is to reduce as much as possible the E_{th} of the telescope. The new method of coating the ET 9116/9117A PMTs enhances the MAGIC detection efficiency by about 19%; which implies a reduction of the telescope E_{th} by a factor 1.19. I would like to point out that this is a very simple and cheap technique. The same reduction in the E_{th} achieved by increasing the area of the MAGIC reflector would introduce additional problems related to the increase in the weight and the inertia of the telescope. In addition, it is worth mentioning that this increase in the reflector surface would cost $\sim$200000 Euros; whereas the material needed to coat all the PMTs of the MAGIC Telescope cost less than 100 Euros.

Due to the simplicity, reduced cost and significant effectiveness of this technique, the MAGIC collaboration decided to coat all the PMTs with this special lacquer, which we now name the *"MAGIC lacquer"*. This coating was carried out in July 2002; more than 625 PMTs[8] were coated with the MAGIC lacquer.

4.8 Prospects of the coating method

Firstly, I would like to point out that this technique to increase the PMT *QE* can be used in many other PMT applications, not only in *IACTs*. The only constraint is that the PMT should not be optically coupled to its light source, since the dispersion of the photons is based in a rough surface between two media with different refractive index.

Secondly, I want to mention that this technique might be still not optimal; *i.e,* improvements might be still feasible. A possible way to do that is by using a transparent plastic

---

[8] The camera is equipped with 577 PMTs, yet some additional PMTs were coated to be used as spare.

(a) (b)

Figure 4.18: *July 2002, a) several PMTs before being coated; b) the same PMTs after being coated with the standard mixture.*

Figure 4.19: *Photograph of the camera of the MAGIC Telescope during the coated PMT installation.*

binder with a refractive index larger than that of the Paraloid B72 (n = 1.5). The larger the difference in the refractive index between the air and the frosted layer, the larger the scattering and trapping of the photons. Yet a further increase in the PMT *QE* is not obvious, since a higher refractive index would produce two negative effects: *a)* a somewhat larger light reflectivity in the interface between the air and the coating layer; *b)* no optical coupling in the interface between the coating layer and the PMT glass, which would cause the back-reflection of some photons. Studies are needed to clarify what is the net effect. Some attempts were already performed using Polystyrene (n $\sim$ 1.6), and the enhancements achieved were mostly below the ones obtained when using Paraloid B72.

Another way of improving the technique might be to perform the coating of the PMTs under specific conditions of temperature and humidity. Special facilities are needed to control these variables. We found a slight improvement when coating the PMTs at relatively high temperatures (about 35°C) and relatively dry environments (provided by air conditioning), which we attributed to a faster evaporation of the solvent. However, the *QE* enhancements achieved were only of about 1% higher, which is close to the uncertainties of the measurement, and thus not significant.

Finally, I would like to mention that this technique might be used to produce PMTs with higher *QE* by reducing the fraction of converted *phe*s which do not escape the *PhC*. The idea is to produce PMTs with thinner *PhC* layers (than in "standard PMTs"), which should increase the probability of the electrons produced in the *PhC* to escape into the vacuum. In order to compensate for the thinner *PhC* layer, the path length of the photons inside the PMT *PhC* could be enlarged by using lacquers similar to the one discribed in section 4.2, and the non-absorbed photons could be recycled by coating the internal parts of the PMT with a high reflective material. It is worth noticing that the absorption of the photons in a *PhC* (also called internal *QE*) is particularly large at short wavelengths; at 400 *nm*, about 70% of the photons are typically absorbed in a bialkali *PhC*. Yet the *QE* of these PMTs (*i.e,* the fraction of released *phe*s with respect to the incoming photons) is only about 25%. Therefore, this technique of reducing the thickness of the *PhC* and recycling the photons could increase the peak *QE* of a bialkali *PhC* by a factor well above 2, in the ideal case in which the internal QE remained approximately equal and that most of the produced *phe*s could escape the PhC. In practise, there are some effects that will limit the QE enhancement. These effects are the following ones: *a)* the reflectivity of the inner parts of the PMT being not larger than 85%; *b)* light that escapes the PMT after being reflected in the inner part of the PMT (crossing the PhC, the glass window and the coating layer); *c)* photons that are converted in regions of the PhC where the collection efficiency onto the first dynode is poor; and *d)* the fraction of *phe*s absorbed inside the PhC, which will never become zero. However, I would like to stress that the potential enhancement in the QE that could be achieved by this technique is huge. In addition, the development cost of these "new generation PMTs" would be comparable to the actual cost of "standard PMTs", since no new devices/machines are required in this production. Therefore, PMTs with the internal part fully reflective, with thin PhCs and with proper PMT coatings could become photosensors competitive (at wavelengths below 500 *nm*) to Hybrid Photomultipliers (HPDs) with a reduction of 1 order of magnitude in cost. Indeed, when willing to detect light in the short wavelength range ($\lesssim$ 450-500 *nm*), which is the case in $IACTs$, these new generation of PMTs might be a better cost-effective choice than HPDs.

Chapter 5

Vertical Cavity Surface Emitting Lasers (VCSELs) for the optical transfer of short analogue signals

As stated in section 3.3.3, the very short pulses (2-3 *ns* FWHM) from the PMT camera are transferred to the 100 *m* distant central data acquisition building (where the signals are digitized) by a system based on optical fibers with drivers and receivers working in analogue mode. The advantages of using *optical links* instead of *coaxial cables* are a lower signal attenuation, basically no pulse dispersion, less weight, no crosstalk between channels, no electromagnetic pickup, no grounding problems and immunity against lightening strikes.

In this section I will justify the usage of VCSELs as electric-to-light signal converters instead of other (more conventional) semiconductor light sources. Then, I will report about the problems we encountered when using these novel devices and how these problems were solved. Finally, I will present the achieved performance of the optical link system used in the MAGIC Telescope.

5.1 Introduction and working principle of VCSELs

A *Vertical Cavity Surface Emitting Laser* (VCSEL) is a laser diode that emits light

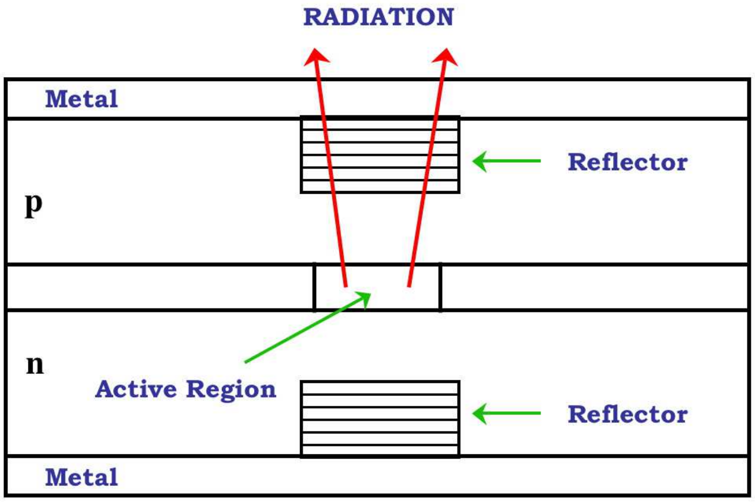

Figure 5.1: *Typical structure of a VCSEL. The reflectors are made from a stack of dielectric layers whose index of refraction alternates between high and low values, resulting in a high reflection. The upper reflector is partially transmissive at the laser output wavelength.*

perpendicular to its surface, rather than from its side, as it occurs in traditional *Edge Emitting Lasers* (EEL). The typical structure of a VCSEL is depicted in figure 5.1. In a VCSEL, the Fabry-Perot cavity is formed by about 20 periods of alternating dielectric layers of high and low refractive index; the so-called *Distributed Bragg Reflector* (DBR). The upper reflector (in figure 5.1 is the *p-mirror*) is partially transmissive at the wavelength defined by the Fabry-Perot cavity and the resonance of the DBR, which allows the vertical laser emission. The dimensions of the VCSEL are such that only one longitudinal mode is allowed. Typically several transverse modes are produced, yet VCSELs emitting one single transverse mode (Single Mode VCSEL) also exist.

The VCSEL structure has several unique features that provide them with significant performance advantages with respect to conventional EELs and LEDs. In the following I will list those ones which guided our decision to use VCSELs for the electric-to-light conversion of the PMT signals.

- Low beam divergence[1] (∼ 15°) in comparison with LEDs (∼ 120°) and EELs (∼ 40° and ∼ 10° in the perpendicular and parallel plane to the semiconductor junction). The narrow beam divergence and circular symmetry allows for an efficient optical coupling to a multimode optical fiber.

- Low lasing threshold current (∼ 3 mA) in comparison to EELs (∼ 25 mA); which makes them easy to drive, and reduces significantly the power consumption and dissipation of the system (non negligible when gathering 600 of these devices, as we do in MAGIC).

- High resistance (∼ 25 Ω) in comparison to EELs and LEDs (∼ 3 Ω), which simplifies the design of the electric driver circuit.

- Low wavelength variations with temperature ($\frac{d\lambda}{dT} \sim 0.06\ nm/^{\circ}C$) in comparison to variations in EELs and LEDs ($\frac{d\lambda}{dT} \sim 0.3\ nm/^{\circ}C$), which makes the system more stable.

- Low effective coherence (coherence length ∼5 cm) due to the emission of multi transverse modes; which makes the system less susceptible to interference effects.

- A rise and fall time of the order of 100 ps, which is comparable to that of current EELs, and much shorter than that of LEDs which is of the order of a few ns. Short rise and fall times are needed in order to follow the shape of the PMT electric pulses.

- A spectral width of less than a nm, which is comparable to that of EELs, and much shorter than that of LEDs, which is about 50 nm. A small spectral width is desirable to reduce the pulse dispersion inside the fiber.

- A large dynamic range (up to 100-200 mA) for short pulses and low duty cycles.

- Cost comparable to that of LEDs, and significantly lower than that of EELs.

VCSELs are relatively novel devices; the first VCSEL reliability study was performed in 1996. Since the inception of IEEE and Fiber Channel standards for high data communication

---

[1] Beam divergence is defined as the total included angle between the $1/e^2$ intensity points.

in 1997, more than 30 million VCSELs have been already shipped into this application. Besides the above mentioned advantages of VCSELs with respect to EELs and LEDs, there are two features that make VCSELs suitable devices for digital communications; *a)* more than 10^5 operating hours for a cumulative percentage failure of 1% [91], and *b)* a bit rate transfer above the GHz[2].

Currently, VCSELs are basically used only in digital communications. Only very few design studies on analogue signal transmission systems based on VCSELs and optical fibers have been carried out (see [92, 70, 93]). So far, there isn't any detector in operation (but MAGIC) with a system in which analogue signals are transmitted successfully via optical links driven by VCSELs. In this respect, the MAGIC Telescope is the first experiment in the world equipped with such novel system.

5.2 The VCSELs used in the MAGIC Telescope

We selected the multimode HFE4080-321 type VCSEL diode from Honeywell for the camera of the MAGIC Telescope. Figure 5.2 shows a photograph of 2 of these devices. These lasers have an active area of about 20×20 μm^2, and allow one to produce light pulses with rise and fall times as short as 100 ps. They emit at a peak wavelength of 850 nm with a maximum beam divergence of 20°, and have a typical lasing threshold current of 3.5 mA. The data-sheet of the HFE4080-321 VCSELs is shown in figure 5.3. Another important feature is that these diodes can be operated up to 200 mA peak current for low duty cycles[3].

The optical coupling between the VCSEL and the multimode graded index optical fiber is performed by means of connectors manufactured by the company DIAMOND. Figure 5.4a shows a photograph of two connectorized VCSELs together with two connectorized optical fibers. Inside the connector of the VCSEL, a spherical lens of 2 mm ϕ focuses the light emitted by the VCSEL onto the 50 μm ϕ core of the optical fiber, as sketched in figure 5.4b.

---

[2] Nowadays, 2.5 Giga Bit Per Second (*GBPS*) VCSELs are commercially produced, and 10 *GBPS* VCSELs already exist.

[3] Private communication from Honeywell

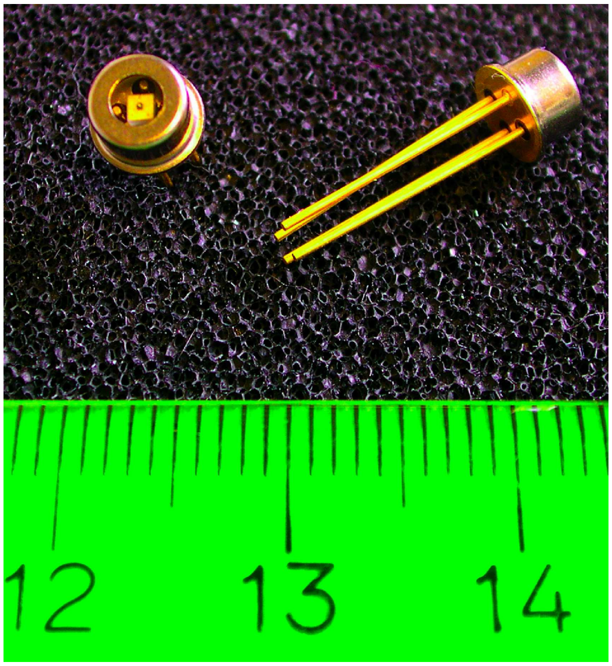

Figure 5.2: *Photograph of two VCSELs of the type HFE4080-321 from Honeywell.*

The connectors have a safety cap which closes automatically when the optical fiber is pulled out from the connector; thus preventing the laser light from hitting someone's eye, as well as preventing dust from entering the precisely machined connectors.

5.3 Evaluation of the performance of the optical link system

As mentioned in section 3.3.3, the use of VCSEL drivers to transmit analogue signals is quite new and rather untested. Therefore, a dedicated setup was built to study the performance of our optical link system. The schematic of the setup is depicted in figure 5.5. We use a special pulse generator to inject PMT like pulses ($\lesssim 3$ *ns* FWHM) of preset amplitudes into the transmitter board, where the VCSEL transforms these signals into light pulses that are sent via optical fibers to the receiver board. In the receiver board, a GaAs PIN-diode converts the light pulses back into electric pulses, which then are read by a digital oscilloscope that is controlled by a PC through a GPIB connection. From now on, the

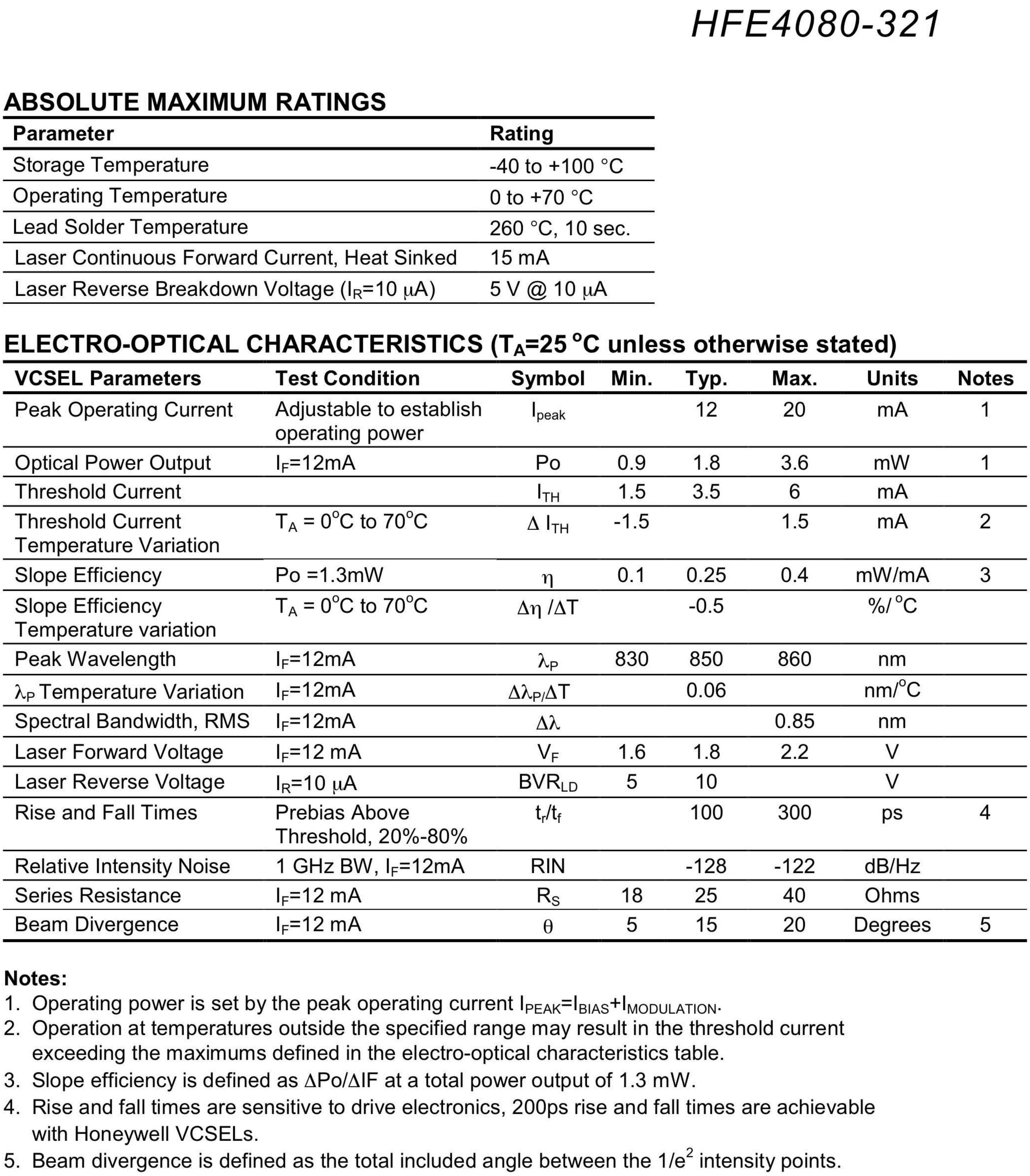

HFE4080-321

ABSOLUTE MAXIMUM RATINGS

Parameter	Rating
Storage Temperature	-40 to +100 °C
Operating Temperature	0 to +70 °C
Lead Solder Temperature	260 °C, 10 sec.
Laser Continuous Forward Current, Heat Sinked	15 mA
Laser Reverse Breakdown Voltage (I_R=10 μA)	5 V @ 10 μA

ELECTRO-OPTICAL CHARACTERISTICS (T_A=25 °C unless otherwise stated)

VCSEL Parameters	Test Condition	Symbol	Min.	Typ.	Max.	Units	Notes
Peak Operating Current	Adjustable to establish operating power	I_{peak}		12	20	mA	1
Optical Power Output	I_F=12mA	Po	0.9	1.8	3.6	mW	1
Threshold Current		I_{TH}	1.5	3.5	6	mA	
Threshold Current Temperature Variation	T_A = 0°C to 70°C	ΔI_{TH}	-1.5		1.5	mA	2
Slope Efficiency	Po =1.3mW	η	0.1	0.25	0.4	mW/mA	3
Slope Efficiency Temperature variation	T_A = 0°C to 70°C	$\Delta\eta /\Delta T$		-0.5		%/ °C	
Peak Wavelength	I_F=12mA	λ_P	830	850	860	nm	
λ_P Temperature Variation	I_F=12mA	$\Delta\lambda_{P}/\Delta T$		0.06		nm/°C	
Spectral Bandwidth, RMS	I_F=12mA	$\Delta\lambda$			0.85	nm	
Laser Forward Voltage	I_F=12 mA	V_F	1.6	1.8	2.2	V	
Laser Reverse Voltage	I_R=10 μA	BVR_{LD}	5	10		V	
Rise and Fall Times	Prebias Above Threshold, 20%-80%	t_r/t_f		100	300	ps	4
Relative Intensity Noise	1 GHz BW, I_F=12mA	RIN		-128	-122	dB/Hz	
Series Resistance	I_F=12 mA	R_S	18	25	40	Ohms	
Beam Divergence	I_F=12 mA	θ	5	15	20	Degrees	5

Notes:

1. Operating power is set by the peak operating current $I_{PEAK}=I_{BIAS}+I_{MODULATION}$.
2. Operation at temperatures outside the specified range may result in the threshold current exceeding the maximums defined in the electro-optical characteristics table.
3. Slope efficiency is defined as ΔPo/ΔIF at a total power output of 1.3 mW.
4. Rise and fall times are sensitive to drive electronics, 200ps rise and fall times are achievable with Honeywell VCSELs.
5. Beam divergence is defined as the total included angle between the $1/e^2$ intensity points.

Figure 5.3: *Copy of the product sheet of the VCSEL HFE4080-321 type from Honeywell.*

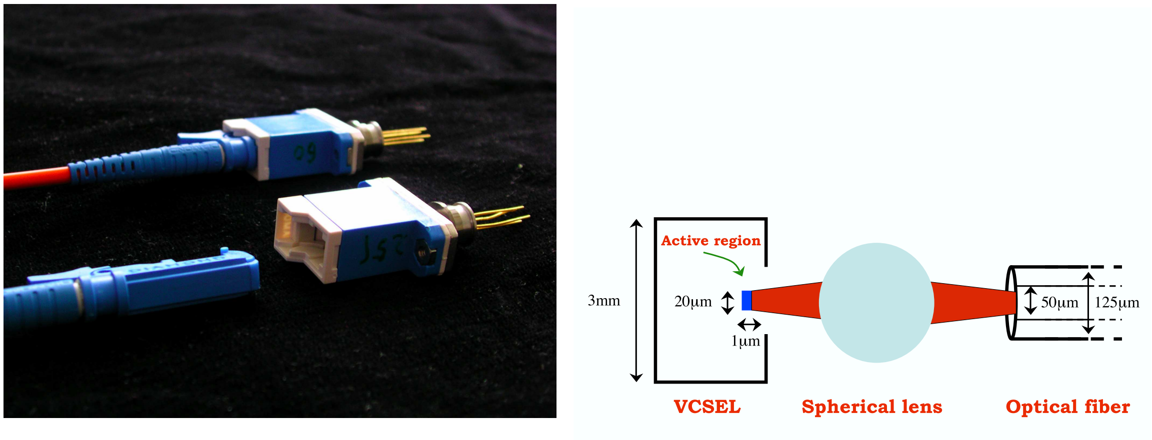

(a) (b)

Figure 5.4: *a) Photograph of two connectorized VCSELs and two connectorized optical fibers; b) basic principle of the optical coupling between the VCSEL and the optical fiber inside the DIAMOND connector.*

electric pulses injected into the transmitter boards will be denoted *input pulses*, and the electric pulses sent to the digital oscilloscope will be denoted *output pulses*. We used this setup to characterize our optical link system by studying both the amplitude and the area of the *output pulses vs.* time and also *vs.* the amplitude of the *input pulses*. Further details about the used experimental setup can be found in Appendix D.1.

The electronic components (transistors, operational amplifiers...) and the PIN-diodes used in the optical link system are well known to be of low noise and stable. Therefore, the measured noise and stability of the *output pulses* reflects, in first order, the performance of the VCSELs.

Figure 5.6 shows both the *input pulse* and the *output pulse* on the display of an oscilloscope. The initial electric pulse was split into two equal pulses with a passive splitter. One of them was fed to the transmitter board and the other one was sent through a two m long RG58C cable (with BNC connectors) to the channel 2 of the oscilloscope. The signal fed to the optical links travelled through eight m long optical fiber, and finally (after being converted back to a electric signal in the receiver board) was sent to the channel 3 of the oscilloscope using a 20 cm (1 ns) long RG58C cable. Note that the shape of the *output pulses*

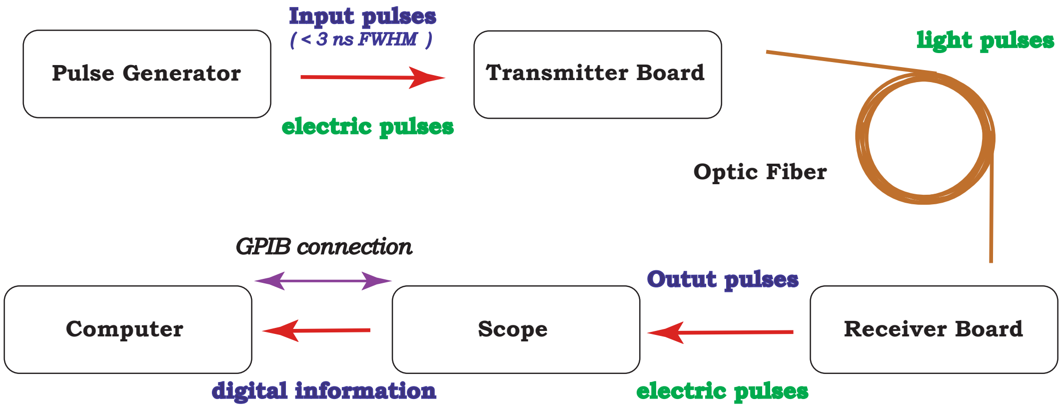

Figure 5.5: *Schematic of the experimental setup used to test the optical link system.*

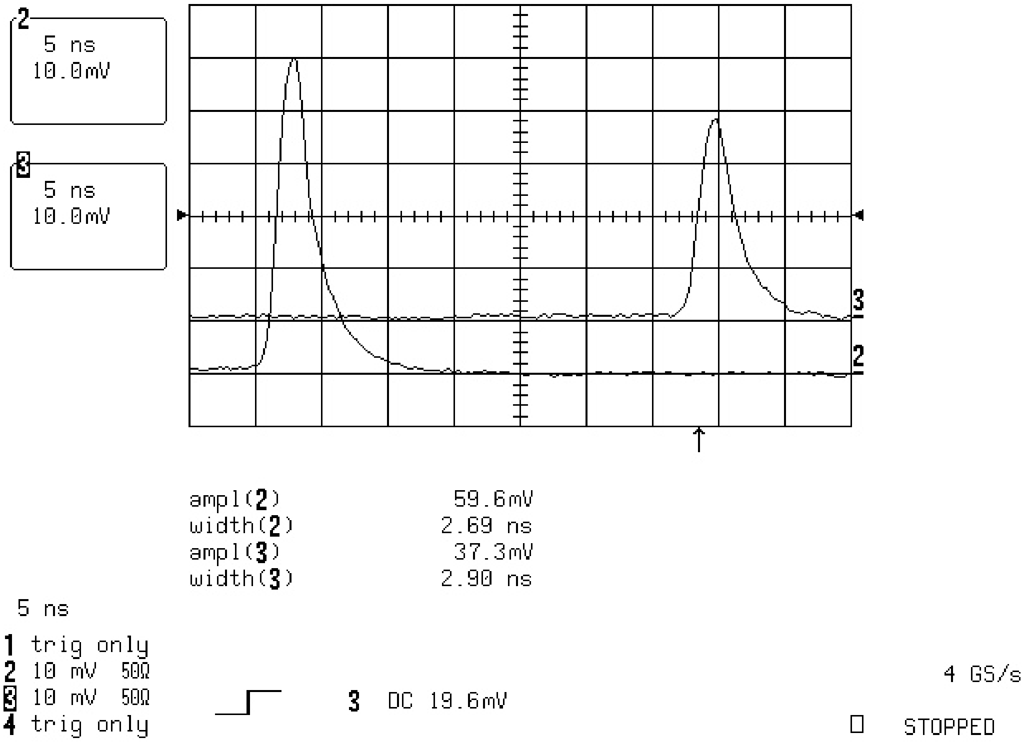

```
2
 5 ns
10.0mV

3
 5 ns
10.0mV

ampl(2)         59.6mV
width(2)       2.69 ns
ampl(3)         37.3mV
width(3)       2.90 ns

5 ns
1 trig only
2 10 mV  50Ω
3 10 mV  50Ω                 3  DC 19.6mV
4 trig only
                                                          4 GS/s
                                                      □  STOPPED
```

Figure 5.6: *Input pulse (left one) and output pulse (right one) on the display of an oscilloscope. See text for further details.*

(∼2.9 *ns* FWHM) is practically the same as that of the *input pulses* (∼2.7 *ns* FWHM).

Figure 5.7 shows an oscilloscope display containing the *output pulse* after travelling through the optical link system with 160 *m* long optical fiber, together with the initial pulse delayed by 156 *m* long RG58C coaxial cable. The used *input pulse* had a FWHM of 2.7 *ns*. Note that the distortion of the pulse that was sent through the coaxial cable (24 $dB/100m$ at 200 *MHz*) is considerably larger than the one that travelled through the optical fiber (0.3 $dB/100m$ at 500 *MHz*). The FWHM of the two pulses is 15 *ns* and 3 *ns* respectively.

It is worth noticing that there are basically no differences between the pulse shape of the signals transmitted by the 8 *m* and the 160 *m* long optical fiber. This is the consequence of the tiny attenuation and large bandwidth of an optical fiber, which makes the transmitter and receiver circuits to be the dominant factor in the dispersion of the pulse. Therefore we can conclude that the optical link system is able to transfer short (∼3 *ns* FWHM) signals over long distances with almost no distortion.

On the other hand, a study of the measured amplitude and area of the *output pulse vs.* time showed that some VCSELs can be quite noisy. As an example I show in figure 5.8 the measured amplitude and area of the transmitted pulses (for equal *input pulses*) for a specific VCSEL. Both the amplitude and area are measured simultaneously every 10 *s*. Note, that the output signal and noise performance can change significantly in time scales of several minutes. The variations in the amplitude and area of the *output pulses* are strongly correlated, yet we found that the relative fluctuations are usually larger in the measured area. This is explained by the presence of fluctuations in the baseline of the signal transmitted by the optical link. Further details will be given in section 5.5.2.

Since the charge of the pulses coming from the PMTs is the variable used to estimate the number of photons impinging on the PMT *PhC*, and the area under the pulse is directly proportional to the number of converted photons[4], we decided to use the measured area of the *output pulses* to characterize the performance of our optical link channels. Therefore, in

---

[4] The Cherenkov light flashes have some time structure due to the nature of the shower development. Hence, the transmitted pulses are not always identical in shape.

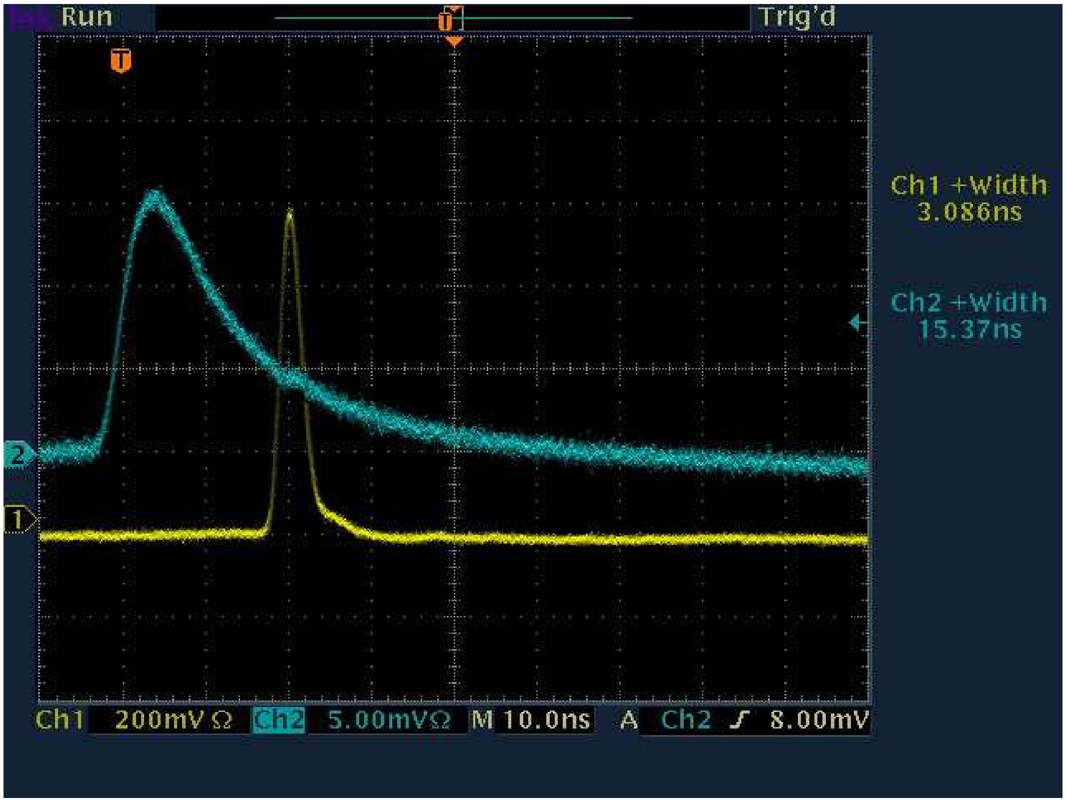

Figure 5.7: *Pulse shape of two signals on the display of a digital oscilloscope. The blue signal travelled through a 156 m long RG58C coaxial cable, whereas the yellow signal travelled through a 160 m long multimode graded index optical fiber. The used initial pulse had a FWHM of 2.7 ns.*

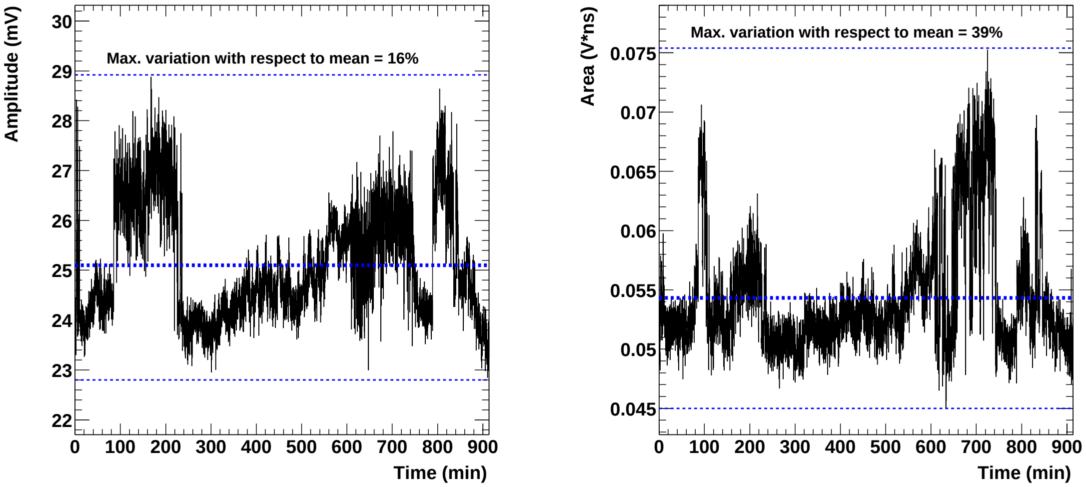

(a) (b)

Figure 5.8: *Amplitude and area of the output pulse vs.time. The input pulse is a 2.2 ns FWHM and 30 mV amplitude Gaussian-like pulse. The fordward current applied to the VCSEL is 7 mA. An offset on the vertical scale have been subtracted in both figures in order to make the effect more visible.*

the following I will only consider the measured area of the *output pulses.* As an estimator of the relative noise in the *output pulse* area, I will use the standard deviation of the measured area values divided by the mean of the measured area values.

We found that the relative noise in the *output pulse* increases when decreasing the amplitude of the *input pulse*, and that the forward current applied to the diode (bias current) can affect this noise too. Figure 5.9 shows the measured area and the relative noise of the *output pulse* for several bias current settings. Note that not only the relative noise changes substantially (appearance of so-called “resonances”), but also the gain (*i.e,* electric signal to light signal conversion) of the VCSEL can vary.

The explanation for this behavior is the activation/deactivation of transverse modes in the VCSEL. This affects the beam divergence angle and the polarization of the light emitted by the laser, which produces variations in the amount of light focused into and transmitted by the optical fiber. The tolerances in the alignment of the laser diode, the spherical lens

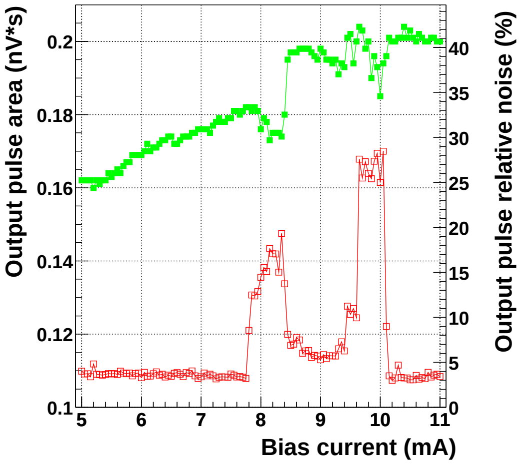

Figure 5.9: *Output pulse area (green filled squares) and relative noise (red empty squares) vs. bias current. The area is the mean of the measured area of 120 pulses, and the relative noise is the computed standard deviation divided by the mean area. The input pulse has a Gaussian-like shape with 40 mV amplitude and 2.7 ns FWHM.*

and the optical fiber play also an important role in the focusing of the light into the *core* of the fiber.

Each VCSEL has its own characteristic dependence on the bias current. Yet I found that the "resonances" and the sudden changes in the VCSEL gain are typically less frequent for low bias currents. I also noticed that, when increasing the amplitude of the *input pulse*, the position of the "resonances" is approximately the same, but their intensity is substantially reduced. Figure 5.10 shows an example of this behavior for a typical VCSEL. It is worth noticing that there are almost no "resonances" when the amplitude of the *input pulse* exceeds 300 mV. This occurs even for the noisiest VCSELs; the performance of the VCSELs improves as the amplitude of the pulse to be transmitted increases.

In order to ensure a good functionality of the optical links (despite of the previously mentioned performance deficiencies of many VCSELs) we made the following two modifications in the system:

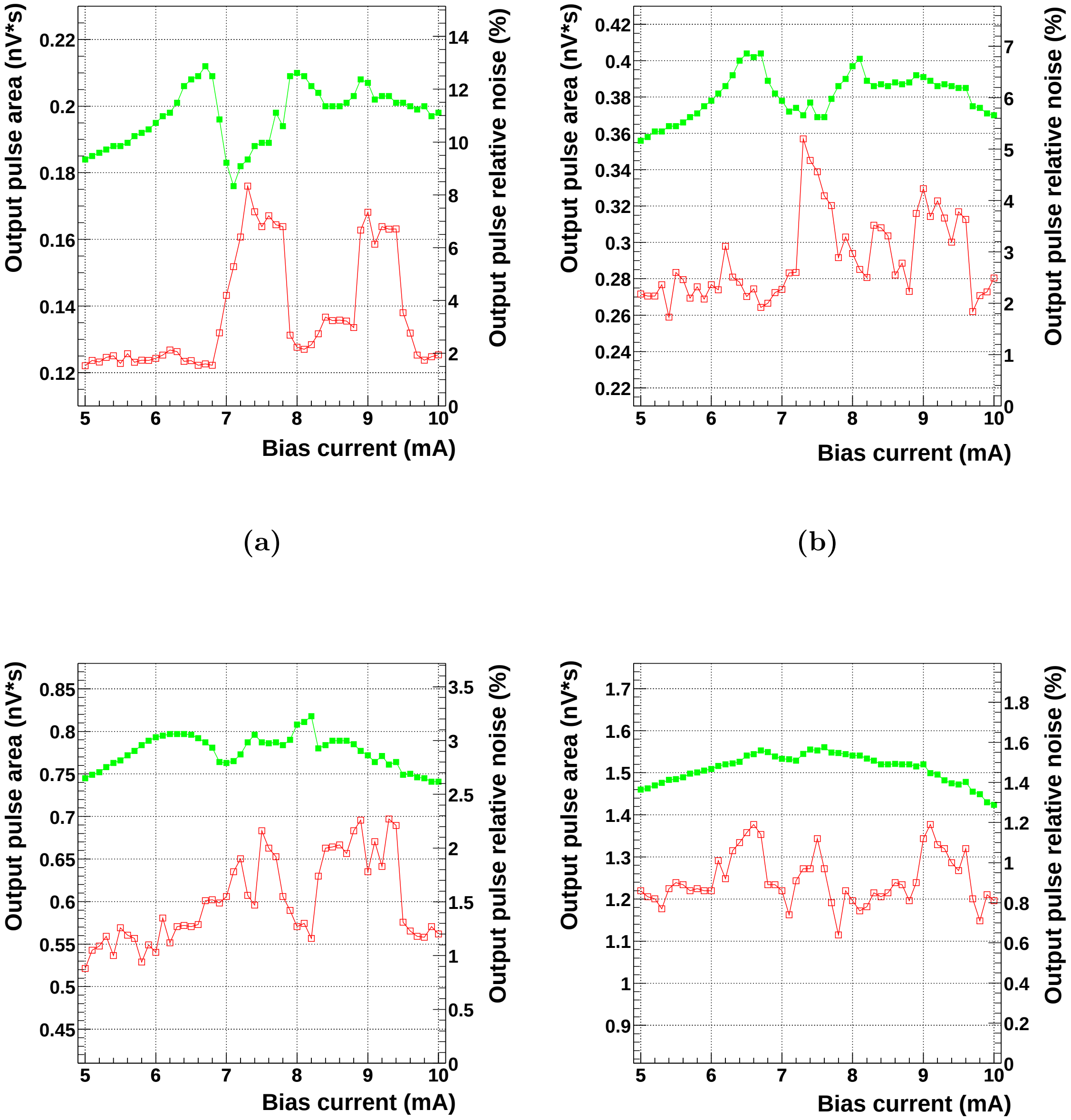

(a) **(b)**

(c) **(d)**

Figure 5.10: *Output pulse area (green filled squares) and relative noise (red empty squares) vs. bias current for 4 different input pulse amplitudes: a) 40 mV; b) 80 mV; c) 156 mV; and d) 312 mV. The area is the mean of the measured area of 120 pulses, and the relative noise is the computed standard deviation divided by the mean area.*

- The signal amplification in the transmitter board was increased by a factor four in order to modulate the light output of the VCSELs by a four times larger pulse. This modification reduces the relative noise of the transferred signals. The performance improvement is particularly important when transferring low amplitude pulses, which (due to the exponential decrease of the fluxes of $\gamma - rays$ and hadrons with the energy) will be the case for most of the observed atmospheric showers.

- The use of 6 mA bias current to drive the VCSELs. This modification reduces the number and the relative intensity of the "resonances" and the sudden changes in VCSEL gain. This current is high enough to ensure that all diodes are working in the lasing mode, *i.e,* well above their threshold currents (see section 5.2). We decided to use only one bias current for all VCSELs in order to simplify the replacement of dead or malfunctioning lasers in the telescope camera.

In addition, due to the significant performance spread among the measured VCSELs, detailed quality checks were carried out for each single VCSEL; and all those lasers not fulfilling the strict requirements to be used in MAGIC were rejected. The details of the quality checks and the selection of the VCSELs are explained in the following section.

5.4 Selection and classification of the VCSELs to be used in MAGIC

In this section I will report about the selection of the VCSELs to be used in the optical link system. At first, I will justify the choice of the *input pulse* used in the selection. Then I will describe the selection tests performed on the VCSELs and the selection criteria used to reject/accept the lasers. Finally, I will summarize the outcome of this selection.

5.4.1 Choice of the *input pulse* to be used in the VCSEL selection

As I discussed in section 5.3, the performance of the VCSEL drivers to transmit analogue pulses depends on the amplitude of the pulse that has to be transmitted. Hence, the choice of the *input pulse* to be used in the VCSEL selection tests has an important impact on the amount of lasers that passes/fails these tests. We decided to use, as *input pulse*, a pulse close to the most frequent PMT pulse expected to be produced in the camera of MAGIC.

As stated in chapters 2 and 3, the most frequent (and most interesting) events that will be detected by the MAGIC Telescope are atmospheric showers produced by sub-100 GeV gammas. For these events, our Monte Carlo simulations predict an average pixel content of about 15 *phe*s. After the multiplication in the dynode system of the PMT, and the gain in the transimpedance preamplifier, these signals are converted into electric pulses of $\lesssim 3$ ns FWHM and ∼10-15 mV amplitude at the input of the transmitter boards. This is the case for a PMT amplification in which a single *phe* impinging on the first dynode of the PMT produces, at the output of the preamplifier, a signal of 1 mV amplitude and 2 ns FWHM. This is the PMT amplification used in the MAGIC Monte Carlo simulations (see [36]); and I will denote it *standard PMT amplification*.

Therefore, we decided to use an *input pulse* of 10 mV amplitude and 2.7 ns FWHM for the VCSEL selection tests. From now on, these pulses will be denoted *standard input pulses*.

It is worth mentioning that a pulse of 10 *phe*s is quite a small signal, and thus, one expects sizeable intrinsic fluctuations when detecting these faint pulses. These intrinsic fluctuations should be taken into account in the VCSEL selection; it is useless to reduce the noise of the optical analogue system to values below 10-20% of the intrinsic noise of the signal that has to be transmitted.

The intrinsic fluctuations in small signals ($\lesssim 100$ *phe*s) coming from the camera pixels are basically produced in the PMTs. For a sufficiently large number of photons impinging on the PMT *PhC* ($\gtrsim 30$ photons), the charge collected in the PMT anode is Gaussian distributed around the mean charge ($< Q >$). The sigma of the charge (σ_Q) fulfills the following equation:

$$\frac{\sigma_Q}{< Q >} = \frac{1}{\sqrt{< m_{phe} >}} \cdot F \qquad (5.1)$$

where $\sqrt{< m_{phe} >}$ is the mean number of *phe*s impinging on the first dynode and F is the *excess noise factor* of the PMT [82]. The first term accounts for the fluctuations in the binomial process of converting photons into photoelectrons in the *PhC* of the PMT[5], whereas the second one accounts for the statistical fluctuations in the amplification of the electrons that takes place in the PMT dynode system. The value of F is about 1.15 for the PMTs and the high voltage settings used in the camera of MAGIC.

According to the equation 5.1, a pulse of 10 *phe*s in a typical PMT of the camera of MAGIC has a statistical fluctuation of about 36%.

It is worth noticing that the use (in the VCSEL selection tests) of an *input pulse* with an amplitude as small as 10 mV has two consequences; *a)* the VCSELs are tested at quite unfavorable conditions, since the noise introduced by the VCSELs increases when reducing the amplitude of the pulse to be transmitted, *b)* the margins in the VCSEL selection are rather wide because the intrinsic (statistical) fluctuations of the signals to be transmitted are already quite large.

5.4.2 Description of the VCSEL selection procedure

The selection of the VCSELs was carried out in two steps. In the first one, the performance of the laser diodes was studied during short periods of time at several bias currents settings, ranging from 5 mA to 7 mA in steps of 0.05 mA. This is the so-called ***bias current scan test***. The VCSELs were accepted/rejected according to the measured performance close to 6.0 mA, which is the selected working point (see section 5.3). Those VCSELs that passed the first test were submitted to the second test, in which their performance was studied at a bias current of 6.0 mA during a time period longer than 10 hours; this is the so-called ***long time test***. Both tests were performed using the *standard input pulse* defined in the previous section. In the following paragraphs I will give more details about the two previously mentioned tests and about the selection criteria used to accept/reject the VCSELs.

The bias current scan test

In the *bias current scan test*, the VCSELs were studied at several bias currents ranging

---

[5] In bialkali *PhC*s (which typically have a mean *QE* of ~15-20% in the wavelength range 300-600 nm), the binomial function can be very well approximated by a Poisson function when $< m_{phe} > \gtrsim 5$.

from 5.00 mA to 7.00 mA, in steps of 0.05 mA. At each bias current, 120 measurements of the *output pulse* area were taken (a measurement every 2 seconds during 4 minutes), and the standard deviation and the mean area were computed. Since the selected bias current to drive the VCSELs was 6.00 mA, we decided to accept/reject the lasers according to their performance in the bias current range 5.70-6.30 mA. I want to point out that variations of 0.1-0.2 mA in the chosen bias current might occur during the telescope operation, specially if the temperature inside the camera changed by $\gtrsim 5$ degrees. Therefore, sudden gain variations and resonances should not be present, at least, in the bias current range 6.0 ± 0.2 mA.

We decided to carry out the *bias current scan test* before the VCSELs were connectorized. The main reason was the price of the encapsulation of a VCSEL in a DIAMOND connector, which was significantly higher than the prize of the laser itself; the cost per VCSEL was 15 Euros, whereas the cost of the connectorization of a single VCSEL was 30 Euros[6]. Therefore, it was cheaper to reject VCSELs before connectorizing them. From now on, the non-connectorized VCSELs will be denoted *naked* VCSELs.

In order to perform the *bias current scan tests* on *naked* VCSELs, the optical link system (transmitter board, optic fibers and receiver board) was replaced by boards where the *naked* VCSELs are connected to the driver circuit and shine directly onto the PIN photodiodes. The details of this measuring setup are given in appendix D.2.

We decided to set very tight selection criteria in the *bias current scan test* in order to reject most of the “noisy” VCSELs before the connectorization. The two criteria used to reject a VCSEL in the *bias current scan test* were *a)* relative noise larger than 4.5% for a given bias current and *b)* light output variations exceeding 3% when the bias current is changed by 0.05 mA. As stated before, both criteria were applied in the current range of 5.70-6.30 mA. We noticed that by setting tighter constraints in any of the two selection criteria mentioned before, the number of rejected VCSELs increased exponentially. I want to stress that we are aware that these tight selection criteria imply that some “acceptable” VCSELs might have been rejected too. However, due to the cheap price of the *naked* VCSELs compared to the high price of the laser connectorization, we think it was worth to apply these

---

[6] Prices from year 2002.

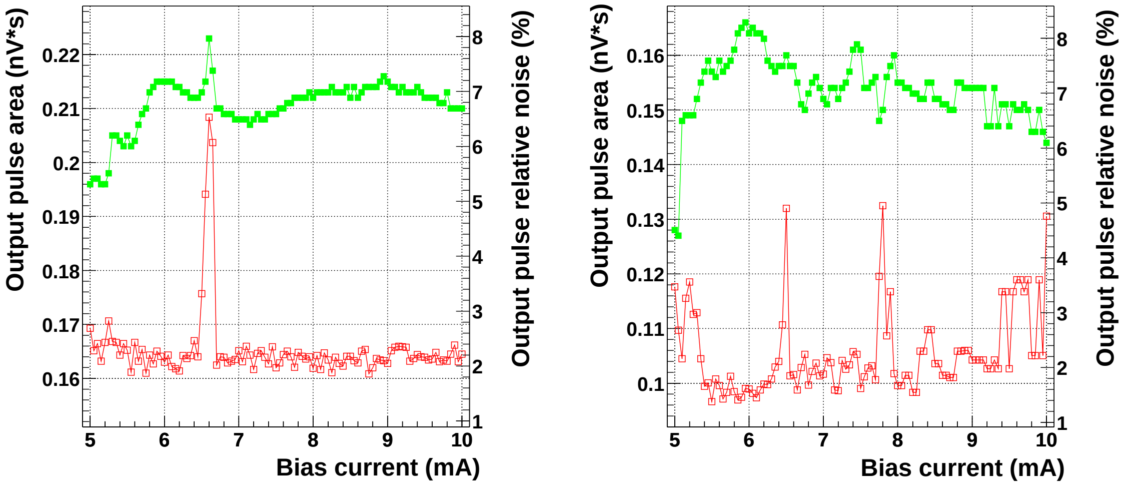

(a) (b)

Figure 5.11: *Output pulse area (green filled squares) and relative noise (red empty squares) vs. bias current for a VCSEL a) before being connectorized and b) after being connectorized. The standard input pulse was used in this test. The differences in the area of the output pulses arise from the losses in the VCSEL-to-fiber, and fiber-to-PIN diode couplings, and also from a somewhat different amplification of the signal after the PIN diodes.*

demanding requirements in the *bias current scan test.*

It must be pointed out that, when comparing *bias current scan tests* for VCSELs before and after being connectorized, we found that the “resonances” occurred at the same bias currents, whereas the relative intensity and width were somewhat different. In some cases, we also observed new “resonances” in the *bias current scan test* carried out on connectorized VCSELs, as I show in figure 5.11. We think that the differences in the outcome of the *bias current scan test* performed on *naked* VCSELs and on connectorized VCSELs arise from imperfections/tolerances in the alignment of the laser diode, the spherical lens and the optical fiber inside the DIAMOND connector. These mechanical imperfections/tolerances modify somewhat the effect (on the output signal) produced by the variations in the lasing spot, which originate from the VCSEL mode “hopping”.

The long time test

In the *long time test*, the area of the *output pulses* was measured every 5 seconds during a time period of 10-12 hours. The VCSEL bias current was set to 6.00 mA. I want to stress that some VCSELs showed long term instabilities (see figure 5.8), and hence it was important to test the performance of the VCSELs during long periods of time. We extended the *long time test* of some VCSELs up to $\gtrsim 50$ hours for comparison purposes, but we did not find significant differences with respect to the 10 hours long tests. We actually noticed that if a connectorized VCSEL is noisy (due to mode "hopping"), the large fluctuations in the measured area of the *output pulse* show up typically during the first 2-3 hours of the *long time test*.

The measuring setup used to perform the *long time test* on the connectorized VCSELs is the one presented in section 5.3, which is fully described in appendix D.1.

Due to the importance of a low noise and reliable signal transmission in the performance of the telescope, we decided to adopt a very conservative approach in the VCSEL selection. The main criteria for rejecting lasers in the *long time test* (which is the last test deciding whether a VCSEL is rejected or not) was a relative noise in the measured area of the *output pulse* exceeding 1/3 of the statistical fluctuation in a PMT signal of 10 *phe*s; *i.e,* $\frac{1}{3} \cdot 36\% = 12\%$.

However, as I showed in figure 5.8, the noise in the signals transmitted by "bad" VCSELs can vary substantially in time scales of several tens of minutes. Therefore, the area of the *output pulse* (which is measured every 5 seconds during more than 10 hours) does not follow a Gaussian distribution; and hence the relative standard deviation of this sample of data is not a good estimate of the noise.

In order to account for these changes in the performance of the VCSELs, we divided the entire sample of data into subsamples of data taken during 5 minutes, in which the standard deviation and the mean area were computed. Under the realistic assumption that in each of these time periods of 5 minutes the noise does not change very much, the measured area of the *output pulse* follows a Gaussian distribution, and thus the calculated standard deviation is a good estimate of the noise. That means that we have a "continuous" measurement of the noise introduced by the VCSELs in the transmitted signal during the entire $\gtrsim 10$ hours long test.

From now on, the relative standard deviation computed in the *long time test* using the whole sample of data will be denoted *relative noise*, while the relative standard deviation computed using the data from the 5 minutes time period where the VCSEL noise is the largest will be denoted *maximum relative noise*.

Following our conservative approach, we decided to use the *maximum relative noise* as "estimator" of the noise of the VCSEL (worst case scenario). And therefore, the VCSELs were rejected if the *maximum relative noise* measured in the *long time test* exceeded 12%.

We introduced an additional selection criteria in the *long time test* in order to account for variations in the mean light output of the VCSEL (see figure 5.8). The lasers were also rejected if they showed drifts in the mean area between two consecutive subsamples (of 5 minutes duration) exceeding 12%. Slower drifts in the signal output of the VCSELs[7] could be easily corrected by the calibration system of the telescope (see section 3.6), and thus they do not affect the performance of the telescope.

5.4.3 Result of the VCSEL selection tests

The outcome of the VCSEL selection is summarized in the tables 5.1 and 5.2, where I list the number of measured, accepted and rejected lasers in the *bias current scan test* and the *long time test* respectively. All VCSELs are from the same type, yet the manufacture date is different. The information presented in the tables is subdivided according to the 3 different manufacture dates; March 1999, October 2000 and September 2002. Note that the percentage of rejected VCSELs decreases for more recent production dates, which implies a steady improvement in the performance of this type of lasers.

We decided to classify the sample of accepted VCSELs into two groups, *inner* VCSELs and *outer* VCSELs, which are used to transmit the signal from the PMTs located in the inner and the outer section of the MAGIC Telescope camera. As stated in section 3.3.3, the MAGIC camera requires 450 and 198 VCSELs for the inner and the outer section respectively.

---

[7] Drifts in the light output of the VCSELs might occur due to temperature changes, which could affect the performance of the lasers directly, and indirectly through the changes in the VCSELs' driver current.

	March 1999	October 2000	September 2002	**Entire VCSEL sample**
Measured	130 (100%)	440 (100%)	400 (100%)	**970 (100%)**
Accepted	84 (64%)	338 (77%)	316 (79%)	**738 (76%)**
Rejected	46 (36%)	102 (23%)	84 (21%)	**232 (24%)**

Table 5.1: *Result of the bias current scan test applied to 970 naked VCSELs. The VCSELs are classified according to the manufacture date.*

	March 1999	October 2000	September 2002	**Entire VCSEL sample**
Measured	84 (100%)	336 (100%)	300 (100%)	**720 (100%)**
Accepted	77 (92%)	302 (90%)	291 (97%)	**670 (93%)**
Rejected	7 (8%)	34 (10%)	9 (3%)	**50 (7%)**

Table 5.2: *Result of the long time test applied to 720 connectorized VCSELs. The VCSELs are classified according to the manufacture date.*

Yet only 576 VCSELs (out of the 648) are used during normal telescope operation. Since most of the air showers are detected in the inner region of the camera, and besides, the inner pixels are used in the telescope trigger (see section 3.4); I selected the VCSELs with the lowest noise for the inner section of the camera.

We found quite some spread in the intrinsic gain (electric signal to light signal conversion) of the accepted VCSELs, whereas the photodiode conversion of light signals back into electric signals (in the receiver boards) showed very little variations over the entire sample. The highest VCSEL gain was two times larger than the lowest one. In order to correct for this spread, the gain of the driver amplifier in the transmitter boards was tuned to ensure an equal conversion (among all the channels) within 10%. After this modification, the overall signal amplification in the optical link system for all channels was 3.3 ± 0.3.

We expect smooth drifts in the bias current ($\lesssim 0.1\ mA$) during the telescope operation; specially if the temperature inside the camera is not well controlled and varies few degrees.

Due to the already mentioned relation between the bias current and the VCSEL gain (see figures 5.9 and 5.10), variations in the amplification of the signal might occur in some of the channels. However, only VCSELs with a rather flat gain *vs.* bias current relation were accepted by the *bias current scan test*. Hence these gain variations, if they happened to occur, they would be small and smooth in time (time scales of tens of minutes); and thus they could be easily corrected by the calibration system of the telescope (see section 3.6).

5.5 The performance of the VCSELs used in the MAGIC Telescope

5.5.1 The noise performance of the VCSELs that passed the selection

The distributions of the *relative noise* and the *maximum relative noise* (computed using data from the *long time test*) for all those VCSELs that passed the two selections are shown in figure 5.12. The intrinsic noise of the measuring setup, which is about 1% when using the *standard input pulses* (see appendix D.1), has been subtracted quadratically. Note that the mean of the corrected *relative noise* is about 2.5%.

Figure 5.13 shows the distributions of the *relative noise* and the *maximum relative noise* for the VCSELs selected for the inner and the outer camera section. We want to stress that, for the inner VCSELs, the mean of the *relative noise* distribution is 2.0%, and the mean of the *maximum relative noise* distribution is 3.8%; *i.e,* well below the statistical fluctuation of *standard input pulses* coming from the PMTs, which is about 36%.

For comparison purposes, quite a few VCSELs were also studied at another pulse amplitudes besides that of the *standard input pulse*. In particular, the *long time test* was carried out using an *input pulse* with an amplitude of 40 mV on 406 VCSELs (all being manufactured in March 1999 or October 2000). Out of these 406 lasers, 37 had failed the *long time test* performed with the *standard input pulse* of 10 mV amplitude (*i.e,* they were tagged as "rejected VCSELs"). Figure 5.14 shows the distributions of the *relative noise* and the *maximum relative noise* for all 406 VCSELs. Note that, for the accepted lasers, the mean of both distributions (*relative noise* and *maximum relative noise*) decreased by about a factor 2

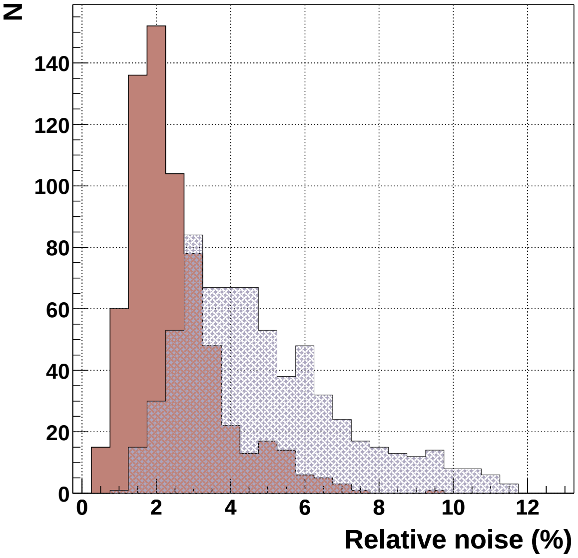

Figure 5.12: *Relative noise (brown filled histogram) and maximum relative noise (blue shadow filled histogram) for all the VCSELs that passed the selection.*

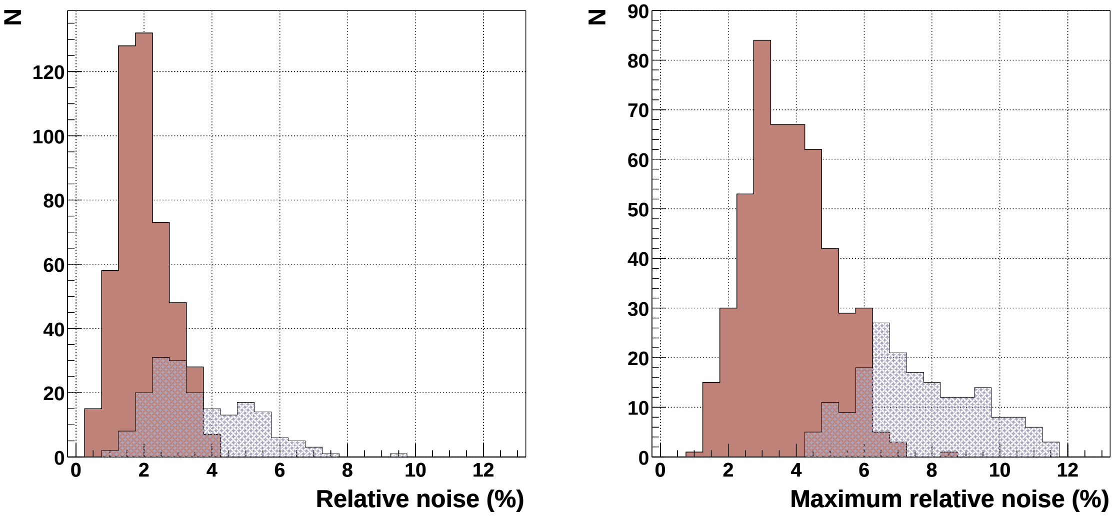

(a) **(b)**

Figure 5.13: *a) Relative noise for the inner VCSELs (brown filled histogram) and the outer VCSELs (blue shadow filled histogram); b) maximum relative noise for the inner VCSELs (brown filled histogram) and the outer VCSELs (blue shadow filled histogram).*

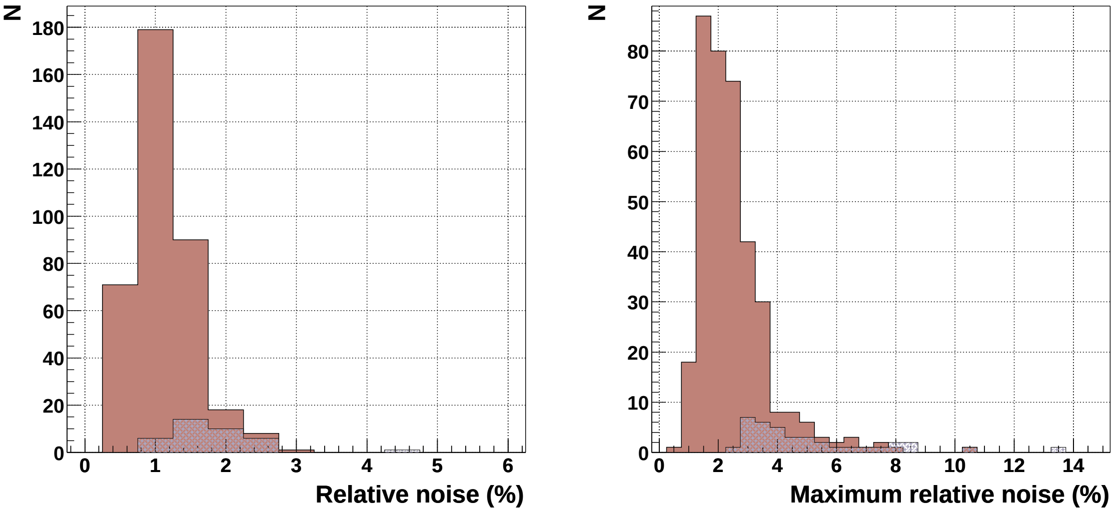

(a) (b)

Figure 5.14: *a) Relative noise and b) maximum relative noise computed from the long time test that was performed on 406 VCSELs using an input pulse with an amplitude of 40 mV. The brown filled histograms display the noise of the 367 VCSELs that passed the long time test performed with the standard input pulse (accepted VCSELs), and the blue shadow filled histograms display the noise of those lasers that failed this test (rejected VCSELs).*

with respect to the analogue values shown in figure 5.12. Besides, the differences between accepted and rejected VCSELs (in the *long time test*) are washed out[8]. As expected, both effects confirm an improvement in the VCSEL performance when increasing the amplitude of the pulse that has to be transmitted.

It is worth mentioning that the mean of the distribution that shows the *maximum relative noise* for the 367 accepted VCSELs is 2.5%, which is also substantially lower than the expected intrinsic statistical fluctuation of a 40 mV pulse in the pixel chain of MAGIC (produced by about 40 phes), which is $\sim$ 18%.

---

[8] However, those VCSELs that failed the *long time test* with the *standard input pulse* do show, when being tested with a 40 mV amplitude *input pulse*, the largest *relative noise* and *maximum relative noise*.

5.5.2 Parametrization of the noise introduced by the optical links

We also performed some studies to parametrize the effect of the optical link system in the electric pulses that have to be transmitted. The goal was to find a probability distribution function that describes the smearing in the charge of the *output pulses* as a function of the amplitude of the *input pulses*.

The main motivation for these studies was to understand better the effect of the optical link system on the evaluation of the signals produced by the atmospheric showers in the camera of the telescope. Besides, such function describing the smearing of the signal could be also used in a Monte Carlo simulation of the signal transmission.

The probability distribution function of the output pulse area, for a given *input pulse* amplitude, can be deduced from the *long time test* data. One can project all the measured area values as function of time onto the "y" axis, thus obtaining a distribution (*i.e,* spectrum) of the *output pulse* area. Normalizing this spectrum such that the integral is one, one gets the probability distribution of the *output pulse* area. A function fitting this distribution is, by definition, the probability distribution function of the area of the *output pulse*.

The first problem we encountered when following this procedure was the drift in the transmitter gain (driver+VCSEL) that occurs in some channels. As I already mentioned, this drift is partly due to temperature variations that affect the performance of the VCSEL directly, and indirectly via the variation of the bias current. We noted that, in the laboratory where all these tests were performed, the temperature could easily vary from 22°to 27°. Despite the fact that these variations in the output signal occur in time scales of several tens of minutes, they cannot be neglected; differences in the measured *output pulse* area of up to 30% could occur in some cases. Besides, this gain drift is different for the different channels, and therefore very difficult to be simulated. An example of such a situation is shown in figure 5.15a, where the distribution of the *output pulse* area observed for this channel is clearly asymmetric, and does not follow a Gaussian distribution. It should be noted that the effect decreases when the amplitude of the *input pulse* increases.

However, this unwanted feature in the signal transmission observed in some channels can be rectified easily by "recalibrating" all channels every few minutes. This task can be carried

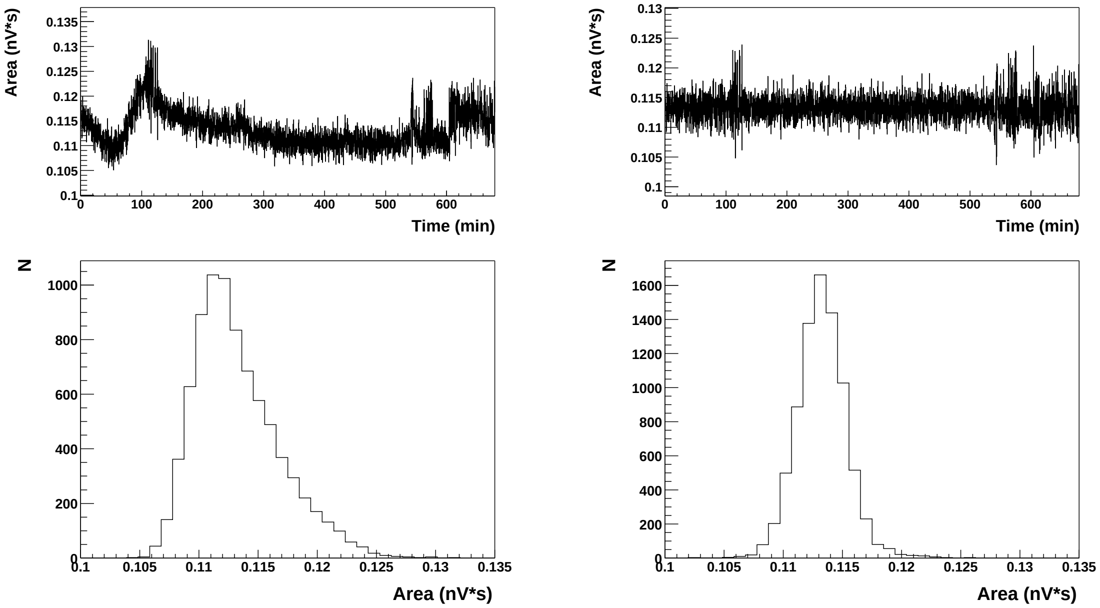

(a) (b)

Figure 5.15: *a) Output pulse area vs. time measured in the long time test (upper left plot) and distribution of the corresponding measured areas (lower left plot); b) output pulse area vs. time measured in the long time test when the data is "recalibrated" every five minutes (upper rigth plot) and distribution of the corresponding measured areas (lower right plot). See text for further explanations.*

out during normal observations of the telescope, since the calibration system is designed such that signal calibrations can be performed during data taking (see section 3.6). By inspecting the *long time test* data of all accepted VCSELs, we found that a recalibration every ten minutes is sufficient to reduce the slow drifts in the signals to just a few percent. Nevertheless, since the conditions in our laboratory might be somewhat different from those ones in the camera of the telescope and, on the other hand, a reduction in the recalibration period does not cause any overload to the calibration system and the normal data taking of the telescope, we decided to perform a calibration run every five minutes.

The effect of a recalibration of the data every five minutes is shown in figure 5.15*b*. The recalibration is performed by multiplying all the measured areas belonging to a given five minutes long subsample i by a calibration constant $K_i = \frac{<area>}{<area>_i}$; where $< area >$ is the average area of the whole sample of data, and $< area >_i$ is the average area of the subsample i. Note that the data recalibration removes completely the slow drift in the transmitter gain, and the distribution of the measured areas is almost Gaussian-like. It is worth noticing (from figure 5.15*b*) that the area spectrum has long tails (wider than expected for a single Gaussian function) due to those periods of time in which the optical link channel is more noisy. This is, in fact, a quite general feature among the tested channels. Because of these tails, we decided to use a parametrization consisted of two Gaussian functions to fit the distributions of the recalibrated *output pulse* area.

Due to the differences in noise performance between inner and outer VCSELs we decided to carry out the study separately for the two groups. We used 8 inner VCSELs and 4 outer VCSELs. In order to combine the measurements for the different VCSELs, the data was individually normalized to 1 instead of to the mean area of the measurement. That implies that the calibration constant for the subsample i is $\frac{1}{<area>_i}$ instead of $\frac{<area>}{<area>_i}$. This normalization removes the spread in the intrinsic gain of the tested VCSELs. Adding the area spectra of the single VCSELs and normalizing the final distribution to get an integral of 1, one finds the (typical) probability distribution for both inner and outer VCSELs separately. The function used to fit these distributions is the following one:

$$P(x)dx \;=\; K_1 \cdot exp\Big(\frac{(\mu_1 - x)^2}{2\sigma_1^2}\Big) + K_2 \cdot exp\Big(\frac{(\mu_2 - x)^2}{2\sigma_2^2}\Big)dx \tag{5.2}$$

where x is the relative area (*i.e,* area normalized to the average area), μ_i and σ_i are the mean and the sigma of the Gaussian i, and K_i are constants which describe the relative contributions of the two Gaussian functions. In order to simplify the procedure, we neglected the small asymmetries in the area spectrums, and fixed μ for both Gaussian functions to 1. In this way, the fitting procedure gave us the constants K_i and the sigmas σ_i.

In order to obtain the dependence of the *output pulse* area with the amplitude of the pulse that has to be transmitted, I repeated the same procedure for the following seven *input pulse* amplitudes: 4 mV, 7 mV, 10 mV, 14 mV, 20 mV, 30 mV, and 40 mV. Note that all seven pulse amplitudes are quite low. I used small *input pulses* because of two reasons: *a)* most of the atmospheric showers observed with MAGIC produce PMT pulses of $\lesssim$ 15 mV amplitude; *b)* the relative noise introduced by the optical link system decreases when increasing the amplitude of the *input pulses.*

For each *input pulse* amplitude j we performed a fit with the function defined by the formula 5.2, from which we obtained the quantities K_i^j and σ_i^j. We observed that both K_i^j and σ_i^j were quite different for the different *input pulse* amplitudes (*i.e,* for different j values). Yet the quantity $K_i^j \cdot \sqrt{2\pi}\sigma_i^j$ was rather similar for all j values. Therefore, we concluded that it was better to parametrize the probability distribution function as the sum of two *normalized* Gaussian functions (centered at 1) and weighted by the quantities C_i^j ($\equiv K_i^j \cdot \sqrt{2\pi}\sigma_i^j$), which were found to be similar (within 10%) for all j values.

$$P(x)dx \;=\; \frac{C_1}{\sqrt{2\pi}\sigma_1} exp\Big(\frac{(\mu - x)^2}{2\sigma_1^2}\Big) + \frac{C_2}{\sqrt{2\pi}\sigma_2} exp\Big(\frac{(\mu - x)^2}{2\sigma_2^2}\Big)dx \tag{5.3}$$

Due to the above mentioned feature, we decided to perform an iterative fit for all amplitudes, in which:

- The parameter values K_i^j and σ_i^j obtained from the *n-1* fit using the function defined by the expression 5.2 are used to compute the weights C_i^j.

- The weights C_i^j computed for the seven amplitudes are combined (the average is calculated) to get the weights $< C_i >$. Because of unitary ($< C_1 > + < C_2 >= 1$), these two weights can be also combined to get a single weight $< C >$; where $< C_1 >\equiv< C >$ and $< C_2 >= 1- < C >$.

- The weight $< C >$ and the parameter values σ_i^j obtained from the *n-1* fit are used to compute new values for the parameters K_i^j ($K_i^{j\,NEW} = \frac{C_i^j}{\sqrt{2\pi}\sigma_i^j}$)

- Before starting the n^{th} fit, the parameter μ is fixed to 1, and the parameters K_i^j are fixed to the previously calculated $K_i^{j\,NEW}$.

- The n^{th} fit is performed using the function defined by the expression 5.2. This fit provides new values σ_i^j.

So, each iteration produces new values σ_i^j with which new values C_i are computed. We found that in the first iterations the values σ_i^j and C_i fluctuated a few percent. However, after the 5^{th} iteration, these values started to converge very quickly. In the 10^{th} iteration, the relative differences in the quantities σ_i^j and C_i with respect to the ones computed in the 9^{th} iteration were smaller than 10^{-5}. This was a clear signature that the iterative fit was converging, and hence that one can use the function 5.3 with constant weights C_1 and C_2 for all *input pulse* amplitudes. The weights found for both the inner and the outer VCSELs are presented in table 5.3

	C_1	C_2
Inner VCSEL	0.708	0.292
Outer VCSEL	0.850	0.150

Table 5.3: *Weights C_1 and C_2 for the two normalized Gaussian functions of the probability distribution function described by the expression 5.3. Values for both the inner and the outer VCSELs are presented.*

Figure 5.16 shows, for the inner VCSELs, the normalized *output pulse* area distributions for four different *input pulse* amplitudes, together with the probability distribution functions computed using the previously mentioned iterative fit (up to 10 iterations). The two normalized Gaussian functions (properly weighted with C_i) are also shown. I want to stress that the weights C_i and the mean μ ($\equiv 1.0$) of the Gaussian functions are constants; the only parameters that change when varying the *input pulse* amplitude are the sigma of the Gaussian functions σ_i. The corresponding plots for outer VCSELs are shown in figure 5.17.

The dependence of σ_i on the amplitude of the *input pulse* can be also parametrized. Figure 5.18 shows the values σ_i for the seven amplitudes used in these tests. The data (for both the inner and the outer VCSELs) agree well with the following function

$$\sigma(\%) = \sqrt{a^2 + (\frac{b}{ampl(mV)})^2} \tag{5.4}$$

where a and b are constants and *ampl* is the amplitude of the *input pulse*. The values of a and b for the four sigmas are shown in table 5.4. Note that, for *input pulse* amplitudes $\lesssim 20\ mV$, the quantity $\frac{b}{ampl(mV)}$ is the dominating term in the noise introduced by the optical link channels.

	INNER VCSELs		**OUTER VCSELs**	
	1^{st} Gaussian	2^{nd} Gaussian	1^{st} Gaussian	2^{nd} Gaussian
a (no units)	0.82	1.39	0.98	2.11
b (mV)	16.17	41.03	25.74	66.74

Table 5.4: *Values of the parameters* a *and* b *which allow the function defined by the expression 5.4 to describe the dependence of* σ_i *on the input pulse amplitude. The values are shown for both the inner and the outer VCSELs.*

Summarizing, we can state that the smearing in the signal produced by the optical transmission can be parametrized by the function 5.3, where the normalized mean μ is fixed to 1, the constants C_1 and C_2 are given in table 5.3, and the normalized sigmas σ_1 and σ_2 are described by the expression 5.4, when using the constants a and b shown in table 5.4.

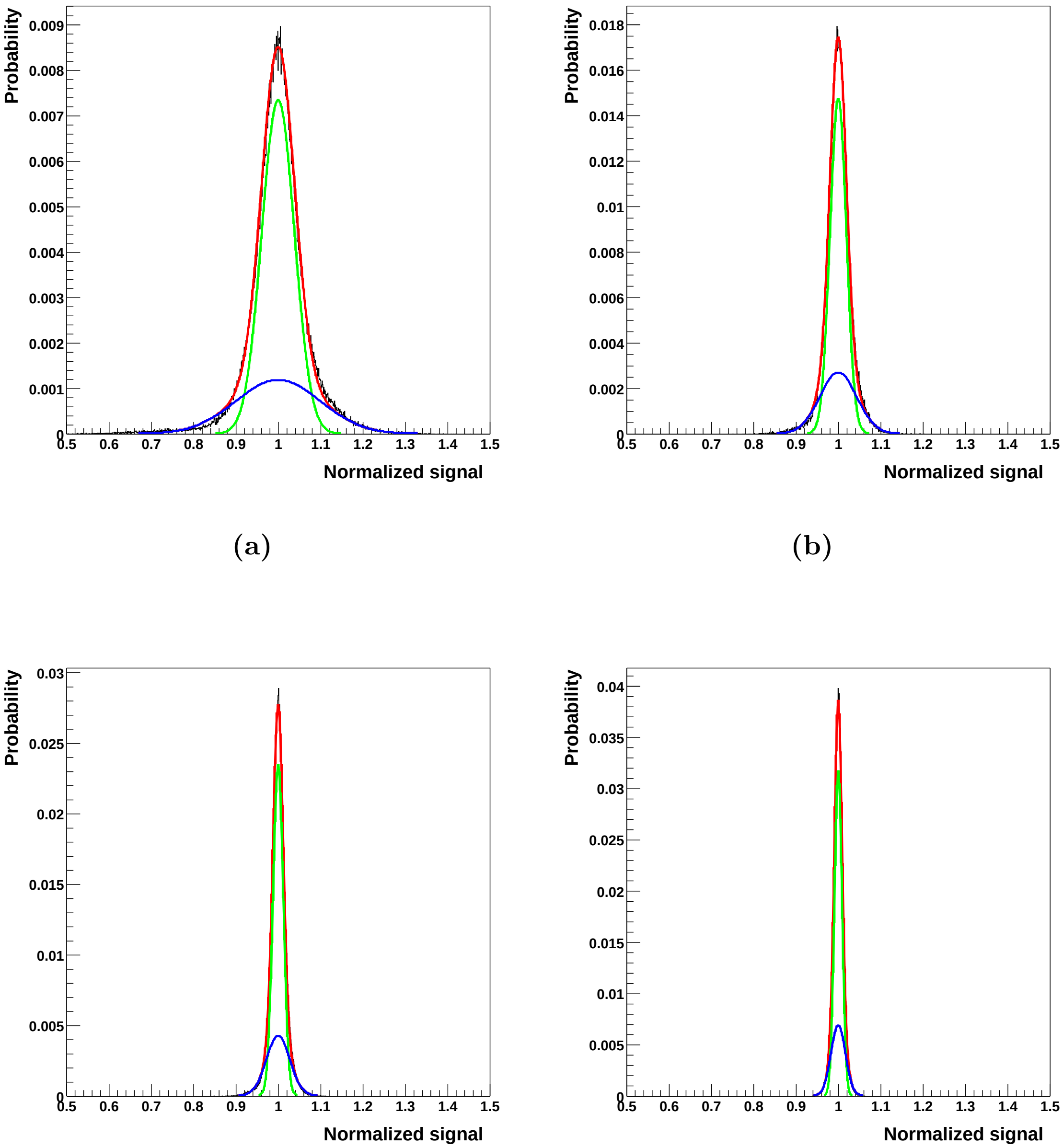

(a) **(b)**

(c) **(d)**

Figure 5.16: *Normalized output pulse area distribution (black) and probability distribution function (red) for INNER VCSELs at four different input pulse amplitudes: a) 4 mV; b) 10 mV; c) 20 mV; and d) 40 mV. The two normalized Gaussian functions (properly weighted) are also shown in green and blue.*

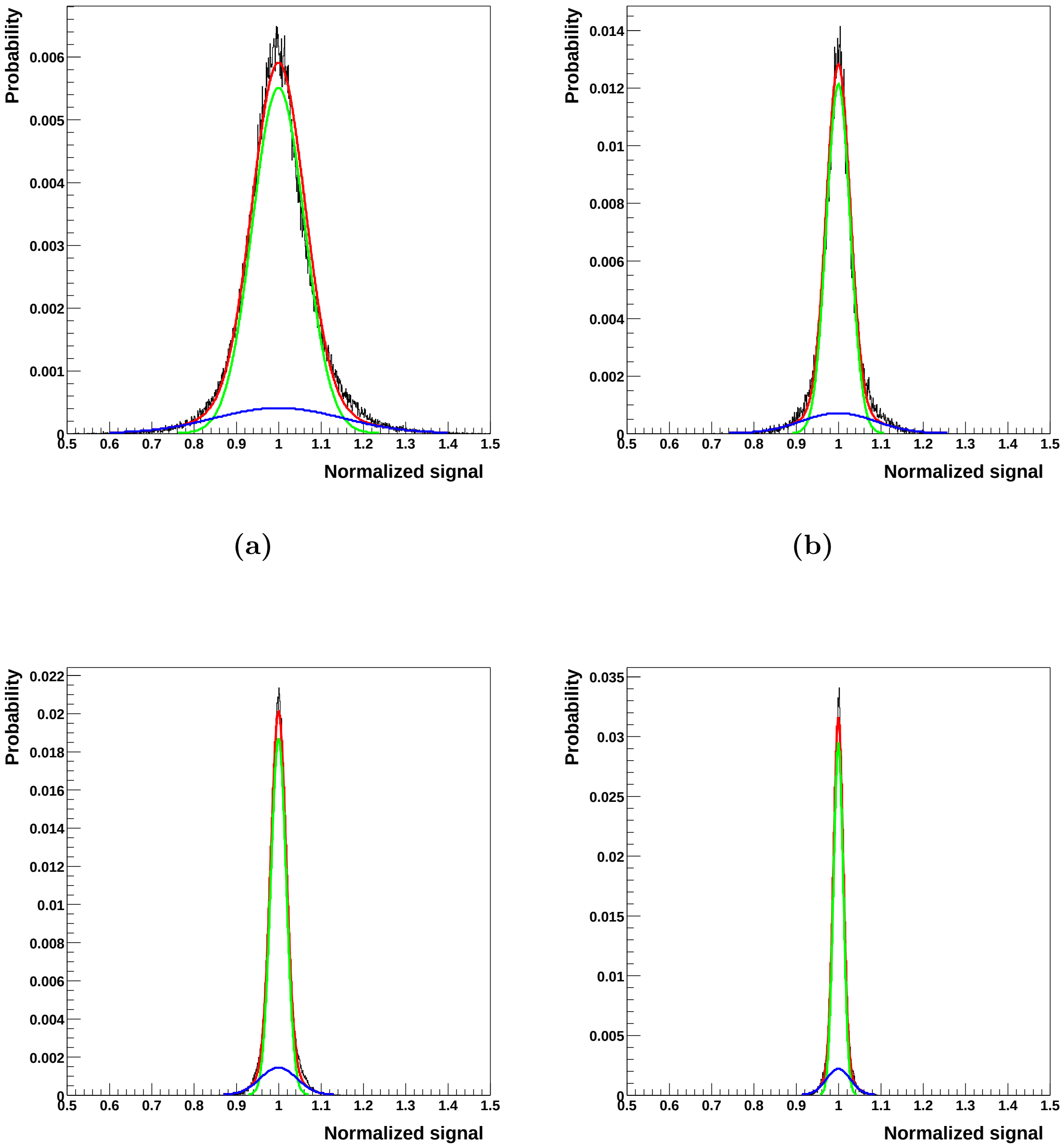

(a) (b)

(c) (d)

Figure 5.17: *Normalized output pulse area distribution (black) and probability distribution function (red) for OUTER VCSELs at four different input pulse amplitudes: a) 4 mV; b) 10 mV; c) 20 mV; and d) 40 mV. The two normalized Gaussian functions (properly weighted) are also shown in green and blue.*

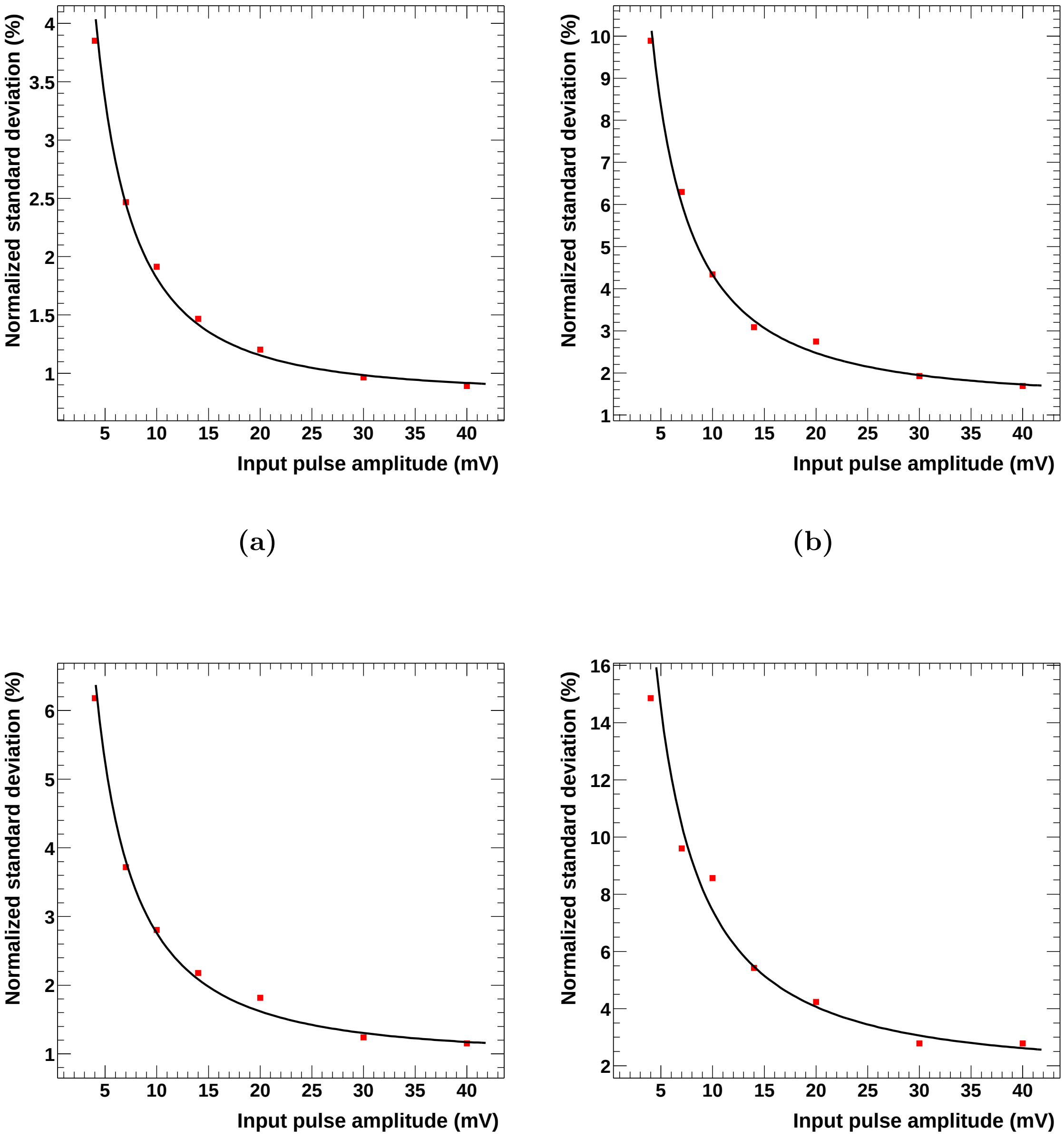

(a) (b)

(c) (d)

Figure 5.18: *Normalized sigma vs. the input pulse amplitude for a) the first Gaussian and b) the second Gaussian of the equation 5.3 for inner VCSELs; and c) the first Gaussian and d) the second Gaussian of the equation 5.3 for outer VCSELs. The red points are the* σ_i^j *values computed by the iterative fit described in the text, and the black line is a simple fit to these data using the equation 5.4.*

From the probability distribution function of the *output pulse* area described by the equation 5.3, one can compute an expression for the relative *RMS vs.* the amplitude of the *input pulse.* This is straight forward, since the probability distribution function is the sum of two normalized Gaussian functions:

$$RMS(\%) \;=\; \sqrt{C_1 \cdot \sigma_1^2 + C_2 \cdot \sigma_2^2} \tag{5.5}$$

Figure 5.19 shows this parametrization for both the inner and the outer VCSELs. The predicted relative *RMS* values at 10 mV *input pulse* amplitude for the inner and the outer VCSELs are 2.8% and 4.5% respectively. Note that these *RMS* values agree quite well with the "measured ones", which can be estimated from the mean of the two histograms showed in figure 5.13; 2.0% and 3.7% for the inner and the outer VCSELs respectively. The predicted *RMS* values are somewhat larger than the measured ones. This could be partially explained by the spread in the performance of this type of VCSEL. I want to point out that only 8 inner and 4 outer VCSELs were used for this study. Indeed, this study was performed before September 2002; hence none of the 12 used lasers[9] was from the group of VCSELs manufactured in September 2002, which are actually 43% of all accepted VCSELs and the ones with the best noise performance (see section 5.4). Therefore, this estimate of the relative *RMS* should be taken as a conservative parametrization at low amplitudes. At large amplitudes, the relative *RMS* decreases and the agreement between predicted and measured values improves, as one can see by comparing figures 5.19 and 5.14.

It is worth to transform the equation 5.4, which parametrizes the relative sigma, into an expression that describes the absolute sigma. This can be done by multiplying that equation by the area of the *output pulse.* By making the realistic approximation of considering that the used pulses have a Gaussian shape, the area (A) under the *output pulse* is given by the expression

$$A(mV\cdot ns) \;=\; G \cdot ampl(mV) \cdot \sqrt{2\pi} \cdot \frac{FWHM^{input\ pulse}(ns)}{2.35} \tag{5.6}$$

---

[9] We used 4 VCSELs manufactured in March 1999 (2 inner and 2 outer), and 8 VCSELs manufactured in October 2000 (6 inner and 2 outer).

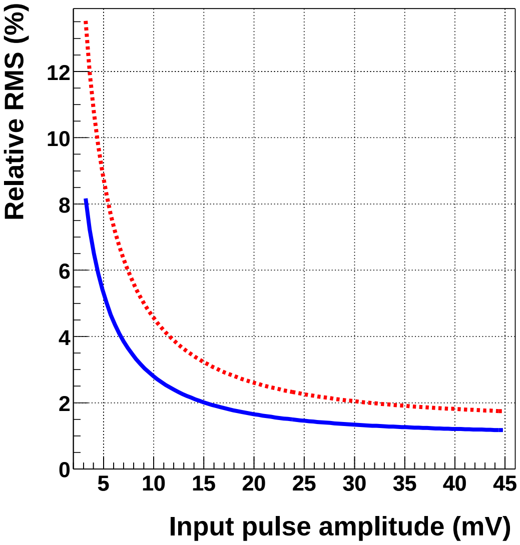

Figure 5.19: *Parametrization of the relative RMS vs. the amplitude of the input pulse for the inner VCSELs (continuous blue line) and the outer VCSELs (dashed red line).*

where *ampl* and $FWHM^{input\ pulse}$ are the amplitude and the FWHM of the *input pulse*, and G is the gain of the optical link system (which includes the amplification in the transmitter board). $FWHM^{input\ pulse}$ is ∼2.7 ns, and G is ∼3.3.

Combining the equations 5.4 and 5.6 one gets the following expression for the absolute sigma σ^{ABS}:

$$\sigma^{ABS}(mV \cdot ns) \sim 0.1(ns) \cdot \sqrt{(a \cdot ampl(mV))^2 + b^2} \ = \ \sqrt{(\sigma_{AC}^{ABS})^2 + \sigma_{DC}^{ABS})^2} \qquad (5.7)$$

Therefore, each of the 4 sigmas (1^{st} and 2^{nd} Gaussian functions for both inner and outer VCSELs), can be considered as the sum in quadrature of two terms; one that depends on the pulse that has to be transmitted (σ_{AC}^{ABS}) and the other one which does not depend on this pulse (σ_{DC}^{ABS}). This gives us important information about the fluctuations in the amount of light produced by the VCSELs and reaching the PIN-diodes at the receiver boards. The term σ_{AC}^{ABS} is related to the fluctuations in the amount of light reaching the receiver boards when the pulses (that have to be transmitted) modulate the forward current passing through the VCSELs. And the term σ_{DC}^{ABS} is related to the fluctuations in the amount of light reaching the receiver boards when there is no pulse modulating the bias current that circulates through the VCSELs.

According to the numbers shown in table 5.4, σ_{DC}^{ABS} is the leading term in the noise observed when the amplitude of the *input pulse* is $\lesssim 20\ mV$; which is actually the kind of PMT pulse that occurs more often in MAGIC. I want to point out that these numbers are only valid when the VCSELs are driven at bias currents close to 6 mA. At different bias currents the transverse modes which are activated/deactivated are different, and hence the terms σ_{AC}^{ABS} and σ_{DC}^{ABS} might be different.

5.5.3 The impact of the noise of the optical links on the trigger

The trigger signal for the DAQ is derived from the amplitude of the signal pulses at the receiver board (see section 3.3.3); and not from the charge of these pulses. In the previous sections I discussed in detail the impact of the noise introduced on the charge of the signals[10] and not on the amplitude. The two reasons for doing that were the following ones: *a)* the pulse area is the quantity related to the total number of detected photons in the PMT, which is ultimately the quantity in which we are interested in; and *b)* the fluctuations in the pulse area were larger than the ones in the pulse amplitude (see section 5.3). We adopted a quite conservative approach by using the pulse area (and not the pulse amplitude) for the characterization and selection of the VCSELs. I want to stress that the optical transfer of analogue signals using VCSEL drivers is, up to some extend, *terra incognita* and, on the other hand, the system plays a key role in the performance of the MAGIC Telescope.

Due to time reasons, I only carried out some preliminary studies in our laboratory for a few VCSELs, and performed a study at the MAGIC site for the 325 channels included in the trigger region of the camera of the telescope. The later study consisted in the measurement of the individual pixel rates at several discriminator thresholds for all 325 channels. During

---

[10] Actually, the quantity that I measured was the area of the pulses; which is directly proportional to the charge of these pulses.

this measurement, the camera was closed, the PMT HV was switched off, and the transmitter boards and the receiver boards were functioning normally. That means that the observed noise in the channels can only originate from the optical links and/or the transimpedance amplifier attached to the PMTs. As stated in section 3.3.2, the estimated output noise of this amplifier is $\sigma_{noise} \lesssim 0.2\ mV$ (see [67] for more details). Therefore, in first order approximation, we can neglect this noise and consider that the observed noise originates from the optical links.

I want to stress that one does not need to work with PMT signals in order to estimate the coarse effect of the optical link noise on the trigger, since (as stated in section 5.5.2) most of the noise introduced by the optical links is due to fluctuations in the VCSEL light output produced by the bias current.

Figure 5.20 shows the individual pixel rate as a function of the discriminator thresholds for 9 of the measured 325 channels. The discriminator thresholds are expressed in DAC counts (see section 3.4). The conversion between DAC counts and pulse amplitude at the input of the transmitter board (output of the PMTs) is $9\ DAC\ counts = 1\ mV$. Note the very fast increase in the rates when decreasing the discriminator thresholds; which is typical from electronic noise. Individual pixel rates above 10^7 *Hz* are not significant due to the saturation of the devices used to perform the measurement.

I computed the distribution of DAC counts at which the individual pixel rate is 1 *kHz* for the 325 channels measured. The resulting distribution is presented in figure 5.21. Note that the distribution is centered at a setting of 1.6 mV (= 14 DAC counts) with a *RMS* of 0.4 mV (3.4 DAC counts). That means that the individual pixel rate produced (purely) by the noise of the optical links is quite low provided the discriminator thresholds are above 2.5 mV (= 22 DAC counts).

The *standard PMT amplification* in MAGIC is such that 1 *phe* produces a signal of 2 *ns* FWHM and 1 mV amplitude at the output of the transimpedance amplifier (*i.e,* at the input of the VCSEL driver). The standard trigger discriminator threshold is set to 36 DAC counts, which is equivalent to 4 mV at the VCSEL driver input. This corresponds to a signal

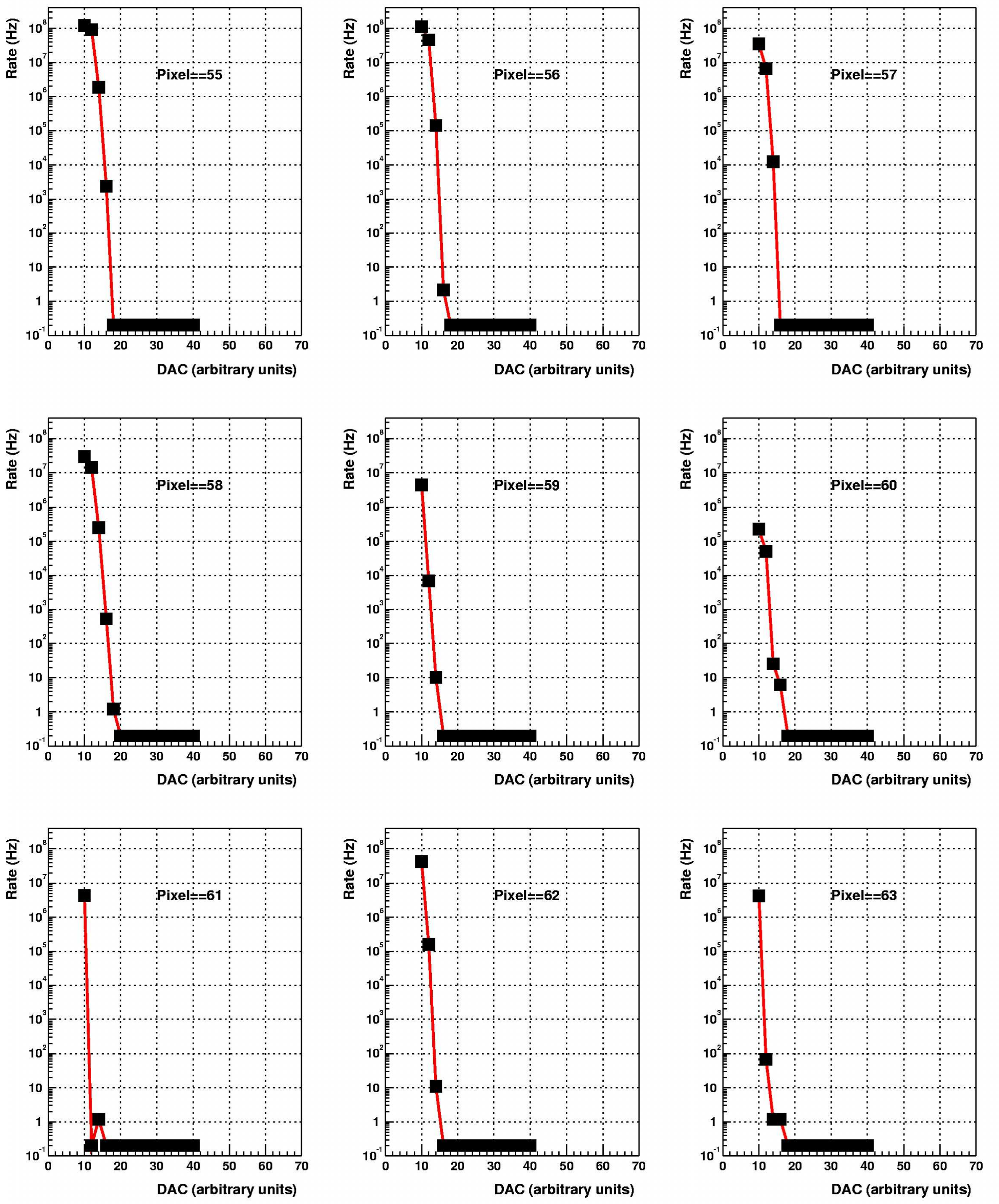

Figure 5.20: *Individual pixel rates vs. trigger setting (in DAC counts) for 9 channels. The camera is closed and the PMT HV is switched off.*

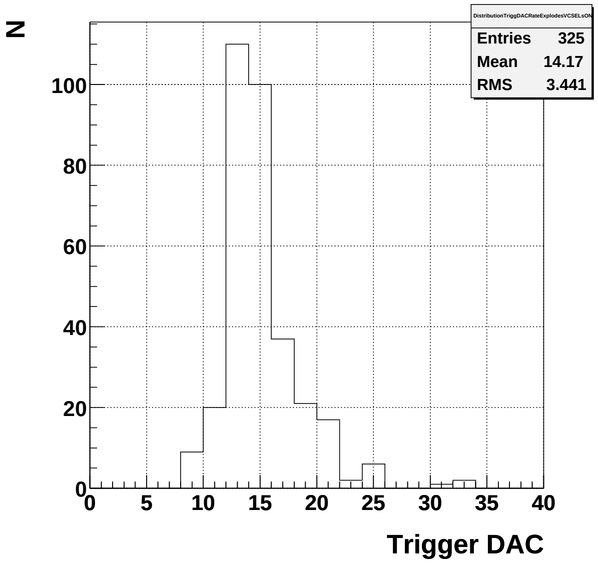

Figure 5.21: *Distribution of trigger thresholds (in DAC counts) for which the individual pixel rate is 1 kHz. The telescope camera is closed, and the PMT HV is switched off.*

of ~ 5 *phes*[11]. It is worth noticing that, for this trigger setting, the rate of accidental triggers produced in the individual pixels purely by the optical link noise is negligible. Besides, I want to point out that the individual pixel rate due to *LONS* photons, for a discriminator threshold of 36 DAC counts ($\sim$5 *phes*), is already about 500 *kHz* (see section 4.6.2).

The noise originated from the optical links can add to the low signals produced by *LONS* photons and Cherenkov flashes from air showers and increase/decrease them such that they are above/below the discriminator threshold. Therefore, in order to perform a detailed evaluation of the impact of the noise of the optical links on the trigger, one needs to test the system with pulses whose amplitude is slightly below/above the discriminator threshold. Studies on this issue are ongoing.

Finally, I would like to point out that the fluctuations produced in the light output of

---

[11] The mean amplitude of a signal produced by 4 *phes* is lower than 4 mV because, in general, the 4 *phes* do not arrive simultaneously to the first dynode of the PMT. Therefore at least 5 *phes* (in average) are required to trigger the telescope.

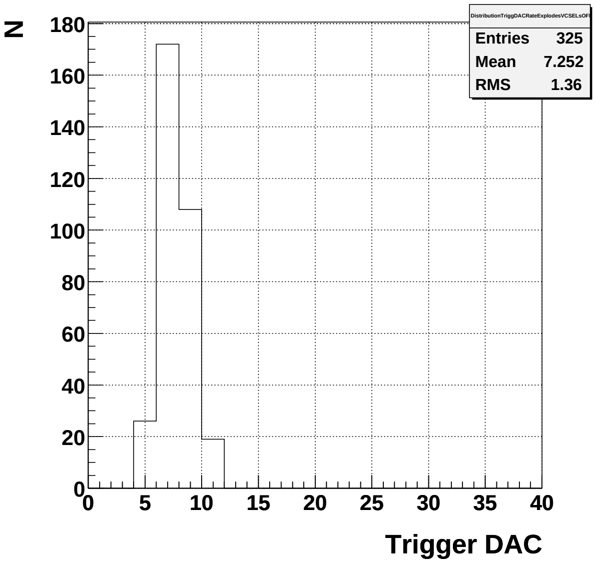

Figure 5.22: *Distribution of trigger thresholds (in DAC counts) for which the individual pixel rate is 1 kHz. The VCSEL drivers are switched off.*

the VCSELs are not the only reason for the previously mentioned individual pixel rates; the receiver electronics is also partially responsible. When performing the same type of measurement, keeping the VCSEL drivers switched off, we obtained the distribution of trigger thresholds (for which the individual pixel rate is 1 *kHz*) presented in figure 5.22.

5.5.4 Linearity of the optical link system

A linearity test was carried out with 8 VCSELs. The correlation between VCSEL driver input and receiver output for one of these channels is shown in figure 5.23. The used *input pulses* had a 2.7 *ns* FWHM and areas ranging from 0.005 $nV \cdot s$ to 3.2 $nV \cdot s$ (amplitudes ranging from 1.5 mV to 940 mV).

The response deviates from a perfect linear behavior by less than 10% in a range of about 56 dB. We found that the amplification of the signal slightly decreases at *input pulse* areas above 0.32 $nV \cdot s$ (*i.e, input pulse* amplitudes above 110 mV). This effect is shown in figure 5.23; points in the area range 0.08-0.32 $nV \cdot s$ (25-110 mV) are above the linear fit whereas points above 1.5 $nV \cdot s$ ($\gtrsim$ 500 mV) are slightly below. This behavior was found in the 8

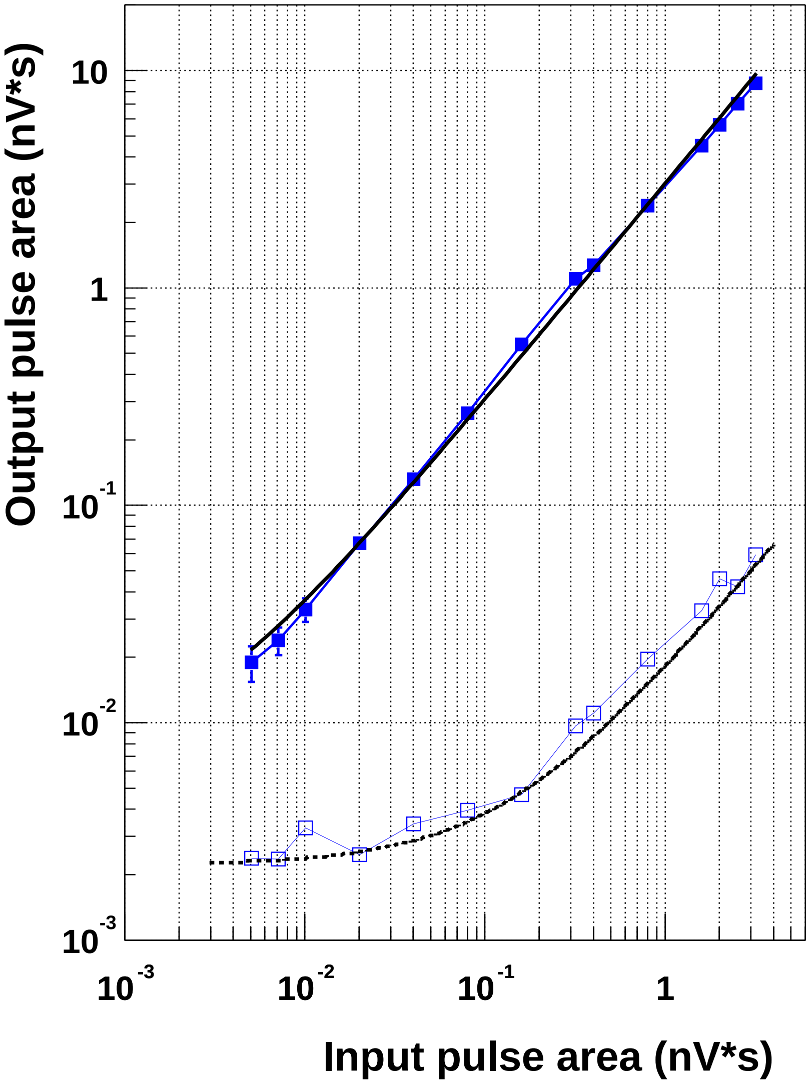

Figure 5.23: *Output signal vs. input signal in the optical links. Filled squares are used for the measured area of the output pulse, the dark continuous line is a simple linear fit. The lowest and the highest point of the plot corresponds to an input pulse of 2.7 ns FWHM and 1.5 mV and 940 mV amplitude respectively. Empty squares are used for the measured RMS. The parametrization of the RMS described by equation 5.5 is shown by a dotted line.*

tested VCSELs.

The linearity studies were performed at three different bias currents; namely 5 mA, 6 mA and 7 mA. We did not find any significant improvement in the linearity when increasing the bias current[12].

I want to point out that the linearity of the system is indeed not limited by the transmitter board, but by the receiver board, which starts to saturate at *output pulse* amplitudes of about 2.5 V (which corresponds to an *input pulse* amplitude of about 0.8 V). This saturation effect is less significant in the area of the *output pulse*. An *input pulse* of 1 V amplitude produces deviations from the linearity (in the measured *output pulse* area) smaller than 15%. It is worth to mention that linearity deviations of even larger signals can be corrected by means of a proper calibration. Measurements of the dynamic range for the complete pixel chain in MAGIC show a total dynamic range larger than 62 dB [75].

Figure 5.23 also shows the measured RMS noise *vs.* the input signal, together with the RMS noise function described by the expression 5.5. Note that the observed RMS is well below the measured signal, and in addition, it is in good agreement with the parametrization of the RMS noise obtained in the study reported in section 5.5.2.

5.6 Conclusion

At the Max-Planck-Institut für Physik München, we have developed and built an optical system that can be used reliably to transmit short pulses ($\lesssim 3$ ns FWHM) over long distances (> 100 m). The attenuation and distortion of the transmitted signals are small, and the noise of the system is understood and reduced to fulfill the requirements of the MAGIC Telescope. The system is already installed and fully operational in the telescope.

Besides, we would like to point out that there is a steady progress in the VCSEL performance which might allow one to further improve this kind of analogue signal transmission systems:

---

[12] We observed that, when increasing the bias current, the linearity improved slightly in 3 of the VCSELs (lower reduced chi square), did not change significantly in 3 of them, and became slightly worse in the other 2.

- The performance of the multimode VCSELs is improving, as was reported in section 5.4.3.
- Many VCSELs are now manufactured with a monitor diode that can be used to stabilize the light yield by correcting the bias current. This new feature needs some tests, but it is very promising since it could reduce significantly the temperature sensitivity of the system.
- Currently, VCSELs can also be produced in array arrangements, which minimizes the amount of individual cables. This requires strip cables and specific connectors of high precision. The strip cables are already available in the market, but the connectors are still a problem. It should be noted that the connectors for analogue signal transmissions need tighter tolerances than those for digital applications.
- The production of new VCSELs with a lower lasing threshold ($\lesssim 1.5\ mA$) is becoming a reality, as well as the production of VCSELs emitting in the infrared range 1.3-1.5 μm, which reduces the light absorption inside the optical fibers.
- VCSELs with a single transverse mode (single mode VCSELs) and high bandwidth ($\sim 1\ GHz$) are now available in the market. Single mode VCSELs require less electrical power, have a smaller light beam divergence and are free from mode “hopping” related problems.

Currently, the MAGIC Telescope is the only working experiment using an optical system based on VCSEL drivers to transmit short analogue signals. However, due to the very many advantages of these systems with respect to conventional coaxial cables to transmit analogue signals over long distances (see sections 3.3.3 and 5.1), and the steady improvement in the performance of the VCSELs, we think that more and more experiments will make use of this novel technique in the future.

Chapter 6

The first γ signals obtained with the MAGIC Telescope

In this chapter I will report about the first significant detections of γ sources obtained with the MAGIC Telescope. The sources observed were Markarian 421 (Mkn 421) and the Crab Nebula. The telescope was in the commissioning phase, and these observations were made in between technical runs.

The Crab Nebula is a plerionic type *supernova remnant* located at a distance of 2 *kpc*. The Crab was the first clear detection in the very high energy gamma domain ($\gtrsim 500\ GeV$) [22]. Due to the fact that the Crab has an apparently high luminosity steady γ emission, it has been the most extensively studied $\gamma - ray$ source with $IACTs$. The purpose of these observations was to refine the methods of observation in this new field, but also to determine the energy spectrum of the radiation. This object has an extraordinary broad spectrum extending from radiowaves to $\sim 10^{14}\ TeV$. The emission in the range 1-100 MeV is attributed to synchrotron radiation from high energy (up to PeV) electrons apparently injected outside the cavity dominated by the pulsar wind. This continuous (synchrotron) spectrum appears to terminate near 0.1 GeV, and the detected GeV to almost 100 TeV $\gamma - rays$ seem to be be generated by *Synchrotron-Self-Compton* emission mechanisms[1]. However, hadronic acceleration and

---

[1] *Synchrotron-Self-Compton* emission is a particular case of *Inverse Compton* emission (see chapter 1), in

γ production from π^0 decays is still not ruled out. The most recent publications concerning the steady emission from the Crab Nebula can be found elsewhere [4, 27, 28].

Mkn 421 is a *BL Lac* object located at a *red shift* $z = 0.031$. It was the first extragalactic source detected in the very high energy range ($E \gtrsim 500\ GeV$) [94]. In contrast to the Crab, this source exhibits strong $\gamma - ray$ outbursts. The last (well documented) one was observed at the first months of 2001, with an average integral flux above 1 TeV of 1.5 times the flux from the Crab Nebula. Mkn 421 shows time variability on a sub-hour time scale at TeV energies, with peak emissions of almost an order of magnitude larger than the steady emission of the Crab. The observed TeV $\gamma - ray$ emission is quite correlated with the *X-ray* synchrotron radiation; which suggests emission mechanisms based on electronic acceleration. However, the results are still not conclusive. Additional information about detections and time variability studies on Mkn 421 in the very high energy domain can be found elsewhere [95, 96, 97]. In February 2004, the WHIPPLE collaboration found Mkn 421 again in flaring state. This was also a reason to observe it with MAGIC.

The purpose of the analysis shown here is to evaluate the initial performance status of the telescope, as well as to demonstrate that significant γ signals could be extracted from the first data taken with the MAGIC Telescope. Besides, these observations allowed us to test the analysis software with experimental data from MAGIC for the first time.

I want to stress that any astrophysics study is beyond the scope of this work. A full physics analysis requires a detailed understanding of the detector and a careful tuning of the simulation programs, as I discussed in section 2.3.5. Work in these directions is still in progress, and it will take at least another half year.

The chapter is divided into 3 sections. In the first section I will describe the "standard" methods which use the Hillas parameters to distinguish γ-induced showers from the *background*. I will use the Monte Carlo simulation chain of MAGIC to illustrate the effect of these techniques in the particular case of the MAGIC Telescope. In the second section I will report about the functionalities of a code that I developed for the analysis of MAGIC data. The analysis is based on the Hillas parameters to describe the characteristics of the shower

---

which the seed photons are the ones radiated by the electrons themselves through *Synchroton emission*.

images. The last section is devoted to the analysis performed on the first observations taken with MAGIC.

6.1 Standard analysis using the Hillas parameters

As stated in section 2.3.1, the pictures formed in the pixelized camera of an *IACT* contain information about the shower development, and hence can be used to estimate the energy, the direction and the type of primary particle. This method is usually called *Imaging Technique.*

The analysis I did on the first data taken with the MAGIC Telescope is based on the classical Hillas parameters [1, 22, 98] as image parameters to describe the light distribution of the shower images.

In this section, I will introduce some of these parameters and I will show how one can use them to distinguish γ-induced showers from *background*-induced showers. For simplicity, I will only define the image parameters that I will use in the analysis of the first signals taken with MAGIC. The definition of the complete set of image parameters can be found in [99].

6.1.1 Definition of the Hillas parameters

The Hillas parameters are grouped into three classes; namely image parameters that depend on *a)* the shape and light content of the shower, *b)* a reference direction, *c)* and a reference point. The image parameters are depicted in figure 6.1, and are defined as follows:

- *Shape parameters*
    - SIZE; the total number of photons in the shower image.
    - LENGTH; the *RMS* value of the light distribution along the main axis of the shower image.
    - WIDTH; the *RMS* value of the light distribution along the minor axis of the shower image.

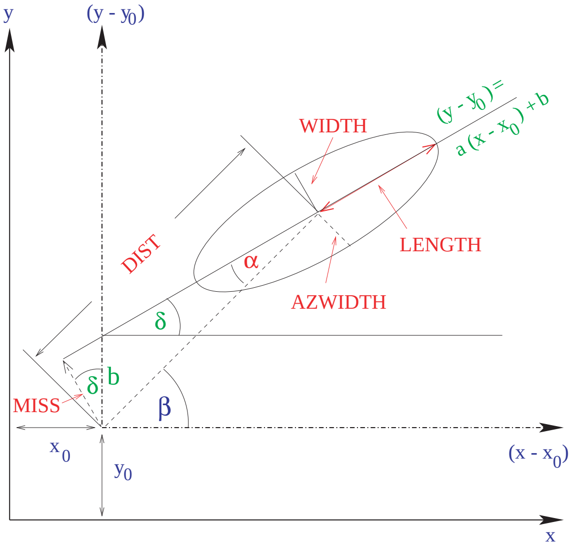

Figure 6.1: *Definition of the Hillas parameters.* (x, y) *are the coordinates in the original camera system and* (x_0, y_0) *are the coordinates of a reference point, like the source position or the center of the camera. Figure taken from [99].*

- *Parameters that depend on a reference direction*
    - DELTA; the angle δ between the shower axis and the x-axis of the camera.
- *Parameters that depend on a reference point*
    - DIST; the distance between the reference point (RF) and the center of gravity (COG) of the shower image.
    - ALPHA; the angle between the shower axis and the line connecting the COG of the shower image with the RF.

The shape parameters LENGTH and WIDTH are basically the Cherenkov light projections (onto the telescope camera) of the geometrical length and width of the EAS, and the parameter SIZE is directly related to the total amount of Cherenkov light produced in the EAS. This amount of light is proportional to the total amount of electrons in the shower (as explained in section 2.2.3), which in turn, is proportional to the energy of the primary particle (see section 2.1.1). Hence the SIZE parameter can be used to estimate the energy of the primary particle[2].

The DIST parameter is roughly the angle between the optical telescope axis and the line connecting the telescope with the shower maximum. For parallel air showers of the same energy, the DIST parameter relates to the *impact parameter* of the shower. The latter is defined as the distance from the telescope location to the point where the shower axis intersects the plane perpendicular to the telescope axis.

The ALPHA parameter is related to the angle between two planes: the plane formed by the telescope axis and the COG of the shower, and the plane formed by the shower axis and the reflector center. ALPHA is close to zero if the two planes coincide, *i.e,* if the telescope axis and the shower axis lie within one plane. This is the particular case when the direction of the primary particle is parallel to the telescope axis.

The image parameters are influenced by the limited Cherenkov angle, the statistical fluctuations in the shower development [15], and (specially at $\gamma - ray$ energies below 100 GeV and observations at zenith angles $\gtrsim 30^\circ$) the Earth magnetic field [17]. The typical distributions of LENGTH, WIDTH, DIST and ALPHA for gamma-induced showers and hadron-induced showers are discussed in section 6.1.4

6.1.2 Calculation of the Hillas parameters

In this section I list the basic formulas used to compute the Hillas parameters. The complete list of the formulas, as well as a detailed explanation of the derivation of these formulas can be found in [99].

I want to point out that, in general, the Hillas parameters are not calculated from the raw events, but from events after pixel calibration and application of some image cleaning procedures. The calibration provides the pixel light content in number of *photons*, and ensures equal response for the different pixels; and the image cleaning procedures remove partly the effect of the $LONS$ and noisy pixels (see section 6.3.2 for details).

---

[2] The estimation of the energy (of the primary particle) improves when using, in addition to the SIZE, the DIST parameter (which is related to the impact parameter of the shower) and the zenith angle of observation.

- *Notation*

(x_i, y_i); coordinates of the pixel i in the original camera system.

(x_0, y_0); reference point in the camera (usually defined by the source position).

N_i; number of photons measured in the pixel i.

w_i; weight for the pixel i.

- *Definition of the moments of the signal distribution in the camera*

$$\begin{aligned}
w_i &= \frac{N_i}{\sum_k N_k} \\
\overline{x} &= \sum_i w_i \cdot x_i \\
\overline{y} &= \sum_i w_i \cdot y_i \\
\overline{x^2} &= \sum_i w_i \cdot x_i^2 \\
\overline{y^2} &= \sum_i w_i \cdot y_i^2 \\
\overline{xy} &= \sum_i w_i \cdot x_i \cdot y_i
\end{aligned} \tag{6.1}$$

- *Definition of the correlations in the signal distribution in the camera*

$$\begin{aligned}
c_{xx} &= \overline{(x-\overline{x})^2} = \overline{x^2} - \overline{x}^2 \\
c_{yy} &= \overline{(y-\overline{y})^2} = \overline{y^2} - \overline{y}^2 \\
c_{xy} &= \overline{(x-\overline{x}) \cdot (y-\overline{y})} = \overline{x \cdot y} - \overline{x} \cdot \overline{y}
\end{aligned} \tag{6.2}$$

- *Definition of the Hillas parameters*

$$\begin{aligned}
\mathbf{SIZE} &= \sum_k N_k \\
\mathbf{LENGTH} &= \sqrt{\frac{c_{xx} + 2a \cdot c_{xy} + a^2 \cdot c_{yy}}{1+a^2}} \\
\mathbf{WIDTH} &= \sqrt{\frac{a^2 \cdot c_{xx} - 2a \cdot c_{xy} + c_{yy}}{1+a^2}} \\
\mathbf{DIST} &= \sqrt{(\overline{x}-x_0)^2 + (\overline{y}-y_0)^2} \\
\mathbf{ALPHA} &= arcsin\Big(\frac{|b|}{DIST \cdot \sqrt{1+a^2}}\Big) \qquad (0^\circ \leq ALPHA \leq 90^\circ)
\end{aligned} \tag{6.3}$$

In the formulas of the Hillas parameters I used the variables a and b, which define the straight line ($y - y_0 \;=\; a[x - x_0] + b$) used to describe the orientation of the shower image in the camera of the telescope (see figure 6.1). The quantities a and b are given by the following expressions

$$\begin{aligned} a &= tan\delta = \frac{c_{yy} - c_{xx} + \sqrt{(c_{yy} - c_{xx})^2 + 4c_{xy}^2}}{2c_{xy}} \\ b &= \overline{y} - y_0 - a \cdot (\overline{x} - x_0) \end{aligned} \tag{6.4}$$

6.1.3 The separation of the γ showers from the background

In the analysis of the air showers recorded by an *IACT*, the separation between *signal*-induced showers and *hadron*-induced showers is one of the most difficult and important tasks to be performed. As stated in section 2.3.3, the images of the $\gamma - rays$ coming from the observed astrophysical source must be distinguished from the images produced by cosmic hadrons (mainly protons, but also nuclei of helium and of higher elements), electrons and the images produced by the Cherenkov light emitted by isolated muons which are produced in hadron-induced showers through $\pi^{\pm}$ and $K^{\pm}$ decays (see section 2.1.2).

Due to the fact that the number of cosmic hadrons (at a given time and energy) is about 10^4 times larger than the expected amount of γ-rays coming from a typical γ-ray point source[3], the hadron-induced showers are, by far, the most important background to be considered in an *IACT*. The muon background produces a telescope trigger rate 5 times smaller than that of hadrons [36], and the cosmic electron background is only important when analyzing very low energy showers ($\lesssim 50\ GeV$) and in observations of extended sources.

In the following subsections I will describe first the *signal/background* separation on the basis of the shape and the position of the shower image in the telescope camera; and then the *signal/background* separation achieved by using the orientation of the image in the telescope

---

[3] This is true for the Crab Nebula (above 300 GeV), which is considered to be the standard candle for *IACTs* located in the northern hemisphere. So far, the largest γ-ray fluxes detected with *IACTs* were observed for the *AGN*s Mkn 421 and Mkn 501 when they were in a flaring state. The mean γ-ray fluxes measured above 1 TeV were only about 2-3 times the flux of the Crab Nebula. Yet the peak fluxes could be one order of magnitude larger than the one of the Crab [100, 97].

camera. As discussed in section 2.3.3, the former *signal/background* separation only rejects cosmic hadrons and muons whereas the later can be applied to all backgrounds.

I want to point out that there are other techniques which exploit the physical differences between γ and hadron induced air showers, and which can be used, in addition to the image parameters, to enhance the γ/h separation power. In my opinion, the most promising ones, are the consideration of "empty" regions in the shower images (the so-called "island analysis") [38, 101], and the use of the arrival times of the Cherenkov photons at the pixels contained in a shower image [102]. These techniques are still quite novel, and not fully developed; so far none of them have been applied to real data, but only to Monte Carlo simulations. Therefore, they will not be considered in the analysis presented in this thesis.

Separation based on the shape and position of the shower image

Images produced by hadron-induced showers are, in general, longer, wider, and do have more irregularities ("empty" regions in between the image), than those produced by $\gamma - rays$. The physical reason for this difference is the larger longitudinal and lateral particle distribution in hadron-induced air showers, together with the fact that the Cherenkov light originated in a hadron shower comes mainly from the secondary electromagnetic showers induced by gammas from the π^0 decays (see section 2.1.2). That means that the shape parameters LENGTH and WIDTH can be used to distinguish (up to some extent) between hadrons and gammas. This will be shown in figure 6.4 for Monte Carlo data.

Besides, the image parameter DIST is commonly used to reject those images that cannot be well reconstructed (hence not being appropriate for an efficient γ/h separation) or cannot originate from the source location. The DIST parameter is very much correlated to the impact parameter of the gamma showers (see figure 6.5); and it is used to reject those showers developing either very close or very far away from the telescope axis.

Shower images with DIST values $\lesssim 0.4\text{-}0.5^\circ$ are mostly produced by the Cherenkov light emitted by the strongly scattered electrons in the shower tail, and thus, large fluctuations are expected in the images produced by similar air showers (similar energy, zenith angle and identical primary particle type) in the telescope camera. Besides, the lateral distribution of the Cherenkov light at ground peaks at very small impact parameters for *EAS* induced by cosmic hadrons (see figure 2.5b). That means that the probability for a hadron shower to trigger the telescope is maximum at very low impact parameters. Therefore, by rejecting shower images with low impact parameters ($\lesssim 50\ m$), one removes most of the hadrons images and only few gamma images. Unfortunately, the correlation of the DIST parameter with the impact parameter is quite poor for hadron showers (see figure 6.5); low DIST values do not correspond (necessarily) to low impact parameters.

The large reflector area and the high sensitivity and fine pixelized camera of the MAGIC Telescope allow showers with impact parameters outside the dominant *Cherenkov light pool* (120-130 m radius) to produce images that have a light content and a number of illuminated pixels large enough to be properly analyzed. Despite of the lower trigger probability and somewhat worse image reconstruction of showers with large impact parameters, they are quite numerous; and hence they contribute significantly to the sample of detected $\gamma - rays$. Therefore, it is worth accepting images with large DIST values. In the analysis presented in section 6.3, I select images with DIST values of up to 1.4° for SIZE values larger than 10^4 photons. By applying to the Monte Carlo sample described in section 6.1.4 the selection cuts optimized on real data from Mkn 421 (see section 6.3.5), I found that half of the gamma events surviving the selection cuts have an impact parameter larger than 125 m. This number should be taken as a rough value only. At this early stage of the experiment, there are still some differences between the Monte Carlo simulated data and the experimental data (see section 6.3.1 and appendix E).

As to the muons, the relevant quantities used to reject them are LENGTH/SIZE and WIDTH, since images produced by isolated muons have a quite characteristic brightness (that depends on the impact parameter of the muon) and a very small WIDTH in the fine pixelized camera of MAGIC (typically WIDTH $\lesssim 0.05°$). Preliminary results show that by exploiting these features one can achieve a muon rejection factor of about 100. A detailed analysis on this topic can be found elsewhere [37, 38].

From now on, the set of cuts based on the shape and position of the shower image in the telescope camera will be denoted *γ/h separation cuts*.

Separation based on the orientation of the shower image

As discussed in section 2.3.3, all backgrounds can be reduced substantially by exploiting the fact that the γ-rays we want to detect come always from a given direction (the direction where the cosmic point source is located), whereas all backgrounds are isotropically distributed[4]. For the shower images, this means that the γ-showers point to the position (x_0, y_0) of the source whereas the showers from the background are randomly oriented in the camera. In terms of the image parameter ALPHA this is expressed by a peak around ALPHA $= 0°$ for the γ-showers and a uniform ALPHA distribution for the background showers.

Due to the fact that ALPHA is not correlated with any of the other parameters, it is quite common to produce an ALPHA distribution (the so-called *alpha plot*) with all the events surviving the *γ/h separation cuts*; and then, the cut in the ALPHA parameter is chosen based on the shape of this distribution.

In this thesis ALPHA is defined in the range 0-90°. The γ-rays coming from the cosmic (point) sources tend to accumulate close to ALPHA $= 0°$; in a region that might extend up to 10°-30° depending on the energy of the primaries (see section 6.1.4). By cutting in the ALPHA parameter, one increases the rejection power (achieved by using the other image parameters) by a factor 3-9, depending on the threshold energy. As I will show in section 6.1.4, the hadron rejection by cutting in ALPHA can be increased further if one can afford a reduction in the acceptance of the gamma signal.

From now on, the region of small ALPHA values containing almost all γ-induced showers will be called *signal region* (of the *alpha plot*); and the region of large ALPHA values, which contains mostly *background*-induced showers, will be denoted *background region* (of the *alpha plot*). The boundaries of the *signal region* and the *background region* depend on the energy range under consideration, as will be shown in figure 6.8.

---

[4] Cosmic electrons below 30 GeV are significantly deflected by the Earth magnetic field, and hence they are no longer isotropically distributed [34].

6.1.4 Hillas parameters for simulated γ/h induced air showers

In this section, I will use the output of the standard MAGIC simulation programs to show the typical shapes (Hillas parameters values) of the images produced by cosmic *hadrons* and $\gamma - rays$ in the telescope camera.

The simulated showers that I will use in this section were produced by Abelardo Moralejo. The program CORSIKA 6.019 was used to simulate the development of the atmospheric shower; the propagation of the Cherenkov photons in the atmosphere and their reflection at the telescope mirror was simulated with the program Reflector 0.6; and finally the program Camera 0.6 was used to simulate the detection of the Cherenkov light by the camera of the MAGIC Telescope. Details about CORSIKA 6.019 and the MAGIC simulation programs can be found elsewhere [12, 44, 45, 46, 47].

The Monte Carlo data sample is formed by 5.2 million gammas, 28.5 million protons and 15.3 million helium nuclei. The gammas were simulated in the energy range from 10 GeV to 30 TeV with an energy distribution that follows a power law spectrum with a spectral index of -2.6. The hadrons were simulated in the energy range from 30 GeV to 30 TeV with a spectral index of -2.75 and -2.62 for protons and helium nuclei, respectively. All showers were simulated in the zenith angle (ZA) range 0-30°[5], and at two azimuthal angles (ϕ) 0° and 90°, which correspond to showers coming from the South and from the East, respectively. The shower simulation at two perpendicular azimuthal angles is particularly important at low energies ($\lesssim$ 100 GeV) and large zenith angles ($ZA \gtrsim 30°$), where the effect of the Earth magnetic field on the shower development is quite sizeable [17, 16]. The showers were simulated with impact parameters distributed uniformly in the circle defined by a radius (with respect to the telescope axis) of 300 m for gammas and 400 m for hadrons.

In the Monte Carlo simulations, the MAGIC Telescope trigger was set to the *standard* one; coincidences of four "closed-packed" pixels whose signals' amplitude are above 4 mV (see section 3.4). The image cleaning applied to the Monte Carlo data was the one defined in section 6.3.2; with a minimum required number of six *core pixel*s per image. Besides, in

---

[5] The hadrons were simulated in 5° semiaperture cones, centered at values of $cosZA$ = 1.00, 0.99, 0.98... ($\Delta(cosZA) = 0.01$), while for the gammas ZA was varied in a continuous way.

order to get rid of images which could be truncated by the camera dimensions, I also removed all events whose light content in the outer most ring of the camera was larger than 25% of the total light content (SIZE) of the image.

The sample of events that survived the simulated telescope trigger and the image cleaning procedures consists of 237552 gammas, 27215 protons and 6611 helium nuclei. This corresponds to 4.6%, 0.095% and 0.043% of the total number of simulated gammas, protons and alpha particles respectively.

Further details about the Monte Carlo production can be found in [36].

Dependence of the parameter SIZE on the energy of the primaries

The first thing I want to discuss is the dependence of the measured SIZE of the shower image on the energy of the primary particle. This is shown in figure 6.2 for simulated gammas, protons and helium nuclei. As it was already mentioned in section 2.3.3, at a given energy, γs produce more Cherenkov light than hadrons. This general feature of the shower development translates into larger light contents for gamma images than for hadron images in the telescope camera.

In addition, it is worth mentioning two interesting features that one can infer from figure 6.2:

- *1)* Protons below ~300 GeV and helium nuclei below ~600 GeV have a lower probability to trigger (compared to higher energy events), and most of the triggers originate from showers that (because of statistical fluctuations) have a larger (than the mean) light yield in the camera. This effect is visible in figure 6.2, where the slopes of the profile histograms of protons and helium nuclei change significantly as the energy decreases. Note also that[6] the smallest (mean) SIZE of the hadrons that trigger is about

---

[6] I neglect the 102 helium events below 100 GeV; they are too few to be considered as a significant sample. The amount of proton events below 100 GeV is 6086, and the amount of gamma events below 30 GeV is 58455. It must be pointed out that, at very low energies, the image cleaning is decisive in the rejection/acceptance of events. The image cleaning procedures used to compute figure 6.2 are the same as those applied to the experimental data (see section 6.3.2).

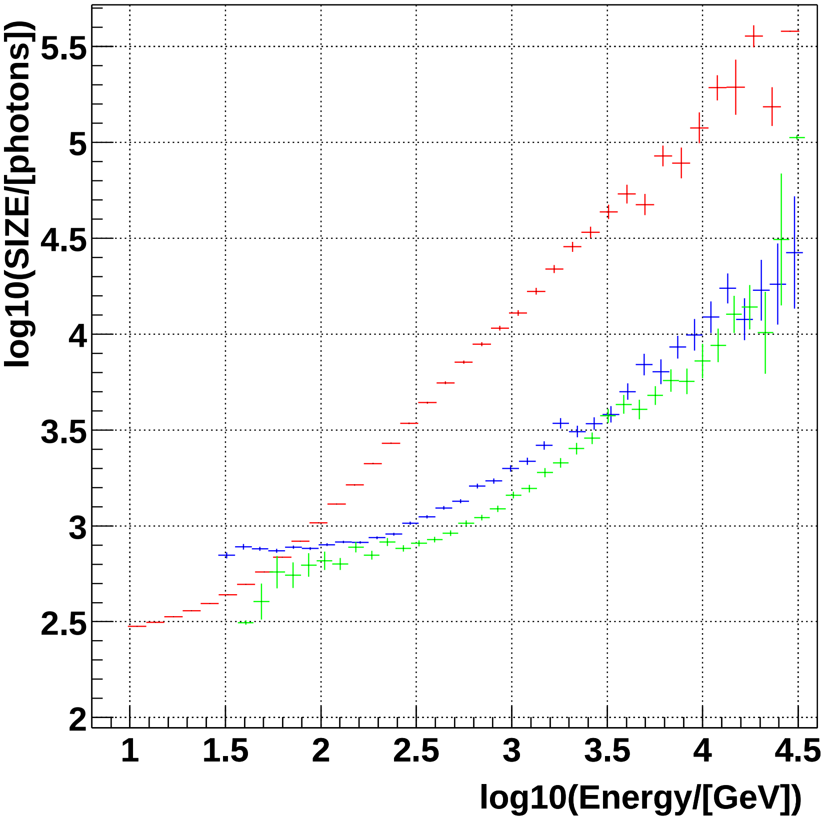

Figure 6.2: *Dependence of the Hillas parameter SIZE on the energy of the simulated primary particle for gammas (red), protons (blue) and helium nuclei (green) after passing the trigger of the telescope and the image cleaning procedures. The points show the mean of the SIZE distribution for each bin of log(energy), and the vertical error bars show the error of the mean.*

700 photons, whereas it is about 350 photons for gammas.

The significantly larger (mean) SIZE of proton showers compared to that of gamma showers at very low energies ($\lesssim 60\ GeV$) is explained by the contribution of "isolated" muons. Figure 6.3 shows the dependence of the SIZE of the shower image on the energy of the primary protons separately for images with a relative light contribution due to muons below 90%, and above 90% (the so-called "isolated" muons). The dependence of the SIZE on the energy for gamma showers has been also included in this figure for comparison purposes. Note that the mean SIZE of the images produced by the "isolated" muons is about 1000 photons for proton shower energies between 30 GeV and 300 GeV. This is expected from the fact that the amount of Cherenkov photons detected from a single muon does not depend on the energy of the muon[7], but only on the length of the muon track observed. It is worth mentioning that at energies below 100 GeV, from the 6086 proton showers that triggered the telescope, 2948 images have a relative light contribution due to muons above 90%. The effect is similar for showers induced by helium nuclei, but shifted to higher energies. At energies below 300 GeV, from the 1175 events that trigger the detector, 468 (*i.e,* 40%) are due to "isolated" muons. Therefore, the $\gamma/background$ separation at the lowest energies can improve if it takes into account that about half of the background images are produced by "isolated" muons.

The mean SIZE of the proton showers not containing "isolated" muons decreases when reducing the energy of the primary proton. At energies below 50 GeV the mean SIZE is quite similar to that of the gamma showers, in spite of the fact that proton showers produce less Cherenkov light than gamma showers (see section 2.2.2). This is a consequence of the trigger of the telescope. As I mentioned before, the sample of proton showers at low energies ($\lesssim 300\ GeV$) which are able to trigger the telescope have a somewhat larger (than the mean) Cherenkov light yield in the camera. This effect increases when lowering the energy of the primary protons. Hence the proton

---

[7] This statement only applies if the energy of the muon is above the the threshold for Cherenkov light production.

events shown in figure 6.3 at energies below 50 *GeV* are significantly "biased" (up fluctuations) to larger SIZE values.

- *2)* As I showed in figure 2.7, the difference between the total amount of Cherenkov light produced by gamma and hadron showers decreases as the energy of the primary particle increases. Conversely, as observed from figure 6.2, the difference between the (mean) SIZE of gamma and hadron images (after the telescope trigger and the image cleaning[8]) increases as the energy of the primary particle increases. Gammas of energy 100 *GeV* (which produce on average a signal of 1000 photons in the telescope camera) do compete (on average) with protons of about 300 *GeV* and helium nuclei of about 600 *GeV*; while gammas of energy 250 *GeV*(which produce on average a signal of 3000 photons) do compete with protons of about 2 *TeV* and helium nuclei of about 2.8 *TeV*.

This effect is explained by the compactness of the gamma images in comparison to the dispersion in the light distribution of the images produced by hadrons. As stated in sections 2.1 and 2.3, the Cherenkov light in hadronic showers originates in secondary electromagnetic showers induced by gammas from π^0 decays. Because of the directionality of the Cherenkov radiation, the light emitted by some of the electromagnetic sub-showers (generated within a single hadronic shower) could be focused outside the camera (*i.e,* images completely outside the camera), or it might not even reach the telescope. The higher the energy of the primary hadron, the larger (in average) the number of electromagnetic sub-showers that are produced; and hence the larger (in average) the number of electromagnetic sub-showers that are not detected by the telescope in a given detected hadronic event. Consequently, the fraction of Cherenkov light (with respect to the total amount of Cherenkov light produced in a detected hadronic shower) measured in the camera of an *IACT* decreases as the energy of the primary hadron increases.

---

[8] The image cleaning procedures used to remove (partly) the *LONS* and the noisy pixels from the images (see section 6.3.2) can also remove the fraction of the signal (produced by Cherenkov light) that is away from the main ellipse. This effect will occur more often in hadron induced images than in gamma induced images.

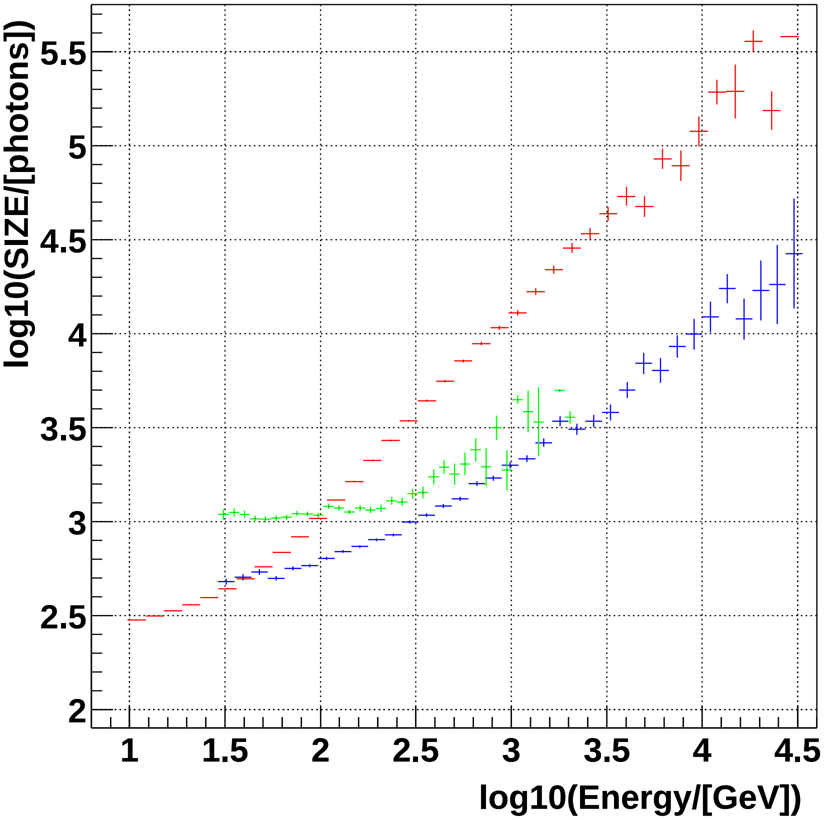

Figure 6.3: *Dependence of the Hillas parameter SIZE on the energy of the simulated primary particle for gammas (in red), and protons after passing the trigger of the telescope and the image cleaning procedures. The proton showers producing images with more than 90% of the Cherenkov light content originating from muons are shown in green, and the rest of the proton showers are shown in blue. The points show the mean of the SIZE distribution for each bin of log(energy), and the vertical error bars show the error of the mean.*

Therefore, the telescope trigger already provides a substantial γ/h separation by exploiting the compactness of the γ-images. The effect is significant because of the steep power law spectra of the CRs. I want to point out that this effect justifies the absence of simulations of heavy cosmic hadrons, which are much less abundant than protons and alpha particles and have a substantially lower probability to trigger the telescope; and hence they do not contribute significantly to the amount of triggered events. Besides, their simulation requires a larger amount of time, since they produce many more secondary particles which have to be traced.

Distribution of basic image parameters for gamma and hadron showers

A comparison of the Hillas parameters of shower images produced by gammas (from a point source) and hadrons is shown in figure 6.4. The helium events are weighted such that their number corresponds to 42% of the total number of protons, which is the quantity observed above 30 GeV [103]. The weight applied to the helium events is computed as $(simulated\ protons/simulated\ helium\ nuclei) \times 0.42 = 0.782$. Due to the fact that the protons and alpha particles are already simulated with their energy spectra, the above mentioned weightening procedure reproduces the abundances observed in nature. The cut $SIZE > 2000$ photons has been applied to both gammas and hadrons. This cut in SIZE has been chosen for comparison purposes, since it is also applied in the analysis of the experimental data from the first observations performed with the MAGIC Telescope (see section 6.3). Note that (for a comparable SIZE) the gamma images have (in general) a smaller WIDTH, LENGTH and ALPHA value. It is therefore possible to achieve an efficient gamma-hadron separation and retain a significant amount of gammas by limiting the admissible image parameter range.

Dependence of the image parameters on the shower characteristics

The values of the image parameters depend very much on the energy of the primary particle; and they are also sensitive to the impact parameter of the shower and the zenith angle (only important above 30°) of observation. Figure 6.5 shows the dependence of the parameters LENGTH, WIDTH and DIST with the energy and the impact parameter for

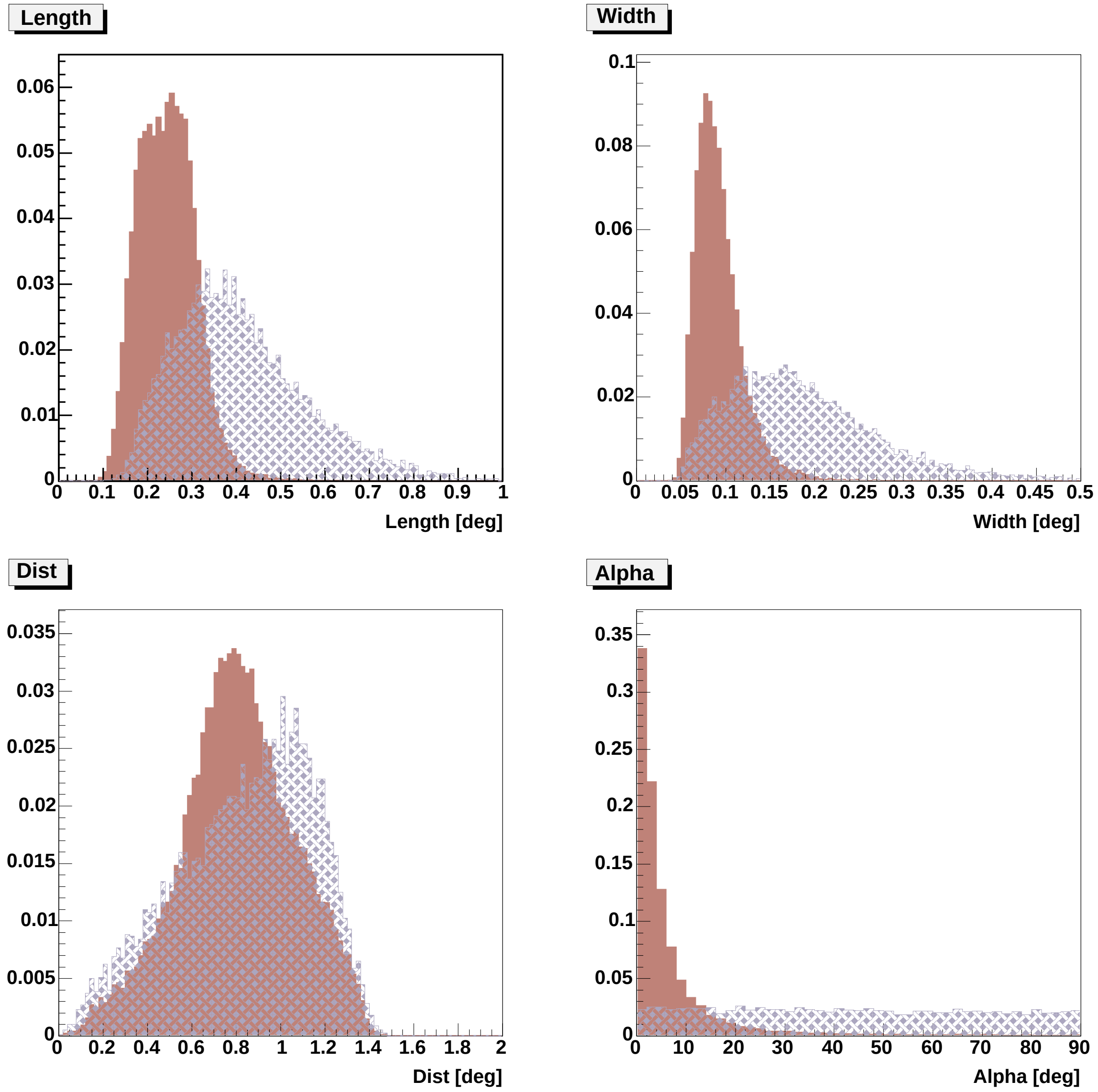

Figure 6.4: *Distribution of LENGTH, WIDTH, DIST and ALPHA parameters for simulated gamma-induced showers (brown filled histograms) and hadrons-induced showers (blue shadow filled histograms) after passing the trigger of the telescope and the image cleaning procedures. All distributions are normalized to unit area for a better comparison. The cut* $SIZE > 2000$ *photons has been applied to both gammas and hadrons.*

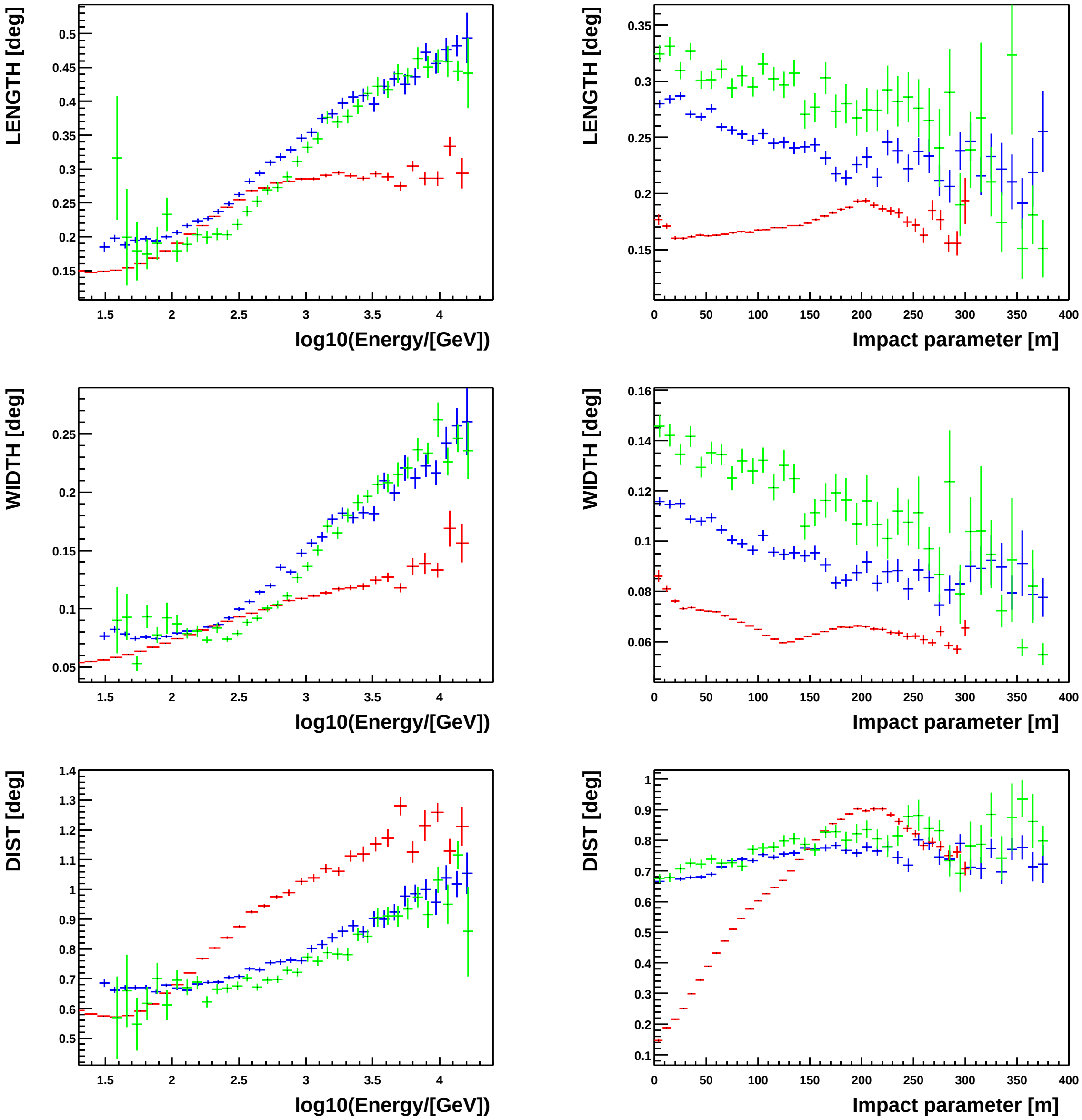

Figure 6.5: *Dependence of the parameters LENGTH, WIDTH and DIST on the energy and the impact parameter for simulated gammas (red), protons (blue) and alpha particles (green) after passing the trigger of the telescope and the image cleaning procedures. The points show the mean value of the distribution for each bin of log(energy) and impact parameter, and the vertical error bars show the error in the estimated means. No SIZE cut has been applied in these plots.*

simulated gammas, protons and alpha particles. The dependence on the zenith angle is negligible (and thus not shown), since all the events used were simulated at low ($< 30°$) zenith angles.

Note that the DIST parameter is highly correlated to the impact parameter for simulated gammas, but not for hadrons. A slight increase in the mean LENGTH and WIDTH of the simulated gammas *vs.* the impact parameter occurs at about 130 m. This distance is roughly the radius of the brightest region of the *Cherenkov light pool* of a γ-induced shower, that is produced by the Cherenkov radiation from the electrons which are close to the shower axis (*core particles*), as shown in figure 2.5b. At large impact parameters ($\gtrsim 150\ m$), the viewing angle of the EAS is larger, the number of electrons that contribute to the Cherenkov light yield in the camera is smaller, and thus a somewhat higher energy is required to trigger the telescope. This means that the sample of gamma showers that trigger the telescope is slightly biased to higher energies, and hence the larger LENGTH and WIDTH. Besides, the smaller amount of *halo* electrons (compared to the amount of *core* electrons) in the EAS also implies a somewhat larger fluctuation in the angles with which the Cherenkov light reaches the telescope, thus producing more extended images. At impact distances larger than 200 m, the trigger efficiency drops very fast, and hence the amount of γ events that trigger the telescope is very small ($\sim$3% of the total amount of gammas shown in figure 6.5).

Figure 6.6 shows the dependence of the parameters LENGTH, WIDTH and DIST on the SIZE and the DIST parameter for simulated gammas, protons and alpha particles. Note the strong dependence on the SIZE of all parameters, while the dependence on the DIST parameter is softer. The increase in the shape parameters at DIST values close to 0.9° is the consequence of the reduced trigger region in the telescope camera (see section 3.4). At large DIST values ($\gtrsim 1°$) the shower images must be elongated enough to reach the trigger region, and hence the sample of events that trigger are biased to extended images. If the cut $SIZE > 2000$ photons is applied to the data, the small images are removed and the bias to extended images is less visible, as shown in figure 6.7. With this cut in SIZE, the shape parameters vary smoothly with the DIST parameter. The increase in LENGTH and WIDTH at very low DIST values ($\lesssim 0.2°$) of the simulated gammas is due to the fact that,

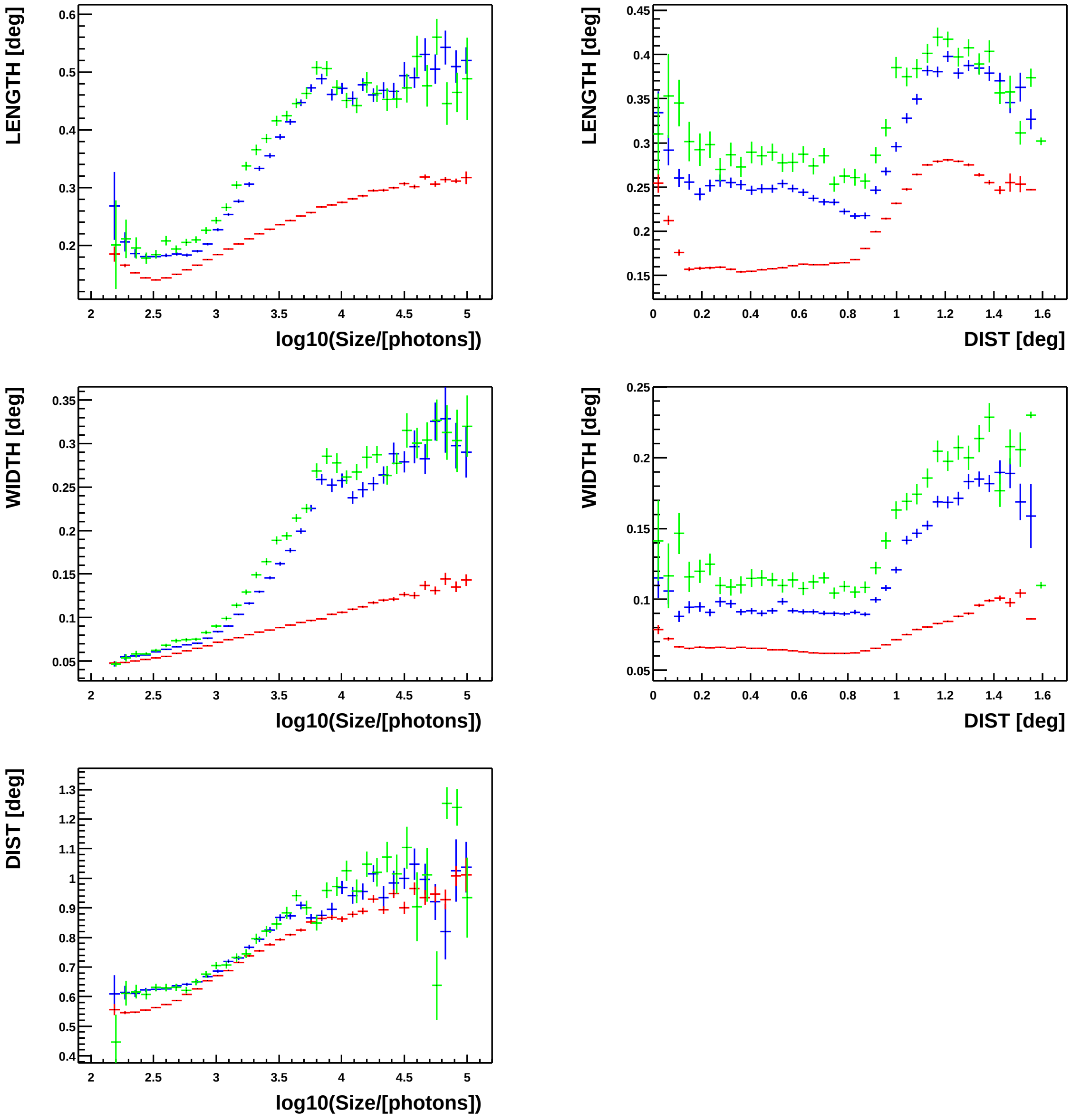

Figure 6.6: *Dependence of the parameters LENGTH, WIDTH and DIST with the SIZE and the DIST parameter for simulated gammas (red), protons (blue) and alpha particles (green) after passing the trigger of the telescope and the image cleaning procedures. The points show the mean value of the distribution for each bin of log(SIZE) and DIST, and the vertical error bars show the error of the means. No SIZE cut has been applied in these plots.*

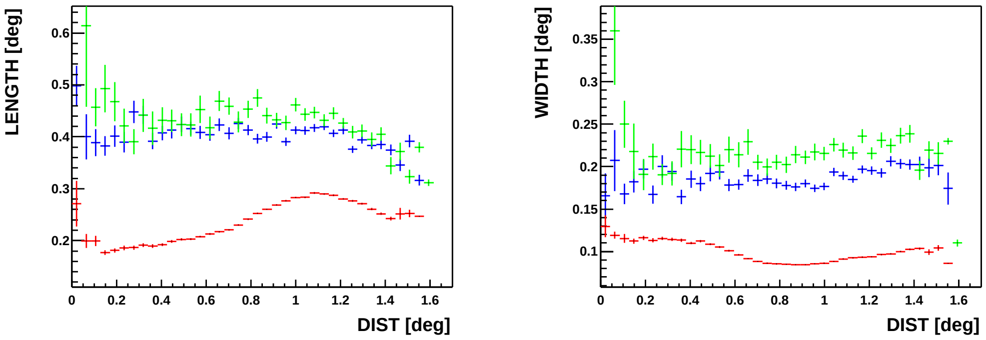

Figure 6.7: *Dependence of the parameters LENGTH and WIDTH with the DIST parameter for simulated gammas (red), protons (blue) and alpha particles (green) after passing the trigger of the telescope and the image cleaning procedures. The points show the mean value of the distribution for each bin of DIST, and the vertical error bars show the error of the mean. The cut* $SIZE > 2000$ *photons has been applied.*

at these small distances from the telescope, only the light from the very strongly scattered electrons of the shower tail can reach and trigger the telescope. The images produced by these electrons are in general more irregular and extended (more "hadron-like").

As can be seen from the figures 6.6 and 6.7, the separation between gammas and hadrons (based on cuts in the image parameters) becomes easier as the energy of the primaries increases. This is an important feature that was considered when defining the strategy to analyze the data from the first observations performed with MAGIC (see section 6.3).

Below a γ energy of 100 GeV (corresponding to mean SIZE values below 1000 photons), the separation between gamma and hadron events based on the shape parameters becomes less efficient. However, as I showed in figure 2.7, at these low energies the amount of Cherenkov light produced by hadrons showers is quite low (in comparison to that of $\lesssim$ 100 GeV gamma showers) and thus the fraction of hadron showers capable of triggering the telescope is substantially reduced (in comparison to that of gamma showers). This effect compensates partly the less efficient gamma-hadron separation based on the shape parameters, and allows *IACTs* to work also in this energy domain.

Figure 6.8 shows the distribution of ALPHA values for gamma showers (from a point source) and hadron showers after the application of four different SIZE cuts; SIZE larger than 500, 1000, 2000 and 4000 photons. According to figure 6.2, these four SIZE values correspond to a gamma energy of about 50, 100, 180 and 350 GeV. Note that, as the energy of the events considered decreases (lower energy threshold), the ability to reconstruct the direction of the initial shower worsens, and hence the distribution of ALPHA becomes wider. Because of that, the hadron rejection obtained by cutting in the ALPHA parameter also worsens. This is especially important for rejecting the background due to cosmic electrons, because ALPHA is the only parameter that shows differences between gamma and cosmic electron induced showers. However, even for the smallest SIZE values most of the gamma events (from a point source) still concentrate at low ALPHA values. For the lowest SIZE cut of 500 photons, the cut ALPHA $> 10°$ rejects roughly 89% of hadrons and cosmic electrons and still retains 61% of all gammas.

6.1.5 Estimation of the background in the distribution of ALPHA

As I mentioned in sections 2.3.3 and 6.1.4, there are always *background*-induced images (*background events*) that survive the γ/h *separation cuts*, and thus add to the *signal*-induced images (*signal events*) in the *alpha plot*. The proper estimation of the *background events* surviving the γ/h *separation cuts* is essential in the computation of the amplitude and the significance of the detected signal.

There are several techniques to estimate this background:

- *1) Consecutive ON-OFF observations.* The method consists in taking data (*ON data*) with the telescope pointing to the cosmic source (*ON observation*); and then, take data (*OFF data*) directing the telescope to a sky region which is sufficiently displaced from the source location and does not contain strong gamma sources (*OFF observation*). The number of background events is determined as the number of OFF events that survive the γ/h *separation cuts* and the cut in ALPHA. The *signal events* are computed by subtracting the number of background events from the number of ON events surviving the same set of cuts. The number of background events must be properly normalized to account for the different observation times between the *OFF* and the *ON observations*.

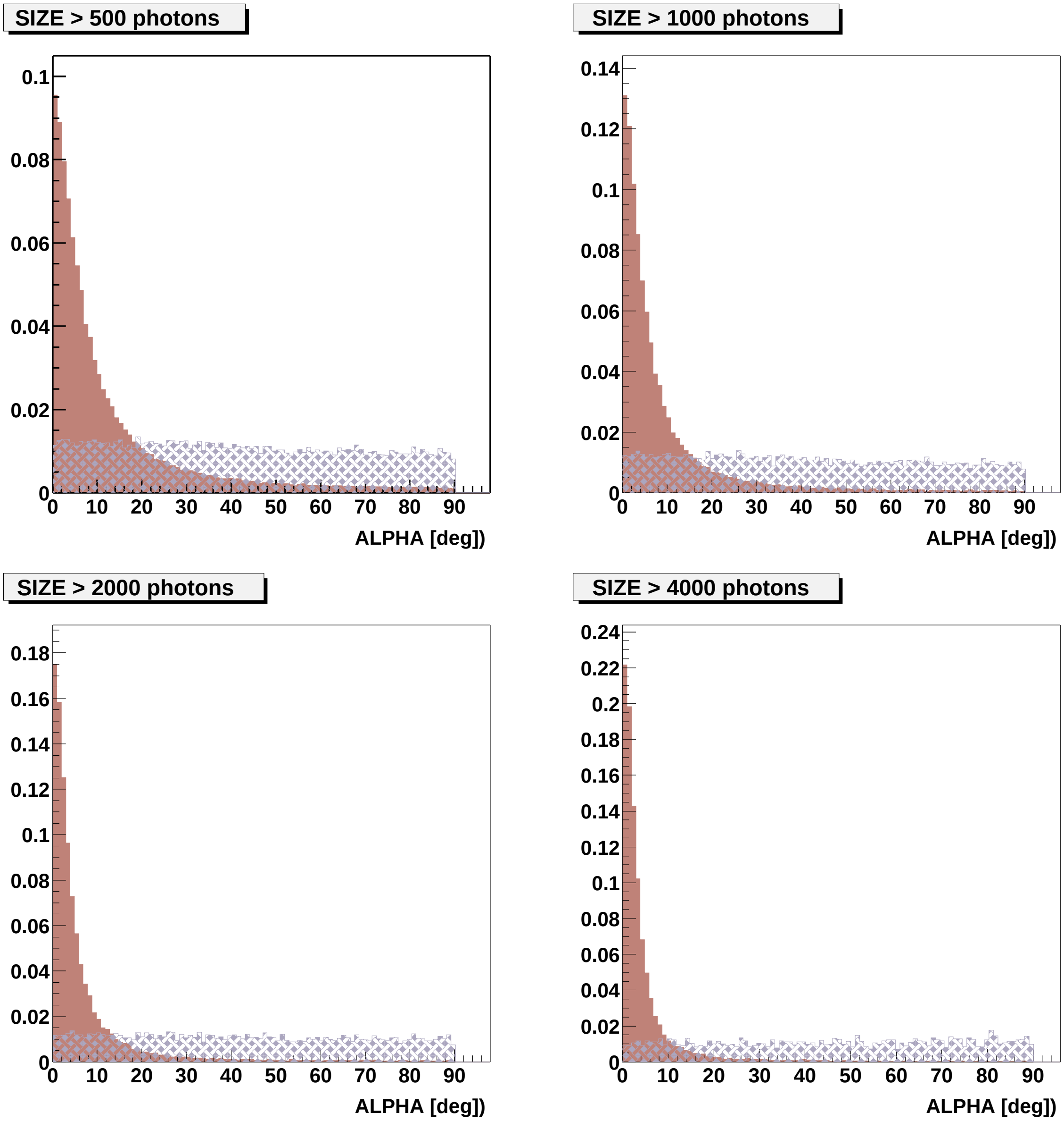

Figure 6.8: *Distribution of ALPHA values for simulated gamma-induced showers (brown filled histograms) and hadrons-induced showers (blue shadow filled histograms) for four SIZE cuts: SIZE larger than 500, 1000, 2000, and 4000 photons. All distributions are normalized to unit area for a better comparison.*

I want to stress that this method is only valid if the *ON data* is taken under the same conditions (telescope performance, weather conditions) as the *OFF data*. In order to get close to this situation, one usually switches between *ON-OFF observations* every 20-30 minutes, and the *OFF observations* are performed at similar zenith angles (and galactic coordinates) to that of the *ON observations*.

- *2) Wobble-mode observations.* The method consists in taking *ON* and *OFF observations* simultaneously. The telescope is directed to a sky location which is displaced from the source position by a given angle $\Delta\beta$. The "*ON data*" are obtained by reconstructing the shower images with respect to the shifted source position (the *signal events* point to that location of the camera). The "*OFF data*" are obtained by reconstructing the same shower images with respect to some other point in the camera (the so-called "anti" source position) which is not too close to the source position [104, 105]. As before, the *signal events* are obtained by subtracting (after cuts) the *OFF data* from the *ON data*. The basic assumption in this procedure is that the computed *OFF data* represent a good approximation of the background contained in the *ON data*. Obviously, the acceptance (trigger efficiency) of the detector must be equal for the two positions (source and "anti" source); otherwise the background would be over/underestimated. I want to note that by displacing the source position away from the camera center, the efficiency of the telescope for detecting gamma showers is somewhat reduced (by an amount that depends on the displacement value and the characteristics of the camera). On the other hand, one saves the time of the *OFF observations*, and thus the source can be observed during a longer time, which makes *Wobble-mode observations* more efficient than *consecutive ON-OFF observations*.

- *3) Background estimation by using the alpha plot from the ON data.* The method consists in applying the γ/h *separation cuts* to the *ON data* and produce an *alpha plot* with the surviving events. Then, in order to estimate the background content in the *signal region*, the alpha distribution in the *background region* (where almost no *signal events* are expected) is extrapolated into the *signal region* [100, 97]. Note that the

> ALPHA distributions of the simulated hadrons shown in figure 6.8 are very smooth (nearly flat) for the four SIZE cuts, and thus they can be safely extrapolated into the *signal region*. The cuts in the shape parameters LENGTH and WIDTH hardly affect the alpha distribution, yet the cuts in the parameter DIST could vary (smoothly) the shape of the original (nearly) flat distribution, as one can see in the ALPHA distributions shown in section 6.3.4. The cuts in the DIST parameter would not modify the shape of the ALPHA distribution if the camera was uniform and large enough so that the images never reached the camera edges. This is obviously not the case in the MAGIC camera because of the reduced trigger region and the ~3.6° *FOV*. The main advantage of this technique is that *OFF observations* are basically not needed[9], and therefore, more time can be used for the *ON observations*. The advantage compared to the *Wobble-mode method* is that the source is located at the center of the camera, and hence, the gamma acceptance is maximum.

In the extraction of the first signals from data taken with the MAGIC Telescope which will be presented in section 6.3, I determined the background content in the *signal region* by means of *consecutive ON-OFF observations*. The methods *2)* and *3)* do have some advantages with respect to *1)*, and they will surely be used in future observations with the MAGIC Telescope. However, they require a stable telescope performance and a good agreement between the experimental and the simulated data. Thus they are not suitable procedures for a detector in the commissioning phase.

6.1.6 The supercuts method to optimize the *signal/background* separation based on the Hillas parameters

I showed in sections 6.1.3 and 6.1.4 that the image parameters reflect the physical differences between γ-induced showers and *background*-induced showers, and thus that they can be used to perform a *signal/background* separation. In this section I will briefly describe the *supercuts method* as a technique to find the "cuts" on the image parameters that maximize

---

[9] A small amount of *OFF data* is needed to check the reliability of the method.

the "quality" of the detected signal.

The general algorithm of the supercuts method consists in the following steps:

- *0)* Definition of a set of initial cuts on a chosen set of image parameters.
- *1)* Application of the set of cuts to the *ON* and *OFF data*.
- *2)* Extraction of the γ signal.
- *3)* Estimation of the "quality" of the γ signal.
- *4)* Variation of the cuts.
- *5)* Continuation with step 1) as long as the "quality" of the γ signal is not optimum.

In this thesis, the *ON-OFF data* are the data taken during *consecutive ON-OFF observations*, as explained in section 6.1.5; and the γ signal is computed by subtracting (after cuts) the *OFF* events from the *ON* events, as I will describe in section 6.2.1.

The "quality" of the signal is determined by the value of a given quantity, that I will denote $Q_{estimator}$. In this work I used the significance of the signal (as defined in section 6.2.2); yet there are many other possible $Q_{estimator}$s, like the number of detected signal events, the *signal/background* ratio, the ratio of the cut efficiencies (*i.e,* the percentage of events surviving the cuts) for signal and background events (only valid for Monte Carlo data), or a function that combines these quantities. By specifying the $Q_{estimator}$ one defines the criteria for evaluating the performance of a given set of cuts.

The steps *4)* and *5)* are related to the optimization of the cuts, and they will be discussed in section 6.2.3.

I want to point out that there are other methods to perform a $signal/background$ separation which are also based on the image parameters; like *neural networks* and *random forest.* The so-called *linear discriminant analysis*, which was used in [97], is a particular case of a neural net; it is a linear neural net with only one hidden neuron, and trained by an analytical method, rather than doing a stepwise optimization. In these analysis methods, one uses a combination of the image parameters to compute a variable (discriminant variable) that estimates how much the shower images resemble typical shower images produced by $\gamma - rays$.

The *signal/background* separation is performed by a cut in this discriminant variable. These techniques have to "learn" how signal and background events look like; which implies that they completely rely on the description of the shower development and telescope performance provided by the Monte Carlo simulations. As I will discuss in section 6.3.1 and appendix E, our Monte Carlo simulations do not describe the current performance of the telescope sufficiently well, and hence neither the *neural networks* nor the *random forest* are suitable methods at this early stage of the experiment.

6.2 Development of a program to analyze reconstructed shower images using the supercuts method

I wrote a set of classes and C++ routines that allow one to optimize the cuts on the Hillas parameters, and to extract the gamma signal from the *reconstructed shower images*. The *reconstructed images* are the shower images after the calibration, the application of the image cleaning procedures and the computation of the Hillas parameters. The code has been developed within the Magic Analysis and Reconstruction Software (*MARS*) framework [106, 107]. The *MARS* software is a *ROOT* (see *http://root.cern.ch*) based collection of C++ classes driven by a central event loop. A *MARS* software release is documented and available at the web page *http://magic.astro.uni-wuerzburg.de/mars/* .

The programs are based on already existing classes and routines (also within the *MARS* environment) written by W. Wittek to analyze reconstructed shower images. The main difference of the code I wrote with respect to the one written by W. Wittek is the usage of *ON* and *OFF data* to extract the gamma signal, instead of using only *ON data*[10], and also the possibility to perform the optimization of the cuts independently in different *cosZA* bins. The main advantages of the new programs are:

- The ALPHA distribution of the background events in the *ON* sample is estimated

---

[10] In the analysis performed by Wittek's code, the background content is estimated from the *background region* of the *ON data alpha plot*, as explained in section 6.1.5.

from the *OFF* data. That means that no assumption about the shape of this distribution in the *signal region* is needed.

- The new programs are applicable also in the case where the ALPHA distribution of the *signal events* extends to large ALPHA values.

6.2.1 Extraction of the γ signal

The number of *signal events* (γ signal) is calculated as

$$N_{signal} = N_{ON}^{AfterCuts} - \alpha \cdot N_{OFF}^{AfterCuts} \tag{6.5}$$

where $N_{ON}^{AfterCuts}$ and $N_{OFF}^{AfterCuts}$ are the number of events surviving the γ/h *separation cuts* plus the cut in ALPHA, and α is a normalization factor that accounts for differences in the amount of the *ON* and the *OFF* data sets. In the following I will explain how I compute the normalization factor and the number of events after the selection cuts.

Calculation of the normalization factor α between *ON* and *OFF data*

There are several ways of computing the normalization factor α, namely:

- Ratio of the effective observation times (the dead time is subtracted),

$$\alpha = \frac{T_{ON}}{T_{OFF}} \tag{6.6}$$

- Ratio of the number of reconstructed events before applying the γ/h *separation cuts*,

$$\alpha = \frac{N_{ON}^{BeforeCuts}}{N_{OFF}^{BeforeCuts}} \tag{6.7}$$

- Ratio of the number of reconstructed events before applying the γ/h *separation cuts* corrected for the contamination of gammas in the original sample of *ON data*,

$$\alpha = \frac{N_{ON}^{BeforeCuts}}{N_{OFF}^{BeforeCuts}} - \frac{N_{signal}/\epsilon_\gamma}{N_{OFF}^{BeforeCuts}} \tag{6.8}$$

where ϵ_γ is the gamma efficiency of the cuts applied to the data.

- Ratio of the number of reconstructed events located in the *background region* of the *alpha plot* after applying the γ/h *separation cuts*,

$$\alpha = \frac{N_{ON}^{AfterCuts}}{N_{OFF}^{AfterCuts}}\Big|_{background\ region} \tag{6.9}$$

In the programs that I wrote, α can be calculated by means of any of the last three methods. All of them have advantages and disadvantages.

The calculation of α performed by equation 6.6 has the following problem. If during the *ON* and *OFF observations* the weather conditions and/or the telescope performance vary slightly[11], the ratio of the observation times leads to a (slightly) wrong *normalization* of the *ON-OFF* data.

The normalization factor α computed by formula 6.7 is not optimum, since the *ON data* is "contaminated" by the gamma signal (which might be up to 1-2% of the total amount of data), and hence, α is slightly overestimated. Equation 6.8 corrects the value of α using N_{signal} and ϵ_γ. This is obviously an iterative process, in which N_{signal} is computed using first the uncorrected value of α, and then it is computed again using the corrected value of α. Since the correction to the value α is (typically) only of about 1-2%, it is not worth more than one iteration. In case the cut parameters need to be optimized (see section 6.2.3), the α value used in the optimization is the uncorrected one.

The value of ϵ_γ can only be known by studying the effect of the γ/h *separation cuts* on a simulated gamma sample. Nevertheless, since the correction to α is small, the uncertainties in the value of ϵ_γ (typically between 0.4 and 0.7) have only little influence on the calculated value of α by equation 6.8.

On the other hand, the observation conditions when taking the *ON data* and the *OFF data* might not be exactly the same; which would lead to subtle differences in the distribution of their image parameters. It is worth pointing out that the shape parameters LENGTH and WIDTH are sensible to variations in the *LONS* or in the *ZA* of observation; a higher *LONS* and/or a larger *ZA* would decrease (in average) the LENGTH and the WIDTH of the images.

---

[11] The variations in the observation conditions are not large enough to produce a failure in the *ON-OFF* data comparison tests.

Therefore, if the observation conditions were not the same for the *ON* and the *OFF data*, the efficiency of the cuts might be somewhat different; and that would produce a wrong *ON-OFF normalization* after the application of the γ/h *separation cuts* and consequently, a wrong estimation of the background content in the signal region.

In order to by-pass this problem, one can compute the normalization factor α using equation 6.9. If the mean energy of the gamma showers (which is higher than the E_{th} of the telescope) is not too low, say $< E_\gamma > \gtrsim 100\ GeV$ (*i.e,* images with SIZE $\gtrsim$ 1000 photons at low ZA), the amount of gamma events outside the *signal region* of the *alpha plot* is still quite small. Note from figure 6.8 that, if the *background region* of the *alpha plot* is defined by ALPHA values larger than 30°, only 8% of the gamma events are located in the *background region* at values of SIZE $>$ 1000 photons. For images with SIZE $>$ 2000 photons, the fraction of gamma events in this *background region* is 5%. Indeed, this fraction decreases substantially when applying the γ/h *separation cuts*. It is worth mentioning that, if the γ/h *separation cuts* optimized on real data from Mkn 421 (see section 6.3.5) are applied to the Monte Carlo data (only images with SIZE $>$ 2000 photons are considered), 43% of the simulated gammas are removed from the initial sample; *i.e,* the gamma efficiency ϵ_γ of the selection cuts (the cut in ALPHA is not included) is 57%. However, the fraction of gamma events with ALPHA $> 30°$ decreases from 5% to 0.2%. So, the simulated gamma events with large ALPHA values are clearly more *hadron-like*, and hence the initial (small) fraction of gamma events located in the *background region* is practically removed by the γ/h *separation cuts*. Therefore, the formula 6.9 provides a very good estimate of the normalization factor α. The basic assumption in this calculation is that, after the γ/h *separation cuts*, the shape of the ALPHA distribution of the *OFF data* is similar to the one of the background events contained in the *ON data*. This assumption can be checked at least in the *background region* of the *alpha plot*.

Calculation of $N_{OFF}^{AfterCuts}$, $N_{ON}^{AfterCuts}$ and their corresponding errors

The default procedure to compute $N_{OFF}^{AfterCuts}$ (and its corresponding error $\Delta N_{OFF}^{AfterCuts}$) is to fit the distribution of ALPHA values for the *OFF data* in the range 0-90° with a function; and then to integrate this function in the *signal region*. As discussed in section

6.1.3, the values of the ALPHA parameter are expected to be uniformly distributed (in the range 0-90°) for the background events. Deviations from a flat distribution might occur due to the geometry/acceptance of the camera and the γ/h *separation cuts*; but they are small, as it can be noted from the figures shown in section 6.3.4. Therefore, the use of a smooth function to estimate the background content in the *signal region* is justified.

The function used to fit the ALPHA distribution is a second order polynomial function. The linear term of this function is set to zero, because the distribution of ALPHA values for the *OFF data* must be flat at ALPHA = 0°.

If the fit is acceptable, which can be judged on the basis of the χ^2-probability of the fit, the estimated value $N_{OFF}^{AfterCuts}$ is in general better than the one resulting from simply counting the events. Hence its corresponding error is smaller than $\sqrt{N_{OFF}^{AfterCuts}}$. That means that when using the values extracted from the fit the computed significance of the gamma signal is higher than the one obtained by just counting the events. I'll come back to this issue in section 6.2.2. In case the second order polynomial does not fit the ALPHA distribution of the *OFF data* properly, which might occur in pathological cases, the significance is computed using the counted number of *OFF* events in the *signal region*. In this case its error is given by the square root of the counted number (*i.e,* $\Delta N_{OFF}^{AfterCuts} = \sqrt{N_{OFF}^{AfterCuts}}$).

$N_{ON}^{AfterCuts}$ is estimated by simply counting the *ON* events after applying the γ/h *separation cuts* in the *signal region* of the *alpha plot*. Its error is given by the square root of the counted number.

6.2.2 Calculation of the significance of the signal

The significance of the signal is computed as defined by formula 17 of the *Li&Ma* paper [108]:

$$\begin{aligned} S &= \sqrt{2}\cdot\Big\{N_{on}\cdot ln\Big[\frac{1+\Gamma}{\Gamma}\cdot\Big(\frac{N_{on}}{N_{on}+N_{off}}\Big)\Big] \\ &\quad +N_{off}\cdot ln\Big[(1+\Gamma)\cdot\Big(\frac{N_{off}}{N_{on}+N_{off}}\Big)\Big]\Big\}^{1/2} \end{aligned} \tag{6.10}$$

where N_{on} is the number of events from the *ON data* surviving the γ/h *separation cuts* and located in the *signal region* of the *alpha plot* (*i.e,* $N_{ON}^{AfterCuts}$), and N_{off} and Γ are derived from the normalization factor α, the estimated $N_{OFF}^{AfterCuts}$ and its related error $\Delta N_{OFF}^{AfterCuts}$:

$$\begin{aligned} \Gamma \cdot N_{off} &= \alpha \cdot N_{OFF}^{AfterCuts} \\ \Gamma \cdot \sqrt{N_{off}} &= \alpha \cdot \Delta N_{OFF}^{AfterCuts} \end{aligned} \tag{6.11}$$

Which means that the variables N_{off} and Γ are given by the following expressions:

$$N_{off} = \Big(\frac{N_{OFF}^{AfterCuts}}{\Delta N_{OFF}^{AfterCuts}}\Big)^2 \qquad and \qquad \Gamma = \alpha \cdot \frac{\Big(\Delta N_{OFF}^{AfterCuts}\Big)^2}{N_{OFF}^{AfterCuts}} \tag{6.12}$$

Note that the smaller the error $\Delta N_{OFF}^{AfterCuts}$ (which is obtained from the fit if the χ^2-probability of the fit is acceptable), the smaller the value of Γ, and consequently the higher the value of the significance computed with the expression 6.10.

6.2.3 Optimization of the cuts

The application of simple "constant cuts" (the so-called **static cuts**) on the entire data set implies that the image parameters of all gamma shower events must lie within a constant range. However, as I showed in section 6.1.4, the image parameters depend strongly on the energy of the showers (and also on the impact parameter and the zenith angle). Due to the steep power law spectrum of all presently known $\gamma - ray$ sources, the optimization of static cuts is dominated by the smallest energy showers (close to the threshold energy). As a consequence, the cut efficiency worsens at large energies. A solution to this problem is to introduce cuts that depend on the SIZE, the DIST and the ZA; the so-called **dynamical cuts**. This approach was used successfully for first time by D. Kranich [109, 100], and I will also use it to analyze the data from the first observations performed with MAGIC. The main difference with respect to the approach of D. Kranich is that I use both *ON data* and *OFF data* (instead of *ON data* only) for extracting the γ signal.

The SIZE and the DIST parameters are strongly correlated with the energy and the impact parameter of the shower, as shown in figures 6.2 and 6.5. Therefore, the dependence on the main shower parameters (energy, impact parameter and ZA) is introduced in the cuts applied to the data. Each individual cut ($LENGTH_{up}$, $LENGTH_{low}$, $WIDTH_{up}$ ...)

is parametrized as a polynomial function (up to second order) of the variables $ln(SIZE)$, $DIST^2$, and $cosZA$. Purely geometrical considerations lead to the dependence on $cosZA$; and $ln(SIZE)$ is more appropriate in the important low energy range[12]. $DIST^2$ is more suitable to describe the rapid changes (in the values of the image parameters) at DIST values larger than 1° (see figure 6.6).

The optimal set of cut parameters is found by following the steps defined in section 6.1.6. The optimization procedure is rather modular. It allows the user to add new parameters, or to modify $Q_{estimator}$ quite easily. The $Q_{estimator}$ implemented by default is the significance of the signal (as defined in section 6.2.2), yet it can be replaced by another one, like the *signal/background* ratio, the number of *signal events*, the ratio of the cut efficiencies for gamma and hadrons (only valid when using Monte Carlo data), or a function that combines some or all these quantities.

The optimization of the cuts on the selected parameters that maximize $Q_{estimator}$ is performed by minimizing the quantity $-Q_{estimator}$ using the MINUIT package [110]. The method *SIMPLEX* was used, since the quantity to be minimized is not a continuous function of the free parameters because of the event selection produced by the cuts.

6.2.4 Additional features implemented in the code

In this section I will describe briefly two additional novel features (as compared to the previous approaches performed by Kranich and Wittek) implemented in the programs I wrote.

The programs allow the user to divide the data into subsamples according to $cosZA$, and to optimize the cuts for each $cosZA$ range independently. The results of the optimization for all the data subsamples can be combined to compute an overall signal amplitude and significance. This feature might be very useful to find an optimal parametrization of the dependence on $cosZA$. Due to the low ZA ($ZA \lesssim 30$ °) of the first observations, this feature won't be used in the analysis presented in section 6.3.

---

[12] Besides, the (natural) logarithm of the SIZE (which is proportional to the logarithm of the energy of the primary gamma) is in first order proportional to the position of the maximum (X_{max}) of the atmospheric shower (see equation 2.1).

The second characteristic is the storage of the cut values applied to the events (*ON* and *OFF*), together with the image parameters of the events (LENGTH, WIDTH ...) in a ROOT tree-like structure into a ROOT file. This feature allows the user to easily inspect (a posteriori) the cuts (and their dependences) which were applied to the data, and to check whether the cuts make sense from the physics point of view. Besides, it also allows one to study the events that passed/failed a certain subset of the applied cuts.

6.3 Analysis of the first observations performed with the MAGIC Telescope on the Crab Nebula and Markarian 421

In this section I will describe the analysis that I carried out on the observations performed on Markarian 421 (Mkn 421) and the Crab Nebula with the MAGIC Telescope on 14th-15th February 2004. The telescope was in the commissioning phase, and these observations were taken in between technical runs.

The purpose of the analysis was to evaluate the initial performance status of the telescope, as well as to demonstrate that significant γ signals could be extracted. In addition, these observations allowed me to test the analysis procedures that I developed (and were discussed in the previous sections) using real data from MAGIC.

A physics analysis is beyond the scope of this thesis. At this stage of the experiment, the Monte Carlo simulations do not agree well with the experimental data (see appendix E), and therefore the efficiency of the telescope to detect $\gamma - rays$ cannot be accurately known (see section 2.3.5).

6.3.1 Observational details

The details of the observations performed on the Crab Nebula and Mkn 421 are summarized in tables 6.1 and 6.2 respectively. The *background* was estimated by means of *consecutive ON-OFF observations*, as explained in section 6.1.5.

By the time of these observations, we knew that there were quite some problems in the performance of the telescope. The most relevant ones are listed below:

Sample	Zenith angle range (°)	Azimuth angle range (°)	Time duration (h:mm:ss)
ON	18 - 37	253 - 269	1:25:02
OFF	20 - 38	218 - 268	1:00:42

Table 6.1: *Details of the observation performed on the Crab Nebula.*

Sample	Zenith angle range (°)	Azimuth angle range (°)	Time duration (h:mm:ss)
ON	9 - 28	-40 - 62	1:45:18
OFF	9 - 22	-44 - 58	0:49:37

Table 6.2: *Details of the observation performed on Mkn 421.*

- *The active mirror control (AMC) was still not functioning as expected.* The procedure to focus the mirrors is carried out by pointing the telescope to a calibration lamp located at the "Roque de los Muchachos", which is at $ZA\sim 75°$. The AMC is expected to modify the inclination of the mirrors as the telescope moves to compensate the frame deformation. Because of the performance problems of the AMC, at low ZA some of the mirrors were not properly focussed, and hence the optical quality of the images was somewhat deteriorated.

- *Data corruption due to a malfunction of the FADC/DAQ.* From time to time missing or duplicated bytes were observed in the sequence of the digitized data. From that moment on, the raw data were corrupted. In order to minimize the data losses, certain data-checking routines were implemented in the DAQ so that, whenever this kind of error was detected, the run was immediately stopped, and a new run was started.

- *Defective heat dissipation in the electronics racks containing the receiver boards and FADCs.* The heat dissipation was not carried out properly, and overheats could occur during data taking. Because of that, the observations had to be interrupted quite often.

- *The Calibration system was not operative.* Due to some CAN-BUS communication problems, the calibration system developed for the MAGIC Telescope (see section 3.6), could not be used. The calibration of the data is mandatory, especially at the first stage of the telescope. It not only provides the *ADC*-to-*photon* conversion factor for each channel (and thus equalizing the response among all the camera pixels) but also can be used to get valuable information about the stability and reliability of the complete electronic chain. Because of the importance of this sub-system, I installed in the MAGIC Telescope a calibration system that had been used previously in the old CT1 telescope of the HEGRA experiment (see section 6.3.2).

- *Non-stable gain in some of the pixels.* Some of the pixels showed significant variations in the amount of signal detected when being illuminated with equal light pulses during the calibration runs. The amplitude and the period of these signal variations were different for the affected pixels. Indeed, the number of pixels affected was also changing; we found that during some nights in November 2003 the complete camera was affected by this problem.

In addition, while analyzing the data from the observations carried out on Crab and Mkn 421 we realized about other problems in the performance of the telescope. The most important ones are listed as follows:

- *Problems in the telescope pointing and tracking.* Because of the mispointing of the telescope, the source position was not at the camera center, but at an unknown position[13]. Besides, due to the *ALT-AZ mount* of the telescope (which does not compensate the sky rotation) the location of the source was changing with time. And in addition, due to telescope tracking deficiencies, the movement of the source could not be described by a simple rotation with respect to the center of the camera. The telescope mispointing and bad-tracking were the deficiencies that complicated most the analysis. A (partial) solution to this problem is briefly explained in section 6.3.3.

---

[13] During our analysis we found that the source was about 0.1-0.2° from the camera center (see section 6.3.3).

- *About 50 non-operative pixels.* 30 of these PMTs were plugged into one of the six outer sector boards of the camera that broke at the beginning of the shift period of February. The other pixels showed a gain very close to zero, and were also considered as "dead". The origin of this problem is still under investigation. I want to point out that the voltage applied to these pixels was already the maximum allowed (1350 V) and thus the gain could not be increased further.

- *Event synchronization problems among pixels.* Some of the *FADC* boards seemed to not receive the trigger signal in some of the events. Because of that, the internal event numbers of the channels related to that boards were not incremented, and from then, these channels contained wrong event numbers for the rest of the run. Since the events are reconstructed according to the internal event number of the channels, from that moment on, the images were screwed up. Because of the *DAQ* problems mentioned before, the runs were quite short (typically less than a minute), and hence this problem did not occur very often.

- *Time jitter in the location of the signal within the FADC slices.* As mentioned in section 3.5, whenever a *level 2* trigger arrives to the *FADC* modules, the *FADC* chip stops digitizing, determines the position of the signal in the ringbuffer and writes 30 time slices of 1-*Byte* (15 for *high gain* and 15 for *low gain*) into the *FiFo* buffer for each pixel. We found a *jitter* of ± 2 slices in the position of the signal within the 15 *FADC* slices (of the *high/low gain*). In many cases this jitter was the same for all channels, but not always. This effect had to be taken into account when extracting the signal from the *FADC* slices (see section 6.3.2).

- *High/low gain inconsistencies.* Calibration studies showed that the gain ratio between the high and the low gain (see sections 3.3.3 and 3.5) was not the nominal factor 10 that we expected from the electronics of the receiver boards, but lower. The reason seemed to be that part of the saturated pulse in the 15 slices from the *high gain* could be sometimes contained in the following 15 slices from the *low gain.* This fraction of the *high gain* signal was not properly removed when extracting the *low gain* signal, and hence the *low gain* signal was somewhat overestimated.

It is not worth to go into the details of all these problems, since many of them were already corrected by the time I am writing this, and many others will be fixed in the following months. The main point here is that the first analysis of the MAGIC data allowed us to pinpoint quite some deficiencies in the initial performance of the detector; and thus, it helped substantially to correct and improve the performance of the MAGIC Telescope.

Obviously, all these problems made the analysis more difficult. However, as I will show in the following sections, we managed to detect very clear signals from Mkn 421 and Crab.

6.3.2 The preprocessing of the data

The preprocessing of the raw data consists in the following steps:

- *1)* The raw data is converted into a ROOT format. This is the so-called *rootification* of the data.
- *2)* The recorded *FADC* counts (together with the pedestal and *RMS* of the pedestal) are converted into Cherenkov photons for each pixel. This is the so-called *calibration* of the data.
- *3)* The pixels not having a “significant” light content are removed from the image. This is the so-called *image cleaning*.
- *4)* The Hillas parameters are computed, and some basic filter cuts are applied to remove unusable events. This is the *reconstruction* of the data.

In the next paragraphs I will describe briefly how these steps were carried out on the data from 14th-15th February 2004.

Rootification of the data

The *rootification* of the data is a trivial (technical) step performed using the program *merpp*; which combines the raw data from the *DAQ* and several telescope subsystems and produces a unique root file.

Calibration of the data

The signals of each channel i are calibrated basically by multiplying the recorded charge in this channel Q_i (measured in *FADC* counts) by its corresponding calibration factor C_i, thus obtaining the signals in number of Cherenkov photons S_i. The calibration factors C_i can be computed using a system that illuminates the camera with equal (and/or known) light pulses (during the so-called *calibration runs*), as explained in section 3.6.

Unfortunately, as I mentioned above, the calibration system intended to be used in MAGIC (see section 3.6) was still not operative in February, and a much more simple calibration system, the *CT1 calibration box*, had to be used. This calibration box had been used previously in the CT1 telescope of the HEGRA experiment. The system was built by Jürgen Gebauer in 2002, and consists of a small box (water resistant) with 10 *UV* LEDs and a diffuser. The 10 LEDs produce (simultaneously) a light pulse of about 4-5 *ns* when a pulse of charge (coming from the discharge of some capacitors) flow through them. The amplitude and frequency of the calibration pulses could be adjusted manually. The spectral emission of the LEDs is centered at $370nm$, *i.e,* close to the *QE* peak of the PMTs (see figure 4.5a) and the median of the spectrum of the Cherenkov light reaching the telescope (see figure 4.15).

At the end of October 2003, I installed the *CT1 calibration box* at the center of the main reflector; a position from which the LEDs from the calibration box could illuminate uniformly the whole camera of MAGIC. The system worked as a stand alone device, and it was not connected to the trigger system. This means that the calibration run data were contaminated with some cosmic events, which had to be removed a posteriori. This could be easily done by requiring that a large number of pixels (I used 300 pixels) had a significant signal content ($\gtrsim 50$ *ADC* counts).

The calibration constants were calculated using the *excess noise factor method* described in section 3.6. The mean number of *phe*s produced per calibration pulse was estimated using formula 3.2 with $F = 1.15$. The charge Q from the pulses was computed by adding the content (in *ADC* counts) of those six consecutive *FADC* slices yielding the highest charge. Note that this procedure (the so-called “sliding window” method) of extracting the signals from the *FADC* slices overestimates the signal content for very small signals. However, due to the time *jitter* problems described in section 6.3.1, this method gave better results than the extraction of the signal using a fixed range of *FADC* slices, which would miss a fraction of the signal in some events.

The estimated mean number of *phe*s per calibration pulse can be used to obtain the conversion between *FADC* counts and number of *phe*s impinging onto the first dynode of the PMTs. Yet in order to compute the above mentioned calibration factors C_i, one needs to know also the conversion between Cherenkov photons arriving at the camera plane and *phe*s impinging onto the first dynode of the PMTs. This conversion depends on the wavelength of the Cherenkov photons. We estimated an effective conversion efficiency (QE_{eff}) by folding the $QE(\lambda)$ of the coated PMTs shown in figure 4.5a with the Cherenkov photon spectrum from figure 4.15, and then multiplying the resulting value by constant factors describing the efficiency in the transmission of the plexiglas window (0.92) and the light guides (0.94). In addition, the *phe* collection efficiency *CE* of the ET9116A and ET9117A PMTs was also taken into account. This number is not well known and should be also wavelength dependent. In the absence of any precise measurement, we used a guess value of 0.9 (for all wavelengths)[14]. Using all the previously mentioned numbers we obtained a QE_{eff} of 18%.

We expect some differences in the real value of QE_{eff} for the different pixels; which arise from the spread in the efficiency of the light guides, the *QE* and *CE* of the used PMTs. In order to remove the dispersion in the detection efficiency of the different pixels, we adjusted the calibration constants so that the mean (calculated) number of photons (per unit area and calibration pulse) was identical for all pixels. For the inner pixels, the number used as a reference was the mean (calculated) number of photons (per pixel and calibration pulse) of all inner pixels[15]. For the outer pixels, the used reference was four times the reference used for the inner pixels.

Based on the calibration data, I also tagged pixels with erratic behaviors. Simple criteria were used for this procedure, namely *a)* an average signal (in *ADC* counts) $\lesssim$ 3 times lower

---

[14] Engineers from the PMT company *Electron Tubes* confirmed that a *CE* value of 90% is reasonable for this type of PMTs.

[15] Those pixels showing erratic behaviors were removed from the computation of the mean.

than the mean reference signal, and *b)* an estimated number of *phe*s (per calibration pulse) 4 standard deviations away from the reference mean. The calibration constants of the pixels tagged as erratic were set to zero, and their signal content in the data runs was interpolated (whenever it was possible) from the light content of the neighboring pixels. This task was performed during the image cleaning procedures (see below). For these observations, about 80 pixels were set as erratic pixels. This number contains the 50 non-operative pixels mentioned in 6.3.1.

In addition to the *calibration runs* described previously, special runs used to compute the signal pedestals (and the *RMS* of these pedestals) were also taken. These runs are the so-called *pedestal runs*; which consist in sending artificial trigger signals to the *DAQ* in order to acquire data when there are no cosmic events. The pedestal and the *RMS* of the pedestal extracted from the *pedestal runs* were also converted into Cherenkov photon equivalent numbers using the same calibration constants used to calibrate the data from the telescope observations (the so-called *data runs*).

The *data runs* were preprocessed using the closest (in time) *calibration* and *pedestal run* in order to minimize the effect of possible drifts in the electronics (gain, noise...), as well as the effect of stars in the camera field of view.

It is worth pointing out that the *CT1 calibration box* (as well as the simple calibration procedures described previously) worked quite stably and reliably during the first half year of the commissioning phase, and allowed us not only to calibrate the data, but also to perform many detector tests.

Image cleaning of the data

The fluctuations in the pixel signals induced by *LONS* or electronic noise do affect the computed image parameters and thus spoil the analysis of the events. This is particularly important because the 2^{nd} moment calculation of the shape image parameters does not take into account the errors (fluctuations) in the pixel signals, but only the calibrated signals. A partial solution to this problem consists in removing (from the image) those pixels whose signal could have originated from a large positive pedestal fluctuation. This procedure is the so-called *image cleaning*.

The selection of the "meaningful" pixels in a given image is performed by comparing their calibrated signals (S_i) with their calibrated noise, which is estimated by the calibrated pedestal *RMS* (RMS_i^{Ped}). The image cleaning that I applied to the data consisted of the following four steps:

- *1) Correction of "dead" pixels.* The signal content of "dead" pixels which had at least 3 neighboring "live" pixels was interpolated from the light content of the neighboring pixels.

- *2) Selection of core pixels.* The pixels fulfilling the condition $S_i \geq 4.0 \cdot RMS_i^{Ped}$, and having at least a neighboring pixel fulfilling the same requirement were tagged as *core pixel*s.

- *3) Selection of boundary pixels.* The pixels (which are not *core pixel*s) fulfilling the condition $S_i \geq 3.0 \cdot RMS_i^{Ped}$ and having at least a *core pixel* as a neighbor were tagged as *boundary pixel*s.

- *4) Removal of the noisy pixels from the image.* The signals of the pixels which were neither *core pixel*s nor *boundary pixel*s were set to zero.

I decided to apply a rather "strong" image cleaning cuts; 4 and 3 times the calibrated noise for *core pixel*s and *boundary pixel*s respectively. The purpose was to minimize the bias introduced by the method used to extract the signals (the "sliding window" method), which slightly overestimates small signals.

Reconstruction of the data and application of basic filter cuts

The image parameters were computed applying to the "cleaned" calibrated images the formulas described in section 6.1.2. Non-conventional filter cuts were applied in order to minimize the possible effects caused by the performance problems described in section 6.3.1. The idea of the filter cuts was to restrict the analysis to a parameter space where the *signal/background*-separation is easy and efficient. This could be done by removing images with a small SIZE. As I discussed in section 6.1.4, at large SIZE values the *signal/background* separation based on the shape parameters LENGTH and WIDTH, as well as on the ALPHA parameter, is more efficient (see figures 6.6 and 6.8). Besides, the shower images are typically more extended when the SIZE is large, and thus the effect caused by some of the telescope deficiencies (like the presence of 80 "dead" pixels, or a somewhat deteriorated image due to the problems with the AMC) is reduced.

Following the strategy of analyzing only large images, I applied the following filter cuts to the data:

- *1)* SIZE $>$ 2000 photons.
- *2)* $5 < N^{core\ pixel} < 200$
- *3)* LENGTH $> 0.08°$.
- *4)* WIDTH $> 0.05°$.
- *5)* LEAKAGE $< 25\%$.

The filter cuts *1)* and *2)* remove all the small images, whereas the cuts in WIDTH and LENGTH have very little effect on the reduction of the cosmic event images (see figures 6.10 and 6.11). I used them to reject events in which a large fraction of the signal is concentrated in one single pixel. These events occurred only occasionally, and their origin is still not understood; yet it is clear that they are not showers induced by $\gamma - rays$.

The upper limitation on the number of *core pixel*s removes events which might be produced by accidental illumination of the camera by car lights.

The LEAKAGE parameter was defined as the fraction of the signal contained in the outer most ring of PMTs in the camera, in comparison to the total signal (SIZE) of the image. The purpose of limiting this value to 25% was to remove those events that might extend considerably outside the telescope camera.

6.3.3 Location of the position of the source in the telescope camera

As I mentioned in section 6.3.1, one of our major problems to analyze the data taken on 14th-15th February 2004 is that the telescope was not pointing exactly to the source location, but to a region slightly (0.1°-0.2°) displaced from it. By definition (see section 6.1.1), the location of the source is quite irrelevant (provided the LEAKAGE is small) in the computation of the shape parameters (SIZE, LENGTH and WIDTH), but it is vital in the calculation of the parameters DIST and ALPHA. In particular, if the ALPHA parameter is computed with respect to a wrong source location, the distribution of ALPHA values (after the *γ/h separation cuts*) gets wider and the peak moves away from 0°. As a result, the estimated amplitude and significance of the signal, computed as described in sections 6.2.1 and 6.2.2 respectively, are reduced.

Due to the *ALT-AZ mount* of the telescope, the sky image in the camera rotates around the camera center when a source is tracked. This means that if the source is not located at the tracked sky location (*i.e,* the source is not located at the camera center), it will move around the camera center. That makes the search for the source location more difficult.

In addition, we also found that the telescope did not track properly; *i.e,* the telescope was not pointing always to the same position of the sky. Because of that, the movement of the source could not be described by a simple rotation with respect to the camera center.

In order to determine the movement of the source we divided the entire data set (for Crab and Mkn 421) into sub-samples ordered chronologically. For each of the subsamples the so-called *false source method* analysis was applied to obtain the respective source position. In the *false source method* analysis one defines a grid ($1° \times 1°$ in our case) with $N \times N$ bins (41×41 in our case) centered at the camera center. For each bin the analysis is applied (application of the *γ/h separation cuts* and extraction of the γ signal) calculating the source location dependent parameters with respect to the center of the bin. If there is a strong γ point source, the number of excess events will be maximum in that region of the grid where the source is located.

The results of this procedure applied to the entire data set from the Crab Nebula and Mkn 421 are shown in figure 6.9. The figures show the combination of all the grids (for all the subsamples) shifting the source location (determined for each subsample) to the reference point $(0, 0)$.

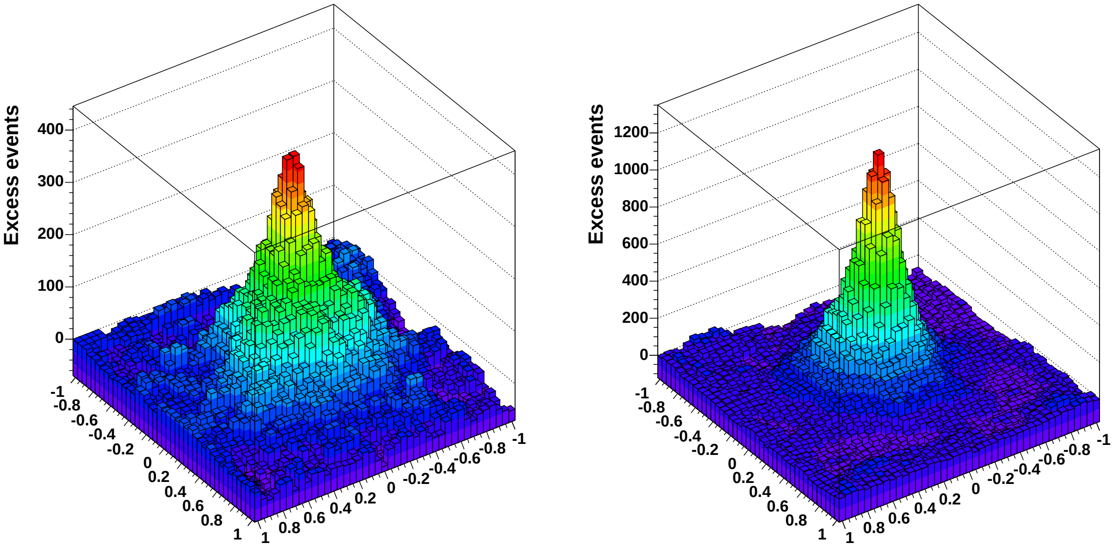

(a) (b)

Figure 6.9: *False source method applied to the data from a) Crab and b) Mkn 421. The vertical axis shows the number of signal events and the two horizontal axis show relative camera coordinates.*

I want to point out that this was an iterative process. At the very beginning, we applied very simple and generous (static) cuts, obtaining a first estimate of the location of the source for each subsample. Then, we reconstructed the events of each subsample with respect to the estimated source position, and performed a (dynamical) cut optimization, as described in section 6.3.5[16]. Finally, the *false source method* was performed again on all the subsamples using the optimized dynamical cuts. In this way, the detected γ signals were larger and thus we obtained a better estimate of the source position.

The size of the subsamples was chosen such that the signal (number of *signal events*) in the bin/bins where the source is located was at a significance level of at least 5 sigmas above noise. The position of the source location was obtained by a weighted average (using the number of *signal events* in the region ALPHA $< 5°$) over the bins of the grid.

---

[16] The linear dependence on $DIST^2$ in the cut parametrization defined by equation 6.13 was removed from this cut optimization.

Note that the peak of excess events is broader for the Crab sample. This is partly explained by the weaker γ signal from Crab compared to that from Mkn 421; which influenced the duration of the data subsamples used to unfold the position and the movement of the source in the telescope camera. The duration of the data subsamples from Mkn 421 was about 5 minutes, whereas the duration of the data subsamples from Crab was about 14 minutes.

6.3.4 Comparison of ON-OFF data

As explained in section 6.1.5, the basic assumption in the analysis of *consecutive ON-OFF observations* is that the *OFF* events surviving the *γ/h separation cuts* represent a good approximation of the background contained in the *ON* events surviving the same *γ/h separation cuts*. Due to the fact that most of the events that trigger the telescope are *background*-induced events, the distributions of the image parameters before the *γ/h separation cuts* for the *ON data* and the *OFF data* should be very similar. Therefore, the above mentioned assumption can be (up to some extent) tested.

Figure 6.10 shows the distribution of the parameters LENGTH, WIDTH, DIST and ALPHA for *ON* and *OFF data* taken for the Crab Nebula. The filter cuts defined in section 6.3.2 have been applied to the data, and the events were reconstructed using the source positions obtained from the *false source method* described in the previous section. Note that the distributions are very similar (yet not identical), and thus one can assume that the weather conditions, the *LONS* and telescope performance were very similar for *ON* and *OFF observations*.

The image parameters distributions for the *ON* and *OFF data* taken for Mkn 421 are shown in figure 6.11. Note that the agreement between the *ON-OFF* distributions of LENGTH values and (especially) WIDTH values is not as good as in the case of the Crab. This effect is partly explained by the fact that the zenith angle *ZA* of the *ON observation* is somewhat larger than that of the *OFF observations* (see table 6.2), and thus the images from the *ON data* are (in average) somewhat smaller (*i.e,* smaller LENGTH and WIDTH) than those from the *OFF data*.

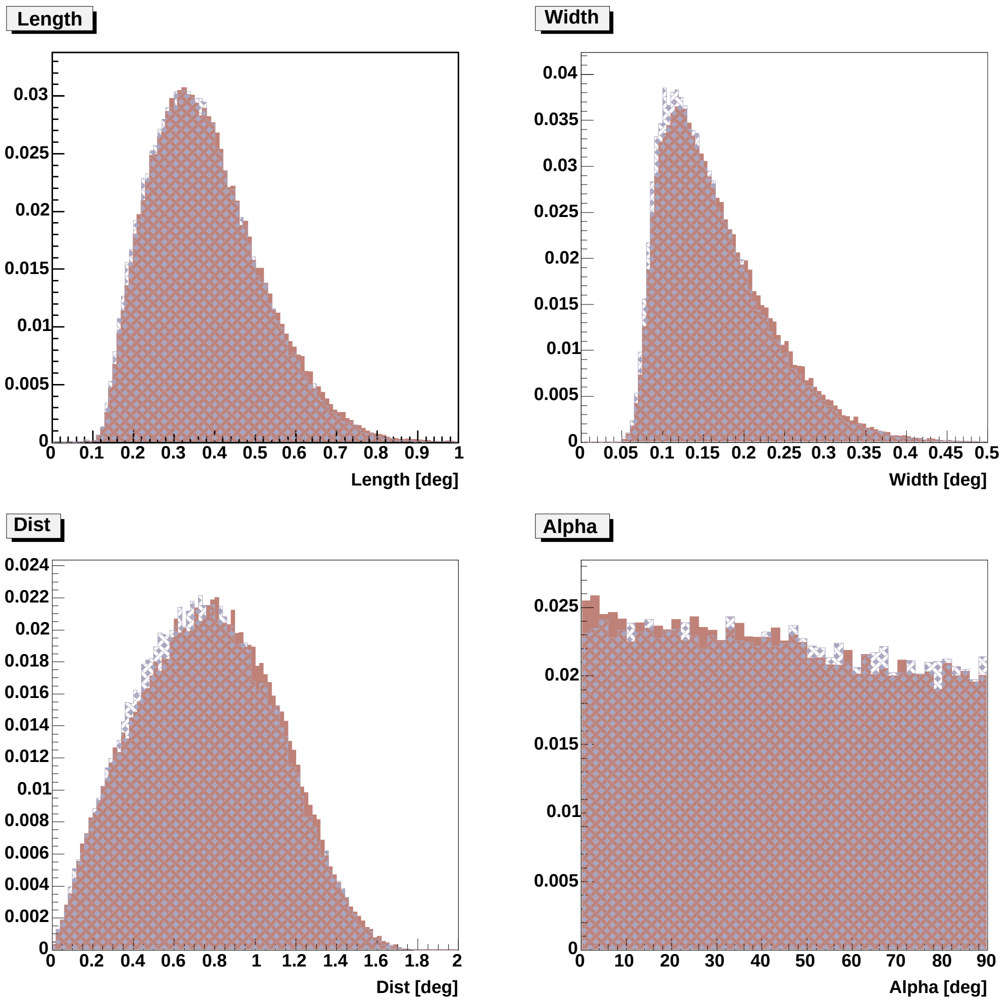

Figure 6.10: *Distribution of LENGTH, WIDTH, DIST and ALPHA parameters for shower images from ON data (brown filled histograms) and OFF data (blue shadow filled histograms) from the observations performed on the Crab Nebula. All distributions are normalized to unit area for a better comparison. The filter cuts defined in section 6.3.2 were used, but no γ/h separation cuts were applied to the data.*

It is worth to point out that the γ signal in the case of Mkn 421 is so strong, that it is very well visible at low ALPHA values by just applying the filter cuts. Note that at ALPHA values above 10° the agreement between *ON* and *OFF data* is very good.

I want to point out that the distribution of the image parameters for Crab and Mkn 421 are quite similar. The strong image cleaning together with the strong filter cuts removed all the small images, and the remaining (large) images are not very much affected by the possible performance problems/variations during the night. Note also that the somewhat larger *LONS* at the Crab sky location (galactic source) as compared to the sky location of Mkn 421 (extragalactic source) does not have a big influence on the (large) images that survive the data preprocessing described in section 6.3.2.

6.3.5 Optimization of cuts which depend on SIZE and DIST

The optimization of the cuts was performed using real data. At the current state of the telescope, the Monte Carlo simulations do not describe the experimental data sufficiently well, as I show in appendix E. Hence the simulated data could not be used to optimize the *γ/h separation cuts.*

I decided to optimize the cuts on a fraction of the data from Mkn 421, and then to apply the optimized cuts to both the data from Mkn 421 and the data from Crab. The arguments supporting this strategy were the following ones:

- *1)* The γ signal from Mkn 421 was significantly stronger than the one from Crab, as one can notice from the ALPHA distributions shown in figures 6.10 and 6.11. Therefore, the optimization of the cuts is easier in the data set from Mkn 421.

- *2)* The location of Mkn 421 in the telescope camera was determined more accurately than the one of Crab. This is basically due to *1)*.

- *3)* The distribution of the image parameters for Crab and Mkn 421 are quite similar, as one can note by comparing figures 6.10 and 6.11. Therefore, the *γ/h separation cuts* optimized on data from Mkn 421 should also reject efficiently (in first order) the background events contained in the data set from the Crab Nebula.

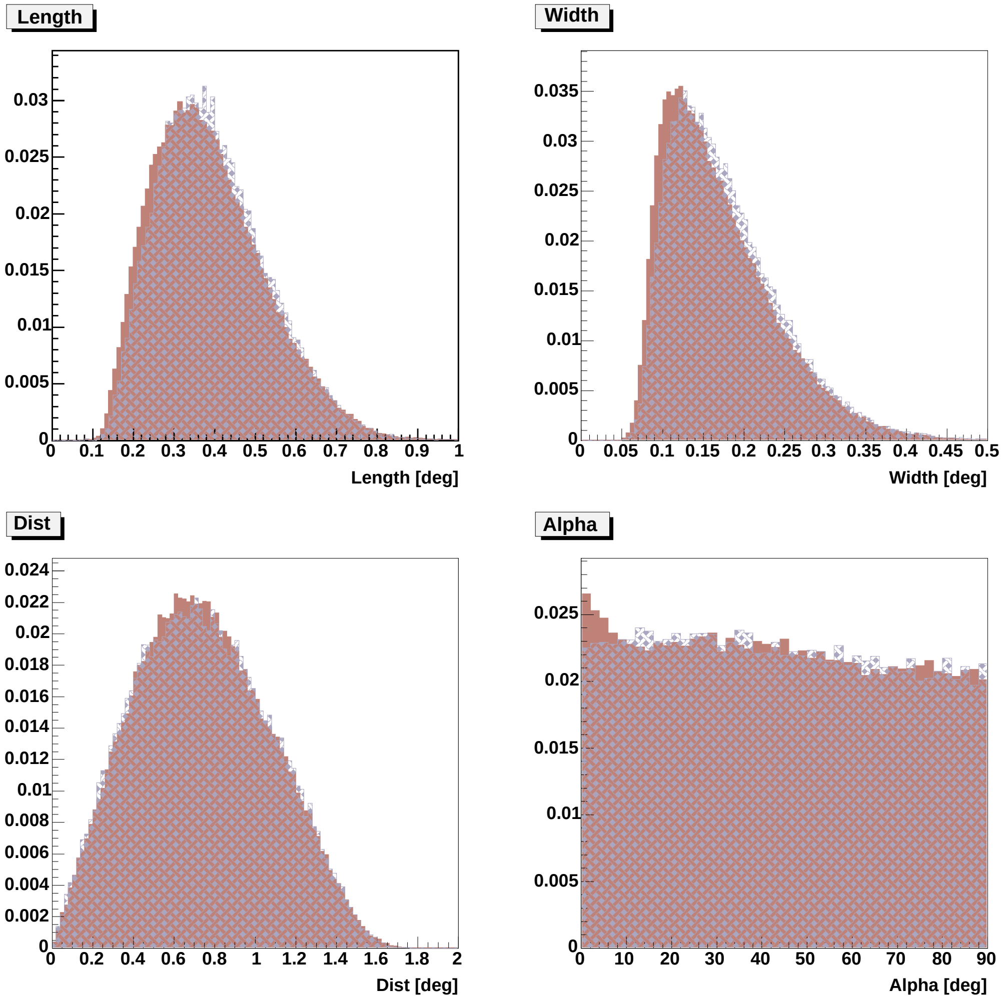

Figure 6.11: *Distribution of LENGTH, WIDTH, DIST and ALPHA parameters for shower images from ON data (brown filled histograms) and OFF data (blue shadow filled histograms) from the observations performed on Mkn 421. All distributions are normalized to unit area for a better comparison. The filter cuts defined in section 6.3.2 were used, but no γ/h separation cuts were applied to the data.*

The optimized γ/h *separation cuts* were determined as explained in section 6.2.3. The (upper and lower) cuts in LENGTH, WIDTH and DIST were parametrized as:

$$\begin{aligned} CUT^i \quad = \quad & CUT_0^i \; + \; a^i \cdot [DIST^2 - DIST_{OFFSET}^2] \; + \\ & b^i \cdot [lnSIZE - lnSIZE_{OFFSET}] \; + \\ & c^i \cdot [lnSIZE - lnSIZE_{OFFSET}]^2 \end{aligned} \tag{6.13}$$

where $DIST_{OFFSET}$ and $SIZE_{OFFSET}$ were set to 0.9° and 3000 photons respectively.

The cut in the ALPHA value was fixed to 12°. Introducing additional parameters or correlations between the parameters (like higher order dependences on $DIST^2$) did not improve significantly the results. Actually, in some cases it was found that, when including more parameters and/or correlations, the optimized cut parameters were *overtrained.* This might be due to the relatively small sample of data (less than two hours) we were working with.

When optimizing the cuts, the upper cut in the DIST value was restricted to values below 1.4°(*i.e,* $CUT_{UP}^{DIST} \leq 1.4°$). From the Monte Carlo simulations we know that there are basically no γ images above 1.4° (see figure 6.4). However, due to the fact that the source is not located at the center of the camera, but 0.1°-0.2°apart, the acceptance of the camera for γ showers might be somewhat different from that of the Monte Carlo, and this upper limit might not be optimum. In any case the fraction of events (mainly hadrons) in real data above 1.4° is quite small, as can be seen from figures 6.10 and 6.11.

Because of the small differences between the *ON* and *OFF* distributions of the image parameters of both the Crab and Mkn 421 data (see section 6.3.4), the efficiency of the γ/h *separation cuts* will be in general somewhat different for *ON* and *OFF data*. In order to by-pass this problem, I used formula 6.9 for the computation of the normalization factor α. The *background region* in the *alpha plot* used for this calculation was chosen to be from 30° to 90°. Note that, due to the real γs contained in the *ON data*, the normalization constant computed in this way might slightly overestimate the calculated background content in the signal region. As discussed in section 6.2.1; only 0.2% of the total amount of simulated gamma images with SIZE > 2000 photons lie at ALPHA > 30° after the application of the γ/h *separation cuts* presented in this section (see table 6.3). Because of the differences between simulated and real data (see appendix E), I can only consider this number as a coarse estimate of the fraction of the real γs lying in the *background region* of the *alpha plot*. In any case, the possible overestimation in the number of *background events* would mean that the computed number of *signal events* is somewhat underestimated. Therefore, the proposed method is a conservative approach to extract the γ signal from the data.

In order to check the reliability of the optimization and to recognize a possible *overtraining*, I divided the entire data set from Mkn 421 into two statistically independent samples that contained (roughly) the same number of events. I optimized the cut parameters in one of them (the *training sample*), and then I tested the optimized cut parameters on the other one (the *test sample*). A (statistically) significant difference in the number of excess events between the *training sample* and the *test sample* would indicate an overtraining.

The *alpha plot*s obtained when applying the optimized γ/h *separation cuts* on the *training sample* and the *test sample* from Mkn 421 data are shown in figure 6.12. The red curve shows the second order polynomial fit to the *OFF data* after the γ/h *separation cuts*. Note that the quality of the fit (based on the χ^2-probability value) is good for both the *training sample* and the *test sample*; and hence the background content in the *signal region* of the *alpha plot* (ALPHA $< 6^\circ$ in this case) can be estimated by using the fit function. The blue line is a fit to the *ON data* points using a second order polynomial function (background) plus a gaussian function (signal). The purpose of this fit is just to guide the eye of the reader and provide a qualitative impression of the goodness of the signal; yet I do not use it to quantify the quality of the γ signal (*i.e,* computation of the number of excess events and the significance of the γ signal), as it has been done elsewhere [100, 97].

Note that the detected number of *signal events* (*excess events* in the *alpha plot*s) in the *training sample* and the *test sample* are statistically compatible. The shape of the distribution of ALPHA values for the *training sample* and the *test sample* are also very similar for both *ON data* and *OFF data*. So we concluded that the optimization procedure was quite unbiased.

The value of the parameters CUT_0^i, a^i, b^i and c^i that define the shape of the optimum dynamical cuts are shown in table 6.3.

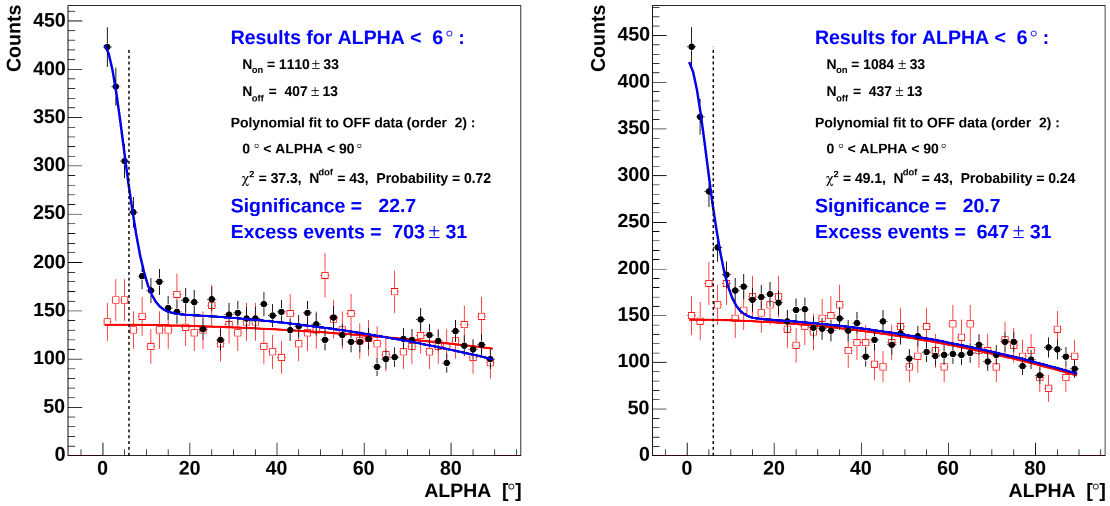

(a) **(b)**

Figure 6.12: *Alpha plots for a) the training sample and b) the test sample from the Mkn 421 observations. The black filled circles represent the ON data, and the red empty squares the OFF data; both after the application of the optimized γ/h separation cuts. The red curve is the second order polynomial fit to the OFF data, which is used to estimate the background content in the signal region of the alpha plot (i.e, $ALPHA < 6°$). The blue line is a fit to the ON data points using a second order polynomial function (background) plus a gaussian function (signal). The number of excess events and the significance of the signal are computed as described in sections 6.2.1 and 6.2.2 respectively. Only statistical errors are considered.*

CUT	CUT_0 ([°])	a (1/[°])	b ([°])	c ([°])
$LENGTH_{UP}$	0.291	0.0768	0.0320	0.00197
$LENGTH_{LOW}$	0.137	0.0673	-0.00329	0.00347
$WIDTH_{UP}$	0.121	0.00942	0.0130	-7.67e-05
$WIDTH_{LOW}$	0.0553	0.00677	0.0127	0.00111
$DIST_{UP}$	1.22	0.0	0.106	0.00212
$DIST_{LOW}$	0.608	0.0	0.0390	1.48e-4

Table 6.3: *Value of the parameters that define the shape of the dynamical cuts that maximize the significance of the signal in the training sample.*

Figure 6.13 shows scatter plots displaying the value of the cuts $LENGTH_{UP}$, $LENGTH_{LOW}$, $WIDTH_{UP}$, $WIDTH_{LOW}$, $DIST_{UP}$ and $DIST_{LOW}$ applied to the events of the entire Mkn 421 data set that survived the γ/h *separation cuts*. The value of the cuts is displayed *vs.* log(SIZE) to demonstrate the substantial variation of the cuts with the SIZE parameter. The dependence on the DIST parameter is smaller, as can be noticed from the available range of cut values for a given SIZE value. Note that the strong increase in the cut parameters with the SIZE is in very good agreement with the tendency observed in the simulated γ events shown in figure 6.6. The small variation of the cuts in LENGTH and (especially) WIDTH with the DIST value is also in agreement with the small variations shown in figure 6.7.

It is worth noticing that the cuts optimized on the experimental data from MAGIC (at SIZE $>$ 2000 photons) would work quite efficiently on the image parameter distributions of the Monte Carlo simulated data shown in figure 6.4. The efficiency of this set of cuts on the simulated data can be quantified by using the *quality factor* $\mathcal{Q}$, which is defined as

$$\mathcal{Q} = \frac{\epsilon_\gamma}{\sqrt{\epsilon_\kappa}} \tag{6.14}$$

where ϵ_γ and ϵ_κ are the cut efficiencies for γs and *hadron*s respectively, and are defined as the ratio of the number of events after the cuts to the number of events before the cuts. The

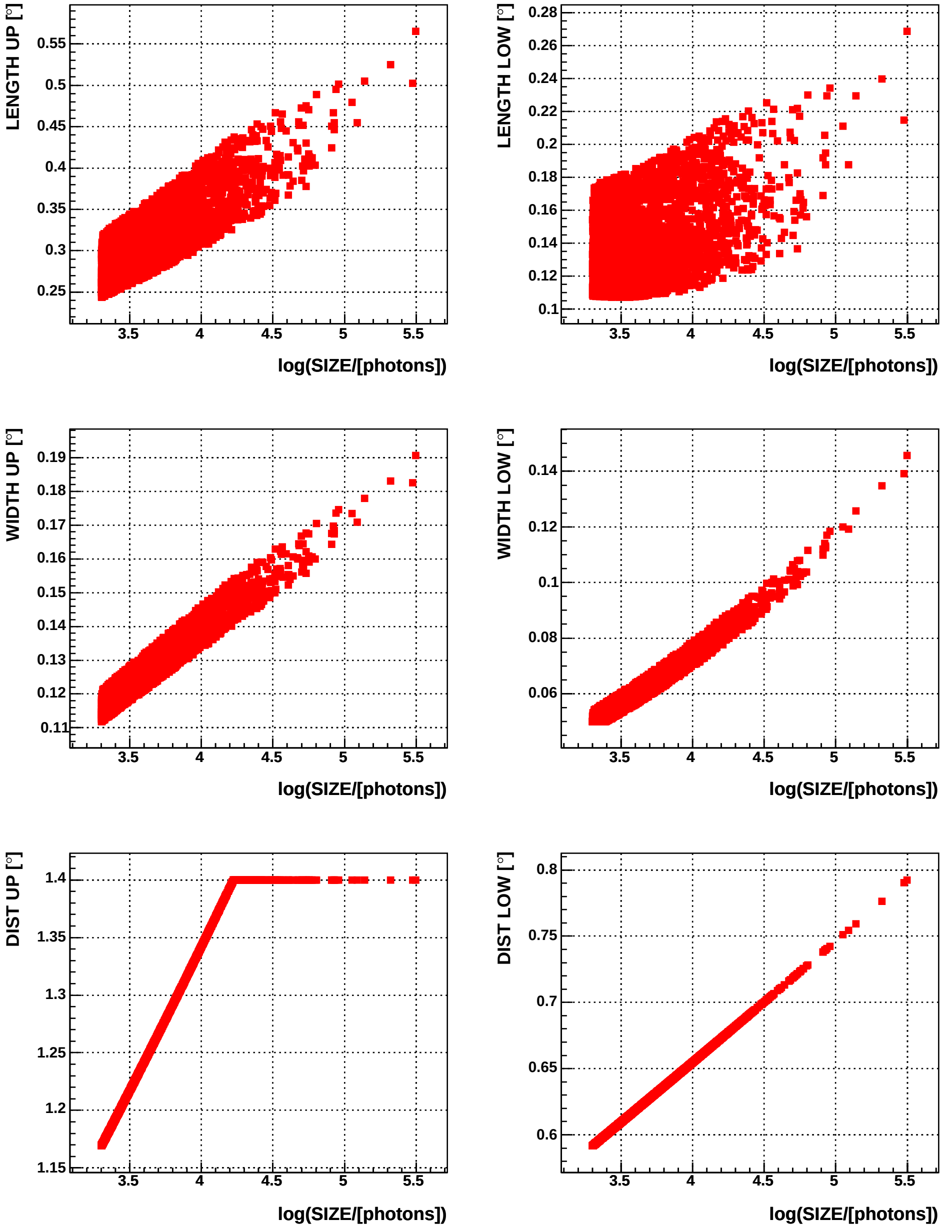

Figure 6.13: *Value of the cuts* $LENGTH_{UP}$, $LENGTH_{LOW}$, $WIDTH_{UP}$, $WIDTH_{LOW}$, $DIST_{UP}$ *and* $DIST_{LOW}$ *applied to the events from the entire Mkn 421 data set that survived the* γ/h *separation cuts. The value of the cuts is displayed vs. the log(SIZE) of the event. The available range of cut values (in LENGTH and WIDTH) is due to the linear dependence on* $DIST^2$ *in the cut parametrization described by equation 6.13.*

factor $\mathcal{Q}$, defined in this way, evaluates the $\gamma/hadron$ separation efficiency after the telescope trigger and the image cleaning procedures. Note that the detector trigger and the image cleaning procedures applied to the data would affect significantly the initial sample of events at low energies (*i.e,* close to the E_{th}). Yet when the images are large enough (which is the case when the cut SIZE $>$ 2000 photons is applied to the data), the effect of different trigger settings and/or image cleaning procedures on the number of events contained in the initial data sample is small.

The application of this set of cuts to the simulated data gives a $\mathcal{Q}$ of 6. This is not far away from the $\mathcal{Q}$ of 8 obtained with the *random forest* method [36]. It is worth mentioning that the higher $\mathcal{Q}$ obtained in [36] is expected because of the following two reasons:

- The number of image parameter cuts optimized in [36] is 14, and the dependences among all them are naturally considered in the *random forest* method. In the analysis presented in this section I optimized 6 cut parameters, which were assumed to depend only on 2 parameters.

- The $\gamma/hadron$ separation performed with the *random forest* was optimized on the Monte Carlo data whereas the dynamical cuts shown in table 6.3 were optimized on experimental data.

Therefore, we consider a very satisfactory result the $\mathcal{Q}$ value of 6 obtained when applying the analysis presented in this section (which is optimized on real data from MAGIC) to the Monte Carlo data.

6.3.6 Results and Discussion

From the good agreement observed between the results obtained with the *training sample* and the *test sample* of Mkn 421, we concluded that the optimized cuts were not significantly biased by peculiarities (statistical fluctuations) of the *training sample*. Therefore, we decided to apply the optimized cuts on the entire sample of Mkn 421 in order to compute the overall detected γ signal. The resulting *alpha plot* is shown in figure 6.14.

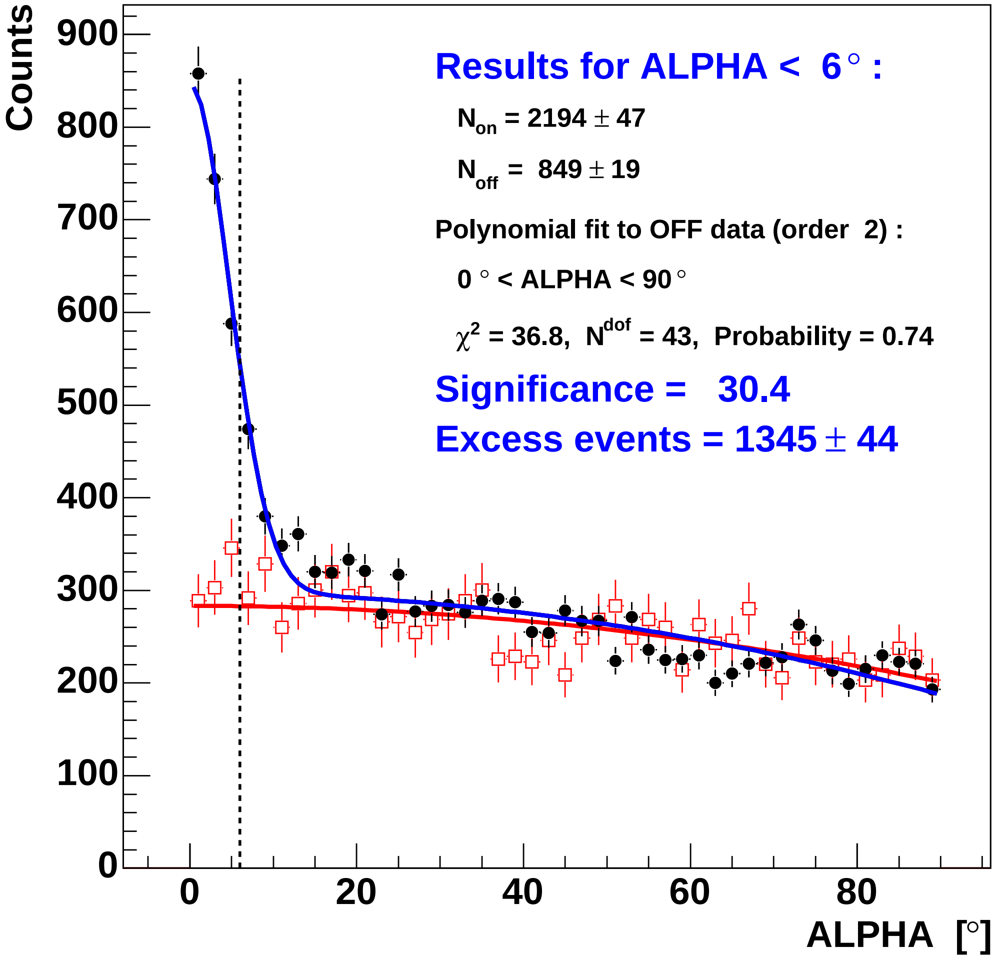

Figure 6.14: *Alpha plot for the entire data set of Mkn 421. The black filled circles represent the ON data, and the red empty squares the OFF data; both after the application of the optimized* γ/h *separation cuts. The red curve is the second order polynomial fit to the OFF data, which is used to estimate the background content in the signal region of the alpha plot (i.e, ALPHA* $< 6°$*). The blue line is a fit to the ON data points using a second order polynomial function (background) plus a gaussian function (signal). The number of excess events and the significance of the signal are computed as described in sections 6.2.1 and 6.2.2 respectively. Only statistical errors are considered.*

It is worth noticing the narrowness of the peak in the ALPHA distribution shown in figure 6.14; the FWHM of the signal peak is $\lesssim 6^\circ$. The analogue FWHM of the γ signals obtained with the small CT1 telescope of the HEGRA experiment was around 9°, despite the fact that the threshold energy of that telescope was 4-5 times larger [100, 97]. This is basically due to the fine pixelization of the MAGIC camera (inner pixels of 0.1° ϕ) compared to the large size of the pixels of the CT1 camera (0.25° ϕ). Besides, the reconstruction of the ALPHA parameter is also influenced by the small light content (typically SIZE $\lesssim 1000$ photons) of the CT1 images compared to that of the images used in this analysis (SIZE > 2000 photons).

Due to the sharp ALPHA peak, the significance of the signal, as well as the number of detected γs (excess events in the *alpha plot*) is very sensitive to the cut in the ALPHA variable. Figure 6.15 shows the variation in the number of *signal events* and significance of the signal as a function of the cut in the ALPHA value. Note that the maximum significance of the signal (exceeding 30 sigmas above noise) is obtained by cutting at 6°. Using this cut in ALPHA, the number of detected γs is 1345 ± 44, which implies a detected γ rate of 12.8 ± 0.4 γ/min. Instead, if the cut ALPHA $< 20^\circ$ is applied, the number of excess events increases up to 1906 ± 93, and the detected γ rate is 18.2 ± 0.9 γ/min.

It is worth mentioning that the error in the rates only includes statistical fluctuations. The computation of systematic errors would require a deeper study of the performance of the telescope, which we consider to be of minor value and interest for a detector which is still in commissioning phase.

Note from figure 6.14 the good agreement between the *ON* and the *OFF data* at large ($\gtrsim 30^\circ$) ALPHA values. However, at ALPHA values between 15° and 30° the amount of *ON* events is slightly larger than that of *OFF* events. Figure 6.15 shows that there are ∼1800 excess events in the ALPHA range between 0° and 15°, whereas in the range between 15° and 30° there are ∼200 excess events; which is about 11% of the events located at ALPHA $< 15^\circ$.

In the particular case of simulated γ images with SIZE > 2000 photons, the fraction of events in the ALPHA range between 15°and 30°, relative to the number of events at ALPHA $< 15^\circ$, is 7.5% (see figure 6.8). However, this fraction decreases to 2.1% when applying the *γ/h separation cuts* defined by equation 6.13 and the parameter values given in

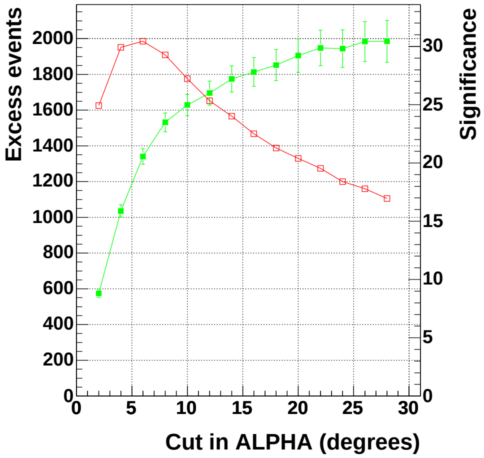

Figure 6.15: *Number of excess events (filled green squares) and significance (empty red squares) of the signal computed from the entire data set of Mkn 421 for several cuts in the ALPHA value. The number of excess events and the significance are computed as described in sections 6.2.1 and 6.2.2 respectively. Only statistical errors are considered.*

table 6.3. Because of the current disagreements between simulated data and real experimental data (see appendix E), this number should be just considered as a rough estimate of the real fraction of γ events located in the ALPHA range between 15° and 30°.

On the other hand, a possible reason for the presence of *signal events* at relatively large ALPHA values is a wrong reconstruction of the ALPHA parameter for some events. This could have happened due to a miscalculated position of the source location for these events, or due to problems in the quality of data. Because of the performance problems described in section 6.3.1 we cannot exclude these possibilities.

By applying the above mentioned *γ/h separation cuts* to the entire data set of the Crab Nebula we also found a significant signal. The resulting *alpha plot* is shown in figure 6.16, and the variation of the number of *signal events* and significance of the signal as a function of the applied cut in ALPHA is shown in figure 6.17. Note that the peak in the ALPHA distribution is broader than that of Mkn 421, and consequently the significance of the signal is less sensitive to the cut in ALPHA. By accepting events with ALPHA $< 10°$, the signal is significant at a level of 12.5 sigmas, and the excess is 543 ± 43, which implies a detected γ rate of 6.4 ± 0.5 γ/min. Instead, if the cut ALPHA $< 20°$ is applied, the number of excess events increases up to 758 ± 67, and the detected γ rate is 8.9 ± 0.8 γ/min. As stated before, we have only considered statistical errors so far.

The detected γ rate measured for the Crab Nebula is about half the one we measured for Mkn 421. However, the $\gamma - ray$ flux of Mkn 421 is usually an order of magnitude lower than that of the Crab Nebula. Therefore, we concluded that Mkn 421 was in a strong flaring state during the night of 14th-15th February. It is worth mentioning that the increase in the photon flux from Mkn 421, during February 2004, had been already observed in the very high energy $\gamma - ray$ domain ($\gtrsim 300\ GeV$) by the WHIPPLE Telescope, and also in the *X-ray* domain (2-10 keV) by the All Sky Monitor detector (ASM) borne on the Rossi X-ray Timing Explorer satellite (RXTE).

In the ALPHA range from 15° to 30° of the *alpha plot* shown in figure 6.16, the number of *ON* events is substantially larger than that of *OFF* events. By comparing the number of *OFF* events (after the γ/h *separation cuts*) from Crab and Mkn 421, one can notice that the background level from both observations agree quite well. The background content in the *signal region* of the *alpha plot* shown in figure 6.16 is $N_{OFF}^{AfterCuts}= 1212 \pm 20$. This value can be compared to that of the *alpha plot* shown in figure 6.14, which is 849 ± 19, if it is multiplied by the ratio of the observation times (105 min/85 min) and the ratio of the cuts in ALPHA (6°/10°). The resulting (converted) $N_{OFF}^{AfterCuts}$ from the Crab Nebula is 898 ± 15, which is statistically compatible to that of Mkn 421. Therefore, we concluded that the *OFF data* related to the Crab observations behaved normally. We think that this significant "excess" of *ON* events in the range 15°-30° is due to real γ events whose ALPHA values were not well reconstructed. As mentioned for Mkn 421, possible reasons for the γ events to be located outside the "alpha peak" are a somewhat wrong source location in the camera, or a somewhat poor data quality. We want to stress that both effects are expected to have a larger impact in the case of Crab because of the smaller γ signal. The worse source location (in the telescope camera) for the Crab Nebula compared to that of Mkn 421 was already pointed out in section 6.3.3.

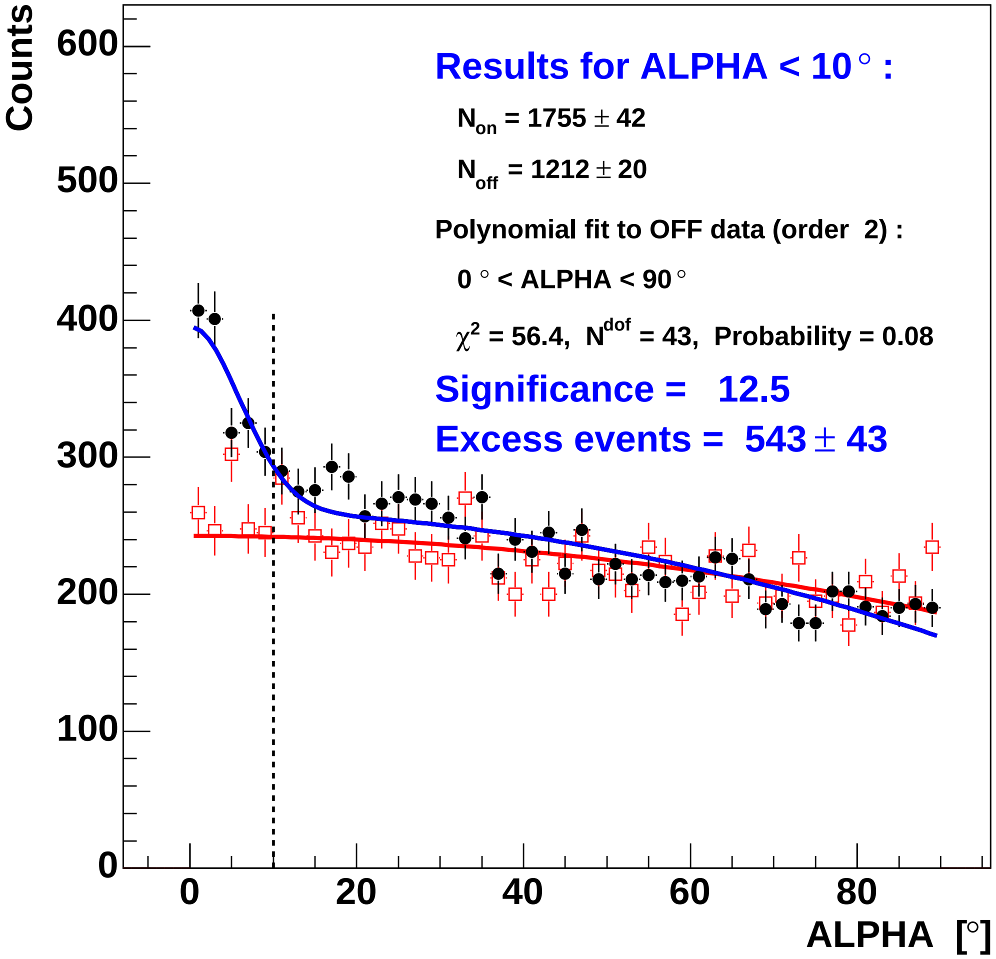

Figure 6.16: *Alpha plot for the entire data set of the Crab Nebula. The black filled circles represent the ON data, and the red empty squares the OFF data; both after the application of the optimized* γ/h *separation cuts. The red curve is the second order polynomial fit to the OFF data, which is used to estimate the background content in the signal region of the alpha plot (i.e, ALPHA* $<$ *10°). The blue line is a fit to the ON data points using a second order polynomial function (background) plus a gaussian function (signal). The number of excess events and the significance of the signal are computed as described in sections 6.2.1 and 6.2.2 respectively. Only statistical errors are considered.*

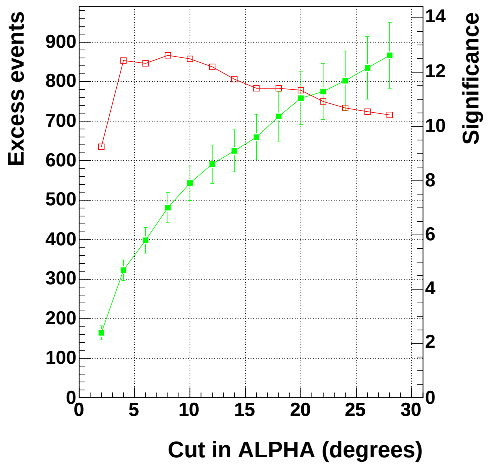

Figure 6.17: *Number of excess events (filled green squares) and significance (empty red squares) of the signal computed from the entire data set of the Crab Nebula for several cuts in the ALPHA value. The number of excess events and the significance are computed as described in sections 6.2.1 and 6.2.2 respectively. Only statistical errors are considered.*

The γ rate from the Crab Nebula can be used to give a very rough estimate of the *threshold energy* of the telescope. The idea is to compare the measured γ rate with that expected from the known $\gamma - ray$ flux of the Crab and the efficiency of the MAGIC Telescope to detect $\gamma - rays$. This estimation is based on two assumptions: *a)* the flux of the Crab at low energies ($\sim 100\ GeV$) can be extrapolated from the measured flux of the Crab Nebula at energies above 300 GeV, and *b)* the Monte Carlo simulations describe in first order the experimental data.

The efficiency of the telescope to detect $\gamma - rays$ is computed in terms of the *collection area* (see section 2.3.5). By calculating the collection area of the telescope using the optimized cuts described in section 6.3.5 (which were applied to the experimental data), and folding it with the expected $\gamma - ray$ flux from the Crab, one can compute the γ rate expected to be detected from the Crab Nebula.

I performed this calculation using the following $\gamma - ray$ flux determined by the WHIPPLE collaboration [4]:

$$\frac{d\mathcal{F}_\gamma(E)}{dE} = 3.25 \times 10^{-7} \times \left(\frac{E}{[TeV]}\right)^{-2.44-0.151\cdot log_{10}(E/[TeV])} \; m^{-2}s^{-1}TeV^{-1} \qquad (6.15)$$

This flux was obtained by combining the data from the WHIPPLE Telescope with those from *EGRET* above 1 GeV, and fitting the resulting spectrum with a power law whose index is energy dependent.

The γ rate expected for this flux (using the same preprocessing and γ/h *separation cuts* applied to the experimental data) is 10.4 γ/min. As mentioned before, the measured γ rate from the Crab (ALPHA $< 10°$) is 6.4 γ/min; which, at this early stage of the experiment, we interpreted as a very satisfactory result. Note that a better reconstruction of the ALPHA parameter (provided by a better source position determination) would increase substantially the number of excess events inside the peak of the *alpha plot*.

The differential γ rate for simulated data obtained when using the photon flux given by the expression 6.15 and the analysis approach described in this section (data preprocessing and γ/h *separation cuts*) shows the maximum at about 150 GeV. The peak in the differential rate after the analysis is usually considered to be the *physics threshold energy* of the detector[17]. The lower detected γ rate from the Crab Nebula (compared to the one obtained from the Monte Carlo simulations), provides a very preliminary estimate of ~200 GeV as the *physics threshold energy* of the MAGIC Telescope. We want to point out that this value is computed for the performance of the MAGIC Telescope during the night 14th-15th February 2004 (still in the commissioning phase) and the data analysis described in this section. This analysis considers only images with SIZE $>$ 2000 photons; which rejects most of the low energy events.

6.4 Conclusions

The analysis of the first observations performed with the MAGIC Telescope during the night of 14th-15th February 2004 (still in the commissioning phase) was a challenging task

---

[17] Note that the threshold energy E_{th} of the telescope is defined as the peak in the differential trigger rate, which is always lower than the physics threshold energy.

where the analysis procedures which I developed could be tested with real experimental data for the first time. The outcome of this analysis was more successful than it was anticipated. It pinpointed some performance problems in the telescope, and thus, it was very useful to debug the telescope performance. In spite of the initial telescope deficiencies (see section 6.3.1), we managed to detect very clear signals from both Mkn 421 and the Crab Nebula. Even in this preliminary analysis, one can already get a flavor of the superior quality of the signals (*alpha plot*s) of the MAGIC Telescope compared to previous telescopes like the CT1 of the HEGRA experiment.

I also want to point out that the full potential of the programs which were developed has not yet been exploited. As the performance of the telescope improves, also the analysis procedures will get better tuned (additional cut parameters, additional dependences among them...) and stronger signals at lower energies will be achieved. The universe is waiting for us...

Appendices

Appendix A

Measurement of the *QE* of the used PMTs

In this section I will report about the method used to measure the QE of the PMTs. I will describe the instruments used in the experimental setup and I will estimate the error related to the measured QE value.

A.1 Description of the method used to measure the *QE*

The QE is a quantity used to express the sensitivity of a photosensor. It is defined as the number of photoelectrons emitted from the PhC divided by the number of incident photons ($i.e,\ \ QE = N_{phe}/N_{ph}$). The QE depends on the wavelength (λ) of the incoming photons. In order to perform a direct measurement of the QE of a PMT for a wavelength λ_0, one needs to measure both the photocurrent produced in the PhC when it is illuminated with light of wavelength λ_0 ($I(\lambda_0)$), and the incident light flux for this particular wavelength ($F(\lambda_0)$). Since $F(\lambda_0)$ is difficult to measure in our laboratory, we decided to obtain the $QE(\lambda)$ indirectly, that is to say, through the comparison with a reference photosensor whose

$QE(\lambda)$ is well known,

$$\frac{QE^{PMT}(\lambda_0)}{QE^{REF}(\lambda_0)} = \frac{\frac{N_{phe}^{PMT}(\lambda_0)/\ t}{N_{ph}(\lambda_0)/\ t}}{\frac{N_{phe}^{REF}(\lambda_0)/\ t}{N_{ph}(\lambda_0)/\ t}} = \frac{\frac{I^{PMT}(\lambda_0)}{F(\lambda_0)}}{\frac{I^{REF}(\lambda_0)}{F(\lambda_0)}} = \frac{I^{PMT}(\lambda_0)}{I^{REF}(\lambda_0)} \tag{A.1}$$

where $I^{PMT}(\lambda_0)$ and $I^{REF}(\lambda_0)$ are the photocurrents measured in the PMT and in the reference photosensor respectively. Therefore, the QE of the PMT for a wavelength λ_0 is given by the following expression:

$$QE^{PMT}(\lambda_0) = \frac{I^{PMT}(\lambda_0)}{I^{REF}(\lambda_0)}\, QE^{REF}(\lambda_0) \tag{A.2}$$

If the wavelength of the light is varied from an initial wavelength λ_1, to a final wavelength λ_2, the curve $QE(\lambda)$ can be found for this range of wavelengths.

In order to measure the photocurrent produced in the *PhC* of the PMT, we short-circuited all dynodes to the anode, and applied a voltage of 200 V between the *PhC* and the anode to ensure that all the *phe*s produced are collected.

A.2 Description of the setup used to measure the *QE*

We used the PIN diode *S1337-1010BQ* from HAMAMATSU as reference photosensor. It has a square shape, and its surface area is 1 cm^2 . Its entrance window is made from quartz, which makes it sensitive to light well below 300 *nm*. Figure A.1 shows a picture of this PIN diode together with a ET9116A PMT.

The diode has a detailed data-sheet where it is reported its spectral response in the wavelength range from 200 *nm* to 1200 *nm*. The spectral response of the used diode was measured by the *Solid State Division* of HAMAMATSU in 2002. In the data-sheet, the spectral response of the diode is given in terms of the *Radiant Sensitivity* (S_k). The S_k is the photoelectric current from the photocathode divided by the incident light energy flux at a given wavelength, and it is usually expressed in units of amperes per watts (A/W). The relation between the QE and the S_k is

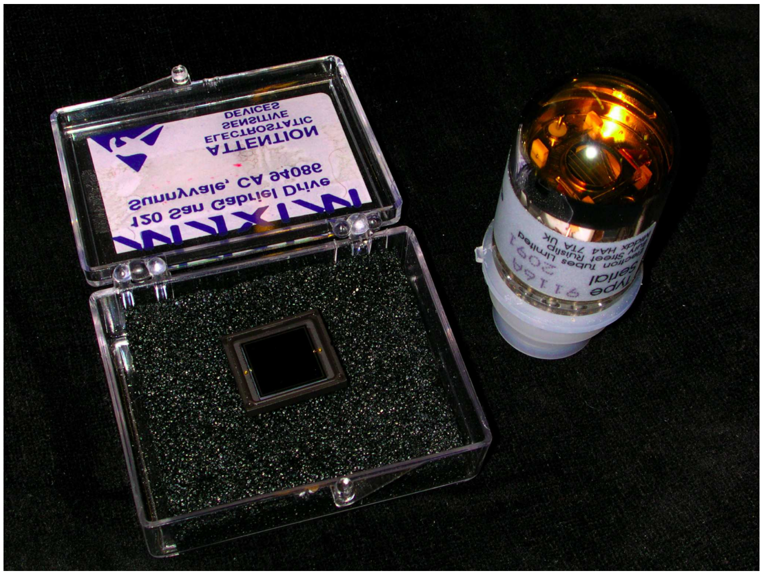

Figure A.1: *Photograph of the PIN diode S1337-1010BQ from HAMAMATSU (left) together with a ET9116 PMT (right).*

$$QE(\%) = \frac{h \cdot c}{\lambda \cdot q_e} \cdot S_k \cdot 100\% = \frac{1240}{\lambda(nm)} \cdot S_k(A/W) \cdot 100\% \tag{A.3}$$

where h is the Planck's constant, λ is the wavelength of the incident light, c is the speed of light and q_e is the electron charge. The S_k and the QE of the used reference diode are shown in figure A.2. The S_k values are taken from the data-sheet of the diode, and the QE values are calculated using the formula A.3.

We used the spectrofluorometer SFM 25 type from KONTRON INSTRUMENTS (figure A.3*a*) to produce monochromatic light. The device is equipped with a Xenon lamp that produces a wide light spectrum (from 250 *nm* to 750 *nm*), and a monochromator with a diffraction grating of 1200 grooves/*mm*, and 450 *nm* blaze wavelength (see appendix B for details about the physics of diffraction gratings). The accuracy in the peak of the transmitted wavelength range is $\lesssim 1$ *nm*, and the produced spectral bandpass is about 5 *nm*.

The intensity of the light produced by the SFM 25 spectrofluorometer at wavelengths below 340 *nm* is rather faint compared to that emitted at other wavelengths, and hence the

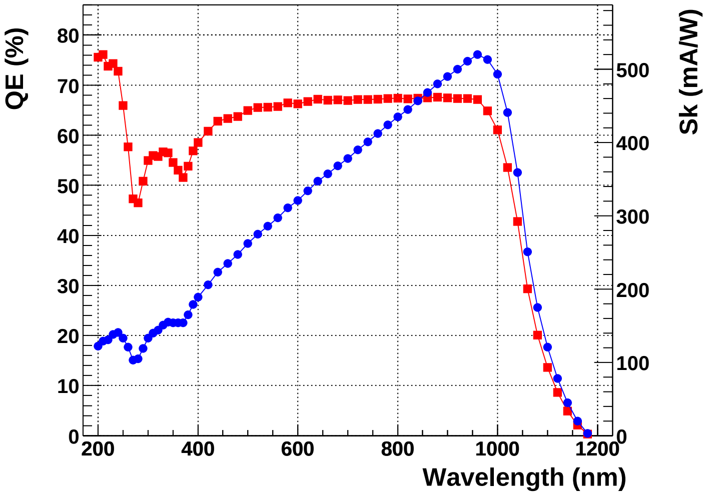

Figure A.2: *Quantum Efficiency (red squares) and Radiant Sensitivity (blue circles) of the PIN diode used as reference photosensor.*

contribution from *stray light*[1] may not be negligible. In order to block a large fraction of this unwanted light, we used a band pass filter; the *U-340* type from *Edmund Scientific*. The transmitted spectral bandpass of this filter is centered at 340 *nm*, and has a FWHM of 85 *nm*. The *U-340* was used in the wavelength range between 260 *nm* and 380 *nm*.

The light is collimated and directed to the *PhC* of the PMT. The illuminated region has an area of about 0.3 cm^2. Figure A.3*b* shows the PMT and the diode attached to the collimator, which is illuminated by the exit light beam from the monochromator.

In picture A.3*a* it is also visible the picoamperimeter used to read the currents, the *Keithley model 485*; and the power supply used to apply the voltage between the *PhC* and the dynode system of the PMT, the NGM 280/0.1 type from *Rohde and Schwarz*.

A.3 Estimation of the error in the measured QE value

The error in the PMT QE measurement can be obtained by simple error propagation on

---

[1] The stray light is the light from undesired wavelengths which is not totally absorbed inside the monochromator and adds to the exit light beam.

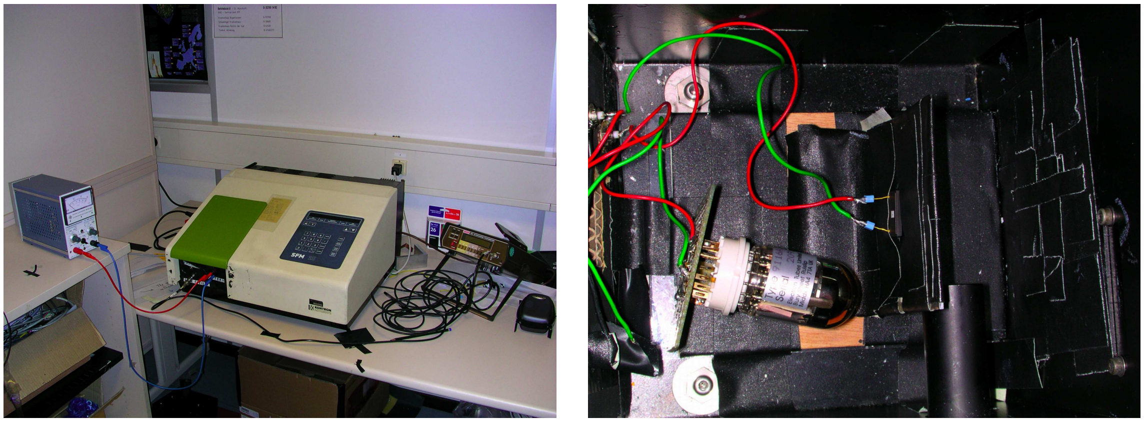

(a) **(b)**

Figure A.3: *a) Photograph of the experimental setup that was used to measure the QE of the PMTs. From left to right; power supply NGM 280/0.1 type from Rohde and Schwarz, spectrofluorometer SFM 25 type from KONTRON INSTRUMENTS, and picoamperimeter modell 485 from Keithley. b) PMT and reference diode in the interior of the spectofluorometer; the diode is attached to the 0.3* cm^2 *hole of the collimator.*

formula A.2[2]

$$\frac{\Delta_{QE^{PMT}}}{QE^{PMT}} = \sqrt{\Big(\frac{\Delta_{I^{PMT}}}{I^{PMT}}\Big)^2 + \Big(\frac{\Delta_{I^{REF}}}{I^{REF}}\Big)^2 + \Big(\frac{\Delta_{QE^{REF}}}{QE^{REF}}\Big)^2} \tag{A.4}$$

where $\Delta_{QE^{REF}}$ is given by the data-sheet of the *S1337-1010BQ* diode, and the quantities $\Delta_{I^{PMT}}$ and $\Delta_{I^{REF}}$ come from the accuracy in the current reading.

The S_k of the diode is given in the data-sheet with an accuracy of 0.001 A/W. Neglecting the error in the wavelength (which is about 1 nm), the relative error in the QE is given by

$$\frac{\Delta_{QE^{REF}}}{QE^{REF}} \approx \frac{\Delta_{S_k}}{S_k} \tag{A.5}$$

Note from the S_k values shown in figure A.2 that, according to formula A.5, $\frac{\Delta_{QE^{REF}}}{QE^{REF}} \lesssim 1\%$ in the wavelength range from 250 nm to 700 nm.

I computed the quantities $\frac{\Delta_{I^{PMT}}}{I^{PMT}}$ and $\frac{\Delta_{I^{REF}}}{I^{REF}}$ as the sum (in quadrature) of the following three terms:

- The accuracy of the current read-out of the Keithley electrometer, which is 1%.
- The reproducibility of the measurement. Mechanical tolerances in the position of the PMT and PIN diode with respect to the collimator, as well as subtle changes in the light intensity produced by the Xenon lamp, prevent us to get exactly the same results when performing two “non-consecutive” measurements. By “non-consecutive” measurements I mean that the PMT and/or diode are taken out from the set-up and put back again few minutes (15-20) later. We found that in most of our tests the currents measured in two “non-consecutive” measurements agree within 1% accuracy[3].
- Stray light from the monochromator and spurious light inside the cavity where the measurements are performed. This light adds to the monochromatic light and produces

---

[2] This formula is applied to each single wavelength λ_0.

[3] Disagreements of up to 2% were found only occasionally.

some additional current in the PMT and/or reference diode. The stray light and spurious light are only significant (and the dominant term) at wavelengths where the relative intensity of the Xenon lamp is low (*i.e,* below 300 *nm*) or where the response of the PMT is poor (*i.e,* below 300 *nm* and above 620 *nm*).

The spurious light inside the cavity was estimated by reading the PMT and the diode currents when the Xenon lamp was switched off. We found these currents to be very low; ∼0.2 *nA* in the PMT, and ∼0.1 *nA* in the diode. The diode has a higher and wider spectral response than the PMT, yet the current produced in the PMT by the spurious light in the cavity is larger than that of the diode. The reason is the hemispherical entrance window of the PMT. As can be seen in figure A.3b, while the diode is attached to the collimator, and the only light sensitive region is the one defined by the hole of the collimator, the PMT is also sensitive to light coming from other directions. Besides, the dark (leakage) current produced by the 200 *V* applied between the *PhC* and the dynode system of the PMT also contributes to the measured 0.2 *nA*. It is worth noticing that the currents produced by the selected monochromatic light were typically larger than 100 *nA*, and thus the effect of the spurious light on the *QE* measurement is negligible.

The stray light[4] from the monochromator is very difficult to measure, since it has to be measured with the Xenon lamp switched on, and thus, the current produced in the photosensors is mainly due to the monochromatic light set in the monochromator. Besides, the stray light depends on the position of the grating inside the monochromator; *i.e,* it is different for the different selected wavelengths. We did a very coarse estimation of the effect produced by the stray light in our setup by measuring the current in the PMT and the diode when the wavelength of the monochromatic light was chosen to be outside the spectral emission of the used lamp; below 200 *nm*, above 800 *nm*, and also above 400 *nm* when using the *u-340* filter. Other estimates (for the PMT) were obtained by reading the currents when the wavelength range was outside the spectral sensitivity of the PMT, which is significant only in the range 270-700 *nm*. The

---

[4] For simplicity, in the definition of stray light I included the light coming from the higher diffraction orders of the monochromator (see appendix B for details related to the diffraction grating physics).

measured currents produced by the stray light (for the different selected wavelengths) spread from 0.1 nA to 0.5 nA. The current produced by the spurious light in the cavity has been already subtracted. Note that the currents produced by the stray light are substantially smaller than the ones produced by the selected monochromatic light, which were typically in the range 100-300 nA. Nevertheless, these small currents might become the leading term in the error when the measured currents (produced mainly by the selected monochromatic light) are below 30 nA, which occurs when using the PMT at wavelengths above 620 nm, and wavelengths below 270 nm (290 nm in non coated PMTs). Due to the complexity of performing a precise estimation of the effect produced by the stray light, I decided to simplify the problem adopting a very conservative approach. I defined the pedestal for current measurements (current produced by spurious light and stray light) to be 0.5 nA for both, the PIN diode and the PMT; and considered possible variations of this current by a factor 2, *i.e,* 1 nA. Therefore, the contribution to $\frac{\Delta_{QE}}{QE}$ produced by this effect was estimated to be $\frac{1}{I(nA)}$, where I is the current of the PMT and/or the reference diode. Note that in the wavelength range between 300 nm and 600 nm (where the measured currents are $\gtrsim 100 nA$) this term is significantly lower than the ones coming from the accuracy of the electrometer and the reproducibility of the measurement.

Inserting all these quantities in formula A.4, one can compute $\frac{\Delta_{QE}}{QE}$ for each single wavelength. In the wavelength range 300-600 nm, $\frac{\Delta_{QE}}{QE} \approx 2\%$.

Appendix B

The diffraction grating physics

The working principle of diffraction physics and monochromators can be found in many text books. I will use [111] and [112] to report about some basic concepts that are useful to understand the setup used to measure the QE of the PMTs.

Monochromators use diffraction gratings to produce monochromatic light from non monochromatic light. A typical diffraction grating consists of a substrate with a large number of parallel grooves ruled or replicated in its surface and overcoated with a reflecting material such as aluminium. The quality and spacing of the grooves are crucial to the performance of the grating.

The basic grating equation is the following one:

$$a(\sin I + sinD) \ = \ m\lambda \tag{B.1}$$

where a is the separation between two grooves, I is the angle of the incident light, D is the angle of the diffracted light, and m is an integer that denotes the order of diffraction.

When a monochromatic light beam strikes a grating, a given fraction of the light is diffracted into each order m = -2, -1 , 0 , 1 , 2 ..., as indicated in figure B.1*a*. On the other hand, if the grating is illuminated with a beam of polychromatic light, the light is dispersed so that each wavelength satisfies the grating equation B.1, as shown in figure B.1*b*.

As the grating is rotated inside the monochromator, the angles I and D vary, although

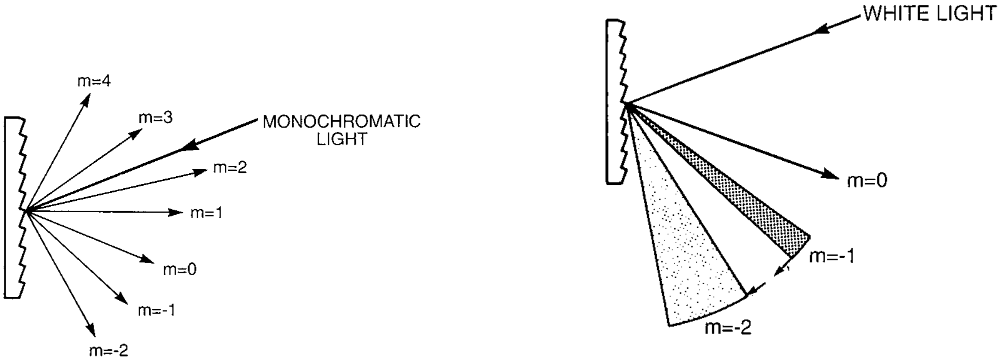

(a) **(b)**

Figure B.1: *a) Monochromatic light diffracted in a diffraction grating b) Polychromatic light diffracted in a diffraction grating (Positive orders have been omitted for clarity).*

the difference between them remains constant and is fixed by the geometry of the monochromator. Thus, a more convenient form of the grating equation to be used when dealing with monochromators is the following one:

$$2 \times a \times \cos\phi \times \sin\theta \;=\; m\lambda \tag{B.2}$$

where $\phi = \frac{I-D}{2}$ and $\theta = \frac{I+D}{2}$. The angle θ is usually denoted *grating angle.* If the angle D is equal to I and of opposite sign, then the grating angle θ is zero, and the light is simply reflected. In this case, the diffraction order m is zero. If the grating angle is positive then the order is positive (m = +1, +2 ...) and if the grating angle is negative, then the order is negative (m = -1, -2 ...).

Note that for a given position of the grating inside a given monochromator (i.e. ϕ and θ are fixed), the grating equation (B.2) is satisfied by several wavelengths at several diffraction orders. Therefore, at the exit of the monochromator, one can have, not only light of wavelength λ_1 (the wavelength that satisfies the equation when $|m| = 1$), but also light of wavelength $\lambda_2 = \frac{\lambda_1}{2}$ for $|m| = 2$, light of wavelength $\lambda_3 = \frac{\lambda_1}{3}$ for $|m| = 3$, and so on.

Usually, only the first order (positive or negative), is desired, and nowadays gratings are optimized so that the fraction of the light diffracted into the first order (called grating efficiency in the first order) is much higher than the fraction of the light diffracted into the other orders[1]. However, the efficiency of any grating in the first order is never 100 %, and what is more, this efficiency is wavelength dependent. The wavelength for which the grating efficiency in the first order is maximum is denoted *blaze wavelength* of the grating.

---

[1] The diffraction efficiency in any given order can be "tuned" by changing the groove facet angles, shape or depth.

Appendix C

Description of the *scan machine* used to measure the uniformity in the response of the used PMTs

In this section I will briefly describe the machine that I used to measure the uniformity in the response of the ET 9116A and 9117A PMTs. This machine, that we named *scan machine*, is a home-made device [60].

The *scan machine* consists of two stepper motors (controlled by software) with the proper mechanical support so that the movement of one of them (*first motor*) turns the PMT in θ direction and the movement of the other one (*second motor*) makes it turning in ϕ (see figure 4.10), preserving always the incident angle of a light beam with the hemispherical PMT entrance. A photo of the device is shown in figure C.1.

The top part of the machine (the piece where the PMT is plugged to), can be moved along the *Z axis*[1]. Hence the position of the PMT can be adjusted along the *Z axis* so that the location of the entrance window is set appropriately according to the rotation axis of the *first motor*. It is mandatory that the rotation axis of the *first motor* passes through the center of the hemispherical window of the PMT, otherwise, when moving the motor in order

---

[1] *Z axis* is defined in figure 4.10

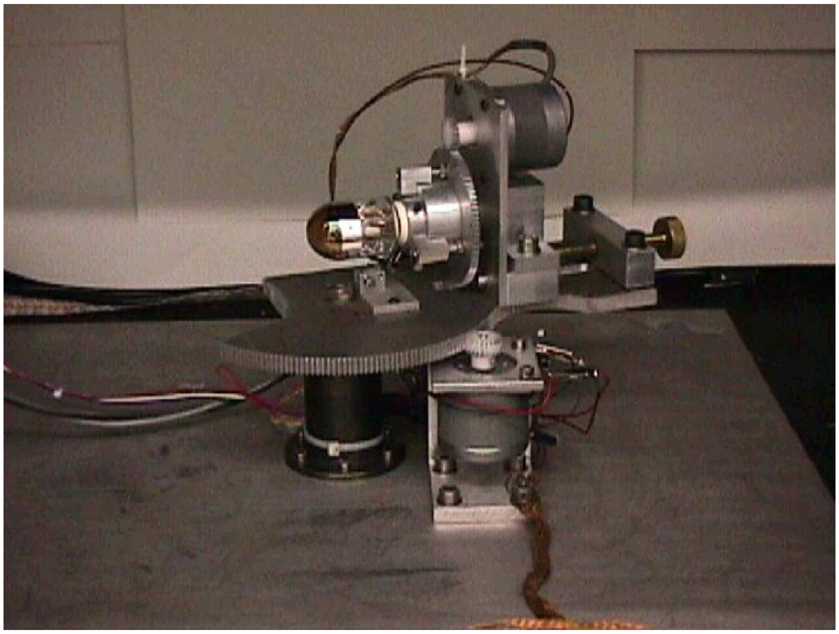

Figure C.1: *Photograph of the machine that was used to perform the spatial response uniformity measurements.*

to produce a rotation of θ_0 in the photocathode, the real effect would be a rotation of θ_0' on the top of a translation along *Z axis*. Consequently, the position of the light spot on the *PhC* would be wrong, and besides the incident angle of the light beam with respect to the entrance window would change.

The intrinsic resolution of both motors is 1.8 degrees. However, they work in combination with teeth plates that introduce a demultiplication factor of 10 and 4.5 for the *first motor* and the *second motor* respectively. Thus, the resolution of the *scan machine* is 0.18° in θ and 0.4° in ϕ direction.

The position accuracy provided by the *scan machine* is limited by the longitudinal alignment of the rotation axis of the *first motor* with the center of the hemispherical window of the PMT. The accuracy in this alignment[2] is $\lesssim 1$ *mm*. This produces an uncertainty in θ below 4° at the largest θ angle measured, which is ∼80°. At lower θ angles, the uncertainty

---

[2] The spread in the radius of the hemispherical entrance window (∼0.3 *mm*, according to the specifications provided by the company) has been taken into account.

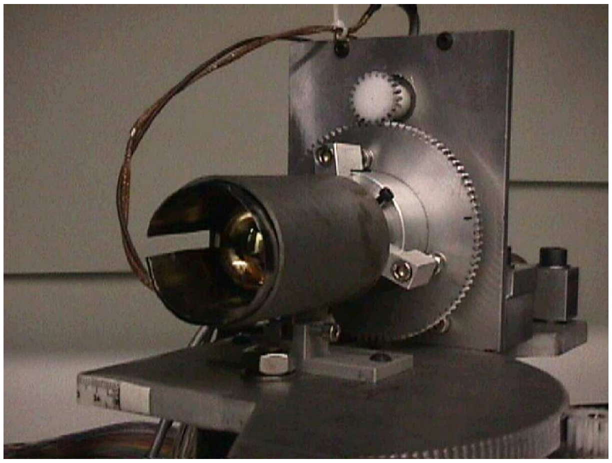

Figure C.2: *Photograph of the mechanical support for the magnetic shield.*

is smaller.

The stepper motors are controlled by LabView routines in combination with a *DCI SmartLab 8255/8253 I/O card* plugged to the computer, a logic circuit implemented in a ALTERA PLD, and a home-made driver that provides the right current to the motors.

As shown in figure C.2, the *scan machine* has also a mechanical support that holds a thin sheet of μ-metal that screens the PMT from the magnetic field, either the Earth's one or the one produced by the stepper motors themselves. With this configuration, the effects produced by the magnetic field on the PMT current measurements were found to be $\lesssim 2\%$. This effect was quantified by attaching the optic fiber (that brings the light from a blue LED) to the pole point of the entrance window and then, comparing the currents read out when the PMT is rotated in both directions θ and ϕ. Regardless to the position of the PMT, the light spot is always in the same point *(θ,ϕ)* of the *PhC*, and hence the variations in the current measured can only be due to the effect produced by the magnetic field on the trajectories of the electrons.

The *scan machine* is placed inside a metallic black box of 80.5 *cm* height, 80.5 *cm* width and 100.5 *cm* length. In this way, the whole system is in an ideal dark environment and protected from external electronic noise.

The blue LED used as a light source is located outside the metallic black box. The emitted light is transferred into the box by means of an optical fiber, and then it is collimated. The collimator (not shown in figure C.1) is usually located at a distance of 2.5 cm from the hemispherical entrance window of the PMT, and it produces a light spot of about 1.5 mm diameter onto the PMT window. The variations in the light intensity produced by the LED were measured to be $\lesssim 1\%$ in 200 minutes.

The Keithley 6517A electrometer used to read out the PMT DC currents is also located outside the metallic box in order to minimize the electronic noise in the measurement setup.

Further details about the performance of the *scan machine* can be found in [60].

Appendix D

Description of the setup used to evaluate the performance of the optical link system

In this section I will describe with some detail all the elements of the setup used to evaluate the optical links, as well as the noise performance of this setup. The appendix is divided into two parts; the first one describes the setup used to test the optical links when the VCSELs are connectorized, and the second one describes the setup used to evaluate the performance of the bare (non-connectorized) VCSELs.

D.1 The setup used to test the optical links with connectorized VCSELs

The schematic of this setup was already presented in figure 5.5. A photograph of the elements of the system is shown in figure D.1. The photograph shows the test transmitter board, the 2 test receiver boards, the 1 m long optical fibers (orange) and the 4 digital oscilloscopes used in the tests. The pulse generator and the computer that controls the oscilloscopes are not shown in the picture.

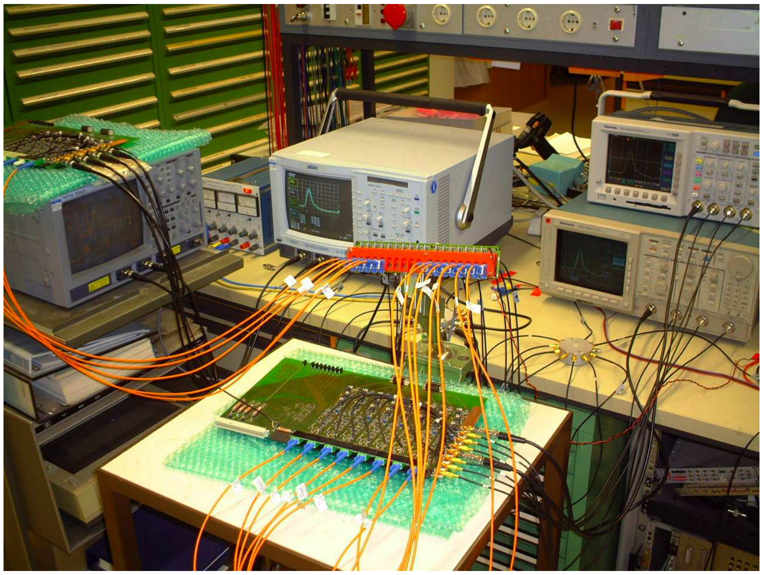

Figure D.1: *Photograph of the experimental setup that was used to evaluate the performance of the optical link system.*

The *input pulses* are generated by the a pulse generator and attenuated according to our needs by a passive attenuator. The pulse generator is a home-made device. The initial pulses of 2.6 *ns* FWHM have an amplitude of 940 mV, and are produced at a frequency of 40 *kHz*. The amplitude of the pulses can be modified with the passive attenuator in steps of 1 dB up to 120 dB with basically no distortion in the pulse shape. After the attenuator, the FWHM of the pulses degrade slightly to 2.7 *ns*.

In order to be able to measure several channels simultaneously, we split this signal by means of passive splitters (they contain only resistors). We used one 2-way splitter and two 10-way splitter (grey cylinders in figure D.1), hence producing 20 equal pulses with an amplitude 20 times lower than the initial pulse. The shape of the pulse is not affected by the passive splitters. Out of these 20 equal signals available, 13 were fed to the transmitter board (center of figure D.1)[1].

The transmitter board used in this setup is identical to the ones installed in the camera

---

[1] The maximum number of channels that can be read simultaneously is limited by the number of oscilloscopes (oscilloscope channels actually) available.

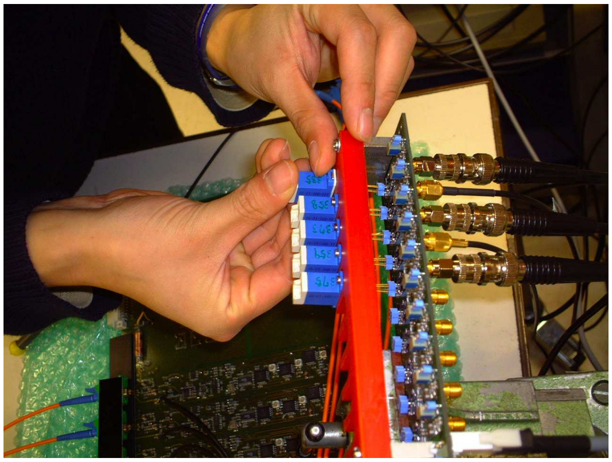

Figure D.2: *Replacement of VCSELs in the test transmitter board that was used in the evaluation of the optical link system.*

of the telescope (see section 3.3.3). The only difference is that the one shown here is modified mechanically so that the VCSELs are not soldered to the electronic circuit, but plugged into. In this way one can exchange easily the VCSELs that have to be tested, as it is shown in figure D.2.

The light pulses produced by the VCSELs are fed to 1 m long multimode graded index fibers (the same kind of fibers that are used in the telescope), which transport them to the 2 test receiver boards (see figure D.1). Because of the low attenuation in the fibers (3 dB/km at 850 nm and 500 MHz), there was no need to use fibers of equal length to the ones used in the telescope. As I discussed in section 5.3, we found basically no differences in the shape of the pulses transmitted via optical fibers of different lengths; and it would have been quite inconvenient to work with 13 channels using 162 m long fibers.

The two test receiver boards used in this setup are also identical to the ones used in the telescope. The only difference is that the signal is taken directly after the transimpidance amplifier, just before the low/high gain branches of the receiver board (see section 3.3.3). The reason for doing that is to disentangle the optical system (which is the system under study) from the rest of the electronic chain.

Finally, the output signals of the receiver boards are fed to the digital oscilloscopes, where the pulses are digitized and the area under the pulse measured. We used four oscilloscopes; all them with an input bandwidth of 500 MHz: the Lecroy LC564 (4 channels, 2 Gsample/s), the Tektronix 3054B (4 channels, 4 Gsample/s), the Tektronix 640A (4 channels, 2 Gsample/s) and the Lecroy 9163C (2 channels, 5 Gsample/s). One of the signals coming from one of the 10-way splitter, is sent directly to one of the channels of the Lecroy 9163C in order to monitor constantly the *input pulses*.

The performance of this measuring setup was evaluated by sending the split pulses directly to the 14 channels of the oscilloscopes. The oscilloscopes took measurements almost simultaneously every 5 s during more than 10 hours (about 8000 measured pulses by every oscilloscope channel). In this way, we could characterize and compare the signals measured by the channels of all the oscilloscopes. We found that the relative *RMS* of the measured area depends slightly on the amplitude of the used *input pulses*, and that there are small variations ($\lesssim$ 10% of the measured *RMS* value) among the different oscilloscopes[2]. When the amplitude of the pulses fed to the oscilloscopes is 40 mV, which is the amplitude of the typical *output pulses* used in the VCSEL selection tests (see section 5.4), the relative *RMS* is somewhat below 1% for all oscilloscopes[3]. We also found that the absolute value of the pulse area measured using the different oscilloscopes coincides within about 3%.

It must be pointed out that, in order to get this level of agreement among the used oscilloscopes, one needs to subtract *pedestals* from the measurements on the area of the *output pulses*. I noticed that if the *pedestal area* is not subtracted, the absolute areas measured for the same pulse can differ significantly ($\gtrsim$ 20%) among the different oscilloscopes, and even among the channels of a given oscilloscope. The *pedestals* were estimated by taking measurements while the *input pulses* were attenuated by a large factor (about 100 dB). In this way, there are effectively no *input pulses* going to the oscilloscopes, and all the elements are connected and switched on. Therefore, the area values measured by the oscilloscopes can be considered as reliable *pedestals* in the area measurements. I noticed that these *pedestal areas* are quite large in the Tektronix oscilloscopes, and that they depend substantially on the used vertical

---

[2] Variations among the channels of a given oscilloscope are even smaller; $\lesssim$ 5% of the measured *RMS* value.

[3] When the *output pulse* amplitudes were 10 mV and 160 mV, the measured relative *RMS* were ~2% and ~0.5% respectively.

scale. The procedure used to get the *pedestal areas* for all the oscilloscope channels was set to the following steps: *a)* adjust appropriately the vertical scale of the oscilloscopes in order to measure the *output pulses* coming from the receiver boards; *b)* attenuate the *input pulses* by about 100 dB to ensure no real pulses going into the oscilloscopes; and *c)* record the measured area values provided by the oscilloscopes during 10 minutes (a measurement every five seconds).

It is worth noticing that the fluctuations observed in the area of the pulses transmitted by the optical link were typically more than 3 times larger than the intrinsic noise of this measuring setup. Indeed, in the VCSEL selection, the lasers were rejected if their relative RMS was larger than 12% (see section 5.4), which is a factor 12 larger than the intrinsic noise of this experimental setup. Therefore, we found this measuring system suitable for the study and selection of the VCSELs.

D.2 The setup used to evaluate the performance of the non-connectorized VCSELs

In order to perform the *bias current scan tests* on non-connectorized VCSELs (the so-called *naked* VCSELs), I introduced some modifications in the measuring setup described in section D.1. The optical link system (transmitter board, optic fibers and receiver board) was replaced by boards where the *naked* VCSELs are plugged and shine directly onto the PIN diodes. Figure D.3 shows a photograph of this setup. The pulse generator, the passive attenuator, the 10-way splitter (located on the white table) and the oscilloscopes are the same that were used in the setup to test connectorized VCSELs.

Figure D.4 shows a picture of one of the above mentioned boards opened; the VCSEL is plugged to the top part (left side in figure D.4), and the PIN-diode that measures the light emitted by the VCSEL is located at the bottom part (right side in figure D.4). Because of the geometry of the system, only light emitted with a beam divergence smaller than 20° can impinge onto the PIN diodes.

In these boards, the signal is also amplified by a factor 4 before reaching the VCSELs, in

Figure D.3: *Photograph of the experimental setup that was used to evaluate the performance of non-connectorized VCSELs.*

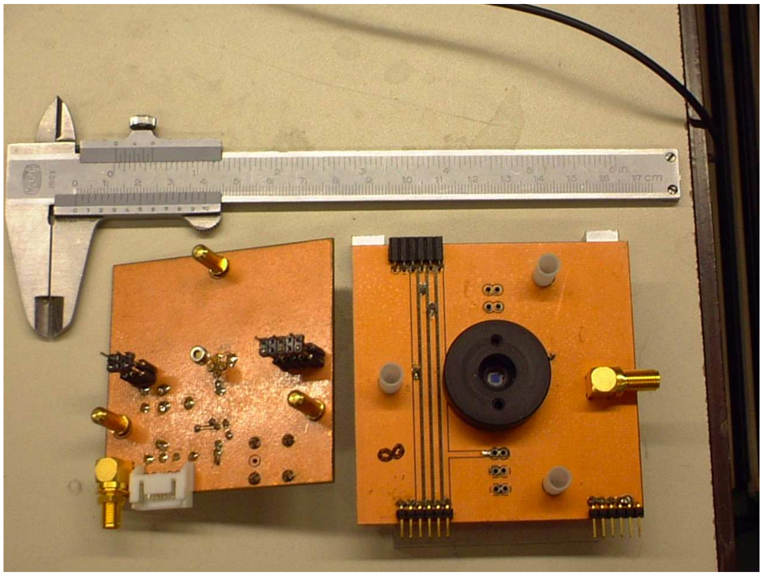

Figure D.4: *Photograph of one of the dedicated boards that was used to evaluate the performance of non-connectorized VCSELs.*

order to be consistent with the transmitter boards used in the optical links.

The forward current applied to the VCSELs is adjusted by a digital potentiometer that can be controlled by the serial port of a PC through a home-made microcontroller (visible in the bottom right corner of figure D.3). The Keithley picoamperimeter (visible also in figure D.3), is used to monitor such forward current, and is also controlled by the computer through GPIB connection. The control of the bias current setting through the computer allowed us to automatize the *bias current scan tests*, speeding up the VCSEL selection tests. Our electronic engineers built 8 of these boards, which allowed us to measure 8 VCSELs simultaneously. The test was performed from 5 mA to 7 mA, in steps of 0.05 mA. At each bias current, 120 pulse measurements were taken (a measurement every 2 seconds during 4 minutes) for each of the VCSELs being tested, and the standard deviation and mean pulse area were computed.

Appendix E

Comparison between experimental data and Monte Carlo data

In this section I will compare the distributions of some basic image parameters for simulated data and real data taken with MAGIC during the night 14th-15th February 2004. First I will discuss the agreement between simulated hadrons and real hadrons, and then I will do the same exercise for simulated gammas and "real" gammas.

Figure E.1 shows a comparison of the distributions of the image parameters LENGTH, WIDTH, DIST and ALPHA for simulated hadrons and real hadrons. The filter cuts defined in section 6.3.2 have been applied to both, simulated and real data. The real data is *OFF data* from the Crab observations, where the source dependent parameters have been calculated with respect to the center of the camera. The used simulated hadrons are those described in section 6.1.4.

The distributions of LENGTH and WIDTH values are similar, but there are still some differences. The somewhat smaller LENGTH values in the real hadrons (compared to those in the simulated hadrons) could be explained by the higher noise (*LONS* and electronic noise) in the real data: the pedestal *RMS* (RMS^{Ped}) of the inner pixels in the Monte Carlo data is 6.6 photons, whereas the one in the real data is about 15 photons[1]. Yet this explanation

---

[1] The RMS^{Ped} of the pixels varies with the pixel and the run considered. Typically it is in the

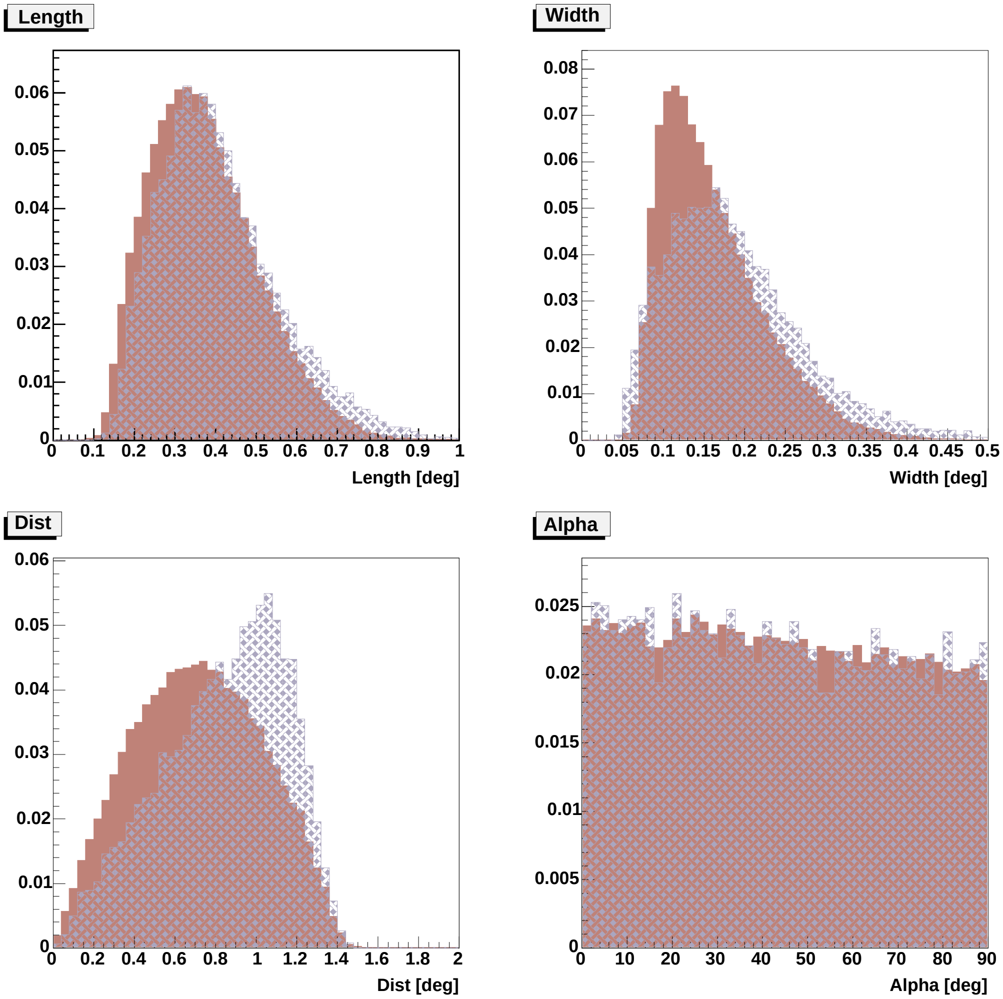

Figure E.1: *Distribution of LENGTH, WIDTH, DIST and ALPHA parameters for shower images from real hadrons (brown filled histograms) and shower images from simulated hadrons (blue shadow filled histograms). The real hadrons are from OFF observations of Crab. The source dependent parameters DIST and ALPHA are calculated with respect to the camera center. All distributions are normalized to unit area for a better comparison. The filter cuts defined in section 6.3.2 (which include the cut SIZE $>$ 2000 photons) have been applied.*

does not hold for the distributions of the WIDTH parameter, where the real hadrons show a quite sharp peak around 0.12°, which is not present in the simulated hadrons. There are also differences in the distributions of the DIST parameter, which are so far not well understood either. On the other hand, the distributions of the ALPHA parameter agree very well. This is a very satisfactory result, since (in the analysis presented in this thesis) ALPHA is the most relevant parameter in the determination of the *background* contained in the *signal*.

The major differences between simulated data and real data are in the SIZE value. Figure E.2 shows the SIZE distributions for simulated hadrons and real hadrons. The same filter cuts have been applied as before, but this time without the cut in SIZE.

In the simulated data there are events down to 150 photons, whereas there are no events below 300 photons in the real data. This is a consequence of two effects:

- *The differences in the* RMS^{Ped} *of the pixels.* The image cleaning (explained in section 6.3.2) requiring at least 6 pixels with a photon signal at least 4 times larger than the RMS^{Ped} sets a low limit to the SIZE of the shower images; which is 160 photons for the simulated data and about 360 photons for the real data. The spread in the RMS^{Ped} observed (for the different pixels) in the experimental data allows some shower images with SIZE $\lesssim$ 360 photons to survive the image cleaning.

- *The differences in the (optical) point spread function.* The point spread function in the used Monte Carlo is a two-dimensional Gaussian function with a sigma of 7 *mm* in the two directions. However, in the data taken with the telescope in February 2004, the optical point spread in the camera was significantly larger due to the problems with the *AMC* reported in section 6.3.1. Preliminary measurements show an optical point spread which is 3-4 times larger than the one used in the Monte Carlo simulations. The larger optical dispersion occurring in the real data prevents the smallest images to fulfill the trigger conditions, and hence the smaller (compared to the simulated data) number of events at low SIZE values.

---

range 10-20 photons.

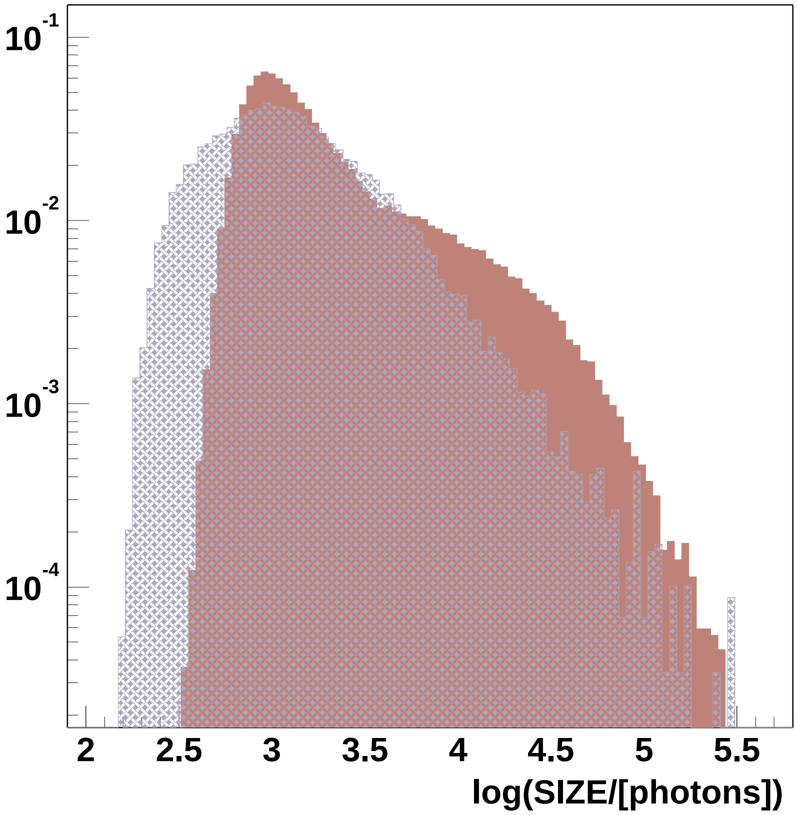

Figure E.2: *Distribution of SIZE values for shower images from real hadrons (brown filled histograms) and shower images from simulated hadrons (blue shadow filled histograms). The real hadrons are from OFF observations of the Crab Nebula. The distributions are normalized to unit area for a better comparison. All filter cuts (but the SIZE cut) defined in section 6.3.2 have been applied.*

In addition, the real data show a clear change of slope at about 3000 photons[2], which is not present in the distribution of the simulated hadrons. The origin of this "bump" is still under investigation.

The agreement is better between the distributions of the simulated gammas and the *ON data* (from Mkn 421) after the γ/h *separation cuts* and the cut ALPHA $< 6^\circ$, which is a sample of "real detected gammas". Note from figure 6.14 that the sample of 2194 ± 47 events used as "real gammas" is actually contaminated with 849 ± 19 (*i.e,* 39%) background events. Hence we do not have a "pure" sample of "real gammas", but a sample of "real gammas" plus hadrons whose images survive a selection criteria for gammas (*i.e,* "γ-like hadrons").

The distributions of the image parameters LENGTH, WIDTH, DIST and ALPHA for simulated gammas and "real gammas" are shown in figure E.3. The sample of simulated gammas used for this comparison is the one described in section 6.1.4. The filter cuts defined in section 6.3.2 have been applied to both, simulated and real data[3]; but no γ/h *separation cuts* were applied to the simulated gammas. In the computation of the distribution of the parameter ALPHA for the "real gammas" the cut in ALPHA was obviously not applied, and the background content estimated from the fit function shown in figure 6.14 was subtracted from the *ON data* surviving the γ/h *separation cuts.*

There are subtle differences in the distributions of the shape parameters LENGTH and WIDTH. The LENGTH values of the "real gammas" are slightly smaller than those of the simulated gammas (as it is also observed in the hadrons), whereas the WIDTH values of the simulated gammas are somewhat smaller than those of the the "real gammas". The smaller WIDTH in the simulated gammas could be due to the substantially smaller optical point spread function of the Monte Carlo with respect to the actual optical point spread of the telescope in February 2004. The WIDTH parameter is more sensible than the LENGTH parameter to the optical quality of the shower images. Hence the differences in the distributions of the LENGTH parameter could be produced mainly by the different pixel noise

---

[2] The position of the point where the slope changes is sensitive to the image cleaning and the filter cuts applied to the data.

[3] The cut WIDTH $> 0.05^\circ$ was not applied to the simulated gammas.

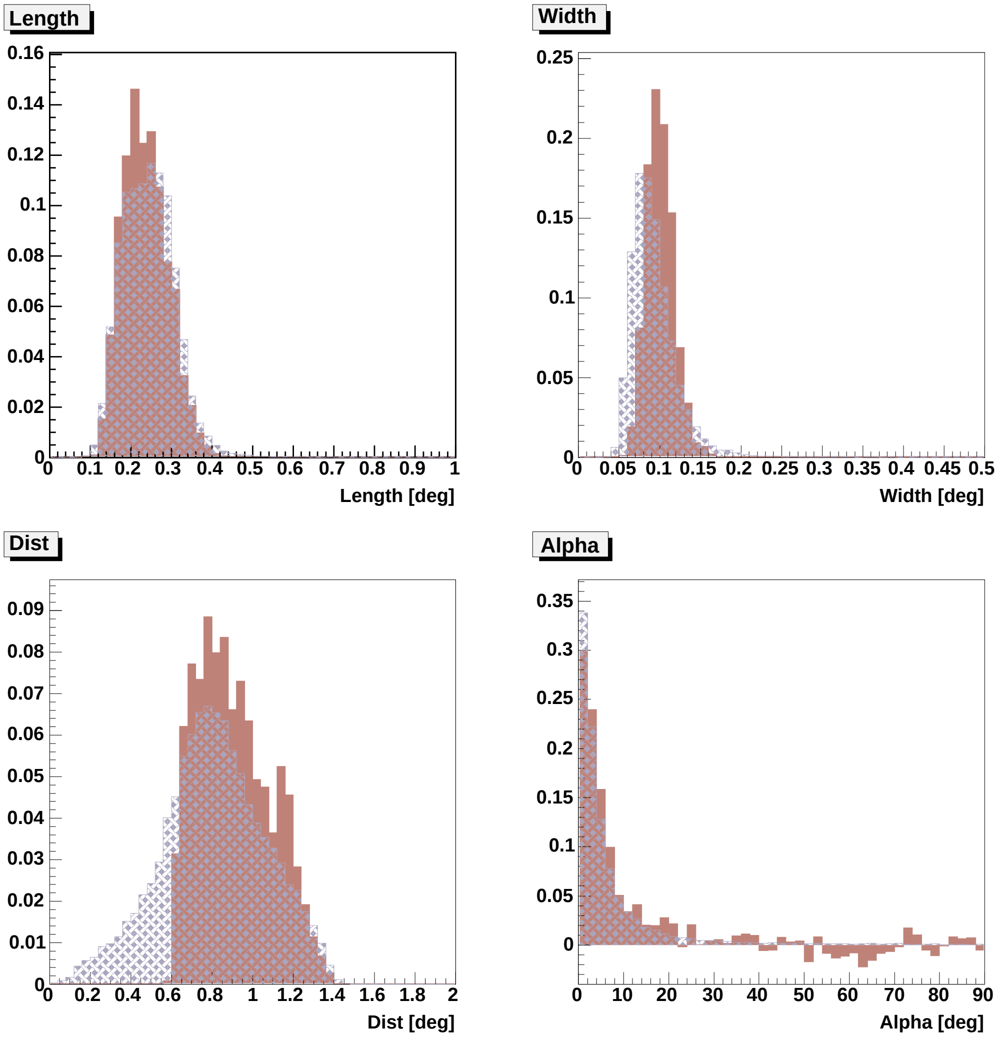

Figure E.3: *Distribution of LENGTH, WIDTH, DIST and ALPHA parameters for shower images from "real gammas" (brown filled histograms) and shower images from simulated gammas (blue shadow filled histograms). The "real gammas" are experimental data from ON observations of Mkn 421 after the application of the optimized γ/h separation cuts defined in section 6.3.5 and the cut ALPHA $<$ 6°. All distributions are normalized to unit area for a better comparison. The filter cuts defined in section 6.3.2 (which include the cut SIZE $>$ 2000 photons) have been applied.*

(RMS^{Ped}), whereas the differences in the WIDTH distributions could be attributed mainly to the different optical point spread between Monte Carlo and real data. In order to test this hypothesis, one should simulate the effect of different optical point spread functions and different pixel noise levels on the telescope camera, which is beyond the scope of this thesis.

On the other hand, the agreement is very good for the distributions of the DIST and the ALPHA parameter. The lack of "real gammas" at DIST $\lesssim 0.6^\circ$ is due to the low cut in the DIST parameter, which was applied to the experimental data and not to the Monte Carlo data.

The distributions of the SIZE parameter for simulated gammas and "real gammas" are shown in figure E.4. The cut SIZE $>$ 2000 photons was not applied in the computation of these distributions. It is worth pointing out that the efficiency of the cuts decreases at SIZE $<$ 2000 photons, and thus the fraction of *background*-induced images surviving the cuts is substantially larger than at SIZE $>$ 2000 photons. When no SIZE cut is applied to the data, the amount of events surviving the cuts is 7148 ± 85, from which 5211 ± 41 (*i.e,* 73%) are estimated to be background events. Therefore, what I call "real gammas" are actually mostly hadrons. However, they are hadrons surviving a selection criteria for gammas[4], and thus they are "γ-like hadrons"; which justifies this exercise.

The discrepancies between "real gammas" and simulated gammas at the lowest SIZE values are similar to those shown for the hadrons. This is expected from the differences in the pixel RMS^{Ped} and the optical point spread function, as discussed before. It is worth noticing from figure E.4 that the "bump" at SIZE $\sim$ 3000 photons observed in the SIZE distribution of the real hadrons (figure E.2) does not exist in the SIZE distribution of the "real gammas". Indeed, the SIZE distributions of the simulated gammas and the "real gammas" agree quite well at SIZE values above 2000 photons (indicated by the dash black line).

---

[4] It should be noted that, because of the reasons discussed in section 6.3.2, the cut optimization was performed restricting the data set to events with SIZE $>$ 2000 photons. Therefore, a good efficiency of the γ/h *separation cuts* below 2000 photons is not granted. The application of this set of cuts (without the cut SIZE $>$ 2000 photons, but with the quality cut SIZE $>$ 300 photons) to the simulated data did not produce a bad result; a $\mathcal{Q}$ of $\sim$1.4, with a E_{th} of $\sim$40 GeV.

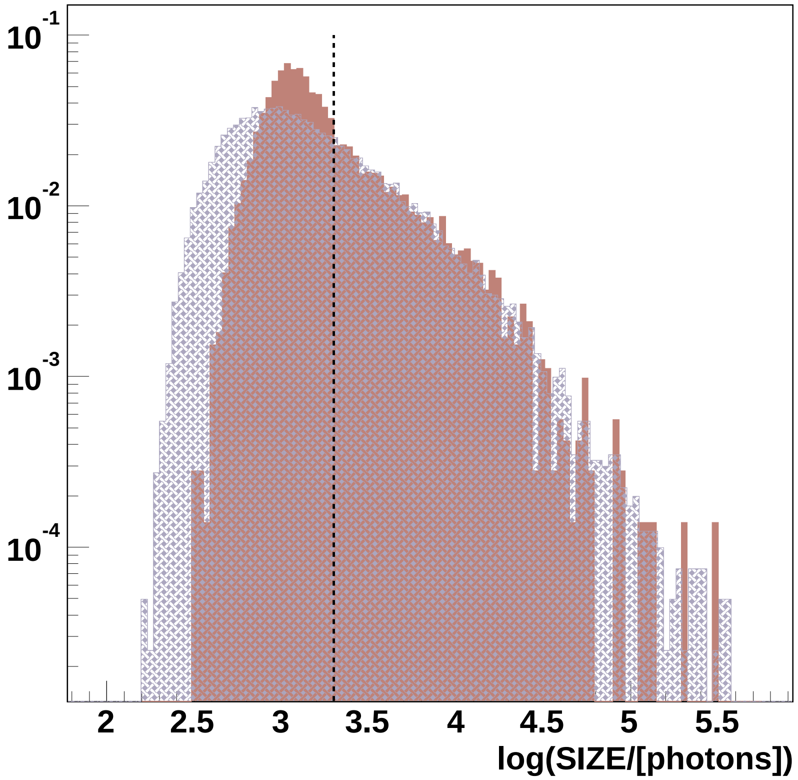

Figure E.4: *Distribution of SIZE values for shower images from "real gammas" (brown filled histograms) and shower images from simulated gammas (blue shadow filled histograms). The "real gammas" are experimental data from ON observations of Mkn 421 after the application of the optimized γ/h separation cuts defined in section 6.3.5 and the cut ALPHA $< 6°$. The distributions are normalized to unit area for a better comparison. All filter cuts (but the SIZE cut) defined in section 6.3.2 have been applied. The dashed black line indicates a SIZE value of 2000 photons.*

The distributions of the parameters indicate that the simulated data give a coarse description of the current performance of the telescope provided images with a relatively large light content (SIZE $\gtrsim$ 2000 photons) are considered. However, there are still differences between the simulated and the experimental data which need to be understood. Therefore, we think that the Monte Carlo data can be used as an indicative reference, but so far they can not be used to perform precise calculations.

List of Figures

List of Tables

Bibliography

[1] A. Hillas, Cherenkov light images of *EAS* produced by primary gamma, in *Proceedings of 19th International Cosmic Ray Conference*, volume 3, pages 445–448, 1985.

[2] M. Takeda et al., *Energy determination in the Akeno Giant Air Shower Array experiment*, Astroparticle Physics **19**, 467–662 (2003).

[3] M. Nagano and A. A. Watson, *Observations and implications of the ultrahigh-energy cosmic rays*, Reviews of Modern Physics **72**, 689–732 (2000).

[4] A.M.Hillas et al., *The spectrum of TeV gamma rays from the Crab nebula*, The Astrophysical Journal **503**, 744–759 (1998).

[5] A. Krys et al., *High energy photoproduction in air showers*, Journal of Physics G **17**, 1261–1269 (1991).

[6] M. S. Longair, *High Energy Astrophysics*, Cambridge University Press, 1992.

[7] Y. Tsai, *Pair production and bremsstrahlung of charged leptons*, Reviews of Modern Physics **46**, 815 (1974).

[8] B. Rossi and K. Greisen, Reviews of Modern Physics **13**, 240 (1941).

[9] T. Gaisser, *Cosmic Rays and Particle Physics*, Cambridge University Press, 1990.

[10] J. Nishimura and K. Kamata, Progress in theoretical Physics **7**, 185 (1952).

[11] K. Greisen, Anual Review of Nuclear Science **10**, 63 (1960).

[12] D. Heck et al., CORSIKA: A Monte Carlo Code to simulate Extensive Air Showers, Forschungszentrum Karlsruhe Report FZKA 6019, Technical report, Forschungszentrum Karlsruhe, 1998.

[13] C. Hofmann et al., *Gamma-ray astronomy at high energies*, Reviews of Modern Physics **71**, 897–936 (1999).

[14] *Handbook of Chemistry and Physics*, CRC Press, 77 edition, 1996.

[15] A. Hillas, *The sensitivity of Cherenkov radiation to the longitudinal development of cosmic ray showers*, J. Phys. G: Nucl. Part. Phys. **8**, 1475–1492 (1982).

[16] P.Jacon et al., A data analysis preprocessing: the effect of the Earth magnetic field on the MAGIC shower images, MAGIC internal note, University of Lodz, 2004.

[17] R. de los Reyes et al., Effect of the Earth magnetic field in the MAGIC telescope effective area for gammas, MAGIC internal note, Universidad Complutense de Madrid, 2003.

[18] J. Jelley, *Cherenkov radiation and its applications*, Pergamon Press, 1958.

[19] R. Schwarz, *Development of a LIDAR for Measuring the Atmospheric Transmission for GeV-TeV-Astronomy with the 17 m MAGIC* Telescope, *Diploma Thesis,* Technische *Universität München*, 2002.

[20] J. Albert et al., *A ground-based low-energy threshold gamma-ray telescope: implementation and performance*, Astroparticle Physics, *in preparation* (2004).

[21] D. Petry, *Beobachtung hochenergetischer γ-Strahlung ($E > 1$ TeV) aus Richtung der aktiven Galaxien Mkn 421 und Mkn 501*, PhD thesis, Technische Universität München, 1997.

[22] T. Weekes et al., *Observation of TeV gamma rays from the Crab nebula using the atmospheric Cherenkov imaging technique*, The Astrophysical Journal **342**, 379–395 (1989).

[23] L. Bohec et al., *A new analysis method for very high definition Imaging Atmospheric Cherenkov Telescopes as applied to the CAT telescope*, Nuclear Instruments and Methods A **416**, 425–437 (1998).

[24] M. Naurois et al., Application of an analysis method based on a semianalytical shower model to the first HESS telescope, in *Proceedings of 28th International Cosmic Ray Conference*, volume 5, pages 2907–2910, 2003.

[25] D. Mazin, Parametrisierung der Schauerbilder und semi-analytische Rekonstruktionsmethode, contribution to DPG spring meeting (German Physical Society), Mainz, 2004.

[26] R. Mirzoyan, Constraints in reducing the threshold of Imaging Cherenkov Telescopes, in *Proceedings: Towards a Major Atmospheric Cherenkov Detector V, Berg (South Africa)*, edited by O. de Jager, 1997.

[27] F. Aharonian et al., *The energy spectrum of TeV gamma rays from the Crab nebula as measured by the HEGRA system of imaging air Cherenkov telescopes*, The Astrophysical Journal **539**, 317–324 (2000).

[28] D. Horns et al., *The Crab nebula and pulsar between 500GeV and 80TeV: observations with the HEGRA system of gamma-ray telescopes*, Astronomy and Astrophysics, *in preparation* (2004).

[29] R. Ong, *Very high-energy gamma-ray astronomy*, Physics Reports **305**, 93–202 (1998).

[30] B. Wiebel, Chemical composition in high energy Cosmic Rays, Technical report, Universität Wuppertal, *WUB 94-08*, 1994.

[31] P. Sreekumar et al., *EGRET observations of the extragalactic gamma-ray emission*, The Astrophysical Journal **494**, 523–534 (1998).

[32] S. Hunter et al., *EGRET observations of the diffuse gamma-ray emission from the galactic plane*, The astrophysical journal **481**, 205–240 (1997).

[33] F. Aharonian et al., *The potential of ground based arrays of imaging atmospheric Cherenkov telescopes. I. Determination of shower parameters.*, Astroparticle Physics **6**, 343–368 (1997).

[34] J. Cortina and J. Gonzalez, *The cosmic electron background in low energy atmospheric Cherenkov telescopes: effect of the geomagnetic field.*, Astroparticle Physics **15**, 203–210 (2001).

[35] B. Wiebel-Sooth, PhD thesis, Universität Wuppertal, 1998.

[36] A. Moralejo et al., A first estimate of the MAGIC capabilities using the new MC simulation chain, MAGIC internal note, Universitá di Padova, 2003.

[37] K. Mase et al., Isolated muon study for the MAGIC telescope, in *Proceedings of 28th International Cosmic Ray Conference*, volume 5, 2003.

[38] K. Mase, PhD thesis, *in preparation*, University of Tokyo, 2005.

[39] J. Cortina, Influence of the NSB on the Hillas parameters, MAGIC internal note, Max-Planck-Institut für Physik, 2001.

[40] C. Benn and S. Ellison, *Brightness of the night sky over La Palma*, New Astronomy Reviews **42**, 503–507 (1998).

[41] R. Böck and W. Wittek, Proposal for the standard analysis of MAGIC data, MAGIC internal note, Max-Planck-Institut für Physik, 2002.

[42] W. Wittek, Rotation of the sky image in a camera of telescopes with ALT-AZ mount, MAGIC internal note, Max-Planck-Institut für Physik, 2000.

[43] A. Stamerra et al., NSB rejection with the level 2 trigger, MAGIC internal note, Universitá di Siena and INFN Sezione di Pisa, 2002.

[44] D. Sobczynska, Mmcs from CORSIKA 6019, MAGIC internal note, University of Lodz, 2002.

[45] A. Moralejo, The reflector simulation program v.0.6, MAGIC internal note, Universitá di Padova, 2003.

[46] O. Blanch, How to use the camera simulation program, MAGIC internal note, Institut de Física d'Altes Energies, 2001.

[47] O. Blanch and H. Kornmayer, Detailed Monte Carlo studies for the MAGIC telescope, in *Proceedings of 27th International Cosmic Ray Conference*, 2001.

[48] R. de los Reyes, *Análisis y simulación de datos de telescopios Cherenkov atmosféricos, Diploma Thesis, Universidad Complutense de Madrid*, 2002.

[49] E. Lorenz, The MAGIC telescope project based on a 17 m diameter parabolic solar concentrator, in *Proceedings: Towards a Major Atmospheric Cherenkov Detector IV, Padova (Italy)*, edited by C. M., page 277, 1995.

[50] J. Barrio et al., The MAGIC Telescope, Technical report, 1998.

[51] R. Hartman et al., *The third EGRET catalog of high-energy gamma-ray sources*, The Astrophysical Journal Supplement Series **123**, 79–202 (1999).

[52] M. Mariotti et al., *Commissioning and first tests of the MAGIC telescope*, Nuclear Instruments and Methods A **518**, 188–192 (2004).

[53] M. Martinez, Status of the MAGIC telescope, in *Proceedings of 28th International Cosmic Ray Conference*, volume 5, pages 2815–2818, 2003.

[54] O. Blanch, Measuring cosmological parameters with MAGIC, in *Proceedings of 28th International Cosmic Ray Conference*, volume 5, 2003.

[55] O. Blanch et al., *Testing the effective scale of quantum gravity with the next generation of gamma ray telescopes*, Astroparticle Physics **19**, 245–252 (2003).

[56] N. Tonello, *Misure ottiche e strategie di trigger per il telescopio MAGIC, Diploma Thesis, Universitá di Padova*, 2002.

[57] D. Bastieri et al., The reflecting surface of the MAGIC telescope, in *Proceedings of 28th International Cosmic Ray Conference*, volume 5, page 2919, 2003.

[58] M. Garczarczyk, *Konstruktion und Bau der aktiven Spiegelsteuerung für das 17m Durchmesser MAGIC Cherenkovteleskop für Hochenergie-Gamma-Astronomie, Diploma Thesis, University of Applied Sciences*, 2001.

[59] A. Laille, PhD thesis, *in preparation*, University of California, Davis, 2006.

[60] D. Paneque, *An optical study of the new hemispherical PMTs from Electron Tubes inc., Diploma Thesis, Universitat Autònoma de Barcelona*, 2000.

[61] A. Ostankov et al., *Some studies of the optical properties of the new hemispherical PMTs from Electron Tubes inc.*, IEEE Trans. Nucl. Sci. **48**, 1215–1219 (2001).

[62] E. Lorenz, *Evaluation of new high QE photomultiplier for air Cherenkov telescopes*, Nuclear Instruments and Methods A **518**, 615–618 (2004).

[63] V. Saveliev, *New type of avalanche photodetector with Geiger mode operation*, Nuclear Instruments and Methods A **518**, 560–564 (2004).

[64] N. Otte et al., *The potential of SiPM as photon detector in astroparticle physics experiments like MAGIC and EUSO*, Nuclear Physics B - Proceedings Supplements, *in preparation* (2004).

[65] R. Mirzoyan et al., *On the influence of afterpulsing in PMTs on the trigger threshold of multichannel light detectors in self-trigger mode*, Nuclear Instruments and Methods A **387**, 74–78 (1997).

[66] A. Ostankov et al., *A study of the new hemispherical 6-dynodes PMT from Electron Tubes*, Nuclear Instruments and Methods A **442**, 117–123 (2000).

[67] G.Blanchot et al., in *Proceedings of the IEEE Nuclear Science Symposium, Toronto*, 1998.

[68] A. Karle, *Analog optical transmission of fast photomultiplier pulses over distances of 2 km*, Nuclear Instruments and Methods A **387**, 274–277 (1997).

[69] T. Weekes et al., *VERITAS: the Very Energetic Radiation Imaging Telescope Array System*, Astroparticle Physics **17**, 221–243 (2002).

[70] J. Rose et al., *Fast analog signal transmission for an air Cherenkov photomultiplier camera using optical fibers*, Nuclear Instruments and Methods A **442**, 113–116 (2000).

[71] I. Bond et al., Design and performance of analog fiber optical links used on the Whipple 10 meter air Cherenkov telescope, in *Proceedings of 27th International Cosmic Ray Conference*, 2001.

[72] D. Corti et al., The Trigger System of the MAGIC Telescope: Online Selection Strategies for Cherenkov Telescopes, in *Proceedings of 28th International Cosmic Ray Conference*, volume 5, page 2959, 2003.

[73] D. Bastieri et al., *A two-level pattern trigger for the MAGIC telescope*, Nuclear Instruments and Methods A **461**, 521–523 (2001).

[74] R. Paoletti, The MAGIC level 2 trigger. A user's manual, MAGIC internal note, Universitá di Siena and INFN Sezione di Pisa, 2003.

[75] F.Goebel et al., The Data Acquisition of the MAGIC Telescope, in *Proceedings of 28th International Cosmic Ray Conference*, volume 5, page 2939, 2003.

[76] J. Cortina et al., The FADC readout of the MAGIC telescope, in *Proceedings of VI Towards a Major Atmospheric Cherenkov Detector Workshop*, 1999.

[77] J. Cortina and J. Coarasa, Description of the DAQ raw data format, MAGIC internal note, Max-Planck-Institut für Physik, 2000.

[78] R. Stiehler, *Konzeption, Entwicklung und Aufbau einer FADC-basierten Ausleseelektronik für das MAGIC Teleskop*, PhD thesis, Universität Siegen, 2001.

[79] J. Coarasa et al., Specifications of the digital DAQ modules and their digital inputs, MAGIC internal note, Max-Planck-Institut für Physik, 2002.

[80] T. Schweizer et al., *The optical calibration of the MAGIC telescope camera*, IEEE Transactions of Nuclear Science (2001).

[81] L. Holl et al., IEEE Transactions of Nuclear Science **35** (1988).

[82] R. Mirzoyan, in *Proceedings of IV Worshop towards a Major Cherenkov Atmospheric Detector*, 1995.

[83] M. Gaug and T. Schweizer, Calibration analysis for the MAGIC telescope, MAGIC internal note, Institut de Física d'Altes Energies, 2002.

[84] M. Gaug et al., An absolute light flux calibration for the MAGIC telescope, in *Proceedings of 28th International Cosmic Ray Conference*, volume 5, page 2923, 2003.

[85] M. Gaug, PhD thesis, *in preparation*, Universitat Autònoma de Barcelona, 2005.

[86] G. Eigen and E.Lorenz, *A method of coating photomultipliers with wavelength shifters*, Nucl.Instrum. Methods Phys. Res. Sect A **167**, 405 (1979).

[87] A. Sommer, *Photoemissive Materials*, Robert E Krieger, 1980.

[88] *Photomultiplier tube handbook, principle to application*, Hamamatsu, 1994.

[89] R. Mirzoyan et al., 3rd International Workshop on Photodetection Developments, Paris, 1996.

[90] F. Dazzi, *Realizzazione ed analisi del trigger di livello 1 del telescopio MAGIC, Diploma Thesis, Universitá di Padova*, 2001.

[91] J. Tatum and J.K.Guenter, The VCSELs are coming, in *SPIE Proceedings*, volume 4994, Issue 2.0.

[92] B. Dinkespiler et al., *Development of an analogue optical link for the front-end readout of the ATLAS electromagnetic calorimeter*, Nuclear Instruments and Methods A **431**, 531–547 (1999).

[93] J. Lozano-Bahilo et al., *A linear optical link using radiation hard VCSELs*, Nuclear Instruments and Methods A **461**, 530–536 (2001).

[94] M. Punch et al., *Detection of TeV photons from the active galaxy Markarian 421*, Nature **358**, 477–478 (1992).

[95] J. Gaidos et al., *Extremely rapid bursts of TeV photons from the active galaxy Markarian 421*, Nature **383**, 319–320 (1996).

[96] F. Aharonian et al., *Variations of the TeV energy spectrum at different flux levels of Mkn 421 observed with the HEGRA system of Cherenkov telescopes*, Astronomy and Astrophysics **393**, 89–99 (2002).

[97] T. Schweizer, *Analysis of the large gamma ray flares of the Mkn 421 as observed with HEGRA CT1 on the island La Palma in 2001*, PhD thesis, Universitat Autònoma de Barcelona, 2002.

[98] P. Reynolds et al., The Astrophysical Journal **404**, 206 (1993).

[99] W. Wittek, Image parameters, MAGIC internal note, Max-Planck-Institut für Physik, 2002.

[100] D. Kranich, *Temporal and spectral charactersitics of the active galactic nucleus Mkn 501 during a phase of high activity in the TeV range*, PhD thesis, Technische Universität München, 2002.

[101] I. Bond et al., *An island method of image cleaning for near threshold events from atmospheric Cherenkov telescopes*, Astroparticle Physics **20**, 311–321 (2003).

[102] D. Sobczynska and E. Lorenz, *Simulation of the trigger performance of air Cherenkov telescopes for gamma-astronomy*, Nuclear Instruments and Methods A **490**, 124–131 (2002).

[103] B. Wiebel-Sooth et al., Astronomy and Astrophysics **330** (1998).

[104] V. Fomin, *New methods of atmospheric Cherenkov imaging for gamma-ray astronomy*, Astroparticle physics **2**, 137–150 (1994).

[105] W. Wittek, A proposed mode of observation for MAGIC, MAGIC internal note, Max-Planck-Institut für Physik, 2003.

[106] T.Bretz and R.Wagner, The MAGIC Analysis and Reconstruction Software, in *Proceedings of 28th International Cosmic Ray Conference*, volume 5, pages 2947–2950, 2003.

[107] T. Bretz, PhD thesis, *in preparation*, Universität Würzburg, 2005.

[108] Li and Ma, *Analysis methods for results in gamma-ray astronomy*, The Astrophysical Journal , 317–324 (1983).

[109] D. Kranich, *Verbesserung der Gamma/Hadron-Trennung in der Hochenergie Gamma Astronomie mit Cherenkov Teleskopen, Diploma Thesis, Max-Planck-Institut für Physik*, 1997.

[110] Minuit users guide, Technical report, *Program Library D506*, CERN, 1994.

[111] E. Popov and E. Loewen, *Diffraction gratings and applications*, Marcel Dekker, 1997.

[112] *The book of photon tools*, Oriel instruments, 1996.

List of acronyms and abbreviations

ADC	analogue to digital converter
A_{eff}	collection area
AGN	active galactic nuclei
AMC	active mirror control
APD	avalanche photodetector
ASM	all sky monitor
CANGAROO	collaboration of australia and nippon for a gamma ray observatory in the outback
CE	photoelectron collection efficiency
COG	center of gravity
CGRO	Compton gamma ray observatory
*CR*s	cosmic rays
DAQ	data acquisition
EAS	extensive air shower
EBL	extragalactic background light
E_c	critic energy
EEL	edge emitting laser
EGRET	energetic gamma ray experiment telescope
ENC	equivalent noise charge
ET	Electron Tubes
E_{th}	threshold energy
F	excess noise factor
FADC	flash analogue to digital converter
FiFo	first input first output
FOV	field of view
FWHM	full width at half maximum
GBPS	giga bit per second
GLAST	gamma ray large area space telescope
GRB	gamma ray burst
HEGRA	high energy gamma ray astronomy
HESS	high energy stereoscopic system
HPD	hybrid photodetector
HV	high voltage
IACT	imaging air Cherenkov telescope
LDE	light detection efficiency
LED	light emitting diode
LONS	light of the night sky
LUT	look up table
NSB	night sky background
MAGIC	major atmospheric gamma ray imaging Cherenkov
Mkn	Markarian
PhC	photocathode
phe	photoelectron

PLD	programable logic device
PMT	photomultiplier
PTP	1.4 p-Terphenyl
$\mathcal{Q}$	quality factor
QE	quantum efficiency
RMS	root mean square
RXTE	Rossi X-ray timing explorer
RF	reference point
SiPMT	silicon photomultiplier
SNR	supernova remnant
STACEE	solar tower atmospheric Cherenkov effect experiment
TDR	technical design report
UV	ultraviolet
VCSEL	vertical cavity surface emitting laser
VERITAS	very energetic radiation imaging telescope array system
WLS	wavelength shifter
W_{th}	work function
ZA	zenith angle

Acknowledgments

First of all I would like to thank Prof. Dr. Siegfried Bethke for providing me with the opportunity to do a doctoral thesis at Max-Planck-Institut für Physik München. My stage at München has been a very fruitful experience from both personal and professional point of view.

Then I would like to thank Dr. Eckart Lorenz for supervising closely my work during the three years of my PhD. Eckart is a very experienced physicist, full of energy and new ideas. It is unquestionable that without him there would be no MAGIC Telescope in La Palma by now. I have had very many discussions with him. I must say that in some of them we did not achieve a final solution/agreement; but absolutely all them provided me with a better understanding of the problem. I have definitely learnt very many things from him, and not only about physics.

I am also very grateful to Dr. Wolfgang Wittek, with whom I have discussed every single step I did in the analysis of the data from the MAGIC Telescope. Because of his character, modest and quiet, many people do not realize about the tremendous amount of work that Wolfgang has done so far. Besides, he spends quite some time and effort in the coordination of the many inexperience PhD students and young postdocs (within the MAGIC collaboration) who work in software and analysis related issues. He has helped me a lot also in the last (and tougher) stages of my thesis.

I would like to thank also other people who have contributed substantially (directly or indirectly) to the work presented in this thesis. Among them, there is Dr. Razmik Mirzoyan from who I have learnt many things related to Cherenkov telescopes, electronics and enjoyed many funny stories. I want to thank also Dr. Abelardo Moralejo for all the many exhaustive discussions related to the Monte Carlo simulations of MAGIC; and Dr. Antonio Coarasa for, among other things, enlightening me with the marvellous world of *Apple*.

I wish to thank many more people working at MPI, who have provided me with a very friendly working environment and an excellent team work. Among them there are senior scientists like Rudy Bock and Masahiro Teshima; engineers like Jürgen Gebauer, Si Tran, Wendelin Pimpl and Ronald Maier; young postdocs like Florian Goebel and Kenji Shinozaki; and many PhD students who I have had the pleasure of working with (or partying with) at a given moment of my PhD, like Daniel Mazin, Keiichi Mase, Nadia Tonello, Hendrik Bartko, Robert Wagner, Markus Garczarczyk, Nepomuk Otte, Mustapha Laatiaoui, Masaaki Hayashida, Vincenzo Vitale, Satoko Mizobuchi and the just arrived Pratik Majumdar.

Last, but not least, I would like to express my sincerely gratefulness to Sybille Rodriguez, Ina Wacker and Ursula Grenzemann for helping me with the most difficult part of my PhD; the buroCRAZY !!!